

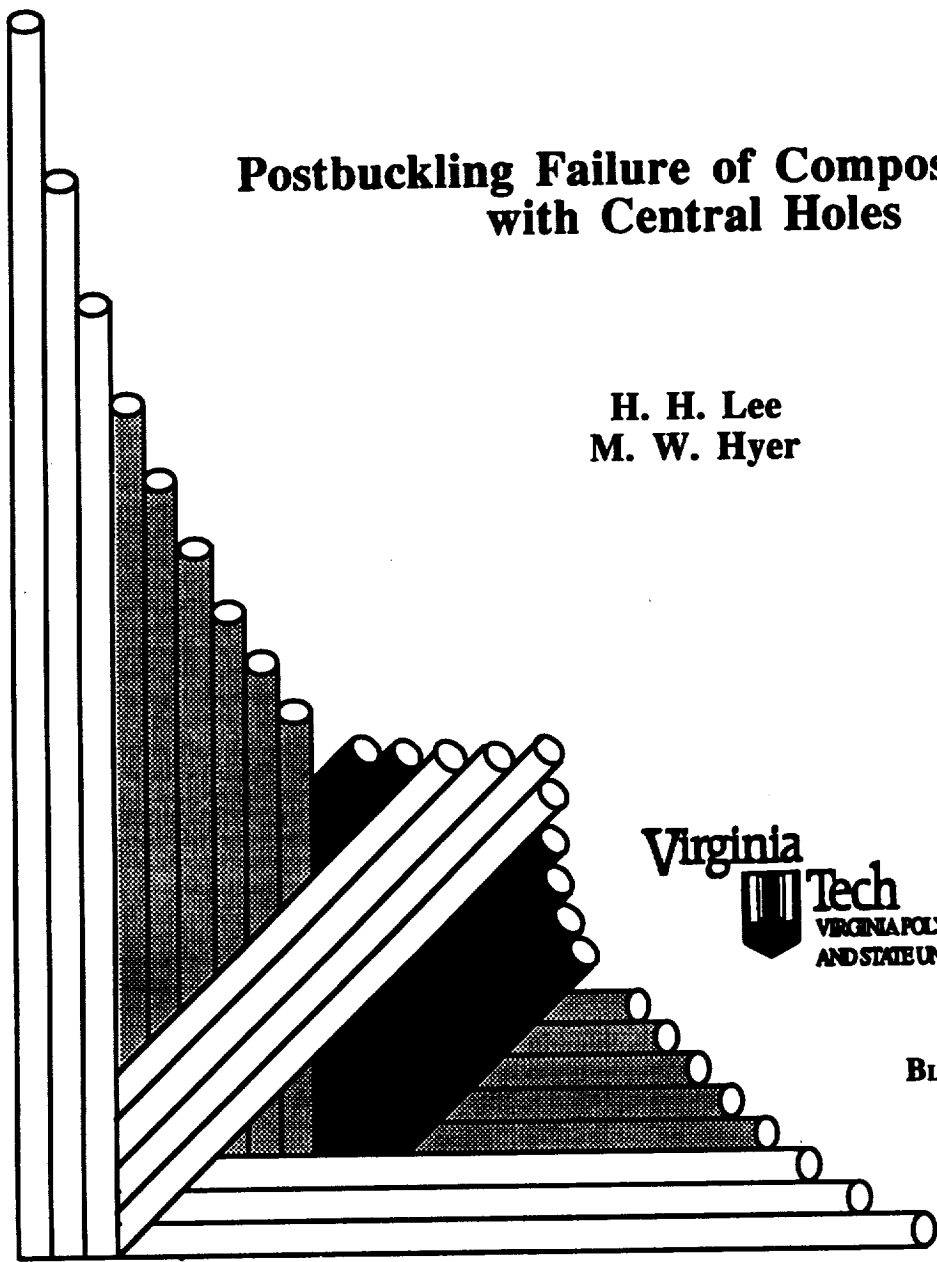
CCMS-92-07
VPI-E-92-07

CENTER FOR COMPOSITE MATERIALS AND STRUCTURES

11-11-90
11-24-90
3/10/91
p-331

Postbuckling Failure of Composite Plates with Central Holes

H. H. Lee
M. W. Hyer



Virginia
Tech
VIRGINIA POLYTECHNIC INSTITUTE
AND STATE UNIVERSITY

BLACKSBURG, VIRGINIA
24061

February 1992

(NASA-CR-190210) POSTBUCKLING FAILURE OF
COMPOSITE PLATES WITH CENTRAL HOLES Interim
Report, Feb. 1990 - Dec. 1991 Ph.D. Thesis
(Virginia Polytechnic Inst. and State Univ.)
331 p

N92-22250

Unclas
CSCL 20K G3/39 0084153



College of Engineering
Virginia Polytechnic Institute and State University
Blacksburg, Virginia 24061

February 1992

VPI-E-92-07
CCMS-92-07

***Postbuckling Failure of Composite Plates
with Central Holes***

H.H. Lee¹
M.W. Hyer²

Department of Engineering Science and Mechanics

Performance period:
February 1990 - December 1991

NASA Grant NAG-1-901
February 1992

Technical Monitor: Dr. Michael P. Nemeth
Aircraft Structures Branch
National Aeronautics and Space Administration
Langley Research Center
Hampton, Virginia 23665-5225

¹ Research Associate

² Professor



ABSTRACT

The postbuckling failure of square composite plates with central holes is analyzed numerically and experimentally. The particular plates studied have stacking sequences of $[\pm 45/0/90]_{2s}$, $[\pm 45/0_2]_{2s}$, $[\pm 45/0_6]_s$, and $[\pm 45]_{4s}$. A simple plate geometry, one with a hole diameter to plate width ratio of 0.3, is considered. Failure load, failure mode, and failure locations are predicted numerically by using the finite-element method. The predictions are compared with experimental results. In the experiments in order to be accommodated by the test fixture it is necessary for the plates to be slightly larger than the analysis region, extending somewhat beyond the supports. The region outside the supports is included in the numerical study. It is shown that not considering these regions can lead to erroneous numerical predictions. In numerical failure analysis the interlaminar shear stresses, as well as the inplane stresses, are taken into account. By comparing the interlaminar shear stress calculations from the finite-element method with analytical results for simple cases, a solid foundation for interlaminar shear stress calculation is established. As a failure criterion, the maximum stress criterion is used. A special test fixture was designed for loading the plates. In the experiments, strain gauges, linear variable displacement transducers (LVDT's), and the shadow moire and acoustic emission tests are used to monitor plate response. An issue addressed in the study is the possible mode shape change of the plate during loading. To account for the fact that plates can experience mode shape change, two deformation configurations are considered. One configuration assumes the plate responds with one half-wave in the loading direction and the other configuration assumes the plate responds with two

half-waves in the loading direction. Failure predictions are made for each configuration. No attempt is made to predict the configuration change. However, it is predicted that the first three laminates fail due to excessive stresses in the fiber direction and, more importantly, that the load level is independent of whether the laminate is deformed in the one half-wave configuration or the two half-wave configuration. The location of failure does depend on the deformed configuration. It is predicted that the fourth laminate fails due to excessive inplane shear stress. Interlaminar shear failure is not predicted for any laminate. For the first two laminates the experimental observations correlated well with the predictions. In the experiments the third laminate failed along the side support due to interlaminar shear. The 12 clustered 0° layers resulted in very low interlaminar shear strength S_{23} . The fourth laminate failed due to inplane shear in the location predicted. However, material softening resulted in an actual failure load quite different from the predicted value.

Acknowledgements

The authors wish to express their appreciation for the financial support of Grant NAG-1-901 with the NASA Langley Research Center, Dr. M. P. Nemeth Grant Monitor. The technical advice of Dr. Nemeth is also appreciated.

Table of Contents

1.0 Introduction	1
1.1 Overview	1
1.2 Literature Review	2
1.2.1 Review of Buckling and Postbuckling of Plates with Holes	3
1.2.2 Review of Postbuckling Failure	11
1.3 Problem Studied	14
1.3.1 Description of Problem	14
1.3.2 Approach	16
2.0 Buckling Finite-Element Formulation	21
2.1 Governing Equations	21
2.2 Finite-Element Formulation	27
2.3 Numerical Procedure and Results	29
3.0 Nonlinear Plate Bending With Initial Imperfection	45
3.1 Governing Equations	46
3.2 Finite-Element Formulation	51

3.3	Newton-Raphson Method	52
3.4	Numerical Results	53
3.4.1	Verification of Present Analysis	53
3.4.2	The Effect of the Portion of the Plate Outside the Supports	57
3.4.3	Results for Plates With and Without Holes	60
3.4.4	Mode Changes During Loading	63
4.0	Calculation of Interlaminar Shear Stresses	72
4.1	Formulation	72
4.2	Comparison with Other Solutions	78
4.2.1	Simply Supported Cross-Ply Plate Under Uniform Loading.	79
4.2.2	Interlaminar Shear Stresses in Nonlinear Cylindrical Bending	81
4.3	Results for Plates with Holes	90
5.0	Numerical Failure Analysis	107
5.1	Failure of Plates with Holes	118
5.1.1	The $[\pm 45/0/90]_{2S}$ Plate with a Hole	118
5.1.2	The $[\pm 45/0_2]_{2S}$ Plate with a Hole	126
5.1.3	The $[\pm 45/0_6]_S$ Plate with a Hole	131
5.1.4	The $[\pm 45]_{4S}$ Plate with a Hole	137
5.2	Failure of Solid Plates	142
5.2.1	The Solid $[\pm 45/0/90]_{2S}$ Plate	142
5.2.2	The Solid $[\pm 45/0_2]_{2S}$ Plate	148
5.2.3	The Solid $[\pm 45/0_6]_S$ Plate	154
5.2.4	The Solid $[\pm 45]_{4S}$ Plate	157
5.3	Summary	163
6.0	Description of Experiment	165

6.1	Test Fixture	165
6.2	Test Set-up	180
7.0	Experimental Results and Comparison with Numerical Results	187
7.1	The $[\pm 45/0/90]_{2S}$ Plates	189
7.1.1	Load vs. Deflection Relations	189
7.1.2	Load vs. Strain Relations	196
7.1.3	Shadow Moire Results	203
7.1.4	Failure and Post-Mortem Analysis	212
7.1.5	Acoustic Emission Results	216
7.2	The $[\pm 45/0_2]_{2S}$ Plates	220
7.2.1	Load vs. Deflection Relations	220
7.2.2	Load vs. Strain Relations	226
7.2.3	Shadow Moire Results	234
7.2.4	Failure and Post-Mortem Analysis	240
7.2.5	Acoustic Emission Results	240
7.3	The $[\pm 45/0_6]_S$ Plates	246
7.3.1	Load vs. Deflection Relations	246
7.3.2	Load vs. Strain Relations	251
7.3.3	Shadow Moire Results	251
7.3.4	Failure and Post-Mortem Analysis	262
7.3.5	Acoustic Emission Results	266
7.4	The $[\pm 45]_{4S}$ Plates	269
7.4.1	Load vs. Deflection Relations	269
7.4.2	Load vs. Strain Relations	271
7.4.3	Shadow Moire Results	282
7.4.4	Failure and Post-Mortem Analysis	285
7.4.5	Acoustic Emission Results	285

7.5	Summary of Findings and Further Results	285
8.0	Concluding Comments and Recommendations	298
8.1	Concluding Comments	298
8.2	Recommendations for Future Research	302
9.0	References	304

List of Illustrations

Fig. 1-1	Problem geometry	15
Fig. 2-1	Force resultants, moment resultants, and direction cosines	25
Fig. 2-2	Comparison with Nemeth's angle-ply results [31] for displacement loaded, clamped $[\pm \theta]_{\theta s}$ laminate	32
Fig. 2-3	Four boundary conditions for quarter-plate buckling analysis	36
Fig. 2-4	Buckling mode shapes of $[\pm 45/0/90]_{2s}$ and $[\pm 45]_{4s}$ plates with holes...	40
Fig. 2-5	Buckling mode shapes of $[\pm 45/0_2]_{2s}$ and $[\pm 45/0_6]_s$ plates with holes ...	41
Fig. 2-6	Buckling mode shapes of solid $[\pm 45/0/90]_{2s}$ and $[\pm 45]_{4s}$ plates	43
Fig. 2-7	Buckling mode shapes of solid $[\pm 45/0_2]_{2s}$ and $[\pm 45/0_6]_s$ plates.....	44
Fig. 3-1	Comparison with ABAQUS [47] for load vs. end shortening relation of solid $[\pm 45/0/90]_{2s}$ plate under displacement loaded, clamped condition.....	55
Fig. 3-2	Comparison with ABAQUS [47] for load vs. out-of-plane deflection relation of solid $[\pm 45/0/90]_{2s}$ plate under displacement loaded, clamped condition	56
Fig. 3-3	Plate models to account for the influence of the region outside the supports.....	58
Fig. 3-4	Influence of the region outside the supports on the load vs. end shortening relation	59
Fig. 3-5	Load vs. end shortening relations for plates with holes.....	61
Fig. 3-6	Load vs. end shortening relations for solid plates	62
Fig. 3-7	Load vs. out-of-plane deflection relations for plates with holes	64

Fig. 3-8	Load vs. out-of-plane deflection relations for solid plates.....	65
Fig. 3-9	Load vs. end shortening relations for $[\pm 45/0/90]_{2s}$ plates.....	67
Fig. 3-10	Load vs. end shortening relations for $[\pm 45/0_2]_{2s}$ plates.....	68
Fig. 3-11	Load vs. end shortening relations for $[\pm 45/0_6]_s$ plates.....	69
Fig. 3-12	Load vs. end shortening relations for $[\pm 45]_{4s}$ plates.....	70
Fig. 4-1	Definition of z coordinate and layer interfaces.....	75
Fig. 4-2	Comparison of interlaminar shear stresses between exact solution and FEM solution for a simply supported square $[0/90]_s$ plates under uniform loading.....	82
Fig. 4-3	Boundary conditions for nonlinear cylindrical bending problem.....	85
Fig. 4-4	Comparison of interlaminar shear stresses between exact solution and FEM solution in nonlinear range at center Gauss point in end element for a $[0/90]_s$ laminate in cylindrical bending, $\bar{q} = 1000$	89
Fig. 4-5	Comparison of interlaminar shear stresses between exact solution and FEM solution in nonlinear range at a Gauss point other than the center Gauss point in end element for $[0/90]_s$ laminate in cylindrical bending, $\bar{q} = 1000$	91
Fig. 4-6	Comparison of interlaminar shear stresses between exact solution and FEM solution in nonlinear range at a center Gauss point in end element for $[\pm 45/0/90]_{2s}$ laminate in cylindrical bending, $\bar{q} = 1000$	92
Fig. 4-7	Finite-element meshes and regions of interest used to study interlaminar stresses.....	94
Fig. 4-8	Dependence of the distribution of τ_{xz} through the thickness on mesh size for a $[\pm 45/0/90]_{2s}$ laminate at $P/EA = 0.00152$ at net-section hole edge (Two half-waves in the loading direction).....	95
Fig. 4-9	Dependence of the distribution of τ_{xz} through the thickness on mesh size for a $[\pm 45/0/90]_{2s}$ laminate at $P/EA = 0.00152$ between the net-section hole edge and the simple support (Two half-waves in the loading direction).....	97
Fig. 4-10	Dependence of the distribution of τ_{xz} through the thickness on mesh size for a $[\pm 45/0/90]_{2s}$ laminate at $P/EA = 0.00152$ at net-section extension region outside the simple support (Two half-waves in the loading direction).....	98
Fig. 4-11	Dependence of the distribution of τ_{yz} through the thickness on mesh size for a $[\pm 45/0/90]_{2s}$ laminate at $P/EA = 0.00152$ at net-section just inside the simple support (Two half-waves in the loading direction).....	100

Fig. 4-12	Distribution of interlaminar shear stresses on the midplane of $[\pm 45/0/90]_{2s}$ along the center of the elements at net-section.....	101
Fig. 4-13	Distribution of interlaminar shear stresses on the midplane of $[\pm 45/0/90]_{2s}$ along the center of the elements on hole boundary.....	102
Fig. 4-14	Through-the-thickness distribution of τ_{yz} for each plate at the net-section hole edge.....	104
Fig. 4-15	Through-the-thickness distribution of τ_{yz} for each plate at the net-section simple support	105
Fig. 5-1	Element numbering for a square plate with hole with a 209 element mesh	115
Fig. 5-2	Element numbering for a square solid plate with an 81 element mesh	116
Fig. 5-3	Shape of the $[\pm 45/0/90]_{2s}$ plate with a hole deflected in the one half-wave configuration at $P/EA = 0.00258$	119
Fig. 5-4	Shape of the $[\pm 45/0/90]_{2s}$ plate with a hole deflected in the two half-wave configuration at $P/EA = 0.00255$	121
Fig. 5-5	Failures and load-end shortening relations for the $[\pm 45/0/90]_{2s}$ plate with a hole.....	122
Fig. 5-6	Predicted failure locations and failure modes of the $[\pm 45/0/90]_{2s}$ plate with a hole in the one half-wave configuration	123
Fig. 5-7	Predicted failure locations and failure modes of the $[\pm 45/0/90]_{2s}$ plate with a hole in the two half-wave configuration	125
Fig. 5-8	Failures and load-end shortening relations for the $[\pm 45/0_2]_{2s}$ plate with a hole.....	127
Fig. 5-9	Predicted failure locations and failure modes of the $[\pm 45/0_2]_{2s}$ plate with a hole in the one half-wave configuration	128
Fig. 5-10	Predicted failure locations and failure modes of the $[\pm 45/0_2]_{2s}$ plate with a hole in the two half-wave configuration	129
Fig. 5-11	Failures and load-end shortening relations for the $[\pm 45/0_6]_s$ plate with a hole.....	132
Fig. 5-12	Predicted failure locations and failure modes of the $[\pm 45/0_6]_s$ plate with a hole in the one half-wave configuration.....	134
Fig. 5-13	Predicted failure locations and failure modes of the $[\pm 45/0_6]_s$ plate with a hole in the two half-wave configuration	136

Fig. 5-14 Failures and load-end shortening relation for the $[\pm 45]_{4s}$ plate with a hole.....	138
Fig. 5-15 Predicted failure locations and failure modes of the $[\pm 45]_{4s}$ plate with a hole in the one half-wave configuration.....	139
Fig. 5-16 Predicted failure locations and failure modes of the $[\pm 45]_{4s}$ plate with a hole in the two half-wave configuration.....	141
Fig. 5-17 Shape of $[\pm 45/0/90]_{2s}$ solid plate deflected in the one half-wave configuration at $P/EA = 0.00289$	143
Fig. 5-18 Shape of $[\pm 45/0/90]_{2s}$ solid plate deflected in the two half-wave configuration at $P/EA = 0.00289$	144
Fig. 5-19 Failures and load-end shortening relations for the solid $[\pm 45/0/90]_{2s}$ plate.....	145
Fig. 5-20 Predicted failure locations and failure modes of the solid $[\pm 45/0/90]_{2s}$ plate in the one half-wave configuration.....	147
Fig. 5-21 Predicted failure locations and failure modes of the solid $[\pm 45/0/90]_{2s}$ plate in two half-wave configuration.....	149
Fig. 5-22 Failures and load-end shortening relations for the solid $[\pm 45/0_2]_{2s}$ plate.....	150
Fig. 5-23 Predicted failure locations and failure modes of the solid $[\pm 45/0_2]_{2s}$ plate in the one half-wave configuration.....	152
Fig. 5-24 Predicted failure locations and failure modes of the solid $[\pm 45/0_2]_{2s}$ plate in the two half-wave configuration.....	153
Fig. 5-25 Failures and load-end shortening relations for the solid $[\pm 45/0_6]_s$ plate.....	155
Fig. 5-26 Predicted failure locations and failure modes of the solid $[\pm 45/0_6]_s$ plate in the one half-wave configuration.....	156
Fig. 5-27 Predicted failure locations and failure modes of the solid $[\pm 45/0_6]_s$ plate in the two half-wave configuration.....	158
Fig. 5-28 Failures and load-end shortening relations for the solid $[\pm 45]_{4s}$ plate.....	159
Fig. 5-29 Predicted failure locations and failure modes of the solid $[\pm 45]_{4s}$ plate in the one half-wave configuration.....	161
Fig. 5-30 Predicted failure locations and failure modes of the solid $[\pm 45]_{4s}$ plate in the two half-wave configuration.....	162

Fig. 6-1	Full assembly of the fixture with plate specimen	167
Fig. 6-2	Top assembly of the fixture	168
Fig. 6-3	Bottom assembly of the fixture	169
Fig. 6-4	Bottom frame of the fixture.....	170
Fig. 6-5	Clamped supports.....	172
Fig. 6-6	Supporting block for clamped supports.....	173
Fig. 6-7	Knife edge.....	175
Fig. 6-8	Supporting block for knife edges	176
Fig. 6-9	LVDT bracket.....	177
Fig. 6-10	Close-up of the fixture in load frame	179
Fig. 6-11	Strain gauging locations on the plate specimen	181
Fig. 6-12	Top view of arrangement of LVDT for out-of-plane displacement measurement and shadow moire.....	183
Fig. 6-13	Equipment layout for experimental test.....	185
Fig. 6-14	Photograph for experimental set-up	186
Fig. 7-1	Comparison of load vs. end shortening relations and failure loads for the $[\pm 45/0/90]_{2S}$ plates.....	190
Fig. 7-2	Comparison of displacements measured from LVDT 1 and LVDT 2 for plate 1 and plate 2.....	194
Fig. 7-3	Comparison of load vs. deflection relations and failure loads for $[\pm 45/0/90]_{2S}$ plates.....	195
Fig. 7-4	Experimentally measured strains of plate 1.....	197
Fig. 7-5	Schematic drawing to explain the sign change of strains.....	199
Fig. 7-6	Experimentally measured strains of plate 2.....	201
Fig. 7-7	Comparison of strains near the clamped support of plate 1	202
Fig. 7-8	Comparison of strains at the net-section hole edge of plate 1	204
Fig. 7-9	Comparison of strains near the simple support of plate 1	205

Fig. 7-10 Comparison of strains near the clamped support of plate 2	206
Fig. 7-11 Comparison of strains at the net-section hole edge of plate 2	207
Fig. 7-12 Comparison of strains near the simple support of plate 2	208
Fig. 7-13 Predicted and measured shadow moire fringe pattern for a [± 45/0/90] _{2s} plate with a one half-wave configuration	209
Fig. 7-14 Predicted and measured shadow moire fringe pattern for a [± 45/0/90] _{2s} plate with a two half-wave configuration.....	211
Fig. 7-15 Failed [± 45/0/90] _{2s} plate in the fixture.....	213
Fig. 7-16 Contour of failure parameters of the [± 45/0/90] _{2s} plates at P/EA = 0.00255	214
Fig. 7-17 Definition of terms related to acoustic emission test [57]	217
Fig. 7-18 Acoustic emission activity and load-end shortening relation for plate 1, [± 45/0/90] _{2s}	218
Fig. 7-19 Acoustic emission activity and load-end shortening relation for plate 2, [± 45/0/90] _{2s}	219
Fig. 7-20 Comparison of load vs. end shortening relations and failure loads for the [± 45/0 ₂] _{2s} plates.....	221
Fig. 7-21 Comparison of displacements measured from LVDT 1 and LVDT 2 for plate 3 and plate 4.....	224
Fig. 7-22 Comparison of load vs. deflection relations and failure loads for [± 45/0 ₂] _{2s} plates.....	225
Fig. 7-23 Experimentally measured strains of plate 3.....	227
Fig. 7-24 Experimentally measured strains of plate 4.....	228
Fig. 7-25 Curvature change at the locations of sg1 and sg3 after mode shape change	230
Fig. 7-26 Comparison of strains near the clamped support of plate 3	231
Fig. 7-27 Comparison of strains at the net-section hole edge of plate 3	232
Fig. 7-28 Comparison of strains near the simple support of plate 3	233
Fig. 7-29 Comparison of strains near the clamped support of plate 4	235
Fig. 7-30 Comparison of strains at the net-section hole edge of plate 4	236

Fig. 7-31 Comparison of strains near the simple support of plate 4	237
Fig. 7-32 Predicted and measured shadow moire fringe pattern for a [± 45/0 ₂] _{2S} plate with a one half-wave configuration	238
Fig. 7-33 Predicted and measured shadow moire fringe pattern for a [± 45/0 ₂] _{2S} plate with a two half-wave configuration.....	239
Fig. 7-34 Failed [± 45/0 ₂] _{2S} plate in the fixture.....	241
Fig. 7-35 Contour of failure parameters of the [± 45/0 ₂] _{2S} plate at P/EA = 0.00206.....	242
Fig. 7-36 Acoustic emission activity and load-end shortening relation for plate 3, [± 45/0 ₂] _{2S}	244
Fig. 7-37 Acoustic emission activity and load-end shortening relation for plate 4, [± 45/0 ₂] _{2S}	245
Fig. 7-38 Comparison of load vs. end shortening relations and failure loads for the [± 45/0 ₆] _S plates.....	247
Fig. 7-39 Comparison of displacements measured from LVDT 1 and LVDT 2 for plate 5 and plate 6.....	249
Fig. 7-40 Comparison of load vs. deflection relations and failure loads for the [± 45/0 ₆] _S plates	250
Fig. 7-41 Experimentally measured strains of plate 5.....	252
Fig. 7-42 Experimentally measured strains of plate 6.....	253
Fig. 7-43 Comparison of strains near the clamped support of plate 5	254
Fig. 7-44 Comparison of strains at the net-section hole edge of plate 5	255
Fig. 7-45 Comparison of strains near the simple support of plate 5	256
Fig. 7-46 Comparison of strains near the clamped support of plate 6	257
Fig. 7-47 Comparison of strains at the net-section hole edge of plate 6	258
Fig. 7-48 Comparison of strains near the simple support of plate 6	259
Fig. 7-49 Predicted and measured shadow moire fringe pattern for a [± 45/0 ₆] _S plate at a lower load level.....	260
Fig. 7-50 Predicted and measured shadow moire fringe pattern for a [± 45/0 ₆] _S plate at a higher load level.....	261
Fig. 7-51 Failed [± 45/0 ₆] _S plate in the fixture.....	263

Fig. 7-52 Contour of failure parameters of the $[\pm 45/0_6]_s$ plates at $P/EA = 0.00169$	264
Fig. 7-53 Acoustic emission activity and load-end shortening relation for plate 5, $[\pm 45/0_6]_s$	267
Fig. 7-54 Acoustic emission activity and load-end shortening relation for plate 6, $[\pm 45/0_6]_s$	268
Fig. 7-55 Comparison of load vs. end shortening relations and failure loads for $[\pm 45]_{45}$ plates	270
Fig. 7-56 Comparison of displacements measured from LVDT 1 and LVDT 2 for plate 7 and plate 8	272
Fig. 7-57 Comparison of load vs. deflection relations and failure loads for the $[\pm 45]_{45}$ plates	273
Fig. 7-58 Experimentally measured strains of plate 7	274
Fig. 7-59 Experimentally measured strains of plate 8	275
Fig. 7-60 Comparison of strains near the clamped support of plate 7	276
Fig. 7-61 Comparison of strains at the net-section hole edge of plate 7	277
Fig. 7-62 Comparison of strains near the simple support of plate 7	278
Fig. 7-63 Comparison of strains near the clamped support of plate 8	279
Fig. 7-64 Comparison of strains at the net-section hole edge of plate 8	280
Fig. 7-65 Comparison of strains near the simple support of plate 8	281
Fig. 7-66 Predicted and measured shadow moire fringe pattern for a $[\pm 45]_{45}$ plate in a one half-wave configuration	283
Fig. 7-67 Predicted and measured shadow moire fringe pattern for a $[\pm 45]_{45}$ plate in a two half-wave configuration	284
Fig. 7-68 Failed $[\pm 45]_{45}$ plate in the fixture	286
Fig. 7-69 Contour of failure parameters of the $[\pm 45]_{45}$ plates at $P/EA = 0.00395$	287
Fig. 7-70 Acoustic emission activity and load-end shortening relation for plate 7, $[\pm 45]_{45}$	289
Fig. 7-71 Acoustic emission activity and load-end shortening relation for plate 8, $[\pm 45]_{45}$	290

Fig. 7-72 Predicted failure locations and failure modes of $[\pm 45/0_6]_s$ plate with hole in the one half-wave configuration with revised value of S_{23}	293
Fig. 7-73 Predicted failure locations and failure modes of $[\pm 45/0_6]_s$ plate with hole in the two half-wave configuration with revised value of S_{23}	294
Fig. 7-74 Predicted failure locations and failure modes of solid $[\pm 45/0_6]_s$ plate in the one half-wave configuration with revised value of S_{23}	296
Fig. 7-75 Predicted failure locations and failure modes of solid $[\pm 45/0_6]_s$ plate in the two half-wave configuration with revised value of S_{23}	297

List of Tables

Table 1-1	Buckling and postbuckling analysis for plates with holes [7].....	5
Table 2-1	Layer material properties of AS4/3502	33
Table 2-2	Anisotropic coefficients for laminates in this study.....	35
Table 2-3	Buckling loads of plates with holes	37
Table 2-4	Equivalent Young's modulus in x direction for each laminate	38
Table 2-5	Buckling loads of solid plates.....	42
Table 5-1	Strengths of AS4/3502 used in this study	109
Table 5-2	Failure loads, failure modes, and failure locations for plates with holes for the one half-wave configuration	111
Table 5-3	Failure loads, failure modes, and failure locations for plates with holes for the two half-wave configuration	112
Table 5-4	Failure loads, failure modes, and failure locations for solid plates for the one half-wave configuration	113
Table 5-5	Failure loads, failure modes, and failure locations for solid plates for the two half-wave configuration.....	114
Table 7-1	Numbering of plates tested in this study.....	188
Table 8-1	Experimentally determined and numerically predicted buckling loads of each laminate.....	299
Table 8-2	Experimentally determined and numerically predicted failure loads of each laminate.....	300

1.0 Introduction

1.1 Overview

Since plates with circular holes and other openings are extensively used as structural members in aircraft design, the buckling and postbuckling behavior of such plates has received much attention. Much of the work done in this area has occurred since the mid-1940's. Owing to the abundant accumulation of information and understanding of the mechanical behavior of isotropic plates, including plates with holes, isotropic plates are often designed to operate in the postbuckling range. As an example, fuselage panels are frequently designed to sustain loads of three or four times the buckling load [1]. This results in a great benefit of weight savings.

With the development of advanced composite materials, the potential application of composite materials to aircraft design has increased rapidly. Consequently, the mechanical behavior of composite plates in the buckling and postbuckling range of loading has become a topic of great interest. As the postbuckling response of com-

posite plates is not yet fully understood, the initial buckling load is usually considered as the ultimate load in composite material applications. For increased efficiency, however, operation in the postbuckling range is important and, as a result, many investigators are conducting research regarding the postbuckling behavior of composite plates for various geometries, loadings, and support conditions. Recent developments [2] show that even composite plates with large holes have load bearing capability beyond the buckling load. The key issue is determining failure load levels in the postbuckling range. Failure in these situations involves a coupling of structural response and material failure. It is a complex topic and because of it, the failure of postbuckled composite plates with holes is not yet fully understood. The present study is devoted to increasing the understanding of the failure of composite plates with holes loaded in the postbuckling range of response. To follow is a review of some of the literature felt to be relevant to the topic studied. Cited are buckling and postbuckling studies of plates with holes, and postbuckling failure studies of composite plates. After the review of the literature, the specific problem addressed in this study are described.

1.2 Literature Review

Buckling analysis of isotropic plates began with the work of Bryan [3] a century ago. However, the history of buckling analysis for composite materials does not go back that far. It began with the analysis for plywood by March [4] in 1942. With the development of advanced composite materials and increasing need for light-weight structural members for flight vehicles, scientists and engineers began to study the

mechanical behavior of composite materials. The history and nature of buckling analyses of composite plates to 1987 are well explained in Leissa's review paper [5].

1.2.1 Review of Buckling and Postbuckling of Plates with Holes

Inevitably some plates used as structural members will contain holes. These holes can be access holes, holes for hardware to pass through, or in the case of fuselages, windows and doors. In some cases holes are used to reduce the weight of the structure. When a plate contains a hole, it is well known that the tensile strength is reduced due to the stress concentration around hole. However, the reduction of tensile strength may have little bearing on the buckling behavior of a plate with a hole. The two problems are quite different. For the buckling problem the prebuckling stresses must first be found, and then the stability of the plate in the presence of these prebuckling stresses be studied. The former problem is an inplane problem, like the tensile problem, and involves inplane stiffnesses. The stability problem, however, involves out-of-plane effects, in particular, bending stiffnesses. Thus the mechanics of the buckling problem are much more complicated than the mechanics of the tensile problem. The study of the buckling of an isotropic flat plate with a central circular hole began with the work of Levy, Wooley, and Kroll [6]. Following Levy, et al. many investigators studied the stability of plates with central holes using various methods to find the prebuckling and buckling solutions. The history of solution techniques and the findings for the stability of plates with holes to 1983 is explained in detail in the literature review of Nemeth's thesis[7]. A brief summary of Nemeth's literature review is presented in Table 1-1 [6, 8-20]. In the present review

of buckling and postbuckling of plates with holes only the papers and reports after 1983 will be explained in detail. Herein, the length of the plate will be denoted as L , the width W , and the hole diameter D . An important parameter when discussing plates with holes is the hole diameter to plate width ratio D/W . Another important parameter is the plate aspect ratio L/W . These notations will be used in this study.

Nemeth [7] investigated the buckling behavior of orthotropic composite plates with central holes by using Kantorovich's method in both the prebuckling and buckling analyses. The loading conditions considered were both uniform stress and uniform displacement on opposite edges. The adjacent unloaded edges were simply supported and the loaded edges were simply supported or clamped. In addition to isotropic and orthotropic plates, quasi-isotropic and symmetric angle-ply plates with very weak anisotropy were analyzed by neglecting D_{16} and D_{26} . From the buckling equation anisotropic parameters were derived. These parameters were used to determine the degree of anisotropy of the plate. The details of this argument were published in ref. 21. The results from this approach were compared with finite-element results. For isotropic plates good correlation with the previous results was obtained. Laminates with all 90° layers appeared to be the least sensitive to changes in hole size, support conditions, and loading conditions. As the number of 0° layers increased, the sensitivity to changes in these variables increased. Quasi-isotropic plates exhibited buckling behavior similar to that of isotropic plates. For symmetric angle-ply plates fiber orientation and type of the loading substantially affected the buckling behavior. The $[(\pm 60)_8]_s$ and $[(\pm 45)_8]_s$ laminates showed high buckling resistance. No experimental results were reported.

**Table 1-1 Buckling and postbuckling analysis for plates with holes [7].
(continued)**

year	Investigator	Num./Exp.	Remarks or Findings
1947	Levy, Wooley, Kroll [6]	Num.	<ul style="list-style-type: none"> - First study on buckling for a plate with hole - Kirsh solution for prebuckling and energy method for buckling - Monotonic decrease with hole size for simple support and stress loading
1949	Kroll [8]	Num.	<ul style="list-style-type: none"> - Similar approach to Levy, et al. - Shear loading is considered - Buckling load is more sensitive to hole size than uniaxial loading
1951	Kumai [9]	Num./Exp.	<ul style="list-style-type: none"> - Same approach as above - w satisfies stress free condition on hole boundary - For uniform stress loading simple support and clamped considered - Simple support : monotonic decrease - Clamped : reaches minimum at about $D/W = 0.2$ then increases
1964	Schlack [10]	Num./Exp.	<ul style="list-style-type: none"> - First study for edge displacement loading - Rayleigh-Ritz method for prebuckling and buckling - Biaxial loading test apparatus designed - Concluded singular term is not necessary - Studied up to $D/W = 0.3$
1967	Yoshiki, Fujita, Kawamura, Arai[11]	Num./Exp.	<ul style="list-style-type: none"> - In addition to size effects of the hole the effect of hole position was examined - Substantial loss of buckling load is possible for eccentric hole
1968	Schlack [12]	Num./Exp.	<ul style="list-style-type: none"> - Studied up to $D/W = 0.7$ - Rayleigh-Ritz solution agrees well up to $D/W = 0.35$
1968	Kawai, Ohtsubo [13]	Num.	<ul style="list-style-type: none"> - FEM for prebuckling and Rayleigh-Ritz for buckling - Good agreement with previous experiments - The role of prebuckling stress distribution explored
1971	Yu & Davis [14]		<ul style="list-style-type: none"> - The prebuckling stress distribution for plate with small hole and large hole is substantially different
1972	Martin [15]	Num./Exp.	<ul style="list-style-type: none"> - First study on composite plate with hole - Rayleigh-Ritz method used

**Table 1-1 Buckling and postbuckling analysis for plates with holes [7].
(concluded)**

year	Investigator	Num./Exp.	Remarks or Findings
1972	Vann & Vos [16]	Num.	<ul style="list-style-type: none"> - FEM used for isotropic plate - The interaction between prebuckling stress distribution and reduction of bending stiffness due to the presence of hole addressed - Loss of bending stiffness dominates for small hole and prebuckling stress dominates for large hole - When the aspect ratio is two or greater, the difference between stress and displacement loading diminishes
1973	Yu & Davis [17]	Exp.	<ul style="list-style-type: none"> - Postbuckling, shear buckling, web crippling
1975	Ritchie, Rhodes [18]	Num./Exp.	<ul style="list-style-type: none"> - Buckling and postbuckling, isotropic plate - FEM for prebuckling and Rayleigh-Ritz for buckling - Up to $D/W = 0.4$ postbuckling prediction agreed with experiment
1978	Knauss, Starnes, Henneke [19]	Exp.	<ul style="list-style-type: none"> - Buckling , postbuckling, failure study - Aspect ratio 2, D/W up to 0.3 - At $D/W = 0.15-0.2$ mode shape changes from full sine wave to half sine wave
1980	Proebrazhenskii[20]		<ul style="list-style-type: none"> - Survey paper for mostly Eastern Europe and some of America, Western Europe, and Asia

In 1983 Azizian and Roberts [22] investigated the buckling and elasto-plastic collapse of an isotropic square plate with a hole. The finite-element method was used for this study. The shape of the hole was either square or circular. The support condition was either simple support or clamped on all four sides. The loading was a uniform displacement on one edge. There was no difference in the buckling load between circular and square holes up to $D/W = 0.3$ for the simply supported case. For $D/W > 0.3$ the plate with a square hole exhibited a slightly higher buckling load. For the clamped case the plate with a square hole showed a higher buckling load regardless of the hole size. In both support cases the decrease in buckling load due to the holes was very small, and for a large hole the buckling load was even higher than for the plate without a hole. Even though the buckling load of a plate with large hole increased, the elasto-plastic collapse load decreased monotonically as the hole size increased. In addition, there was no difference in collapse load between the circular and square hole. When the plate was thin, the reduction in collapse load due to the hole was small. When the plate was thick, the reduction was pronounced.

In 1985 Vandenbrink and Kamat [23] studied the buckling and postbuckling behavior of isotropic and laminated composite square plates with central circular holes. They used three-dimensional finite elements in their analysis. The laminates analyzed were symmetric angle-ply laminates, $([\pm \theta]_s)$, where the fiber angles were $\theta = 0^\circ, 30^\circ, 45^\circ$, and 60° . They studied initial imperfection sensitivity in the postbuckling behavior of plates with a central hole. They concluded that these plates are insensitive to initial imperfection and the postbuckling strength of a plate with a hole is reduced compared to a corresponding plate without a hole.

Marshall, Little, and El-Tayeby [24] studied the stability of composite panels with holes by using an expression which had a one-term double cosine and a one-term exponential for the out-of-plane displacement. They followed a formal energy method solution procedure. They compared their results with their experimental results and previously reported results. They obtained good agreement.

In 1986 Nemeth, Stein, and Johnson [25] performed experiments for orthotropic $[0_{10}]_s$, $[90_{10}]_s$, and $[(0/90)_6]_s$ plates and compared the buckling loads with those from Nemeth [7]. In the experimental apparatus the plates were clamped on the loaded edges and simply supported on the unloaded edges. In all cases the difference between experiment and analysis was less than 13 %.

Sabir and Chow [26] obtained the solutions for the elastic buckling load of square plates with eccentrically located holes. Uniaxial, biaxial, and pure shear loading cases for simply supported and clamped plates were considered. Generally, the buckling loads decreased with eccentricity for holes larger than $D/W=0.2$. The reduction in the buckling load was more appreciable for clamped plates. The exceptional case occurred when the circular hole was within the compression zone of a plate loaded by a uniform shear. The buckling load in this case increased appreciably with eccentricity for both simply supported and clamped plates.

Yettram and Brown [27] studied the effect of biaxial loading on the buckling behavior of isotropic plates with central holes. Uniform edge stress was applied on all four edges. The buckling behavior was studied by changing the ratio of the load in the x direction to the load in the y direction, and the size of the hole. Generally, for all support conditions the buckling load was sensitive to the hole size when the loads in

the x direction were opposite in sign to the loads in the y direction. When the loads were both compressive, the dependence of buckling load on the hole size was not pronounced.

Marshall, Little, and El-Tayeb [28] investigated the membrane stress distribution in the postbuckling range for composite plates with holes. They showed that when the hole size was small, $D/W = 0.2$, the stress concentration effect near the hole boundary diminished and the areas near the supported edges were subjected to higher stresses. When the hole size was large, $D/W = 0.4$, the stress concentration effect still dominated.

Larsson [29] analyzed the buckling and postbuckling behavior of square plates having central circular holes by the finite-element method. Both uniaxial and biaxial compression were considered for various types of boundary conditions. They also studied an annular plate with a hole.

For a single layer the dependence of buckling load on fiber orientation was investigated by Turvey and Sadeghpour [30]. They found that the buckling loads of square carbon-fiber reinforced and glass-fiber reinforced laminates without a hole decreased monotonically as the fiber angle changed from 0° to 90° with respect to the loading direction. The loading was a uniform stress loading and the support conditions were both simple and clamped support. The inplane movement on the unloaded edge was not constrained. When the hole size was $D/W = 0.3$, the buckling load of the simply supported plate was not sensitive to the fiber angle change. However, the buckling load was sensitive to the fiber angle change for the clamped support. For clamped supports the buckling load also decreased monotonically with fiber angle.

In 1988 Nemeth [31] reported experiments focused on the buckling behavior of symmetric angle-ply plates with holes. The results were compared with his numerical results from ref. 7. He conducted a parametric study by changing the hole size, loading and support conditions, and the fiber angle of the laminate. For $[(\pm 15)_m]_s$ laminates, $m \geq 6$, the dependence of buckling load on the aspect ratio, L/W , was studied for simply supported and clamped conditions. The results indicated that the buckling load was independent of the support condition when the aspect ratio was greater than 2.5

In 1989 Lin and Kuo [32] performed several parametric studies for the buckling behavior of laminated plates with a central hole with a shear deformable finite-element formulation. They studied the dependence of buckling load on hole size for uniaxial and biaxial loading, for simple and clamped supports, and for different combinations of anti-symmetric cross-ply laminates. They also studied the dependence of buckling load on the thickness of the plate for different hole sizes. The dependence on the longitudinal-to-transverse stiffness ratio, and the dependence on the biaxial loading ratio, were also studied. For anti-symmetric angle-ply plates the dependence on the fiber orientation was studied for different hole sizes.

Nemeth [2] investigated experimentally the postbuckling behavior of square composite plates with central holes. For $[0_{10}]_s$, $[90_{10}]_s$, $[(0/90)_5]_s$, $[(\pm 30)_6]_s$, $[(\pm 45)_6]_s$, and $[(\pm 60)_6]_s$ laminates with hole sizes from $D/W = 0$ to 0.6 postbuckling behavior was investigated. Results for aluminium plates were reported also. It was observed that some plates failed at low load levels. As an example a $[90_{10}]_s$ plate

failed at low loads when the hole sizes were large. However, no plate failed before the buckling load was reached. This means that even plates with large holes exhibit some postbuckling strength. Depending on the hole size the postbuckling stiffness changed. Most of the plates with holes showed smaller postbuckling stiffness than the plates with no hole. However, some of the highly orthotropic plates with holes showed higher postbuckling stiffness than the corresponding plate without a hole. Failure predictions were not part of this study.

Hyer and Lee [33] studied the buckling load using the curvilinear fiber format in a composite plate with a circular hole. By using the finite-element method and optimization technique they tried to find the curvilinear fiber path which produced the maximum buckling load. They showed that the buckling load of a composite plate can be increased by using the curvilinear fiber format instead of the conventional straight fiber format. They also showed that by combining curvilinear fiber format layers with the straight fiber layers both the buckling load and tensile failure load can be increased.

1.2.2 Review of Postbuckling Failure

There are few references in the literature dealing with the postbuckling failure of composite plates. Starnes and Rouse [34] presented extensive experimental results for composite plates. All of the plates were rectangular and their aspect ratios, L/W , ranged from 2.1 to 6.7. Most of the plates were solid, without holes. Some plates, however, had small circular holes, and some had been subjected to impact

damage. For a few plates experimental results were compared with numerical results from a general-purpose FEM code. They found that most of the specimens failed along a nodal line of the buckling mode in an interlaminar shear failure mode. Failure predictions were not included.

Gurdal, Haftka, and Starnes [35] studied the effect of slots on the buckling, postbuckling, and postbuckling failure of laminated plates. Centrally located slots did not affect the failure loads or the failure modes of the plates. Slots located close to an unloaded edge of a plate reduced the postbuckling strength of the plate and affected the failure mode. For one slightly offset slot location, interaction of out-of-plane deformations with the slot tip was observed to affect the failure mode significantly without affecting the failure load.

Buskell, Davies, and Stevens [36] showed other evidence that in postbuckling the rectangular plates which had aspect ratios, L/W , of 3 - 6.9 failed at the nodal lines and interlaminar shear stresses were the governing parameters. They used acoustic emission tests to monitor the failure development, and with ultrasonic techniques they observed the development of delamination growth from the unloaded edges.

Noor, Starnes, and Waters [37] published numerical failure analysis results which were compared with limited experimental data for composite plates of aspect ratio 2.0. All of the plates were solid plates without holes. As a numerical tool a mixed finite-element formulation was used. The formulation included shear deformation and each node had 13 degrees of freedom. Up to the buckling load the correlation between numerical and experimental results was good. For loads beyond that the numerical results overestimated the postbuckling stiffness. The plates of Noor, et al.

[37], like the plates of Starnes and Rouse [34], failed at the nodal lines in a shear failure mode. From the numerical results Noor, et. al. [37] found that the shear strain energy density was maximum at the nodal lines. In their analysis interlaminar shear stresses were calculated from the three-dimensional equilibrium equations of elasticity by using the inplane stresses obtained from the finite-element analysis. By integrating the equilibrium equation in the thickness direction, the interlaminar shear stresses were calculated.

Shin [38] studied postbuckling failure of solid plates and attempted to find a weight-saving design by changing the stacking sequence so that the postbuckling failure load was maximized. He used the maximum strain failure criterion by considering inplane strains only. The phenomenon of mode shape change has been observed by several investigators [39-42]. Some investigators [43,44] followed Stein's approach [39] in considering the mode shape change. Stein's approach [39] was to find the load-end shortening relation for successive buckling mode shapes and superpose them. Then, the broken continuous curve that forms the lower bound envelope is assumed to be the load-end shortening relation of the plate. In the postbuckling analysis Shin [38] tried to predict mode shape change by examining the energy state for several successive mode shapes. Shin claimed that mode shape change occurs at the point where the energy level crosses, instead of at the crossing point of the load-end shortening relation.

Engelstad, Reddy, and Knight [45] studied postbuckling failure numerically. They used a first-order shear deformable degenerated shell finite-element theory to predict the postbuckling response and failure. By applying a progressive damage failure

mechanism and comparing with Starnes and Rouse's experimental results [34], they obtained good agreement in failure load, failure mode, and failure location.

1.3 Problem Studied

1.3.1 Description of Problem

The plate geometry, nomenclature, and a description of the problem studied are shown in Fig 1-1. The coordinate system used in the study is illustrated in the figure. The origin of the coordinates is at the center of the hole and the x axis is vertical. The positive z axis is out of the plane of the figure. The top edge and the bottom edge are clamped and the two side edges are simply supported. The top edge is loaded by a known uniform inplane displacement denoted as u . The bottom edge is restrained to have zero displacement in the x direction. In numerical simulation the inplane displacement in transverse direction is not restrained on both the simply supported and clamped edges. Figure 1-1 illustrates an important aspect of the problem. Specifically, in the experimental phase that accompanies the numerical analysis, the actual width of the plate, b , is wider than the distance between the simple supports, and the actual length of the plate, a , is longer than the distance between the clamped supports. The width and length of the plate between the supports are denoted as W and L , respectively. The portions of the plate outside the dimensions W and L are necessary from the experimental point of view. To clamp the top and bottom edges part of the plate must be within the clamps. The clamps extend

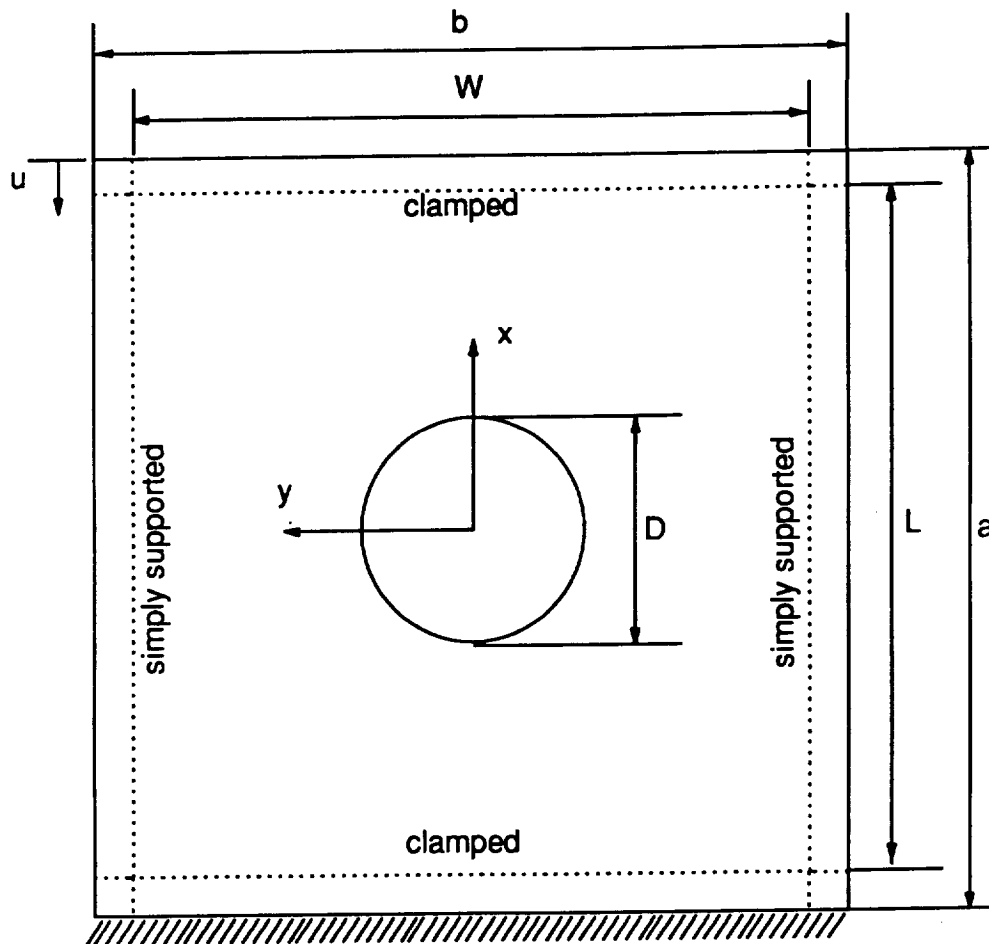


Fig. 1-1 Problem geometry.

inward some distance, yet the known inplane displacement, u , is applied at the outer most edge of the upper clamp, and the zero inplane displacement is enforced at the outermost edge of the lower clamp. Likewise, when the plate deflects out-of-plane due to buckling the simply supported edges move inward. Therefore, the plate must be wider than the distance between supports to accommodate this narrowing, or the plate will not stay in the fixture. In the experimental set-up knife edges are used to simulate simple supports. The dotted lines in Fig. 1-1 indicate the lines of support provided by the knife edges and clamped supports. The hole diameter is given by D and the hole is centrally located. The ratio of hole diameter to plate width is again given by D/W and attention must be given to the definition of W , as opposed to b , in Fig. 1-1.

With the problem described, the statement of the goal of the work is simple: Determine what level of inplane load (or inplane displacement u) at the clamped boundaries causes the plate to fail. Inherent in this is : (1) the definition of failure and (2) the determination of the location of the failure and the mode of failure.

1.3.2 Approach

The approach used to study postbuckling failure involves both analysis in the form of numerical predictions, and experiments. To put the postbuckling analysis into context, the buckling problem is studied first. Then the postbuckling response, or more accurately stated, the geometrically nonlinear response, is computed

The numerical analysis for determining the buckling loads uses a mixed-formulation finite-element method following Reddy [46]. The analysis for studying response in the postbuckling range relies on a shear-deformable finite-element formulation following Reddy and Chao [47]. Imperfections in the plates in the form of initial out-of-plane deformations are being included. The inclusion of imperfections actually precludes the plate from exhibiting ideal postbuckling response. Thus, the study of postbuckling is done using a geometrically nonlinear analysis which predicts out-of-plane deformation response for even small inplane loads. Since the emphasis is on material failure, the calculation of stresses is included in the geometrically nonlinear analysis. Inplane stresses are computed directly from the analysis. The interlaminar stresses are calculated by integrating the three-dimensional equilibrium equations of elasticity in the thickness direction. Failure is predicted by using the maximum stress failure criterion.

The actual responses of the plates are studied by using a specially built fixture designed to uniformly displace the top edge of the plate. The fixture is used within a displacement-controlled Tinius-Olsen load frame. Two linear variable displacement transducers (LVDT's) are used to measure the downward motion of the top edge. The load required to do this is measured with the load cell installed in the load frame. Hence load vs. end shortening relations from the experiment can be compared with similar data from the numerical analysis. The out-of-plane displacement near the center of the plates is measured with a third LVDT. This response can be compared with numerical prediction. Strain gauges at specific locations are used to measure the uniformity of the response and bending effects. The shadow moire method is used to provide a whole-field picture of the out-of-plane displacements. These

whole-field measurements are compared with contour plots generated by the numerical analysis.

The issue of failure, the prime focus of the work, is studied primarily by visual inspection, and by considering the response of the plate as measured by the strain gauges and LVDT's. However, there was an attempt to study failure using acoustic emission. This approach was partially successful in detecting the onset of failure. The failure load, mode, and location, as determined by the instrumentation and by visual inspection, respectively, are correlated with predictions.

The plates actually considered are fabricated from AS4/3502, a graphite-epoxy material. The plates are $a = 11$ in. by $b = 11$ in. square with 3 in. diameter hole. The distance between the simple supports is 10 in. and the distance between the inner edges of the clamped supports is 10 in.. Thus one-half inch on all four sides is used for enforcing the support conditions, and $D/W = 0.3$. Four laminates are considered. The laminates are $[\pm 45/0/90]_{2S}$, $[\pm 45/0_2]_{2S}$, $[\pm 45/0_6]_S$, and $[\pm 45]_{4S}$. All laminates are 16 layers. The first laminate represents a conventional design. The second laminate is also common and represents a departure from the quasi-isotropic nature of the first laminate. There is a preferred direction with the second laminate. The third laminate has a preferred direction, and represents, perhaps, an extreme case. The fourth laminate has no 0° layers and represents a laminate often studied.

To follow are descriptions of each chapter of this study. The next chapter addresses the issue of buckling. The finite-element formulation used is briefly overviewed and the predicted buckling characteristics of the laminates considered in the

experiments are discussed. For contrast, the case of plates with no holes is examined. Buckling loads and accompanying mode shapes are presented.

Chapter 3 addresses the issue of postbuckling response. Since plates generally exhibit imperfections in the form of initial out-of-plane displacements, the chapter actually addresses the geometrically nonlinear response of plates which exhibit an initial out-of-plane deflection. The finite-element formulation to solve the governing equations is explained. The results from the formulation are compared with results from the general purpose code ABAQUS [48]. The postbuckling response of the four laminates with and without holes are studied using the formulation developed. The influence of the plate extensions outside the analysis region is considered in this chapter.

Interlaminar stress calculations are addressed in chapter 4. The formulation for computing the stresses is presented. This formulation is based on integrating the equations of equilibrium from the theory of elasticity through the thickness. Since the finite-element analysis is an approximation, the interlaminar stress calculation is compared with other analyses to validate the numbers. After the validation interlaminar stresses in the plates in this study are examined. The stresses are computed at several locations along the net-section for the case of the plate postbuckling with two half-waves in the loading direction. Stresses at the hole edge, partway between the hole edge and support, and inside and outside the simple supports are considered.

Chapter 5 addresses the primary focus of this study, namely, the analysis of failure. The maximum stress failure criterion is used on a layer-by-layer basis to study

failure. The failure load, failure mode, and failure location for each of the plates studied, both with and without holes, are predicted. A so-called damage accumulation scenario is depicted for each plate. Because of the aforementioned mode shape change, the failure analysis considers failure scenarios for both the one half-wave and two half-wave configurations of deformation in the loaded direction.

Chapter 6 describes the test fixture and experimental set-up. Detail drawings of each part of the fixture are provided. The test procedures and the layout of the equipment are explained in this chapter.

Experimental results and the comparison of experimental results with numerical results are presented in chapter 7. For each laminate the load vs. deflection relations, load vs. strain relations, shadow moire results, failure, and acoustic emission results are discussed. For the $[\pm 45/0]_s$ laminate, which showed a difference between experimental results and numerical predictions, a re-examination of postbuckling failure is attempted, by revising the interlaminar shear strength to take into account the layer clustering effect.

Chapter 8 provides concluding comments and recommendations for future research.

2.0 Buckling Finite-Element Formulation

2.1 Governing Equations

In this chapter the buckling analysis using a finite-element method based on a mixed formulation will be explained. The formulation used in this chapter follows reference [46]. The basic equations used in this mixed finite-element formulation are the stability equation,

$$\frac{\partial^2 M_x}{\partial x^2} + 2 \frac{\partial^2 M_{xy}}{\partial x \partial y} + \frac{\partial^2 M_y}{\partial y^2} + \lambda (n_{10} \frac{\partial^2 w}{\partial x^2} + n_{20} \frac{\partial^2 w}{\partial y^2} + 2 n_{60} \frac{\partial^2 w}{\partial x \partial y}) = 0, \quad (2.1)$$

and the moment-curvature relations,

$$M_x = - (D_{11} \frac{\partial^2 w}{\partial x^2} + D_{12} \frac{\partial^2 w}{\partial y^2} + 2 D_{16} \frac{\partial^2 w}{\partial x \partial y}),$$
$$M_y = - (D_{12} \frac{\partial^2 w}{\partial x^2} + D_{22} \frac{\partial^2 w}{\partial y^2} + 2 D_{26} \frac{\partial^2 w}{\partial x \partial y}), \quad (2.2)$$

$$M_{xy} = - (D_{16} \frac{\partial^2 w}{\partial x^2} + D_{26} \frac{\partial^2 w}{\partial y^2} + 2 D_{66} \frac{\partial^2 w}{\partial x \partial y}).$$

Recall, the coordinate system used was illustrated in Fig. 1-1. Here M_x , M_y , and M_{xy} are moment resultants defined by

$$M_x = \int_{-\frac{h}{2}}^{\frac{h}{2}} z \sigma_x dz, \quad M_y = \int_{-\frac{h}{2}}^{\frac{h}{2}} z \sigma_y dz, \quad M_{xy} = \int_{-\frac{h}{2}}^{\frac{h}{2}} z \tau_{xy} dz, \quad (2.3)$$

where h is the laminate thickness. The symbol λ is the buckling parameter which is defined as

$$\lambda = \frac{N_x}{n_{10}} = \frac{N_y}{n_{20}} = \frac{N_{xy}}{n_{60}}, \quad (2.4)$$

where N_x , N_y , and N_{xy} are the inplane force resultants. These are defined by

$$N_x = \int_{-\frac{h}{2}}^{\frac{h}{2}} \sigma_x dz, \quad N_y = \int_{-\frac{h}{2}}^{\frac{h}{2}} \sigma_y dz, \quad N_{xy} = \int_{-\frac{h}{2}}^{\frac{h}{2}} \tau_{xy} dz. \quad (2.5)$$

The quantities n_{10} , n_{20} , and n_{60} are the inplane force resultants due to a unit load applied on the edge of the plate. Interpreted differently, n_{10} , n_{20} , and n_{60} are the prebuckling force resultants due to a unit applied load. The meaning of unit load is different for a uniform stress loading than it is for a uniform displacement loading. This difference in meaning will be explained in the numerical procedure section of this chapter. The quantity w is the out-of-plane displacement. The quantities D_{ij} are bending stiffness coefficients which are defined as

$$D_{ij} = \int_{-\frac{h}{2}}^{\frac{h}{2}} z^2 \bar{Q}_{ij} dz, \quad (2.6)$$

where \bar{Q}_{ij} is the transformed reduced stiffness matrix. To facilitate the derivation of the variational form, the three moment-curvature relations are expressed in the alternative form as

$$\frac{\partial^2 w}{\partial x^2} = -(\bar{D}_{11} M_x + \bar{D}_{12} M_y + \bar{D}_{16} M_{xy}),$$

$$\frac{\partial^2 w}{\partial y^2} = -(\bar{D}_{12} M_x + \bar{D}_{22} M_y + \bar{D}_{26} M_{xy}), \quad (2.7)$$

$$2 \frac{\partial^2 w}{\partial x \partial y} = -(\bar{D}_{16} M_x + \bar{D}_{26} M_y + \bar{D}_{66} M_{xy}),$$

where

$$\begin{bmatrix} \bar{D}_{11} & \bar{D}_{12} & \bar{D}_{16} \\ \bar{D}_{12} & \bar{D}_{22} & \bar{D}_{26} \\ \bar{D}_{16} & \bar{D}_{26} & \bar{D}_{66} \end{bmatrix} = \begin{bmatrix} D_{11} & D_{12} & D_{16} \\ D_{12} & D_{22} & D_{26} \\ D_{16} & D_{26} & D_{66} \end{bmatrix}^{-1}. \quad (2.8)$$

The variational form of eqs. (2.1) and (2.7) can be established by using the inverse procedure of deriving the governing equations. This procedure appears as

$$\delta J = \iint \delta w \left\{ \frac{\partial^2 M_x}{\partial x^2} + 2 \frac{\partial^2 M_{xy}}{\partial x \partial y} + \frac{\partial^2 M_y}{\partial y^2} + \lambda \left(n_{10} \frac{\partial^2 w}{\partial x^2} + n_{20} \frac{\partial^2 w}{\partial y^2} + 2 n_{60} \frac{\partial^2 w}{\partial x \partial y} \right) \right\} dx dy$$

$$\begin{aligned}
& + \iint \delta M_x \left\{ \frac{\partial^2 w}{\partial x^2} + (\bar{D}_{11} M_x + \bar{D}_{12} M_y + \bar{D}_{16} M_{xy}) \right\} dx dy \quad (2.9) \\
& + \iint \delta M_y \left\{ \frac{\partial^2 w}{\partial y^2} + (\bar{D}_{12} M_x + \bar{D}_{22} M_y + \bar{D}_{26} M_{xy}) \right\} dx dy \\
& + \iint \delta M_{xy} \left\{ 2 \frac{\partial^2 w}{\partial x \partial y} + (\bar{D}_{16} M_x + \bar{D}_{26} M_y + \bar{D}_{66} M_{xy}) \right\} dx dy.
\end{aligned}$$

Using integration by parts and rearranging the terms leads to

$$\begin{aligned}
\delta J = & \delta \left[\frac{1}{2} \iint \left\{ \bar{D}_{11} M_x^2 + \bar{D}_{22} M_y^2 + \bar{D}_{66} M_{xy}^2 + 2\bar{D}_{12} M_x M_y \right. \right. \\
& \left. \left. + 2\bar{D}_{16} M_x M_{xy} + 2\bar{D}_{26} M_y M_{xy} \right\} dx dy \right] \\
& - \delta \left[\iint \left\{ \frac{\partial w}{\partial x} \left(\frac{\partial M_x}{\partial x} + \frac{\partial M_{xy}}{\partial y} \right) + \frac{\partial w}{\partial y} \left(\frac{\partial M_{xy}}{\partial x} + \frac{\partial M_y}{\partial y} \right) \right\} dx dy \right] \quad (2.10) \\
& + \delta \left[\frac{\lambda}{2} \iint \left\{ n_{10} \left(\frac{\partial w}{\partial x} \right)^2 + n_{20} \left(\frac{\partial w}{\partial y} \right)^2 + 2n_{60} \left(\frac{\partial w}{\partial x} \right) \left(\frac{\partial w}{\partial y} \right) \right\} dx dy \right] \\
& + \delta \left[\iint \left\{ Q_n w + M_x \frac{\partial w}{\partial x} \eta_x + M_y \frac{\partial w}{\partial y} \eta_y + M_{xy} \left(\frac{\partial w}{\partial x} \eta_y + \frac{\partial w}{\partial y} \eta_x \right) \right\} ds \right],
\end{aligned}$$

where η_x and η_y are direction cosines, and Q_n is defined as

$$\begin{aligned}
Q_n = & \left(N_x \frac{\partial w}{\partial x} + N_{xy} \frac{\partial w}{\partial y} + \frac{\partial M_x}{\partial x} + \frac{\partial M_{xy}}{\partial y} \right) \eta_x \quad (2.11) \\
& + \left(N_{xy} \frac{\partial w}{\partial x} + N_y \frac{\partial w}{\partial y} + \frac{\partial M_{xy}}{\partial x} + \frac{\partial M_y}{\partial y} \right) \eta_y.
\end{aligned}$$

The direction cosines, force resultants, and moment resultants are shown in Fig. 2-1.

Therefore, the variational functional can be expressed as

$$J(w, M_x, M_y, M_{xy})$$

$$= \iint \frac{1}{2} \left\{ \bar{D}_{11} M_x^2 + \bar{D}_{22} M_y^2 + \bar{D}_{66} M_{xy}^2 + 2\bar{D}_{12} M_x M_y + 2\bar{D}_{16} M_x M_{xy} + 2\bar{D}_{26} M_y M_{xy} \right\} dx dy$$

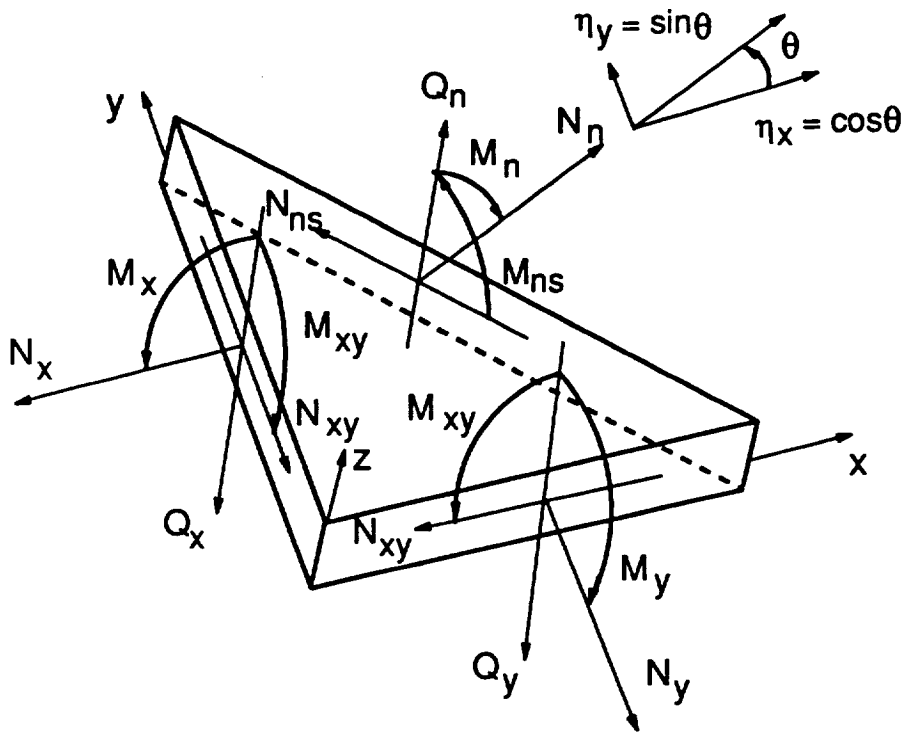


Fig. 2-1 Force resultants, moment resultants, and direction cosines.

$$\begin{aligned}
& + \iint \left\{ \frac{\partial w}{\partial x} \left(\frac{\partial M_x}{\partial x} + \frac{\partial M_{xy}}{\partial y} \right) + \frac{\partial w}{\partial y} \left(\frac{\partial M_{xy}}{\partial x} + \frac{\partial M_y}{\partial y} \right) \right\} dx dy \\
& + \frac{\lambda}{2} \iint \left\{ n_{10} \frac{\partial w^2}{\partial x} + n_{20} \frac{\partial w^2}{\partial y} + 2n_{60} \frac{\partial w}{\partial x} \frac{\partial w}{\partial y} \right\} dx dy \\
& - \int \left\{ M_x \frac{\partial w}{\partial x} \eta_x + M_y \frac{\partial w}{\partial y} \eta_y + M_{xy} \left(\frac{\partial w}{\partial x} \eta_y + \frac{\partial w}{\partial y} \eta_x \right) + Q_n w \right\} ds.
\end{aligned} \tag{2.12}$$

Interpolating the variables w , M_x , M_y , and M_{xy} in terms of nodal values of these variables, and constructing algebraic equations, leads to an eigenvalue problem which will be explained in the following section. From the above procedure to derive a functional it can be observed that the essential variables are

$$w, M_x, M_y, M_{xy}, \tag{2.13}$$

and the natural variables are

$$Q_n, \quad \frac{\partial w}{\partial x} \eta_x, \quad \frac{\partial w}{\partial y} \eta_y, \quad \left(\frac{\partial w}{\partial x} \eta_y + \frac{\partial w}{\partial y} \eta_x \right). \tag{2.14}$$

Note that the natural variables involving the bending moments in the displacement formulation become the essential variables in the mixed formulation.

2.2 Finite-Element Formulation

The quantities w , M_x , M_y , M_{xy} can be interpolated by expressions of the form

$$w = \sum_{j=1}^n \phi_j w_j, \quad M_x = \sum_{j=1}^n \phi_j M_{xj}, \quad M_y = \sum_{j=1}^n \phi_j M_{yj}, \quad M_{xy} = \sum_{j=1}^n \phi_j M_{xyj}, \quad (2.15)$$

where ϕ_j are appropriate interpolation functions, and w_j , M_{xj} , M_{yj} , and M_{xyj} are nodal values of out-of-plane displacement and moment resultants to be solved for. These constants are the nodal values of w , M_x , M_y , M_{xy} , respectively. By substituting eq. (2.15) into eq. (2.12) and equating the variations of J with respect to w_j , M_{xj} , M_{yj} , M_{xyj} to zero separately, a matrix equation of the following form is obtained :

$$\begin{bmatrix} K_{ij}^{11} & K_{ij}^{12} & K_{ij}^{13} & K_{ij}^{14} \\ K_{ij}^{12} & K_{ij}^{22} & K_{ij}^{23} & K_{ij}^{24} \\ K_{ij}^{13} & K_{ij}^{23} & K_{ij}^{33} & K_{ij}^{34} \\ K_{ij}^{14} & K_{ij}^{24} & K_{ij}^{34} & K_{ij}^{44} \end{bmatrix} \begin{bmatrix} w \\ M_x \\ M_y \\ M_{xy} \end{bmatrix} = \lambda \begin{bmatrix} M_{ij}^{11} & 0 & 0 & 0 \\ 0 & 0 & 0 & 0 \\ 0 & 0 & 0 & 0 \\ 0 & 0 & 0 & 0 \end{bmatrix} \begin{bmatrix} w \\ M_x \\ M_y \\ M_{xy} \end{bmatrix}, \quad (2.16)$$

where

$$K_{ij}^{11} = 0, \quad K_{ij}^{12} = \int \frac{\partial \phi_i}{\partial x} \frac{\partial \phi_j}{\partial x} dx dy$$

$$K_{ij}^{13} = \int \frac{\partial \phi_i}{\partial y} \frac{\partial \phi_j}{\partial y} dx dy, \quad K_{ij}^{14} = \int \left(\frac{\partial \phi_i}{\partial x} \frac{\partial \phi_j}{\partial y} + \frac{\partial \phi_i}{\partial y} \frac{\partial \phi_j}{\partial x} \right) dx dy$$

$$K_{ij}^{22} = - \int \bar{D}_{11} \phi_i \phi_j dx dy, \quad K_{ij}^{23} = - \int \bar{D}_{12} \phi_i \phi_j dx dy$$

$$\begin{aligned}
K_{ij}^{24} &= - \int \bar{D}_{16} \phi_i \phi_j dx dy, & K_{ij}^{33} &= - \int \bar{D}_{22} \phi_i \phi_j dx dy \\
K_{ij}^{34} &= - \int \bar{D}_{26} \phi_i \phi_j dx dy, & K_{ij}^{44} &= - \int \bar{D}_{66} \phi_i \phi_j dx dy
\end{aligned} \tag{2.17}$$

$$M_{ij}^{11} = \int \left[n_{10} \frac{\partial \phi_i}{\partial x} \frac{\partial \phi_j}{\partial x} + n_{20} \frac{\partial \phi_i}{\partial y} \frac{\partial \phi_j}{\partial y} + n_{60} \left(\frac{\partial \phi_i}{\partial x} \frac{\partial \phi_j}{\partial y} + \frac{\partial \phi_i}{\partial y} \frac{\partial \phi_j}{\partial x} \right) \right] dx dy.$$

As mentioned in the previous section, moments are essential boundary conditions in this mixed formulation. Therefore these essential boundary conditions must be satisfied exactly. On the hole boundary the moments must satisfy the conditions

$$M_n = 0, \quad M_{ns} = 0, \tag{2.18}$$

where, as shown in Fig. 2-1, M_n is the bending moment in the normal direction on the hole boundary, and M_{ns} is the twisting moment on the hole boundary. However, the nodal values being solved for are the moments in the x-y coordinate system. In order to satisfy eq. (2.18) on the hole boundary, M_n and M_{ns} need to be expressed in terms of the moments in the x-y coordinate system. Such an expression can be obtained from the moment equilibrium equation applied to the differential triangular element shown in Fig. 2-1. The relations are expressed as follows:

$$\begin{aligned}
M_n &= M_x \eta_x^2 + M_y \eta_y^2 + 2 M_{xy} \eta_x \eta_y \\
M_{ns} &= (M_y - M_x) \eta_x \eta_y + M_{xy} (\eta_x^2 - \eta_y^2).
\end{aligned} \tag{2.19}$$

Since M_n and M_{ns} are zero on the hole boundary, from eq. (2.19) the following relations are valid on the hole boundary :

$$M_y = \left(\frac{\eta_x^2}{\eta_y^2} \right) M_x, \quad M_{xy} = - \left(\frac{\eta_x}{\eta_y} \right) M_x. \quad (2.20)$$

Substituting these relations for the nodal values on the hole boundary in eq. (2.15) satisfies the free-edge condition on the hole boundary.

2.3 Numerical Procedure and Results

As stated earlier, the n_{10} , n_{20} , and n_{60} in the stability equation, eq. (2.1), are the prebuckling force resultants which must be calculated before the buckling analysis. These force resultants are calculated at Gauss points so that they can be used in the numerical integration procedure used in conjunction with the last of eq. (2.17). The prebuckling force resultant calculation is a two-dimensional planar analysis. A discussion of this step is not included here because it can be found in any one of a number of books discussing finite elements. For example, refer to [48] for more details on the analysis procedure and the computer program "FEM2D".

For a uniform stress loading if a unit force resultant is applied on the edge, i.e., $N_x = 1$ on the edge, then the resulting eigenvalue λ represents the critical value of N_x . For a uniform displacement loading, an arbitrary but uniform displacement is applied on the boundary. Then the force resultant distributions in the plate and average force resultant on the displaced edge are calculated. The average force resultant on the displaced edge is defined as

$$\bar{N}_x = \frac{1}{W} \int_{-\frac{W}{2}}^{\frac{W}{2}} N_x dy, \quad (2.21)$$

where W represents the width of the plate. It needs to be mentioned that if the analysis includes the region outside the supports, b is used instead of W (refer to Fig. 1-1). The force resultants within the plate are divided by this average force resultant on the displaced edge so distributions of the force resultants due to a unit average force resultant are obtained. These force resultant distributions due to a unit average force resultant are the n_{10} , n_{20} , and n_{60} in the notation used here and these resultants are substituted into the last of eq. (2.17). The resulting eigenvalue equation is eq. (2.16). Again, the resulting eigenvalue λ represents the critical applied average force resultant that results from a uniformly displaced edge.

For verification of the computer program the buckling coefficients were compared with those of Nemeth [31] for symmetric $[\pm \theta]_{ss}$ angle-ply laminates under a displacement loaded, clamped boundary condition. When the plate has the D_{16} and D_{26} components in the bending stiffness matrix, even though the geometry and loading are symmetric with respect to the x and y axes, the out-of-plane deflection is not symmetric with respect to these axes. In this case a full plate analysis must be used. Strictly speaking, a quarter-plate analysis is not correct. However, Nemeth [21] showed that if the anisotropic coefficients defined as

$$\gamma = \frac{D_{16}}{(D_{11}^3 D_{22})^{\frac{1}{4}}}, \quad \delta = \frac{D_{26}}{(D_{11} D_{22}^3)^{\frac{1}{4}}} \quad (2.22)$$

are less than 0.2, a result very close to a full-plate analysis can be obtained with a quarter-plate analysis with D_{16} and D_{26} set to zero. Nemeth used this approach and obtained results from Kantorovich's method. A comparison between Nemeth's results and the present analysis is shown in Fig. 2-2. The buckling coefficient in this comparison is defined as

$$K = \frac{\bar{N}_x^{cr} W^2}{\pi^2 \sqrt{D_{11} D_{22}}} . \quad (2.23)$$

For fiber angles of 0° , 30° , and 45° and changing D/W from 0.1 to 0.5 the results are compared. Fig. 2-2 shows that the present analysis is in good agreement with Nemeth's result. The present analysis considered one-quarter of the plate and assumed $D_{16} = D_{26} = 0$. Nemeth [31] also assumed $D_{16} = D_{26} = 0$.

Considering the plates in the postbuckling study, for a buckling analysis with the finite-element method large computer memory capacity is necessary. In the buckling analysis of a plate with a hole the memory size can be a limitation. The lowest buckling load, and the mode shape corresponding to this load, can generally be obtained with a small number of finite elements. However, it is possible that some of the other low buckling modes would not be detected with a full-plate analysis when using a small number of finite elements. In order to avoid this possibility of missing a buckling mode, yet staying within the limits of the computer capacity, based on Nemeth's argument a quarter-plate analysis is used in this study. However, a variety of boundary conditions, discussed below, must be used to account for the higher modes. Material properties for AS4/3502 used in the present study are tabulated in Table 2-1. With these material properties the anisotropic coefficients of the laminates selected for study, namely $[\pm 45/0/90]_{2s}$, $[\pm 45/0_2]_{2s}$, $[\pm 45/0_6]_s$, and $[\pm 45]_{4s}$ lam-

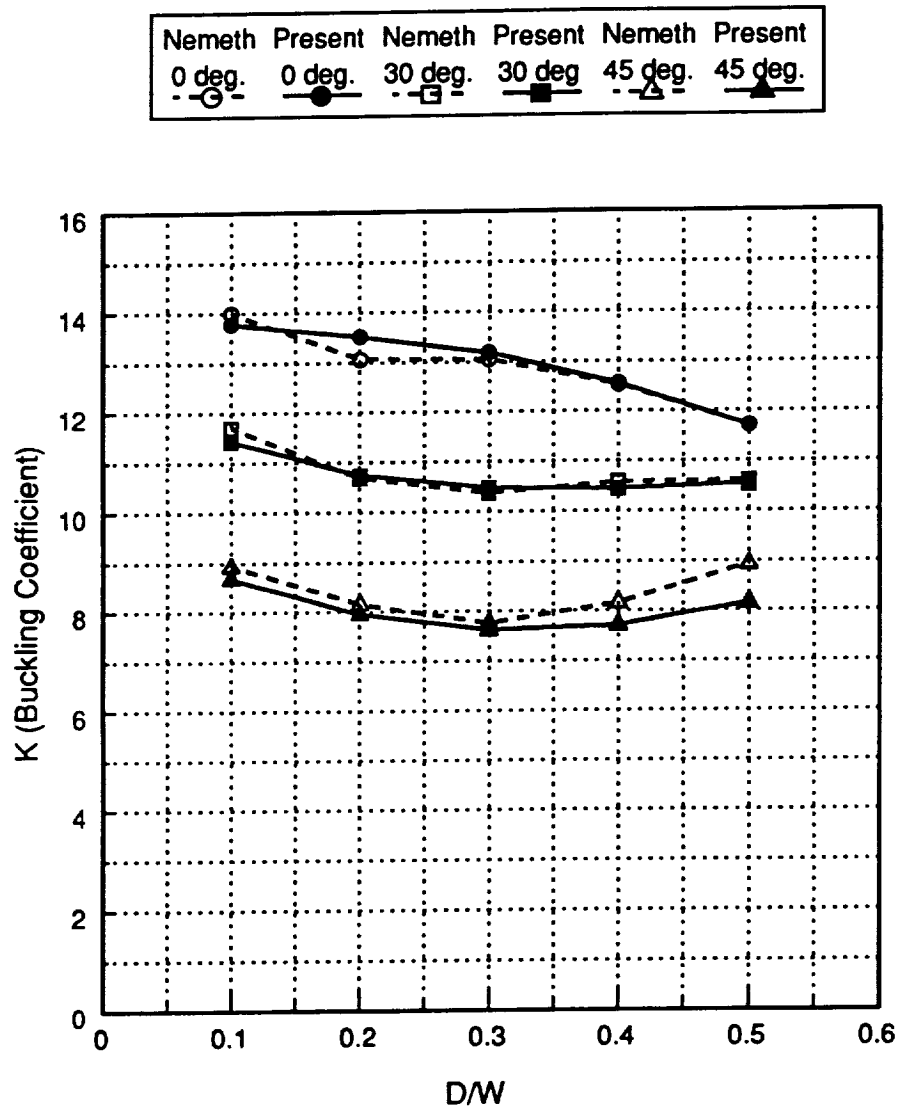


Fig. 2-2 Comparison with Nemeth's angle-ply results [31] for displacement loaded, clamped $[\pm \theta]_{6s}$ laminate.

Table 2-1 Layer material properties of AS4/3502.

E_1	18.500 Msi
E_2	1.600 Msi
G_{12}	0.832 Msi
G_{23}	0.332 Msi
ν_{12}	0.350
thickness	0.00531 in.

inates, are shown in Table 2-2. Since the coefficients are considerably less than 0.2, a quarter-plate analysis can be used with sufficient accuracy.

For a complete study with a quarter-plate analysis, to examine more than one of the lower modes, four kinds of boundary conditions must be considered on the x and y axes. These boundary conditions are explained in Fig. 2-3(a)-(d). The first case is free on the x axis and free on the y axis. This case produces mode shapes that are symmetric with respect to both the x and y axes. The second case is free on the x axis and simply supported on the y axis. This case produces mode shapes that are symmetric with respect to the x axis and anti-symmetric with respect to the y axis. The third case is opposite to the second case. The fourth case is simply supported on both the x and y axes, and this case produces mode shapes that are anti-symmetric with respect to both the x and y axes. Of course, in all of these cases the clamped and simply supported edges remain that way.

From all of the buckling loads calculated with the four sets of boundary conditions, the smallest three values are selected for each plate and they are listed in Table 2-3 for plates with holes. As can be seen as the number of 0° layers is increased, the buckling load increases. The $[\pm 45]_{4s}$ laminate shows the smallest buckling load. For future use the critical (buckling) force resultants are nondimensionalized in the form of $\frac{P_{cr}}{EA}$, where P_{cr} is the buckling load (\bar{N}_x^{cr} multiplied by load applied length), E is the equivalent Young's modulus in the x-direction of the corresponding laminate, and A is the area of the edge of the laminate where the load is applied. The equivalent Young's modulus of each laminate is tabulated in Table 2-4.

Table 2-2 Anisotropic coefficients for laminates in this study.

Laminate	γ	δ
$[\pm 45/0/90]_{2s}$	0.067	0.073
$[\pm 45/0_2]_{2s}$	0.062	0.092
$[\pm 45/0_6]_s$	0.041	0.068
$[\pm 45]_{4s}$	0.134	0.134

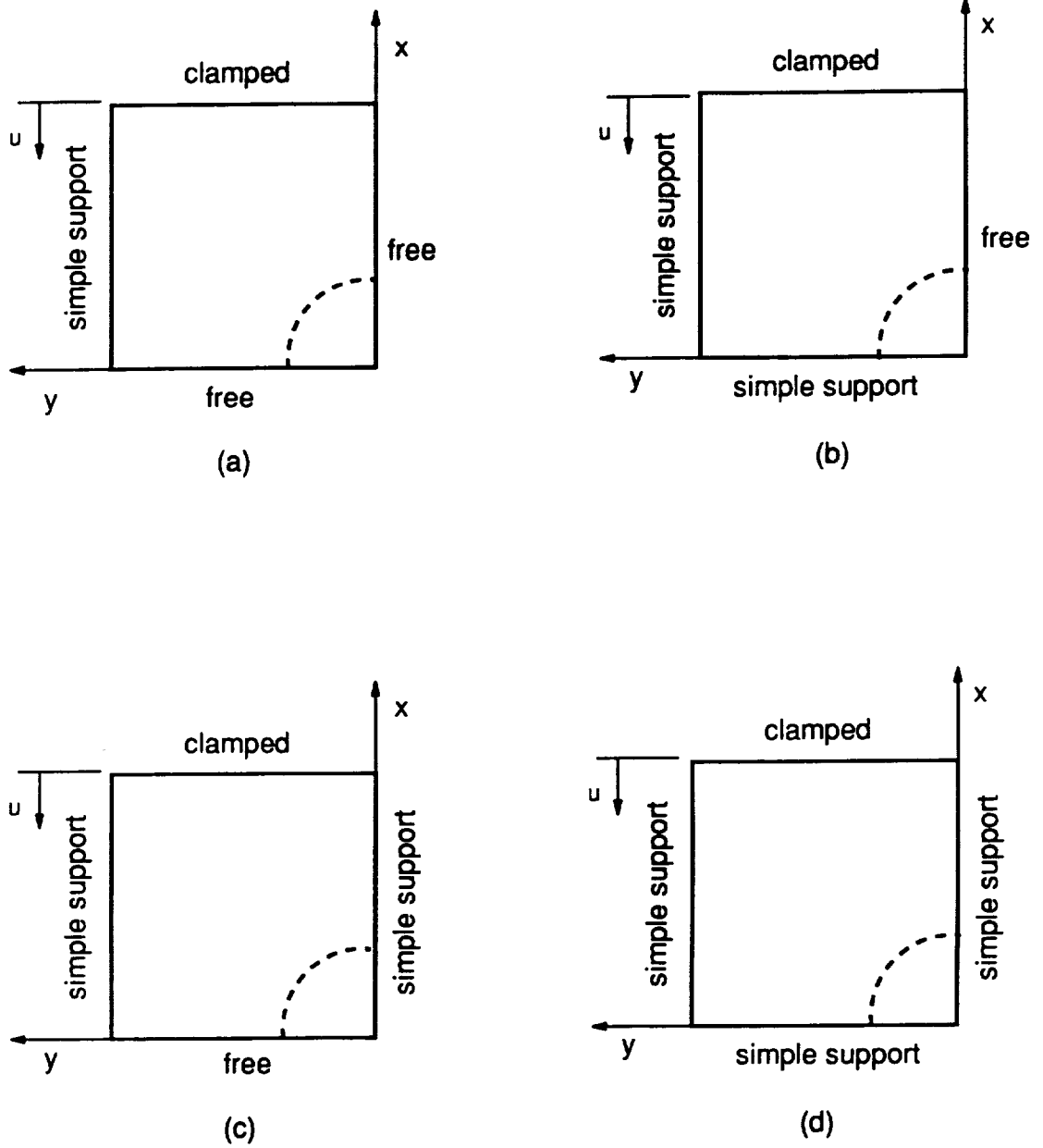


Fig. 2-3 Four boundary conditions for quarter-plate buckling analysis.

Table 2-3 Buckling loads of plates with holes.

Laminate	Parameter	First mode	Second mode	Third mode
[± 45/0/90] _{2S}	\bar{N}_x^{cr}	258	424	470
	$\frac{P_{cr}}{EA}$	0.000411	0.000676	0.000749
[± 45/0 ₂] _{2S}	\bar{N}_x^{cr}	294	496	497
	$\frac{P_{cr}}{EA}$	0.000321	0.000541	0.000542
[± 45/0 ₆] _S	\bar{N}_x^{cr}	318	508	545
	$\frac{P_{cr}}{EA}$	0.000245	0.000407	0.000436
[± 45] _{4S}	\bar{N}_x^{cr}	240	373	427
	$\frac{P_{cr}}{EA}$	0.000980	0.001523	0.001744

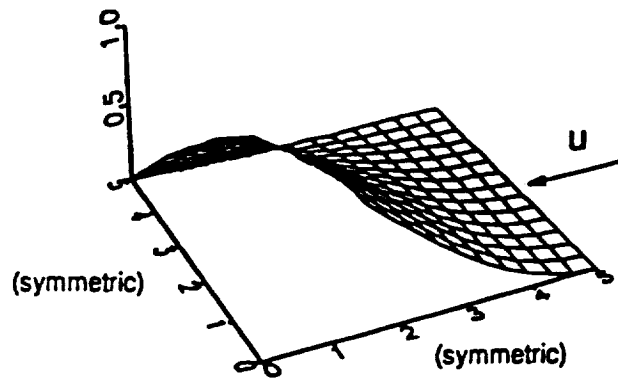
(unit of \bar{N}_x^{cr} = lb/in)

Table 2-4 Equivalent Young's modulus in x direction for each laminate.

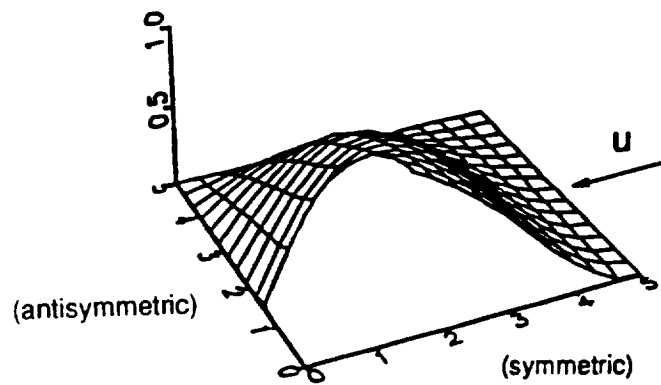
$[\pm 45/0/90]_{2s}$	7.381E+06 psi
$[\pm 45/0_2]_{2s}$	1.078E+07 psi
$[\pm 45/0_6]_s$	1.469E+07 psi
$[\pm 45]_{4s}$	2.881E+06 psi

In conjunction with the buckling loads, the buckling mode shape must be understood. From Fig. 2-4 and Fig. 2-5 it can be seen that for every plate the first mode is one half-wave in both the x and y directions. For the second mode the $[\pm 45/0/90]_{2s}$ and $[\pm 45]_{4s}$ plates have two half-waves in the x direction and one half-wave in the y direction. However, for the second mode the $[\pm 45/0_2]_{2s}$ and $[\pm 45/0_6]_s$ plates have one half-wave in the x direction and two half-waves in the y direction. In the third mode the $[\pm 45/0/90]_{2s}$ and $[\pm 45]_{4s}$ plates have two half-waves in the y direction and one half-wave in the x direction, but the $[\pm 45/0_2]_{2s}$ and $[\pm 45/0_6]_s$ plates have one half-wave in the y direction and two half-waves in the x direction. It is important to note from Table 2-3 how close together the second and third mode buckling loads can be. In an actual experiment it might be impossible to distinguish between these two modes.

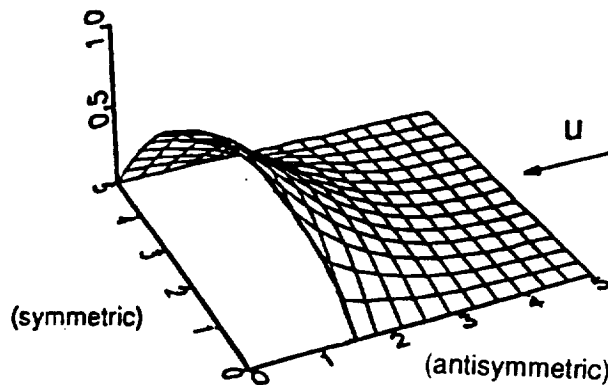
For comparison, the buckling loads of solid plates of the same lamination as the plates with holes were calculated. The smallest three buckling loads for each plate are tabulated in Table 2-5, and the buckling mode shapes are shown in Fig. 2-6 and Fig. 2-7. The buckling loads of solid plates are higher than those of the plates with holes. All the solid plates have the same mode shapes in the first and second modes. The first mode shape is one half-wave in both the x and y directions, and the second mode shape is two half-waves in the x direction and one half-wave in the y direction. In the third mode the $[\pm 45/0/90]_{2s}$ and $[\pm 45]_{4s}$ laminates showed two half-waves in the x direction and one half-wave in the y direction. The $[\pm 45/0_2]_{2s}$ and $[\pm 45/0_6]_s$ plates showed one half-wave in the x direction and two half-waves in the y direction. For the case of plates without holes the buckling loads of the second and third modes are far apart. With the buckling analysis established, and numerical results computed, the next chapter addresses the issue of postbuckling.



First mode

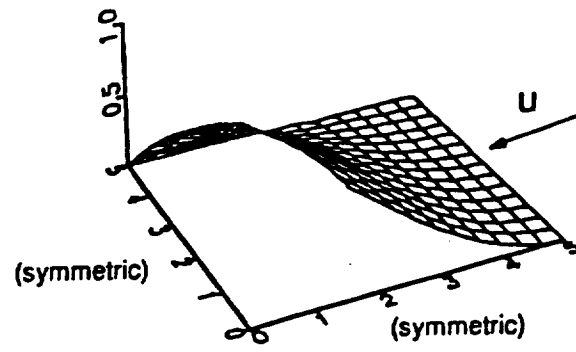


Second mode

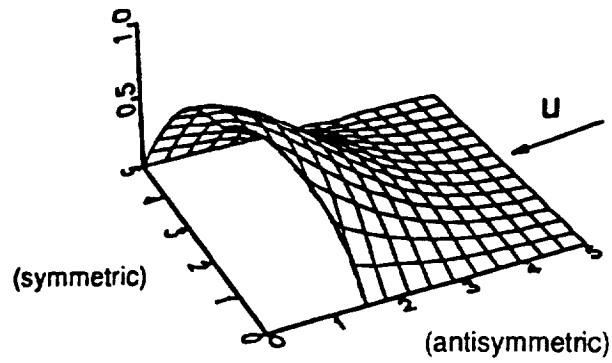


Third mode

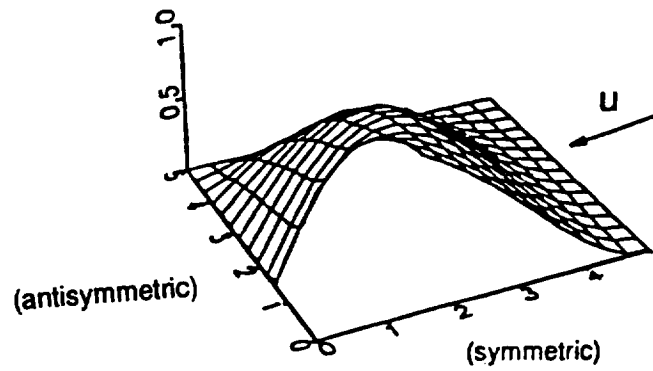
Fig. 2-4 Buckling mode shapes of $[\pm 45/0/90]_{2s}$ and $[\pm 45]_{4s}$ plates with holes.



First mode



Second mode



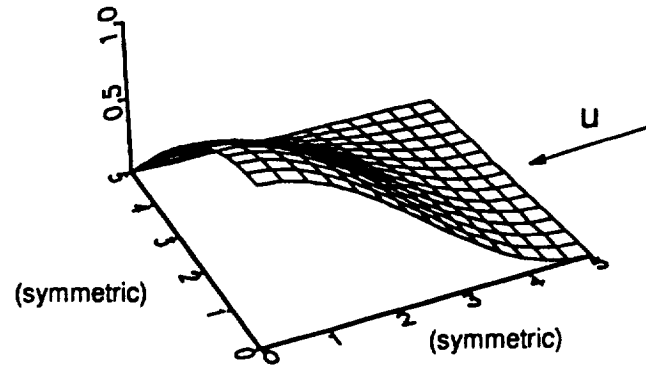
Third mode

Fig. 2-5 Buckling mode shapes of $[\pm 45/0_2]_s$ and $[\pm 45/0_6]_s$ plates with holes.

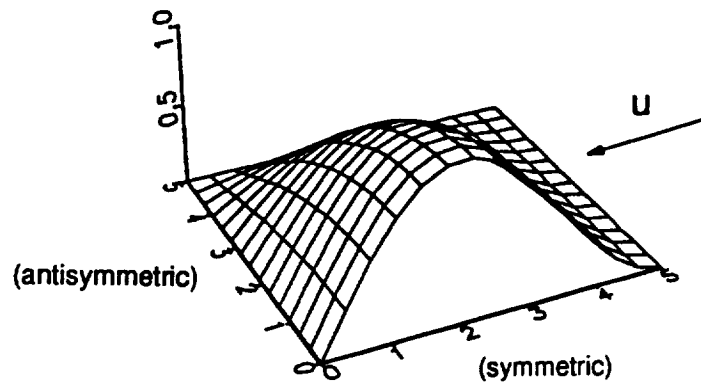
Table 2-5 Buckling loads of solid plates.

Laminate	Parameter	First mode	Second mode	Third mode
[± 45/0/90] _{2S}	\bar{N}_x^{cr}	293	444	762
	$\frac{P_{cr}}{EA}$	0.000467	0.000708	0.001215
[± 45/0 ₂] _{2S}	\bar{N}_x^{cr}	327	528	888
	$\frac{P_{cr}}{EA}$	0.000357	0.000576	0.000969
[± 45/0 ₆] _S	\bar{N}_x^{cr}	340	571	841
	$\frac{P_{cr}}{EA}$	0.000272	0.000457	0.000673
[± 45] _{4S}	\bar{N}_x^{cr}	291	405	650
	$\frac{P_{cr}}{EA}$	0.001188	0.001654	0.002654

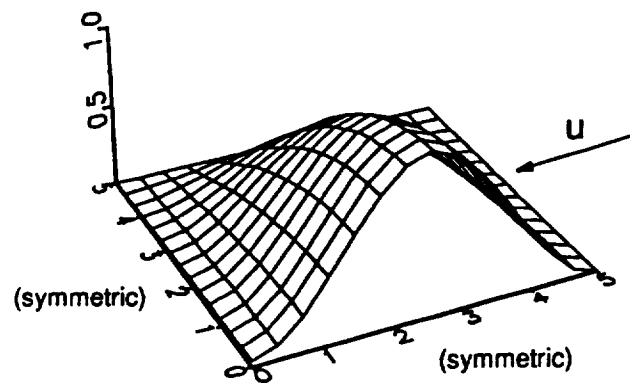
(unit of \bar{N}_x^{cr} = lb/in)



First mode

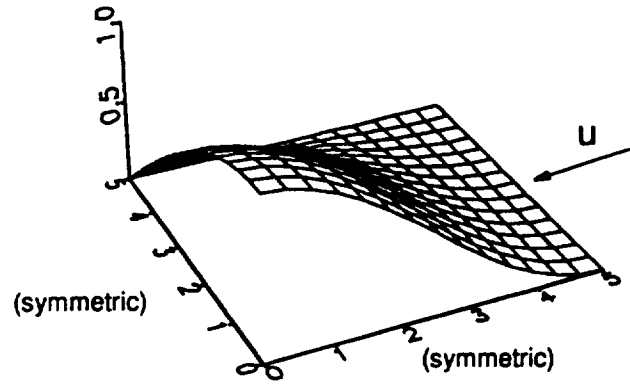


Second mode

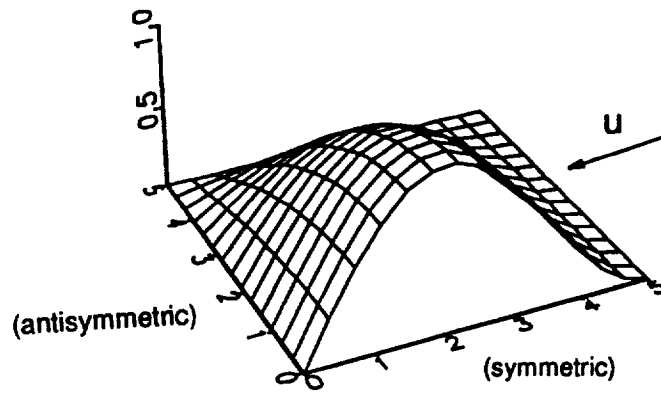


Third mode

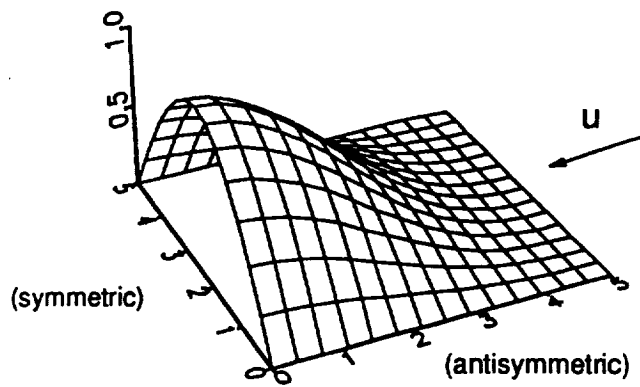
Fig. 2-6 Buckling mode shapes of solid $[\pm 45/0/90]_{2s}$ and $[\pm 45]_{4s}$ plates.



First mode



Second mode



Third mode

Fig. 2-7 Buckling mode shapes of solid $[\pm 45/0_2]_{2s}$ and $[\pm 45/0_s]_s$ plates.

3.0 Nonlinear Plate Bending With Initial Imperfection

For analysis in the postbuckling range of deflection, a plate bending finite-element program which includes the influence of geometric nonlinearity is developed. For an ideal plate the stiffness matrix of the algebraic equations becomes singular at the buckling load. Therefore, in postbuckling studies numerical difficulties can occur at load levels near the buckling load. One of the ways to overcome this singularity problem at the buckling load is to impose a small initial out-of-plane deflection on the plate. As plates fabricated to be flat are rarely without an initial out-of-plane deflection, the inclusion of these effects in the analysis is quite realistic. In addition, numerical difficulties are avoided. This is the approach taken here.

The basic kinematic equations for plate bending with initial imperfection can be found in reference [50]. The finite-element formulation procedure for this development, in the context of a first-order shear deformation theory, will be explained in the following sections. The formulation results in a set of nonlinear algebraic equations.

The resulting nonlinear algebraic equations are solved by the Newton-Raphson method. The general features of the Newton-Raphson method will also be explained in a following section.

3.1 Governing Equations

For a first-order shear deformation theory, the displacement field is assumed to be of the form

$$\begin{aligned}
 u_1(x, y, z) &= u(x, y) + z \psi_x(x, y) \\
 u_2(x, y, z) &= v(x, y) + z \psi_y(x, y) \\
 u_3(x, y, z) &= w(x, y).
 \end{aligned}
 \tag{3.1}$$

Here u_1, u_2, u_3 are the displacements in the x, y, z directions, respectively, u, v, w are the associated midplane displacements, and ψ_x and ψ_y are cross-section rotations of the line elements perpendicular to the midplane in the x - z and y - z planes, respectively. The strains in the plate are expressed as

$$\begin{aligned}
 \varepsilon_x &= \varepsilon_x^0 + z \kappa_x^0 \\
 \varepsilon_y &= \varepsilon_y^0 + z \kappa_y^0 \\
 \gamma_{xy} &= \gamma_{xy}^0 + z \kappa_{xy}^0
 \end{aligned}
 \tag{3.2}$$

$$\gamma_{xz} = \psi_x + \frac{\partial w}{\partial x}$$

$$\gamma_{yz} = \psi_y + \frac{\partial w}{\partial y},$$

where the ε_x^0 , ε_y^0 , and γ_{xy}^0 are the midplane strains, and the κ_x^0 , κ_y^0 , and κ_{xy}^0 are the midplane curvatures. By one of the assumptions of plate theory, lengths normal to the midplane remains unchanged. Therefore the strain in the thickness direction is zero, i.e., $\varepsilon_z = 0$. The midplane strain-displacement relations and midplane curvatures for a plate with an initial imperfection can be written explicitly as

$$\varepsilon_x^0 = \frac{\partial u}{\partial x} + \frac{1}{2} \left(\frac{\partial w}{\partial x} \right)^2 + \frac{\partial \xi}{\partial x} \frac{\partial w}{\partial x}$$

$$\varepsilon_y^0 = \frac{\partial v}{\partial y} + \frac{1}{2} \left(\frac{\partial w}{\partial y} \right)^2 + \frac{\partial \xi}{\partial y} \frac{\partial w}{\partial y}$$

$$\gamma_{xy}^0 = \frac{\partial u}{\partial y} + \frac{\partial v}{\partial x} + \frac{\partial w}{\partial x} \frac{\partial w}{\partial y} + \frac{\partial \xi}{\partial x} \frac{\partial w}{\partial y} + \frac{\partial \xi}{\partial y} \frac{\partial w}{\partial x}$$

$$\kappa_x^0 = \frac{\partial \psi_x}{\partial x} \tag{3.3}$$

$$\kappa_y^0 = \frac{\partial \psi_y}{\partial y}$$

$$\kappa_{xy}^0 = \frac{\partial \psi_x}{\partial y} + \frac{\partial \psi_y}{\partial x},$$

where the influence of geometric nonlinearities has been included and ξ is the initial out-of-plane imperfection.

The governing equilibrium equations can be derived by the principle of virtual work. That principle can be expressed as

$$0 = \delta \hat{U} - \delta \hat{W}, \quad (3.4)$$

where \hat{U} is the internal strain energy and \hat{W} is the work done by external forces. The body force terms are neglected in this equation. The variation of the work done by the external forces is expressed as

$$\delta \hat{W} = \int q \delta w \, dx \, dy + \int (\hat{N}_n \delta u_n - \hat{M}_n \frac{\partial \delta w}{\partial n} + \hat{N}_{ns} \delta u_s - \hat{M}_{ns} \frac{\partial \delta w}{\partial s} + \hat{Q}_n \delta w) dS, \quad (3.5)$$

where \hat{N}_n , \hat{N}_{ns} , \hat{M}_n , \hat{M}_{ns} , and \hat{Q}_n are the specified applied resultants defined by

$$\begin{aligned} \hat{N}_n &= \int_{-\frac{h}{2}}^{\frac{h}{2}} \hat{t}_n \, dz, & \hat{N}_{ns} &= \int_{-\frac{h}{2}}^{\frac{h}{2}} \hat{t}_{ns} \, dz, \\ \hat{M}_n &= \int_{-\frac{h}{2}}^{\frac{h}{2}} z \hat{t}_n \, dz, & \hat{M}_{ns} &= \int_{-\frac{h}{2}}^{\frac{h}{2}} z \hat{t}_{ns} \, dz, & \hat{Q}_n &= \int_{-\frac{h}{2}}^{\frac{h}{2}} \hat{t}_{nz} \, dz. \end{aligned} \quad (3.6)$$

In the above the effect of a transverse load, q , is included for completeness. Here \hat{t}_n , \hat{t}_{ns} , and \hat{t}_{nz} are specified normal and tangential stress components, and u_n and u_s are normal and tangential components of the midplane displacements on the edge. Now, including the strain energy term, the principle of virtual work is expressed as

$$\begin{aligned} 0 &= \int (\sigma_x \delta \varepsilon_x + \sigma_y \delta \varepsilon_y + \tau_{xy} \delta \gamma_{xy} + \tau_{yz} \delta \gamma_{yz} + \tau_{xz} \delta \gamma_{xz}) \, dV \\ &\quad - \int q \delta w \, dx \, dy - \int \hat{N}_n \delta u_n \, dS - \int \hat{N}_{ns} \delta u_s \, dS \\ &\quad + \int \hat{M}_n \frac{\partial \delta w}{\partial n} \, dS + \int \hat{M}_{ns} \frac{\partial \delta w}{\partial s} \, dS - \int \hat{Q}_n \delta w \, dS. \end{aligned} \quad (3.7)$$

To derive the equilibrium equations, in addition to the moment and inplane force resultants defined in eq (2.3) and eq (2.5), respectively, the out-of-plane force resultants Q_x and Q_y defined as

$$Q_x = \int_{-\frac{h}{2}}^{\frac{h}{2}} \tau_{xz} dz, \quad Q_y = \int_{-\frac{h}{2}}^{\frac{h}{2}} \tau_{yz} dz. \quad (3.8)$$

are used. By substituting the strain-displacement relation, eq. (3.3), into the virtual work statement, eq. (3.7), integrating in the thickness direction, applying integration by parts, and using the relations

$$\begin{aligned} N_n &= N_x \eta_x^2 + N_y \eta_y^2 + 2 N_{xy} \eta_x \eta_y \\ N_{ns} &= (N_y - N_x) \eta_x \eta_y + N_{xy} (\eta_x^2 - \eta_y^2) \\ M_n &= M_x \eta_x^2 + M_y \eta_y^2 + 2 M_{xy} \eta_x \eta_y \\ M_{ns} &= (M_y - M_x) \eta_x \eta_y + M_{xy} (\eta_x^2 - \eta_y^2) \end{aligned} \quad (3.9)$$

and

$$\begin{aligned} u_n &= u \eta_x + v \eta_y, \quad u_s = -u \eta_y + v \eta_x, \\ u &= u_n \eta_x - u_s \eta_y, \quad v = u_n \eta_y + u_s \eta_x, \\ \psi_n &= \psi_x \eta_x + \psi_y \eta_y, \quad \psi_s = -\psi_x \eta_y + \psi_y \eta_x, \\ \psi_x &= \psi_n \eta_x - \psi_s \eta_y, \quad \psi_y = \psi_n \eta_y + \psi_s \eta_x, \\ \frac{\partial}{\partial n} &= \eta_x \frac{\partial}{\partial x} + \eta_y \frac{\partial}{\partial y}, \quad \frac{\partial}{\partial s} = \eta_x \frac{\partial}{\partial y} - \eta_y \frac{\partial}{\partial x} \\ \frac{\partial}{\partial x} &= \eta_x \frac{\partial}{\partial n} - \eta_y \frac{\partial}{\partial s}, \quad \frac{\partial}{\partial y} = \eta_y \frac{\partial}{\partial n} + \eta_x \frac{\partial}{\partial s}, \end{aligned} \quad (3.10)$$

where η_x and η_y are direction cosines as shown in Fig. 2-1, the following form of the principle of virtual work is obtained:

$$0 = \int \delta u \left(\frac{\partial N_x}{\partial x} + \frac{\partial N_{xy}}{\partial y} \right) dx dy + \int \delta v \left(\frac{\partial N_{xy}}{\partial x} + \frac{\partial N_y}{\partial y} \right) dx dy$$

$$\begin{aligned}
& + \int \delta w \left(\frac{\partial Q_x}{\partial x} + \frac{\partial Q_y}{\partial y} + \frac{\partial}{\partial x} \left\{ N_x \left(\frac{\partial w}{\partial x} + \frac{\partial \xi}{\partial x} \right) + N_{xy} \left(\frac{\partial w}{\partial y} + \frac{\partial \xi}{\partial y} \right) \right\} \right. \\
& + \left. \frac{\partial}{\partial y} \left\{ N_{xy} \left(\frac{\partial w}{\partial x} + \frac{\partial \xi}{\partial x} \right) + N_y \left(\frac{\partial w}{\partial y} + \frac{\partial \xi}{\partial y} \right) \right\} + q \right) dx dy \quad (3.11) \\
& + \int \delta \psi_x \left(\frac{\partial M_x}{\partial x} + \frac{\partial M_{xy}}{\partial y} - Q_x \right) dx dy + \int \delta \psi_y \left(\frac{\partial M_{xy}}{\partial x} + \frac{\partial M_y}{\partial y} - Q_y \right) dx dy \\
& + \int \delta u_n (N_n - \hat{N}_n) dS + \int \delta u_s (N_{ns} - \hat{N}_{ns}) dS + \int \delta \psi_n (M_n - \hat{M}_n) dS \\
& + \int \delta \psi_s (M_{ns} - \hat{M}_{ns}) dS + \int \delta w (Q_n - \hat{Q}_n) dS.
\end{aligned}$$

Since the variations δu , δv , δw , $\delta \psi_x$, $\delta \psi_y$, δu_n , δu_s , $\delta \psi_n$, and $\delta \psi_s$ are arbitrary, the equilibrium equations are as follows :

$$\begin{aligned}
\delta u : \quad & \frac{\partial N_x}{\partial x} + \frac{\partial N_{xy}}{\partial y} = 0 \\
\delta v : \quad & \frac{\partial N_{xy}}{\partial x} + \frac{\partial N_y}{\partial y} = 0 \\
\delta w : \quad & \frac{\partial Q_x}{\partial x} + \frac{\partial Q_y}{\partial y} + \frac{\partial}{\partial x} \left\{ N_x \left(\frac{\partial w}{\partial x} + \frac{\partial \xi}{\partial x} \right) + N_{xy} \left(\frac{\partial w}{\partial y} + \frac{\partial \xi}{\partial y} \right) \right\} \\
& + \frac{\partial}{\partial y} \left\{ N_{xy} \left(\frac{\partial w}{\partial x} + \frac{\partial \xi}{\partial x} \right) + N_y \left(\frac{\partial w}{\partial y} + \frac{\partial \xi}{\partial y} \right) \right\} + q = 0 \quad (3.12) \\
\delta \psi_x : \quad & \frac{\partial M_x}{\partial x} + \frac{\partial M_{xy}}{\partial y} - Q_x = 0 \\
\delta \psi_y : \quad & \frac{\partial M_{xy}}{\partial x} + \frac{\partial M_y}{\partial y} - Q_y = 0.
\end{aligned}$$

The boundary conditions are :

$$\begin{aligned}
& \text{either } \delta u_n = 0, \text{ or } N_n - \hat{N}_n = 0 \\
& \text{either } \delta u_s = 0, \text{ or } N_{ns} - \hat{N}_{ns} = 0 \\
& \text{either } \delta \psi_n = 0, \text{ or } M_n - \hat{M}_n = 0 \quad (3.13) \\
& \text{either } \delta \psi_s = 0, \text{ or } M_{ns} - \hat{M}_{ns} = 0
\end{aligned}$$

either $\delta w = 0$, or $Q_n - \hat{Q}_n = 0$

3.2 Finite-Element Formulation

In this work a displacement based finite-element formulation for the governing equations derived in the previous section is used. The principle of virtual work statement in the previous section , eq. (3.11), can be expressed in terms of displacements u , v , w , ψ_x , and ψ_y using Hooke's law and the strain-displacement equations. Over a typical element the generalized displacement U , where U represents u , v , w , ψ_x , and ψ_y , is interpolated spatially by an expression of the form

$$U = \sum_i^r U_i \phi_i(x, y), \quad (3.14)$$

where U_i is the value of U at node i , ϕ_i is the finite-element interpolation function at node i , and r is the number of nodes in the element. For simplicity in this formulation the same interpolation function is used for each of the five deformations u , v , w , ψ_x , and ψ_y . Substituting the interpolated expression for the displacements into the principle of virtual work statement, eq. (3.11), and collecting the terms of δU , leads to the following equation for a typical element:

$$[K^e(\Delta)] \{\Delta\}^e = \{F\}^e. \quad (3.15)$$

Here $\{\Delta\}^e$ is the column vector of the nodal values of the generalized displacements, $[K^e(\Delta)]$ is the matrix of the stiffness coefficients, and $\{F\}^e$ is the column vector containing the boundary and transverse force contributions. The notation $[K^e(\Delta)]$ indicates that the stiffness matrix is a function of the nodal values. Thus the problem is

nonlinear in the nodal displacements. The assembled finite-element equations are of the form

$$[K(\Delta)] \{\Delta\} = \{F\}, \quad (3.16)$$

where $[K(\Delta)]$ is the direct stiffness matrix and $\{\Delta\}$ is the global solution vector. This nonlinear set of equations is solved iteratively. Here the Newton-Raphson method is used, and it is illustrated in the next section.

3.3 Newton-Raphson Method

To solve the system of nonlinear equations, eq. (3.16), they are transformed into the form

$$[K^T(\Delta^r)] \{\delta\Delta^r\} = \{R\}, \quad (3.17)$$

where $\{\Delta^r\}$ is the intermediate solution at the r -th iteration and $[K^T(\Delta^r)]$ is the tangent stiffness matrix which is obtained from the relation

$$[K^T(\Delta^r)] = \left[\frac{\partial \{R\}}{\partial \{\Delta^r\}} \right], \quad (3.18)$$

$\{R\}$ is the residual given by

$$\{R\} = [K(\Delta^r)] \{\Delta^r\} - \{F\}, \quad (3.19)$$

and $\{\delta\Delta^r\}$ is the increment of the solution. The tangent stiffness matrix in eq. (3.18) is symmetric. The total displacement at the $(r + 1)$ -st iteration becomes

$$\{\Delta^{r+1}\} = \{\Delta^r\} + \{\delta\Delta^r\}. \quad (3.20)$$

The true solution makes the residual zero, i. e.,

$$\{R\} = 0. \quad (3.21)$$

In this implementation iteration is stopped when the following equation is satisfied:

$$\frac{\sqrt{\sum_{i=1}^N |\Delta_i^{r+1} - \Delta_i^r|^2}}{\sum_{i=1}^N |\Delta_i^r|^2} \leq EPS, \quad (3.22)$$

where the value of EPS is 0.01 in most of the work.

3.4 Numerical Results

3.4.1 Verification of Present Analysis

Based on the argument associated with Table 2-2, a quarter-plate model is again employed in the postbuckling analysis and D_{16} and D_{26} are assumed to be zero. A uniform inplane displacement is applied on one edge. Recall that the displaced edge and the edge opposite to it are clamped, and the two other edges are simply supported. For the initial out-of-plane deflection a one-term double cosine function is used which is of the form

$$\xi = w_0 h \cos\left(\frac{\pi x}{L}\right) \cos\left(\frac{\pi y}{W}\right), \quad (3.23)$$

where h is the plate thickness, and L and W are the plate length and width inside the supports, respectively, as shown in Fig. 1-1. In the above equation, w_0 is the fraction of initial out-of-plane deflection with respect to the plate thickness at the center of the plate. In these results w_0 was taken to be 0.1. As mentioned previously, the nonlinear simultaneous equations are solved by the Newton-Raphson method, an incremental scheme using the solution of the previous load step as the initial guess of the next load step.

For the verification of the computer program, postbuckling results were compared with the widely used commercial computer code ABAQUS [48]. The case of a solid quasi-isotropic plate, a $[\pm 45/0/90]_{2s}$ laminate, was considered. The material properties used in the comparison are given in Table 2-1. The same boundary conditions as in the present study, i.e., clamped on the loaded edge and simply supported on the other two edges, were applied. The dimensions of the plate were also 10" by 10". In ABAQUS [48] the initial imperfect out-of-plane deflection was assumed to be the same as the first buckling mode. This is not quite the same situation as eq. (3.23), but it is close enough. Fig. 3-1 shows the comparison for the load vs. end shortening relation, and Fig. 3-2 shows the comparison for the load vs. out-of-plane deflection relation. The out-of-plane deflection being considered in Fig. 3-2 is the deflection at the center of the plate. Note that the nondimensionalized load parameter, $\frac{P}{EA}$, is the same as in chapter 2. For both the ABAQUS results and the present results 16 elements were used for a quarter-plate. As can be seen, the comparison of the present formulation with the commercially available code is quite good. Note

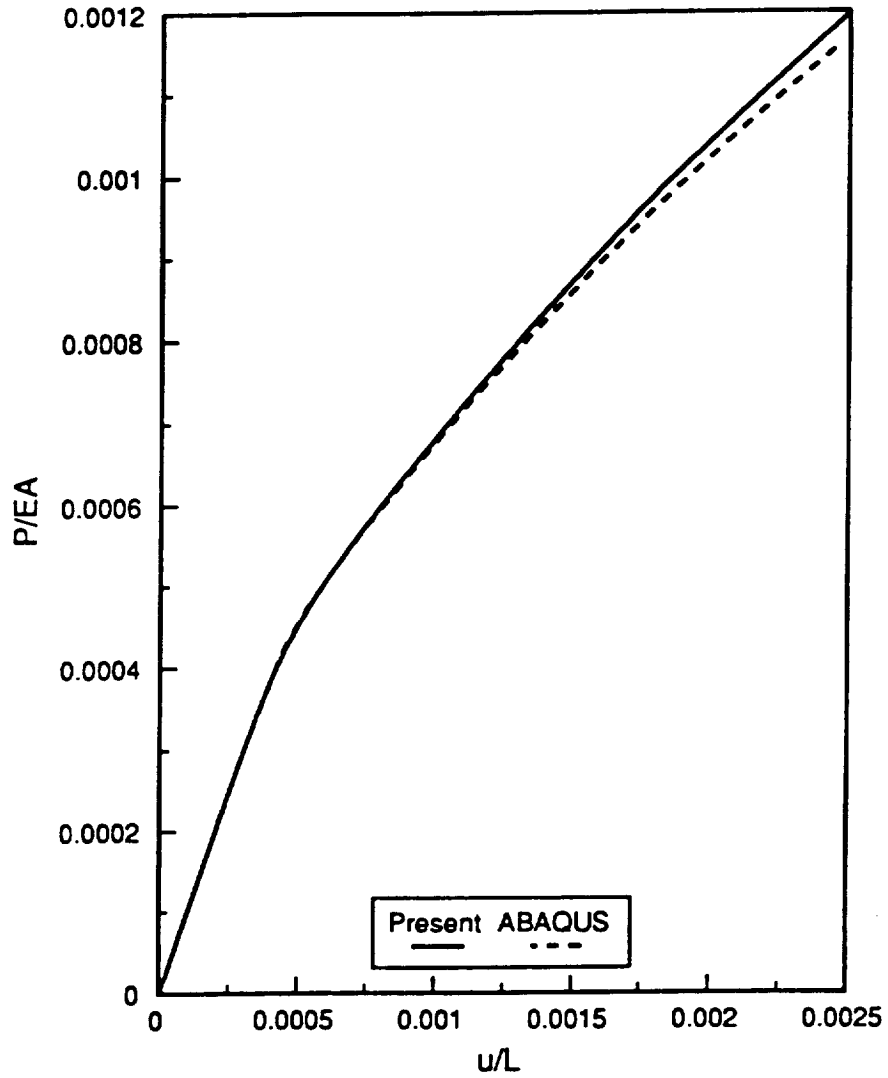


Fig. 3-1 Comparison with ABAQUS [48] for load vs. end shortening relation of solid $[\pm 45/0/90]_{2s}$ plate under displacement loaded, clamped condition.

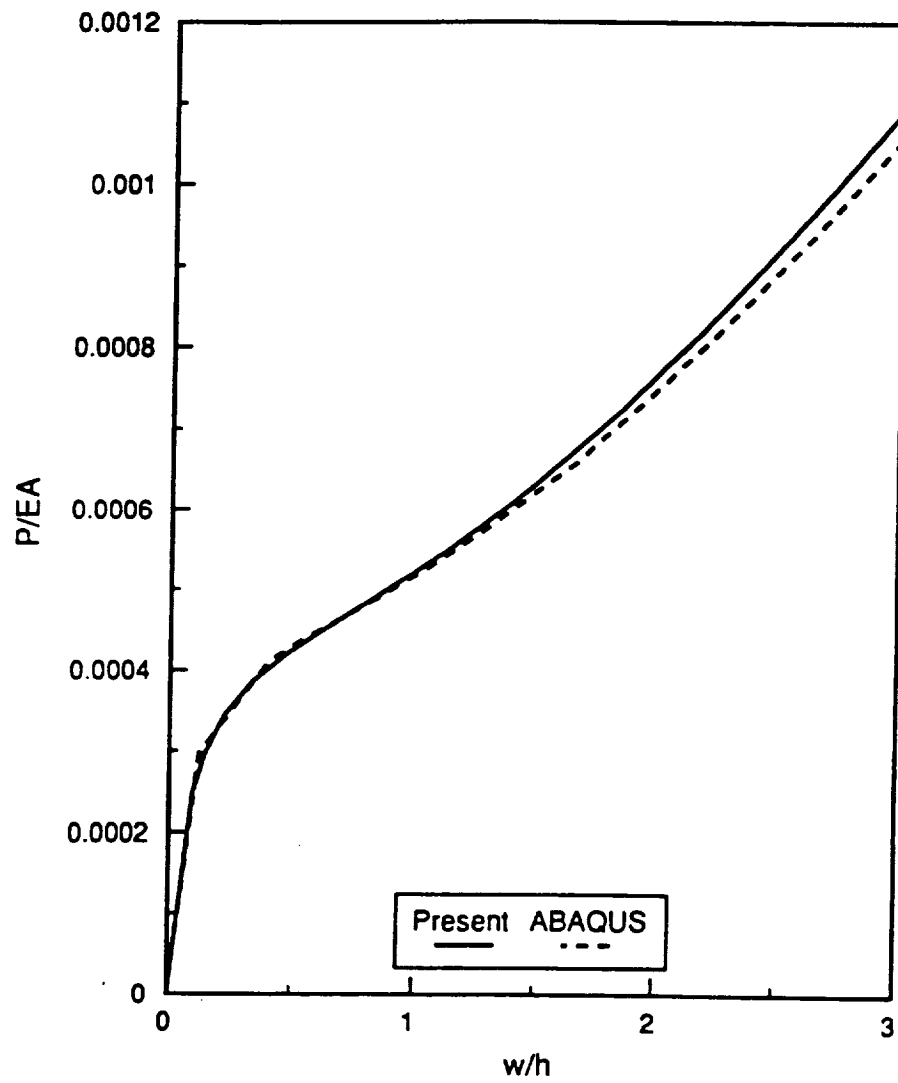
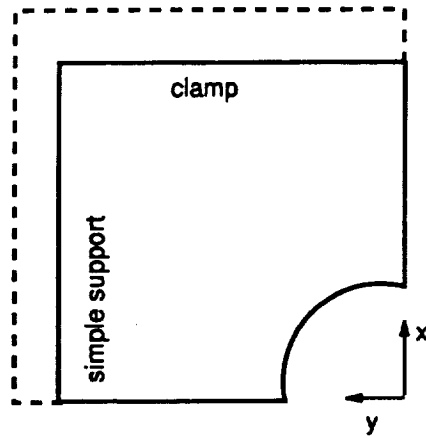


Fig. 3-2 Comparison with ABAQUS [48] for load vs. out-of-plane deflection relation of solid $[\pm 45/0/90]_{2s}$ plate under displacement loaded, clamped condition.

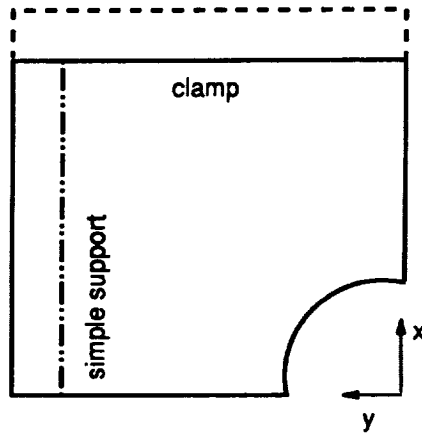
that the load vs. end shortening relation is almost linear until the buckling load is reached. After that load level the slope of the load-end shortening relation decreases sharply. The secondary portion of the relation is associated with the postbuckling response of the plate. The load vs. out-of-plane deflection is also nearly linear until the buckling load is reached. The deflection then increases rapidly with increasing load, the region of high deflection again being associated with the postbuckling response.

3.4.2 The Effect of the Portion of the Plate Outside the Supports

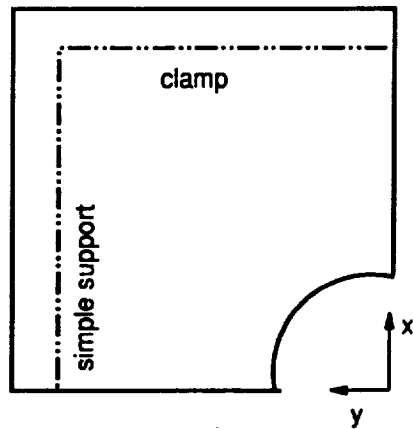
As mentioned earlier, in any real experimental set-up the plate extends outside the supports. It is physically impossible to perform the experiment any other way. Thus it is important to know the influence on the plate response of the portions of the plate beyond the supports, and to determine if they must be included in the analysis of the plate. Here the effects of the extensions on the postbuckling analysis will be studied. To that end, the three cases shown in Fig. 3-3 are studied. In Fig. 3-3 the 'no extension' case represents the usual numerical analysis where only the region inside the supports is considered. The 'simple extension' case represents the case where the portion of the plate beyond the simple support is taken into account. The analysis region is the region of 'no extension' plus the region beyond the simple support. The 'both extensions' case represents the condition where the entire region of the plate is considered. In this case the analysis region is the same as the specimen in the test set-up. For each case in Fig. 3-3 the analysis region is enclosed with a solid line. The postbuckling response for the quasi-isotropic plate with central hole was examined for the above three cases. Figure 3-4 shows the result of the exten-



(a) No extension



(b) Simple extension



(c) Both extensions

Fig. 3-3 Plate models to account for the influence of the region outside the supports.

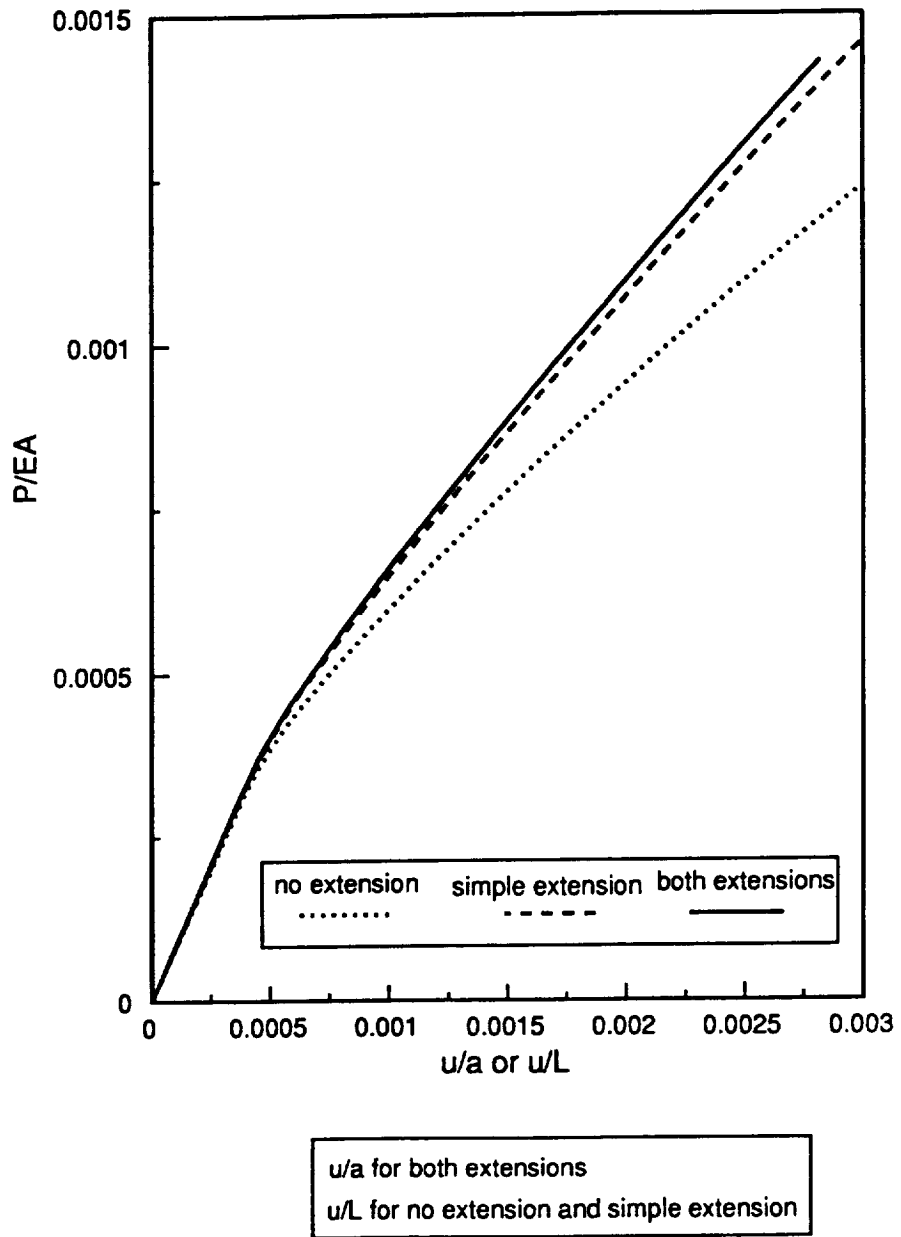


Fig. 3-4 Influence of the region outside the supports on the load vs. end shortening relation.

sion study. The load vs. end shortening relations for the three cases are considered. Note the horizontal axis reflects whether the length within the clamps, L , or the actual length of the plate, a , is being considered. As can be seen from the figure, there is a significant difference in postbuckling response between the case of 'no extension' and the other two cases. By taking into account the extensions the postbuckling response becomes stiffer. There is some difference between the case of 'simple extension' and 'both extensions'. However, there is much more difference between the case of 'simple extension' and 'no extension'. The case of 'both extensions' is somewhat stiffer than the case of 'simple extension'. It can be concluded that the extensions cannot be neglected in postbuckling analysis. In the subsequent discussions in this study the actual dimensions of the test specimen will be analyzed, i.e., the case of 'both extensions'.

3.4.3 Results for Plates With and Without Holes

To provide insight into the types of response that might be expected from the plates to be tested, the load vs. end shortening relations for the four laminates are illustrated in Fig. 3-5 - Fig. 3-6. Figure 3-5 shows results for the case of plates with a hole, $D/W = 0.3$, while Fig. 3-6 shows results for plates with no hole. In the figures the load is again nondimensionalized to be in the form of P/EA . The value of E is different for each plate, the values having been listed in Table 2-4. The results in Fig. 3-5 - Fig. 3-6 were obtained for the imperfection given in eq. (3.23). Though not obvious from Fig. 3-5, the $[\pm 45/0]_s$ laminate is the stiffest, followed by the $[\pm 45/0_2]_{2s}$, the $[\pm 45/0/90]_{2s}$, and then the $[\pm 45]_{4s}$ laminate. To be expected, a

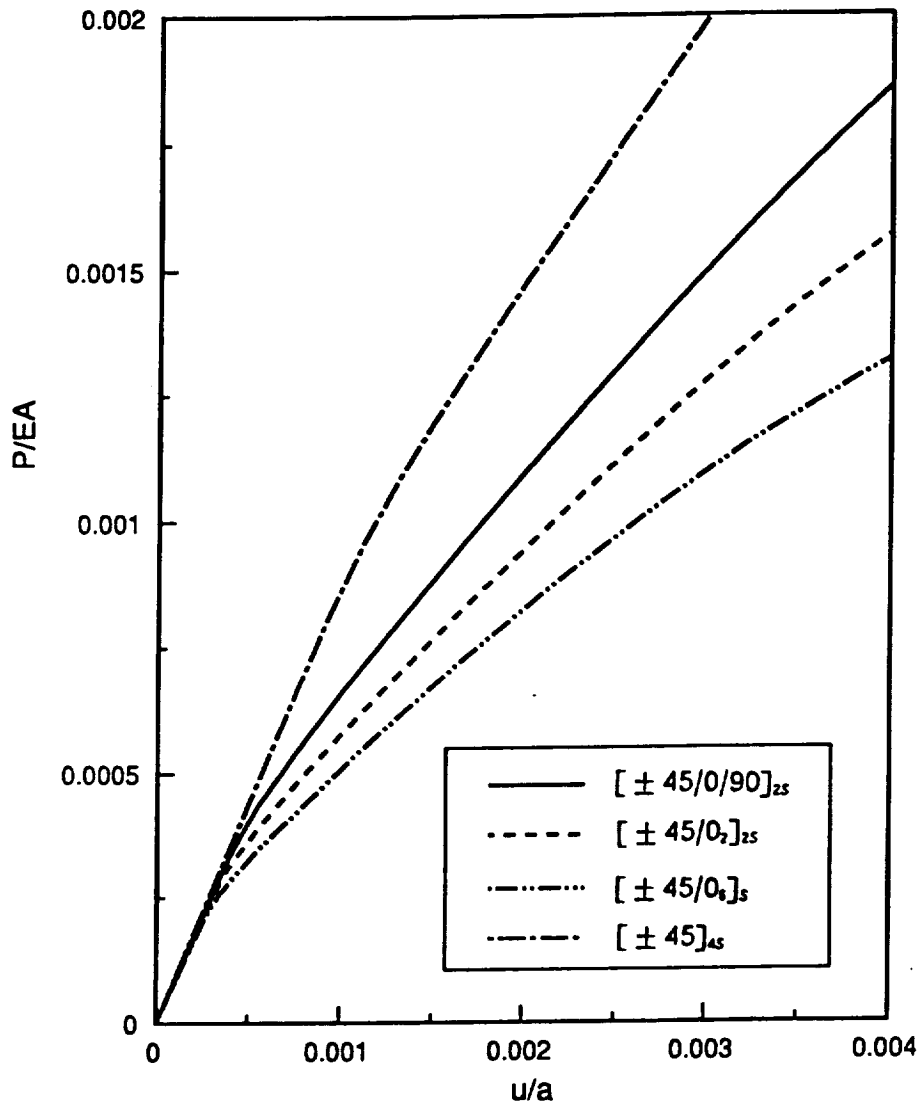


Fig. 3-5 Load vs. end shortening relations for plates with holes.

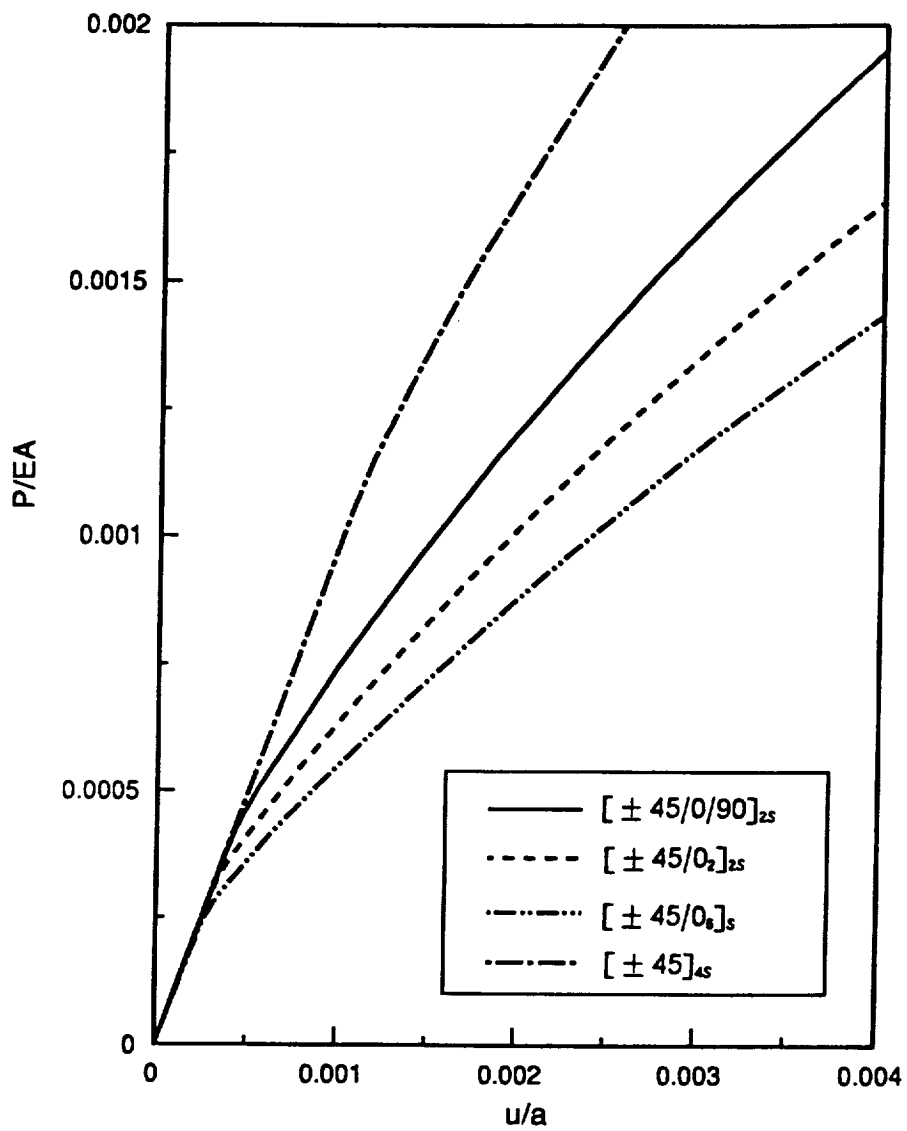


Fig. 3-6 Load vs. end shortening relations for solid plates.

comparison between Figs. 3-5 and 3-6 shows the plate without a hole to be slightly stiffer than the counterpart plates with a hole.

The load vs. midplane deflection relations for the same cases are illustrated in Figs. 3-7 and 3-8. The resistance to out-of-plane deflections as a function of lamination sequence follows the same pattern as for the end shortening deflections, the $[\pm 45/0]_s$ being the stiffest. Though the load vs. deflection relations in Figs. 3-7 and 3-8 seem to indicate that certain laminates will reach higher loads than others, the issue of failure must be superposed on those relations. The key question is at what load level on the postbuckling portion of the response will failure occur. The calculation of stresses and the prediction of failure will be discussed in the next two chapters. However, before those topics are addressed, another issue regarding the postbuckling response will be discussed. This follows.

3.4.4 Mode Changes During Loading

As was discussed in the introduction, it has often been observed that as laminates are loaded into the postbuckling range, there can be an unexpected and sudden change of the postbuckled configuration [38-41]. If the laminate is responding in the postbuckling range by deflecting in a shape similar to the first buckling mode, with a single half-wave in the loading direction, the laminate may suddenly change to a shape associated with the second or higher buckling mode characterized by multiple half-waves in the x direction. Whether or not such a mode shape change occurs is a function of the laminate, the geometry, the boundary conditions, and though hard to quantify, possibly any eccentricities or imperfections in the loading

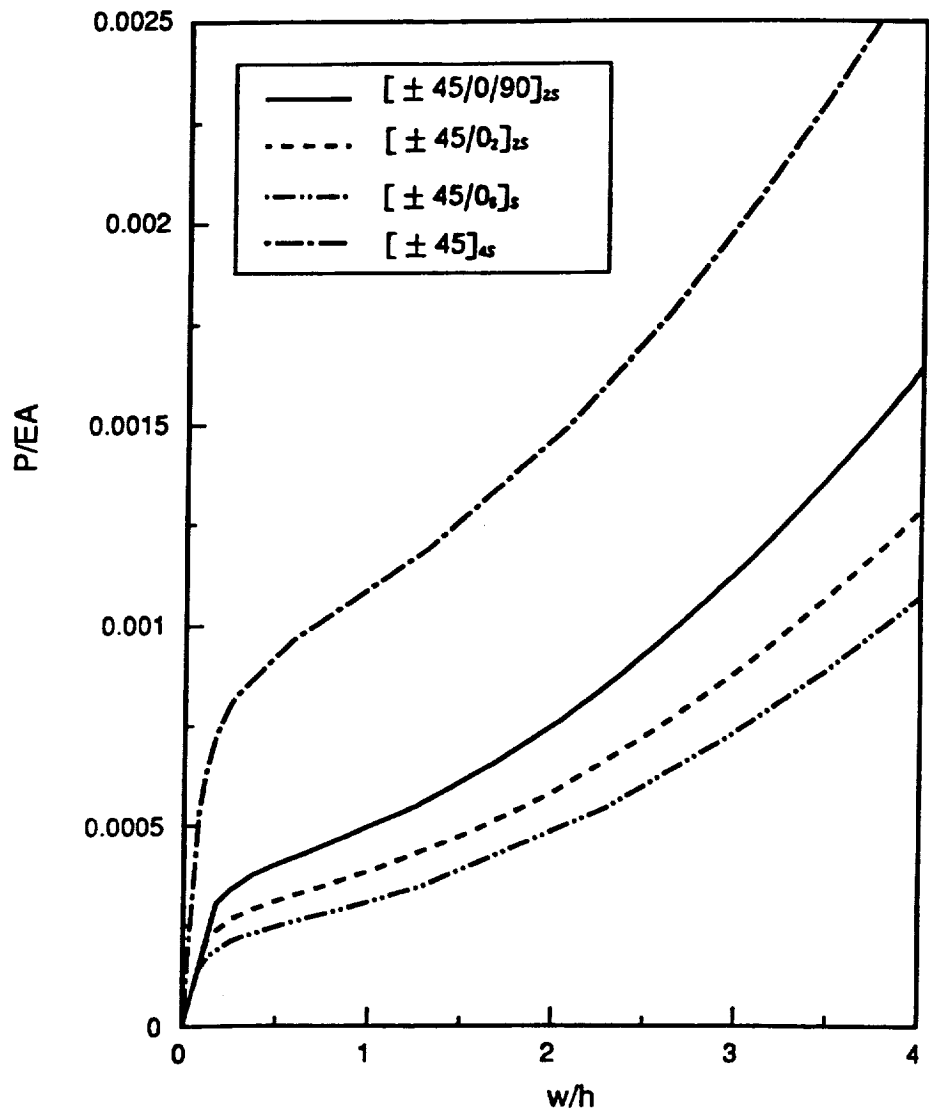


Fig. 3-7 Load vs. out-of-plane deflection relations for plates with holes.

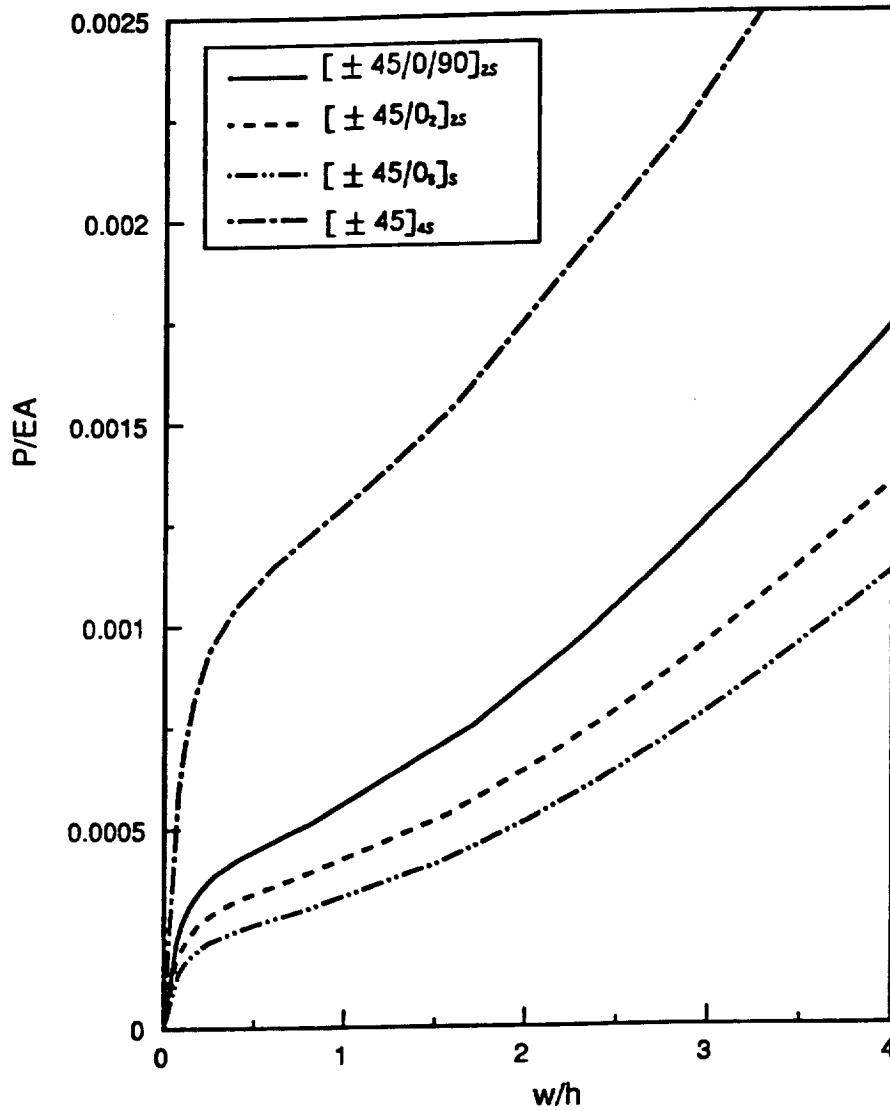
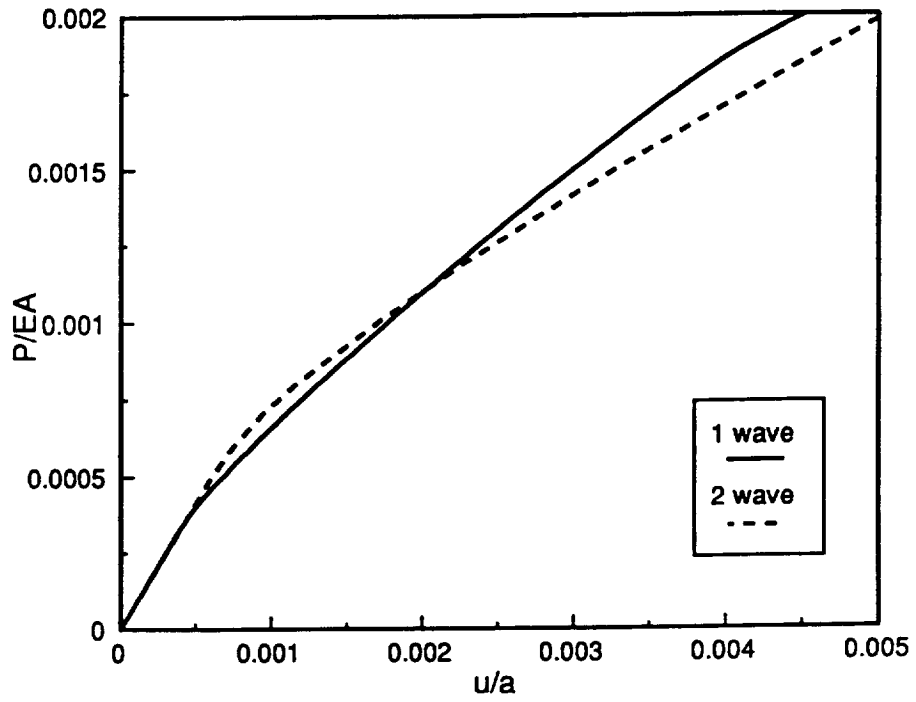


Fig. 3-8 Load vs. out-of-plane deflection relations for solid plates.

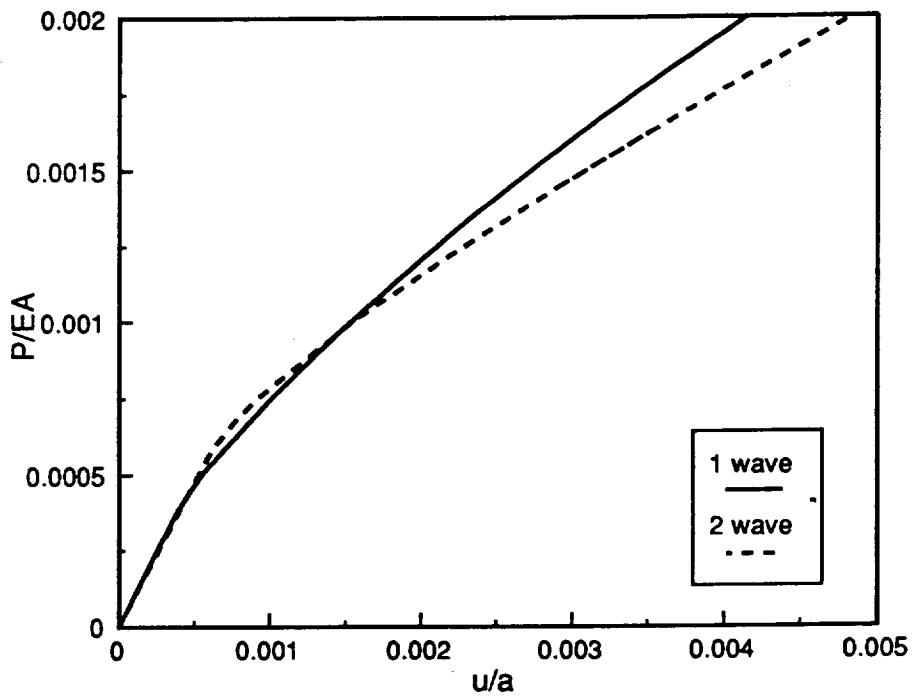
or plate itself. Whether the plate is responding in a shape associated with the first mode or a shape associated with a higher mode can have a profound effect on the failure load and failure mode of the plate. Typically, if the plate responds with multiple wavelengths in the loading direction, interlaminar shear may dominate the stress state. On the other hand, if the plate responds with a single half-wave, inplane stresses may be important. Figures 3-9 through 3-12 show the load vs. end shortening responses of the plates in the study assuming the imperfection in the plate is in the form of two half-waves in the loading direction, i.e.,

$$\zeta = w_0 h \sin\left(\frac{2\pi x}{L}\right) \cos\left(\frac{\pi y}{W}\right). \quad (3.24)$$

For comparison the load vs. end shortening response for each plate with the initial one half-wave imperfection, eq. (3.23), is also shown. Plates with and without holes are considered for each laminate. As can be seen, in all cases the load vs. end shortening relation for the two half-wave case coincides with the one half-wave case until the load reaches the first buckling load. At loads greater than this level the load vs. end shortening relation for the one half-wave case turns toward a postbuckling path, while the two half-wave case continues as an extension of the prebuckling load vs. end shortening relation. At a load level corresponding to the buckling load of two half-waves in loading direction, the load vs. end shortening relation of the two half-wave case then turns toward another postbuckling path. The two postbuckling paths cross and usually at loads greater than the crossing load a sudden change in configuration occurs. It is important to note that the figures with both the one half-wave imperfection and two half-wave imperfection do not represent the complicated phenomenon of the sudden change in postbuckled shape. That phenomenon will not be studied analytically here. There will be no attempts at predicting the load path that

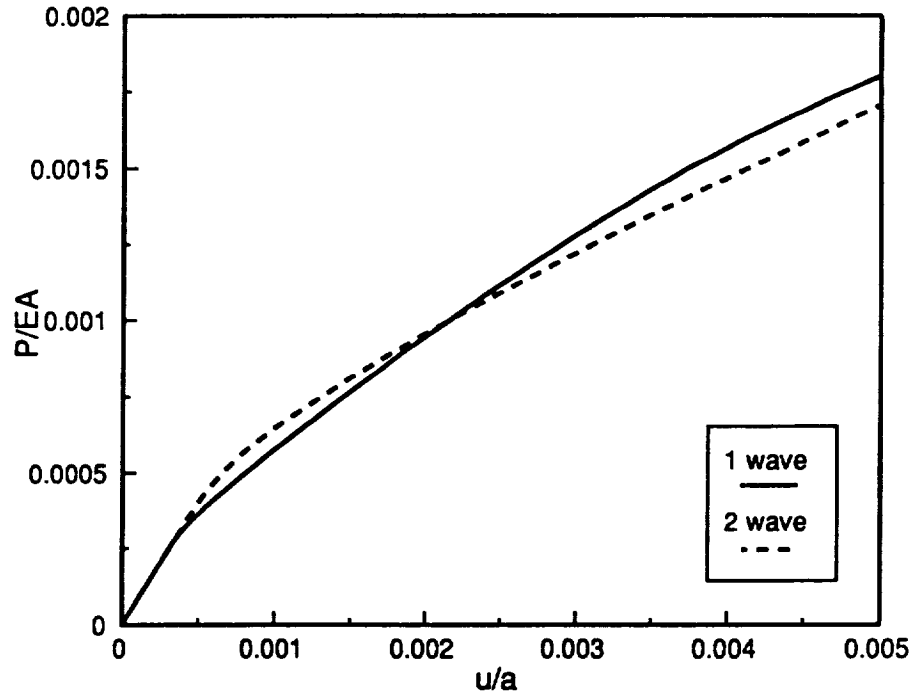


(a) Plate with hole

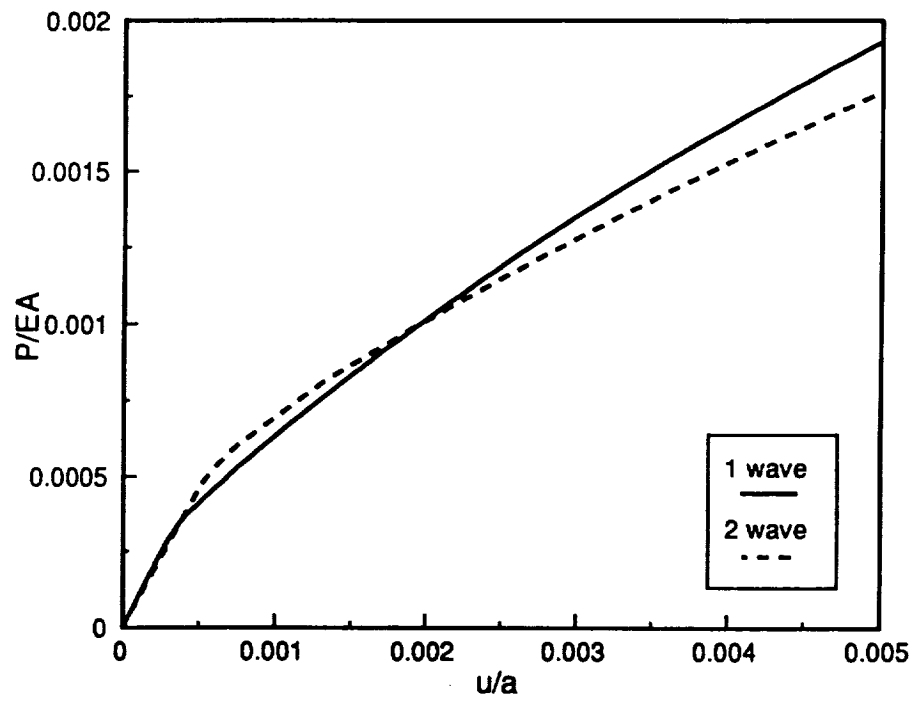


(b) Solid plate

Fig. 3-9 Load vs. end shortening relations for $[\pm 45/0/90]_{2s}$ plates.

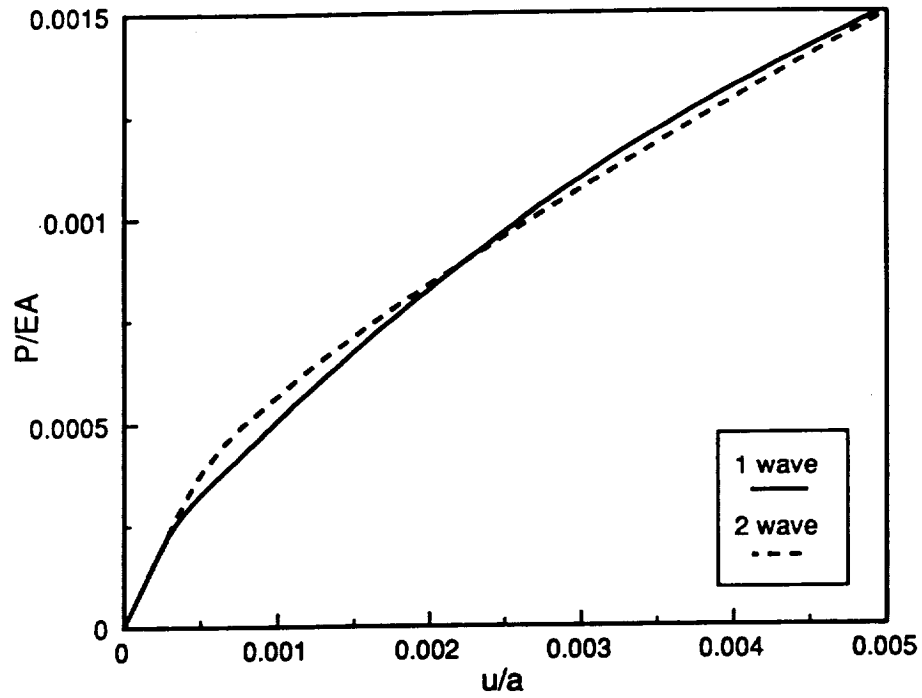


(a) Plate with hole

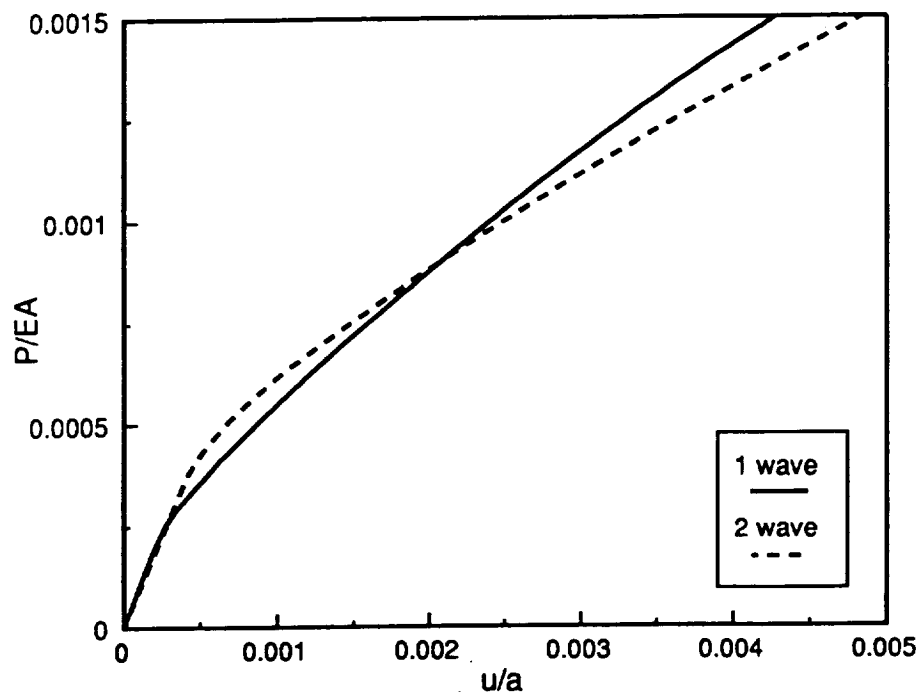


(b) Solid plate

Fig. 3-10 Load vs. end shortening relations for $[\pm 45/0_2]_{2s}$ plates.

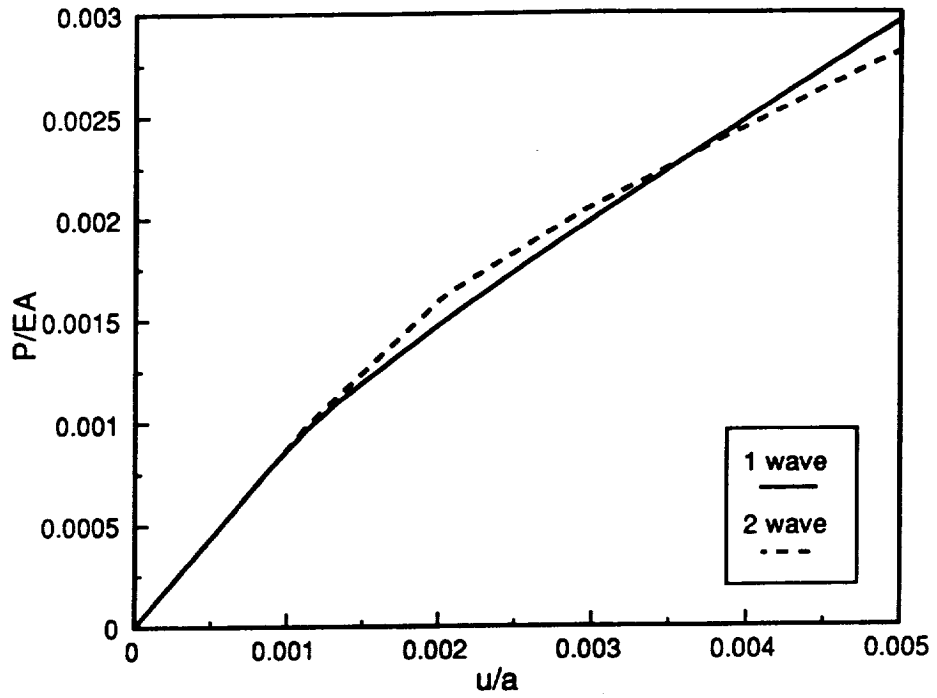


(a) Plate with hole

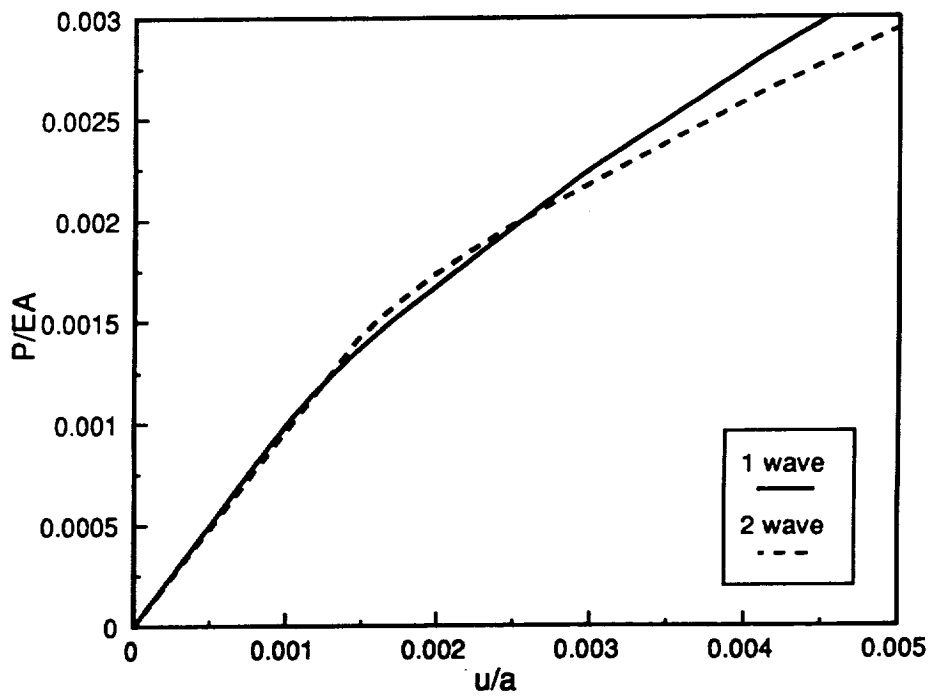


(b) Solid plate

Fig. 3-11 Load vs. end shortening relations for $[\pm 45/0_s]$ plates.



(a) Plate with hole



(b) Solid plate

Fig. 3-12 Load vs. end shortening relations for $[\pm 45]_{4s}$ plates.

leads to the plate being in the two half-wave configuration. However, failure in the postbuckling range due to high interlaminar shear stresses will be studied. That will be addressed by examining the interlaminar shear stresses when the plate is postbuckled in the shape associated with the two half-wave configuration in the loading direction. It should be mentioned that the deflection at the center of the plate is zero when the plate is responding in the two half-wave configuration. Thus there are no load vs. out-of-plane deflection relations shown for that case.

With the analysis to predict the geometrically nonlinear response in hand, attention shifts to the calculation of stresses associated with this response. The calculation of inplane stresses is trivial and is not discussed explicitly. The calculation of the interlaminar stresses, however, is more difficult. That is discussed in the next chapter.

4.0 Calculation of Interlaminar Shear Stresses

4.1 Formulation

Though understanding the deflection response in the postbuckling range of deformation is important for the study of failure, it is absolutely essential to understand the state of stress within the plate. The calculation of the inplane stresses within the laminate is relatively straightforward. None of these stresses is generally zero. However, in classical plate theory the out-of-plane shear stresses are zero by the assumption that the line element perpendicular to the midplane surface remains normal. The out-of-plane normal stress is also assumed to be zero. In a first-order shear deformation theory the out-of-plane shear stresses are constant through the thickness, but the out-of-plane normal stress is still assumed to be zero. In reality there exist out-of-plane stresses that vary from zero to some maximum value as the thickness of the laminate is traversed. This has been shown by Pagano [51]. Using an example of cylindrical bending Pagano obtained the distribution of interlaminar stresses through the thickness by using an elasticity solution. Pagano compared this

elasticity solution, which involves rigorous mathematical calculations, with another solution which was obtained from a simpler approach. This simple approach used the two-dimensional solution obtained from plate theory. By substituting the inplane stress distribution from the two-dimensional solution into the three-dimensional elasticity equilibrium equations and integrating these equations through the thickness, the interlaminar stresses were obtained. This simpler approach showed very good agreement with the elasticity solution. As a result of the calculations these interlaminar, or out-of-plane, stresses were shown to be small. However, even though the out-of-plane stresses may be small, the weakness of the material makes the knowledge of the character of these stresses important. As is well known a composite material is quite poor in resisting all stresses except for the fiber direction normal stress. In this chapter general expressions for the interlaminar shear stresses are developed, the interlaminar stresses being calculated from the inplane solutions of plate theory. The approach follows that of Pagano. With this approach the calculation of interlaminar normal stresses involves derivatives of displacements and rotations that are of a higher order than they are in the calculation of the interlaminar shear stresses. With the discretized results obtained from the finite-element solution, it is very difficult to obtain a converged solution for the higher-order derivatives, and hence a converged solution for the interlaminar normal stress. Fortunately, in the postbuckling problem there is no transverse load. Therefore it can be assumed that the interlaminar normal stress is not important. Because of this assumption the interlaminar normal stress is not included in this study. However, there can still be convergence problems with interlaminar shear stress calculations and hence convergence must be studied. This will be discussed shortly.

Excluding the interlaminar normal stress, σ_z , the two equilibrium equations of importance are

$$\frac{\partial \sigma_x}{\partial x} + \frac{\partial \tau_{xy}}{\partial y} + \frac{\partial \tau_{xz}}{\partial z} = 0 \quad (4.1)$$

$$\frac{\partial \tau_{xy}}{\partial x} + \frac{\partial \sigma_y}{\partial y} + \frac{\partial \tau_{yz}}{\partial z} = 0.$$

Since the distribution of σ_x , σ_y , and τ_{xy} are determined from the two-dimensional solution to the problem, the unknowns are τ_{xz} and τ_{yz} . They can be found from the integration of eq. (4.1) with respect to z , i.e.,

$$\tau_{xz} = - \int \left(\frac{\partial \sigma_x}{\partial x} + \frac{\partial \tau_{xy}}{\partial y} \right) dz + f(x,y) \quad (4.2)$$

$$\tau_{yz} = - \int \left(\frac{\partial \tau_{xy}}{\partial x} + \frac{\partial \sigma_y}{\partial y} \right) dz + g(x,y),$$

where $f(x,y)$ and $g(x,y)$ are unknown functions of x and y , and the definitions of z and the layer interfaces are illustrated in Fig. 4-1. The key constitutive equation for classical lamination theory is

$$\begin{Bmatrix} \sigma_x \\ \sigma_y \\ \tau_{xy} \end{Bmatrix} = \begin{bmatrix} \bar{Q}_{11} & \bar{Q}_{12} & \bar{Q}_{16} \\ \bar{Q}_{12} & \bar{Q}_{22} & \bar{Q}_{26} \\ \bar{Q}_{16} & \bar{Q}_{26} & \bar{Q}_{66} \end{bmatrix} \begin{Bmatrix} \varepsilon_x^0 + z \kappa_x^0 \\ \varepsilon_y^0 + z \kappa_y^0 \\ \gamma_{xy}^0 + z \kappa_{xy}^0 \end{Bmatrix}. \quad (4.3)$$

By using the constitutive equation and the strain-displacement relations in the above equation, performing integration with respect to z on a layer-by-layer basis, and ap-

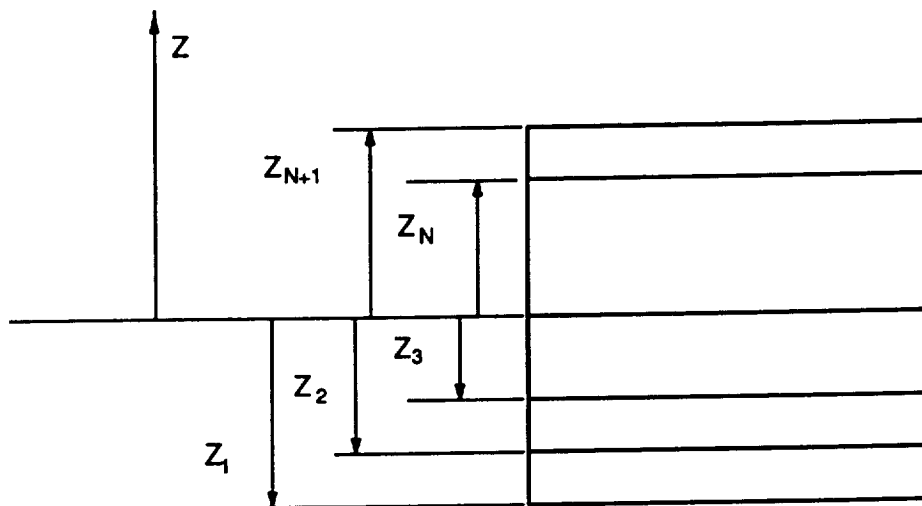


Fig. 4-1 Definition of z coordinate and layer interfaces.

plying boundary conditions on the bottom surface and continuity conditions at the layer interfaces, explicit expressions for interlaminar stresses can be obtained. The interlaminar shear stresses within the k-th layer are expressed as follows :

$$\tau_{xz} = - \sum_{i=1,2,6} \left[\left\{ \bar{Q}_{1i}^k (z - z_k) + \sum_{j=1}^{k-1} \bar{Q}_{1i}^j (z_{j+1} - z_j) \right\} \frac{\partial \varepsilon_i^0}{\partial x} \right] \quad (4.4)$$

$$- \sum_{i=1,2,6} \left[\left\{ \bar{Q}_{i6}^k (z - z_k) + \sum_{j=1}^{k-1} \bar{Q}_{i6}^j (z_{j+1} - z_j) \right\} \frac{\partial \varepsilon_i^0}{\partial y} \right]$$

$$- \frac{1}{2} \sum_{i=1,2,6} \left[\left\{ \bar{Q}_{1i}^k (z^2 - z_k^2) + \sum_{j=1}^{k-1} \bar{Q}_{1i}^j (z_{j+1}^2 - z_j^2) \right\} \frac{\partial \kappa_i^0}{\partial x} \right]$$

$$- \frac{1}{2} \sum_{i=1,2,6} \left[\left\{ \bar{Q}_{i6}^k (z^2 - z_k^2) + \sum_{j=1}^{k-1} \bar{Q}_{i6}^j (z_{j+1}^2 - z_j^2) \right\} \frac{\partial \kappa_i^0}{\partial y} \right]$$

$$\tau_{yz} = - \sum_{i=1,2,6} \left[\left\{ \bar{Q}_{i6}^k (z - z_k) + \sum_{j=1}^{k-1} \bar{Q}_{i6}^j (z_{j+1} - z_j) \right\} \frac{\partial \varepsilon_i^0}{\partial x} \right] \quad (4.5)$$

$$- \sum_{i=1,2,6} \left[\left\{ \bar{Q}_{2i}^k (z - z_k) + \sum_{j=1}^{k-1} \bar{Q}_{2i}^j (z_{j+1} - z_j) \right\} \frac{\partial \varepsilon_i^0}{\partial y} \right]$$

$$- \frac{1}{2} \sum_{i=1,2,6} \left[\left\{ \bar{Q}_{i6}^k (z^2 - z_k^2) + \sum_{j=1}^{k-1} \bar{Q}_{i6}^j (z_{j+1}^2 - z_j^2) \right\} \frac{\partial \kappa_i^0}{\partial x} \right]$$

$$- \frac{1}{2} \sum_{i=1,2,6} \left[\left\{ \bar{Q}_{2i}^k (z^2 - z_k^2) + \sum_{j=1}^{k-1} \bar{Q}_{2i}^j (z_{j+1}^2 - z_j^2) \right\} \frac{\partial \kappa_i^0}{\partial y} \right]$$

Note that for the purpose of the simplification of the equations, the notations for strains and curvatures are changed in above equations. The quantities ε_1^0 , ε_2^0 , ε_6^0 , κ_1^0 ,

κ_x^0 , and κ_y^0 correspond to ε_x^0 , ε_y^0 , γ_{xy}^0 , κ_x^0 , κ_y^0 , and κ_{xy}^0 , respectively. As mentioned earlier, the traction-free boundary conditions on the bottom surface and the continuity conditions at the layer interfaces were used in the process of deriving the above equations. The traction-free boundary condition on the top surface remains redundant. However, the traction-free condition there is automatically satisfied. This can be shown as follows. The shear stress τ_{xz} on the top surface can be obtained by substituting $z = z_{N+1}$ and $k = N$ into the above equations. The result of substitution appears as

$$\begin{aligned} \tau_{xz} = & - \left(A_{11} \frac{\partial \varepsilon_x^0}{\partial x} + A_{12} \frac{\partial \varepsilon_y^0}{\partial x} + A_{16} \frac{\partial \gamma_{xy}^0}{\partial x} + B_{11} \frac{\partial \kappa_x^0}{\partial x} + B_{12} \frac{\partial \kappa_y^0}{\partial x} + B_{16} \frac{\partial \kappa_{xy}^0}{\partial x} \right) \\ & - \left(A_{16} \frac{\partial \varepsilon_x^0}{\partial y} + A_{26} \frac{\partial \varepsilon_y^0}{\partial y} + A_{66} \frac{\partial \gamma_{xy}^0}{\partial y} + B_{16} \frac{\partial \kappa_x^0}{\partial y} + B_{26} \frac{\partial \kappa_y^0}{\partial y} + B_{66} \frac{\partial \kappa_{xy}^0}{\partial y} \right) \\ = & - \left(\frac{\partial N_x}{\partial x} + \frac{\partial N_{xy}}{\partial y} \right). \end{aligned} \quad (4.6)$$

Following the same procedure, it can be shown that

$$\tau_{yz} = - \left(\frac{\partial N_{xy}}{\partial x} + \frac{\partial N_y}{\partial y} \right), \quad (4.7)$$

where A_{ij} and B_{ij} are extension stiffness matrix and bending stiffness matrix, respectively, defined as

$$A_{ij} = \int_{-\frac{h}{2}}^{\frac{h}{2}} \bar{Q}_{ij}^k dz, \quad B_{ij} = \int_{-\frac{h}{2}}^{\frac{h}{2}} z \bar{Q}_{ij}^k dz. \quad (4.8)$$

From the first two of eq. (3.12) it can be seen that the conditions $\tau_{yz} = 0$ and $\tau_{xz} = 0$ on the top surface of the plate are satisfied. One indication of the lack of convergence of the interlaminar stress calculations using numerical solutions is the lack of satis-

fraction of the redundant traction-free boundary condition at $z = z_{N+1}$. This will be discussed more shortly.

4.2 Comparison with Other Solutions

From eqs.(4.4) and (4.5) it can be seen that the expressions for interlaminar shear stresses involve first-order derivatives of strains and curvatures. Since the strains and curvatures are expressed as first-order derivatives of displacements and rotations in shear deformation theory, the interlaminar shear stresses involve the second-order derivatives of the displacements and rotations. If the solution for the displacements and rotations is expressed in a functional form which varies continuously in x and y , the second derivatives can be calculated exactly. However, the finite-element solution is a discrete solution. Therefore, in order to obtain the second derivatives of the displacements and rotations numerical derivatives have to be used. The second derivative obtained numerically can be inaccurate. Thus, in order to examine the accuracy of interlaminar shear stress based on the finite-element method, simple cases are studied where the exact solutions for interlaminar stresses can be obtained in functional form. The numerical values from eq.(4-4) and eq. (4-5) based on finite-element calculations are compared with exact solutions which utilize these same equations but which can take advantage of closed-form expressions for the derivatives. The first case compared is the comparison in the geometrically linear range. The second case is a comparison in the geometrically nonlinear range of deflections.

4.2.1 Simply Supported Cross-Ply Plate Under Uniform Loading.

The governing equation within the framework of linear classical lamination theory for the out-of-plane deflection of a symmetric cross-ply laminate is

$$D_{11} \frac{\partial^4 w}{\partial x^4} + 2(D_{12} + 2D_{66}) \frac{\partial^4 w}{\partial x^2 \partial y^2} + D_{22} \frac{\partial^4 w}{\partial y^4} = q. \quad (4.9)$$

When the four edges of the plate are simply supported, the solution for w can be expressed in the form

$$w = \sum_{m=1,3}^M \sum_{n=1,3}^N W_{mn} \cos\left(\frac{m\pi x}{L}\right) \cos\left(\frac{n\pi y}{W}\right), \quad (4.10)$$

where L and W are the plate length in the x direction and plate width in the y direction, respectively, and the origin of the coordinate system is at the geometric center of the plate. The W_{mn} are the unknown coefficients to be solved as a function of the applied load. From the governing equation and assumed solution form it can be observed that if the transverse load is expanded into a double cosine series, the solution can be obtained easily. The transverse load can be expanded into a double cosine series as

$$q = \sum_{m=1,3}^M \sum_{n=1,3}^N Q_{mn} \cos\left(\frac{m\pi x}{L}\right) \cos\left(\frac{n\pi y}{W}\right). \quad (4.11)$$

When q is a constant (uniform loading), the coefficients Q_{mn} are obtained as

$$Q_{mn} = \frac{16q}{mn\pi^2} (-1)^{\frac{m+n}{2}+1}. \quad (4.12)$$

Substituting the expanded form for q and assumed form for w into the governing equation, eq (4.9), the expression for the unknown coefficients W_{mn} can be obtained as

$$\begin{aligned} W_{mn} &= \frac{Q_{mn}}{D_{11}\left(\frac{m\pi}{L}\right)^4 + 2(D_{12} + 2D_{66})\left(\frac{m\pi}{L}\right)^2\left(\frac{n\pi}{W}\right)^2 + D_{22}\left(\frac{n\pi}{W}\right)^4} \quad (4.13) \\ &= \frac{\frac{16q}{mn\pi^2} (-1)^{\frac{m+n}{2}+1}}{D_{11}\left(\frac{m\pi}{L}\right)^4 + 2(D_{12} + 2D_{66})\left(\frac{m\pi}{L}\right)^2\left(\frac{n\pi}{W}\right)^2 + D_{22}\left(\frac{n\pi}{W}\right)^4}. \end{aligned}$$

The solution developed here is exact as it satisfies all displacement and moment boundary conditions. The only issue is using a sufficient number of terms in the series.

The midplane curvatures are obtained by the following equations :

$$\kappa_1^0 = -\frac{\partial^2 w}{\partial x^2} = \sum_{m=1,3}^M \sum_{n=1,3}^N W_{mn} \left(\frac{m\pi}{L}\right)^2 \cos\left(\frac{m\pi x}{L}\right) \cos\left(\frac{n\pi y}{W}\right) \quad (4.14)$$

$$\kappa_2^0 = -\frac{\partial^2 w}{\partial y^2} = \sum_{m=1,3}^M \sum_{n=1,3}^N W_{mn} \left(\frac{n\pi}{W}\right)^2 \cos\left(\frac{m\pi x}{L}\right) \cos\left(\frac{n\pi y}{W}\right) \quad (4.15)$$

$$\kappa_6^0 = -2 \frac{\partial^2 w}{\partial x \partial y} = 2 \sum_{m=1,3}^M \sum_{n=1,3}^N W_{mn} \left(\frac{m\pi}{L} \right) \left(\frac{n\pi}{W} \right) \sin \left(\frac{m\pi x}{L} \right) \sin \left(\frac{n\pi y}{W} \right). \quad (4.16)$$

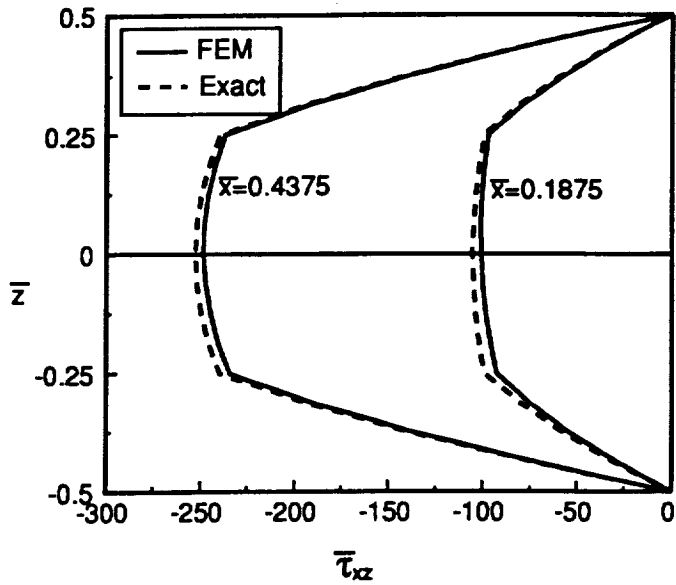
For this problem the inplane displacements, and thus the midplane strains, are zero. Substituting the above expressions into eqs. (4.4) and (4.5), interlaminar shear stresses are obtained. For a square plate with 15 terms in m and n ($M = 15$, $N = 15$), a sufficiently converged solution can be obtained. The stresses from this solution are compared with those calculated by the finite-element method. In the finite-element method the shape functions are used for the calculation of the curvatures and their derivatives. Figure 4-2 shows the comparison between the series and finite-element solutions at several locations within a $[0/90]_s$ plate. The variables appearing in Fig. 4-2 and the ensuing figures are defined as

$$\bar{x} = \frac{x}{L}, \quad \bar{y} = \frac{y}{W}, \quad \bar{z} = \frac{z}{h}, \quad \bar{\tau}_{xz} = \frac{\tau_{xz}}{q}, \quad \bar{\tau}_{yz} = \frac{\tau_{yz}}{q}. \quad (4.17)$$

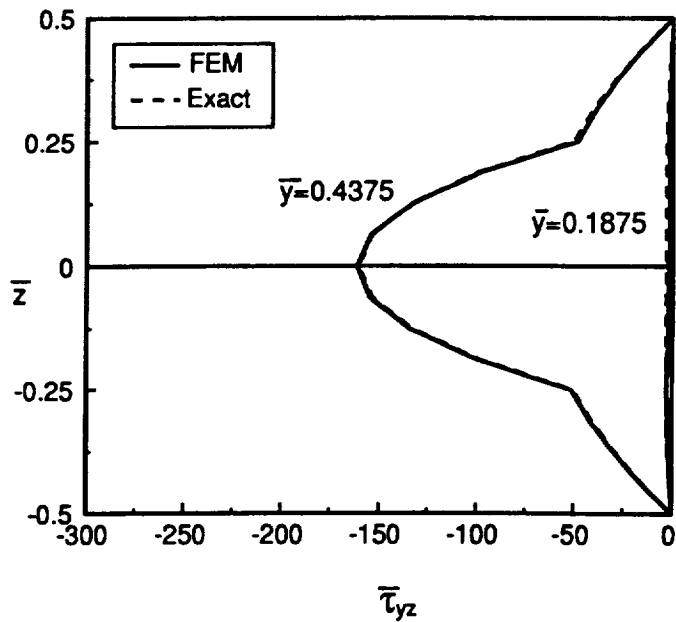
Sixteen elements for one-quarter of the plate (4 elements in the x direction and 4 elements in the y direction) were used for the finite-element calculation. The interlaminar shear stresses were compared at the centroid of each element. The agreement between the exact and finite-element solution is very good.

4.2.2 Interlaminar Shear Stresses in Nonlinear Cylindrical Bending

In the postbuckling problem geometrically nonlinear effects are important and it is not clear that conclusions obtained regarding the accuracy of the interlaminar stresses for the geometrically linear problem can be applied. As in the previous



(a) $\bar{\tau}_{xz}$ along $\bar{y}=0.0625$



(b) $\bar{\tau}_{yz}$ along $\bar{x}=0.0625$

Fig. 4-2 Comparison of interlaminar shear stresses between exact solution and FEM solution for a simply supported square $[0/90]_s$ plates under uniform loading.

sections for geometrically linear problems, a geometrically nonlinear problem for which there is a closed-form solution available, and for which interlaminar stresses can be computed, should be used for checking the finite-element calculations. In the course of this study, for the purpose of comparing interlaminar shear stresses, a geometrically nonlinear problem was posed and solved in closed form. Interlaminar stresses calculated from this solution were compared with the stresses computed using the finite-element approach for the same problem. The problem is essentially the geometrically nonlinear analog of the cylindrical bending studied by Pagano [50]. To follow is the exact solution for the nonlinear cylindrical bending problem.

The governing equations for classical plate bending theory including geometric nonlinearities are

$$\frac{\partial N_x}{\partial x} + \frac{\partial N_{xy}}{\partial y} = 0 \quad (4.18)$$

$$\frac{\partial N_{xy}}{\partial x} + \frac{\partial N_y}{\partial y} = 0 \quad (4.19)$$

$$\frac{\partial^2 M_x}{\partial x^2} + 2 \frac{\partial^2 M_{xy}}{\partial x \partial y} + \frac{\partial^2 M_y}{\partial y^2} + N_x \frac{\partial^2 w}{\partial x^2} + 2 N_{xy} \frac{\partial^2 w}{\partial x \partial y} + N_y \frac{\partial^2 w}{\partial y^2} + q = 0, \quad (4.20)$$

where N_x , N_y , and N_{xy} are force resultants, M_x , M_y , and M_{xy} are moment resultants, w is the out-of-plane displacement of the plate's reference surface, and q is the transverse loading. The basic assumptions for cylindrical bending are

$$v = 0, \quad \frac{\partial}{\partial y} = 0, \quad (4.21)$$

where v is the reference surface displacement in the y direction. With these assumptions the above governing equations are simplified to

$$\frac{dN_x}{dx} = 0 \quad (4.22)$$

$$\frac{d^2M_x}{dx^2} + N_x \frac{d^2w}{dx^2} + q = 0. \quad (4.23)$$

Equation (4.19) is not involved in the solution procedure. The terms of importance in the constitutive equation for a symmetric laminate are expressed as

$$N_x = A_{11}\epsilon_x^0 = A_{11} \left\{ \frac{du}{dx} + \frac{1}{2} \left(\frac{dw}{dx} \right)^2 \right\} \quad (4.24)$$

$$M_x = D_{11}\kappa_x^0 = -D_{11} \frac{d^2w}{dx^2}. \quad (4.25)$$

As usual, u is the displacement in the x direction of the plate's reference surface. Due to the basic assumptions for cylindrical bending, eq. (4.21), ϵ_y^0 , γ_{xy}^0 , κ_y^0 , and κ_{xy}^0 become zero. The boundary conditions studied are shown in Fig. 4-3. Note that the location $x=0$ is at the plate's midspan. The use of symmetry is employed in the application of the boundary conditions and only one half of the plate is analyzed.

The above equations are nondimensionalized as

$$\bar{x} = \frac{x}{L}, \quad \bar{u} = \frac{u}{h}, \quad \bar{w} = \frac{w}{h}. \quad (4.26)$$

By substituting eq. (4.26) into eqs. (4.24) and (4.25), nondimensionalized equations for N_x and M_x are obtained as

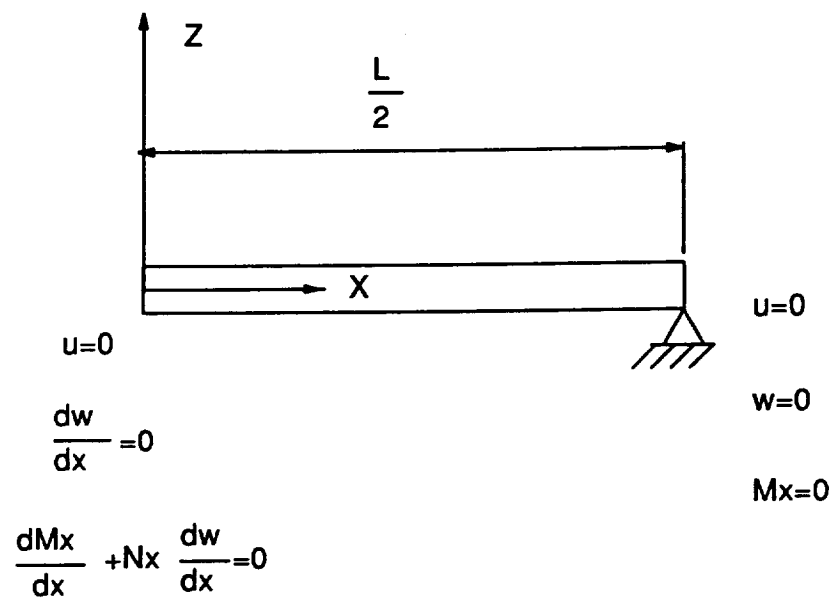


Fig. 4-3 Boundary conditions for nonlinear cylindrical bending.

$$\bar{N}_x = \frac{d\bar{u}}{d\bar{x}} \left(\frac{L}{h} \right) + \frac{1}{2} \left(\frac{d\bar{w}}{d\bar{x}} \right)^2, \quad (4.27)$$

$$\bar{M}_x = - \frac{d^2\bar{w}}{d\bar{x}^2}, \quad (4.28)$$

where

$$\bar{N}_x = \frac{L^2}{A_{11}h^2} N_x, \quad (4.29)$$

$$\bar{M}_x = \frac{L^2}{D_{11}h} M_x. \quad (4.30)$$

By substituting eq. (4.26), (4.29), and (4.30) into eq. (4.23), a nondimensionalized equation for eq. (4.23) is obtained as

$$\frac{d^2\bar{M}_x}{d\bar{x}^2} + \frac{A_{11}H^2}{D_{11}} \bar{N}_x \frac{d^2\bar{w}}{d\bar{x}^2} + \bar{q} = 0, \quad (4.31)$$

where \bar{q} is given by

$$\bar{q} = \frac{L^4}{D_{11}h} q. \quad (4.32)$$

From eq. (4.22) it can be seen that N_x , therefore \bar{N}_x , is a constant. This result that \bar{N}_x is constant makes the problem quite simple. By substituting eq. (4.30) into eq. (4.31) a fourth-order ordinary equation for \bar{w} results, namely,

$$\frac{d^4\bar{w}}{d\bar{x}^4} - \alpha^2 \frac{d^2\bar{w}}{d\bar{x}^2} = \bar{q}, \quad (4.33)$$

where

$$\alpha^2 = \bar{N}_x \frac{A_{11} h^2}{D_{11}} \quad (4.34)$$

and \bar{q} can be a general function of \bar{x} . For simplicity a uniform transverse loading case is considered. By substituting the solution for \bar{w} into eq. (4.27), \bar{u} can be determined. Considering that \bar{w} is an even function of \bar{x} , the solutions for \bar{u} and \bar{w} are expressed as

$$\bar{u} = a_1 \bar{x} - a_2 \left\{ \frac{\sinh(2\alpha \bar{x})}{4\alpha} - \frac{\bar{x}}{2} \right\} + a_3 \left\{ \frac{\bar{x} \cosh(\alpha \bar{x})}{\alpha} - \frac{\sinh(\alpha \bar{x})}{\alpha^2} \right\} - a_4 \frac{\bar{x}^3}{3} \quad (4.35)$$

$$\bar{w} = C_1 \cosh(\alpha \bar{x}) - \frac{\bar{q}}{2\alpha^2} \bar{x}^2 + C_2, \quad (4.36)$$

where

$$a_1 = \frac{h}{L} \bar{N}_x, \quad a_2 = \frac{C_1^2 \alpha^2 h}{2L}, \quad a_3 = \frac{C_1 h}{\alpha L} \bar{q}, \quad a_4 = \frac{h}{2\alpha^4 L} \bar{q}^2. \quad (4.37)$$

In these equations \bar{N}_x , C_1 , and C_2 are unknown coefficients. The above solution satisfies the symmetry conditions at the center of the plate. Applying the boundary conditions at the right end, the following three equations are derived :

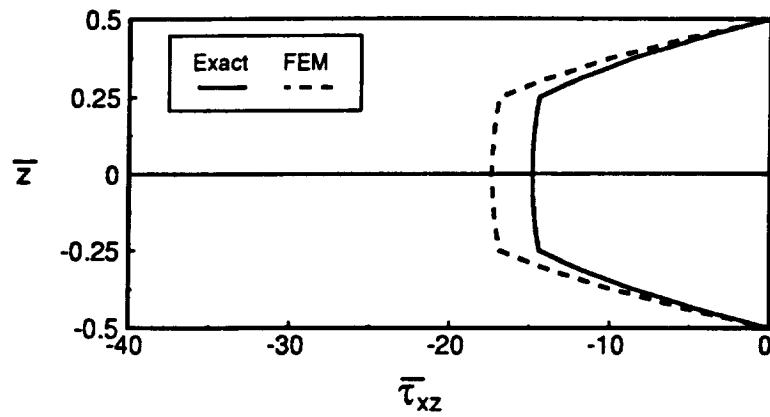
$$\frac{a_1}{2} - a_2 \left\{ \frac{\sinh(\alpha)}{4\alpha} - \frac{1}{4} \right\} + a_3 \left\{ \frac{\cosh(\frac{\alpha}{2})}{2\alpha} - \frac{\sinh(\frac{\alpha}{2})}{\alpha^2} \right\} - \frac{a_4}{24} = 0, \quad (4.38)$$

$$C_1 \cosh\left(\frac{\alpha}{2}\right) - \frac{\bar{q}}{8\alpha^2} + C_2 = 0, \quad (4.39)$$

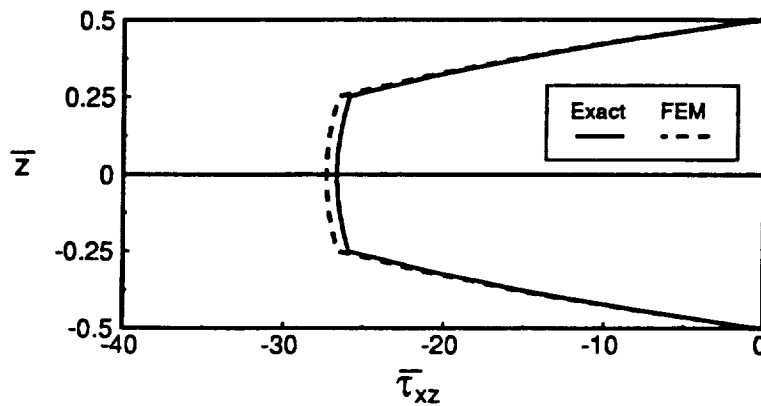
$$C_1 \alpha^2 \cosh\left(\frac{\alpha}{2}\right) - \frac{\bar{q}}{\alpha^2} = 0. \quad (4.40)$$

In the above equations α is a function of \bar{N}_x . From eq. (4.37) a_1 , a_2 , a_3 , and a_4 are therefore functions of \bar{N}_x and C_1 . In the above equations an expression for C_1 in terms of \bar{N}_x can be obtained from eq. (4.40). Substitution of this expression for C_1 into eq. (4.38) gives one nonlinear equation for \bar{N}_x as a function of the uniform load \bar{q} . The final equation is solved numerically for \bar{N}_x as a function of \bar{q} , and C_1 and C_2 are determined by back substitution into eqs. (4.39) and (4.40).

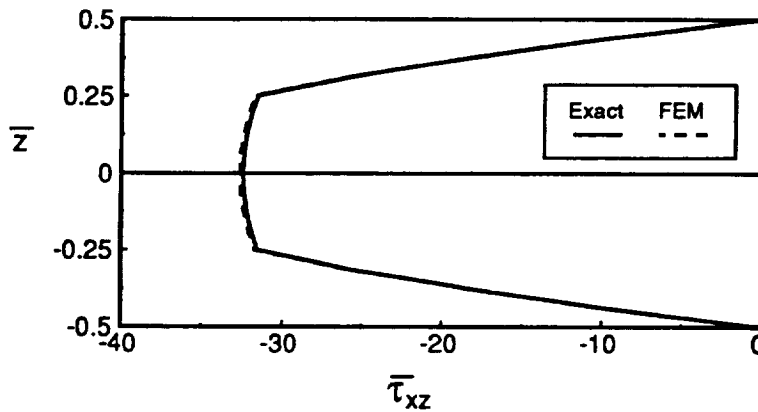
With the displacement response of the plate known, the strains and curvatures, and their derivatives, can be used in eqs. (4.4) and (4.5) and the interlaminar stresses computed. The interlaminar shear stresses calculated by using the above exact solution were compared with finite-element calculations. A $[0/90]_s$ cross-ply laminate with a load level of $\bar{q} = 1000$ is studied. At this load level the maximum deflection at the center of the plate is $\bar{w} = 1.80$, i.e., the plate is deflected 1.80 times its thickness. With the specific boundary conditions this deflection is in the geometrically nonlinear range. With 2, 5, and 10 elements representing one half of a strip across the width of the plate, the convergence of the finite-element solution is studied at the centroidal and other Gauss points in the element at the supported edge. This element is studied because the interlaminar shear stress is the highest at the supported edge. Figure 4-4 shows the comparison of the finite-element solution and the exact solution at the center Gauss point of the element. Even with 2 elements the shear stress on the top surface is zero. As was shown earlier, in the exact sense this has to be the case. However, with numerically obtained second derivatives there is no guarantee that this will happen. Despite the shear stress returning to zero at the top surface, with two elements there is a difference between the finite-element calculation and the exact solution for shear stress within the thickness of the laminate. As the number of elements is increased the finite-element solution approaches the



(a) two elements mesh
($\bar{x}=0.375$)



(b) Five elements mesh
($\bar{x}=0.45$)



(c) Ten elements mesh
($\bar{x}=0.475$)

Fig. 4-4 Comparison of interlaminar shear stresses between exact solution and FEM solution in nonlinear range at center Gauss point in end element for a $[0/90]_s$ laminate in cylindrical bending, $\bar{q} = 1000$.

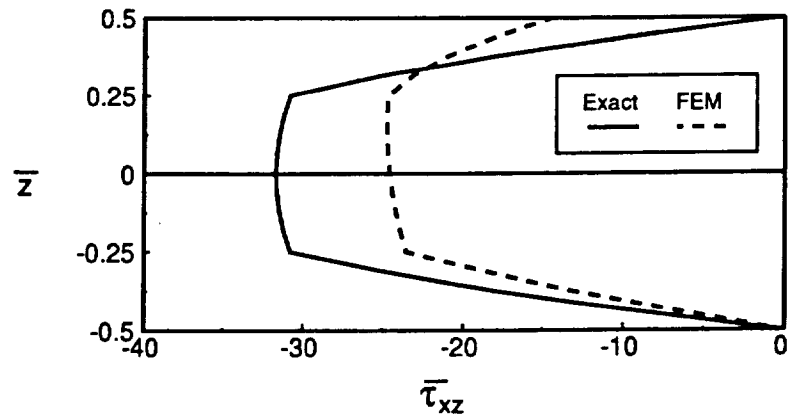
exact solution. (Note that as the number of elements increases, the location \bar{x} where the comparison is taking place moves closer to the edge of the plate, $\bar{x} = 0.50$, and the shear stress actually increases.)

Figure 4-5 shows the convergence study at a Gauss point other than the center Gauss point in the end element. Even with 10 elements the agreement is not good. From this it can be seen that the convergence of interlaminar stress at the Gauss point in the center of the element is better than at other Gauss points. Chaudhuri and Seide discussed this in ref. 51.

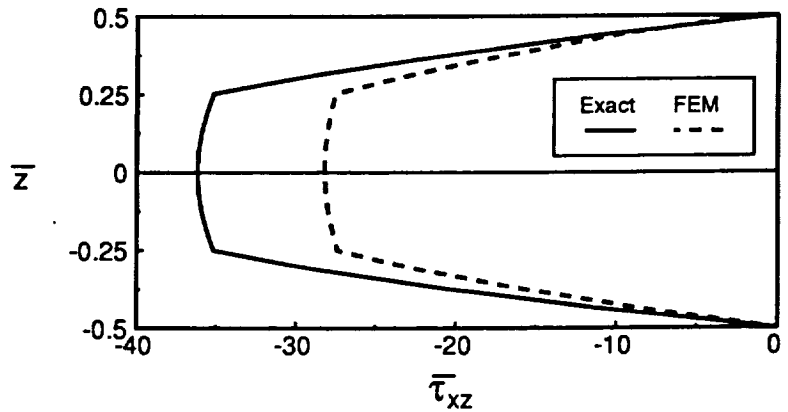
Fig. 4-6 shows the comparison of the finite-element solution with the exact solution for a $[\pm 45/0/90]_{2s}$ laminate with a load level of $\bar{q} = 1000$. In this comparison D_{16} and D_{26} are set to zero. At the load level of $\bar{q} = 1000$, \bar{w} at the center of the strip was 1.58. With 10 elements representing the half-width of the plate, the agreement at the centroid of the element at the supported edge is good.

4.3 Results for Plates with Holes

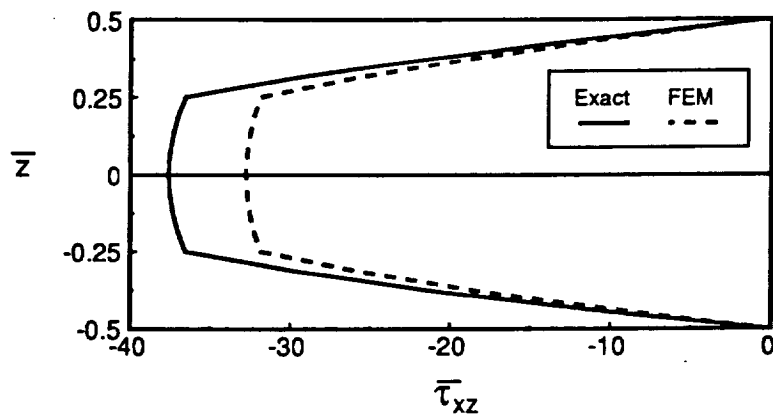
With the above examples it has been shown that the interlaminar shear stress calculation scheme using the finite-element method can be accurate. Some investigators[34, 36, 37] have mentioned that the interlaminar shear stresses along a node line can be an important parameter for determining the failure of solid plates which deform into more than one half-wave in the loading direction during postbuckling. In this study specific interest centers on the interlaminar stresses in



(a) Two elements mesh
($\bar{x}=0.472$)



(b) Five elements mesh
($\bar{x}=0.489$)



(c) Ten elements mesh
($\bar{x}=0.494$)

Fig. 4-5 Comparison of interlaminar shear stresses between exact solution and FEM solution in nonlinear range at a Gauss point other than the center Gauss point in end element for a $[0/90]_s$ laminate in cylindrical bending, $\bar{q} = 1000$.

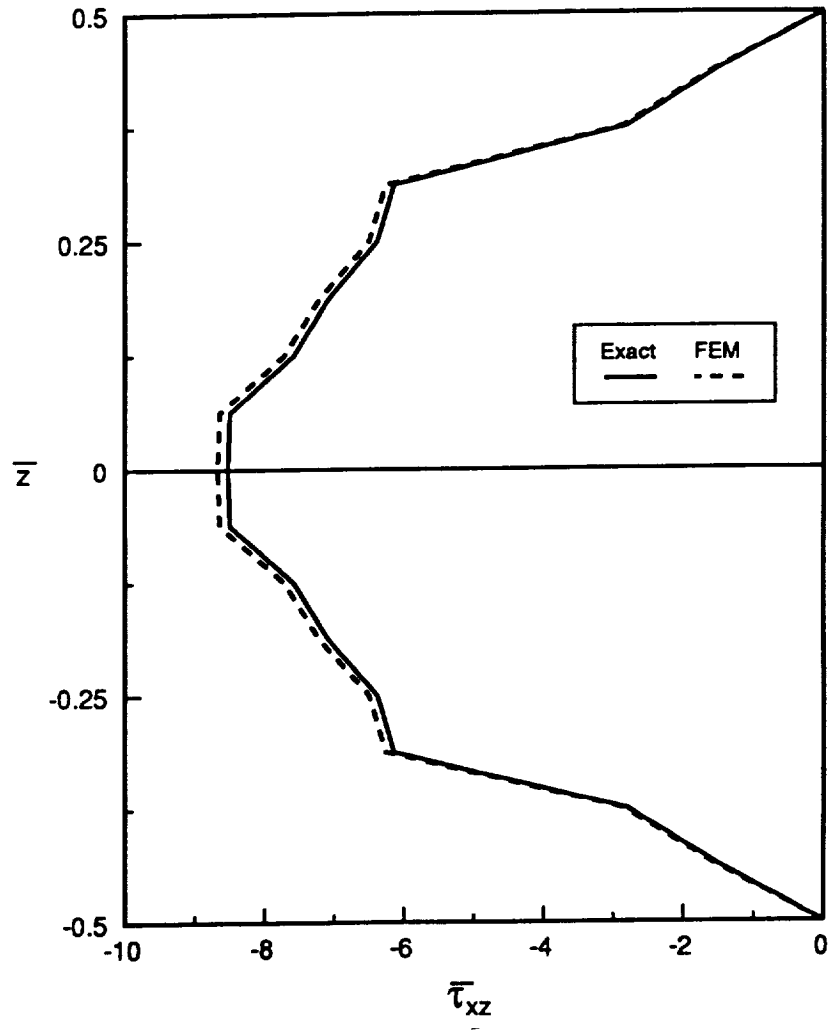


Fig. 4-6 Comparison of interlaminar shear stresses between exact solution and FEM solution in nonlinear range at a center Gauss point in end element for $[\pm 45/0/90]_{2s}$ laminate in cylindrical bending, $\bar{q} = 1000$.

plates with holes loaded in a postbuckled range. In this section for the plates with holes which have deformed into two half-waves in the loading direction, interlaminar shear stresses will be studied. First, convergence of interlaminar stress calculations as a function of the mesh refinement will be studied. Then, insight into the interlaminar shear stress distribution on the midplane will be discussed. Finally, through-the-thickness distributions of interlaminar shear stresses for each laminate in this study will be presented. Shown in Fig. 4-7 are several regions of interest within the plate, namely the net-section hole edge, half way between the hole edge and simple support along the net-section, the region just inside the simple supports on the net-section, and the portion of the plate extending beyond the simple supports on the net-section.

For the convergence study of interlaminar shear stresses three levels of mesh refinement are used. They are a 57 element, a 121 element, and a 209 element mesh representing a quarter plate, as shown in Fig. 4-7. With a $[\pm 45/0/90]_{2s}$ plate interlaminar shear stresses on the elements along the net-section were studied for the above three levels of mesh refinements. The load level ($P/EA = 0.00152$) was selected so that the maximum out-of-plane deflection of the plate was about two plate thicknesses. As shown in Fig. 4-4 and Fig. 4-5, interlaminar shear stress calculations with the present method are most accurate at the center of the element. Thus, calculations are made at the centers of the elements.

One location of interest is the net-section hole edge, the region marked by the double-crossed hatch in Fig. 4-7. The results from three mesh refinements for the through-the-thickness distribution of τ_{xz} at the center of the element at the net-section hole edge are shown in Fig. 4-8. In this figure τ_{xz} is normalized with respect to the

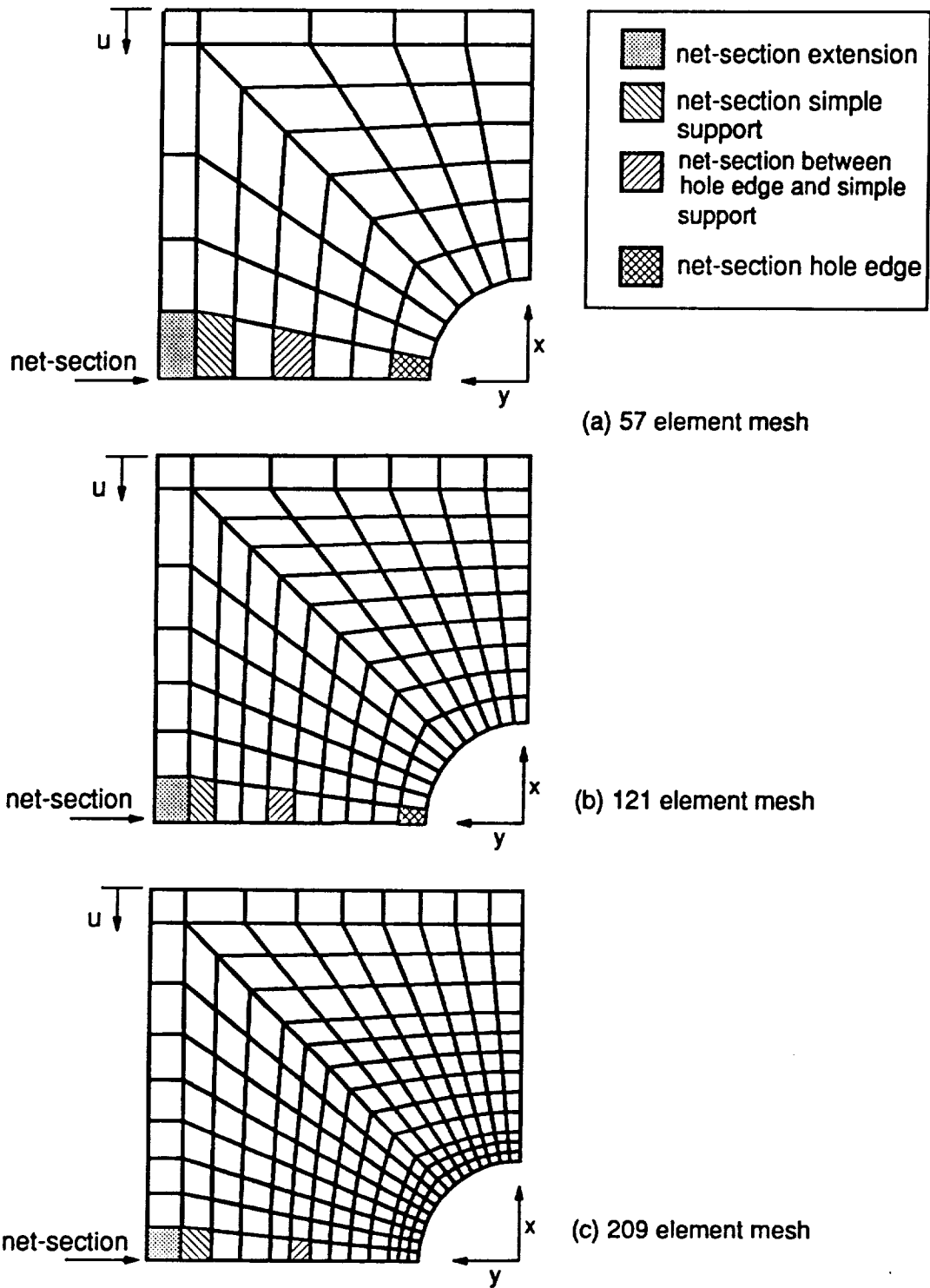
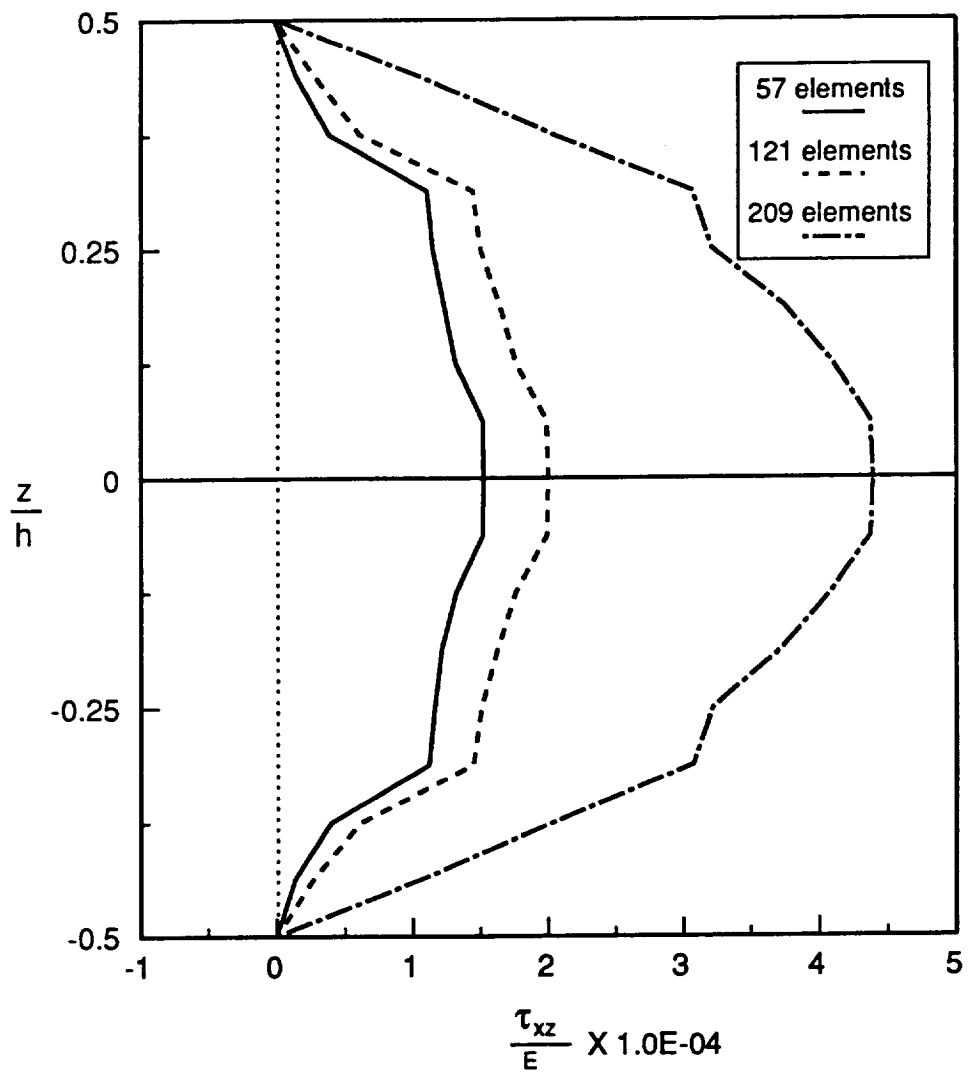


Fig. 4-7 Finite-element meshes and regions of interest used to study interlaminar stresses.



Observation point

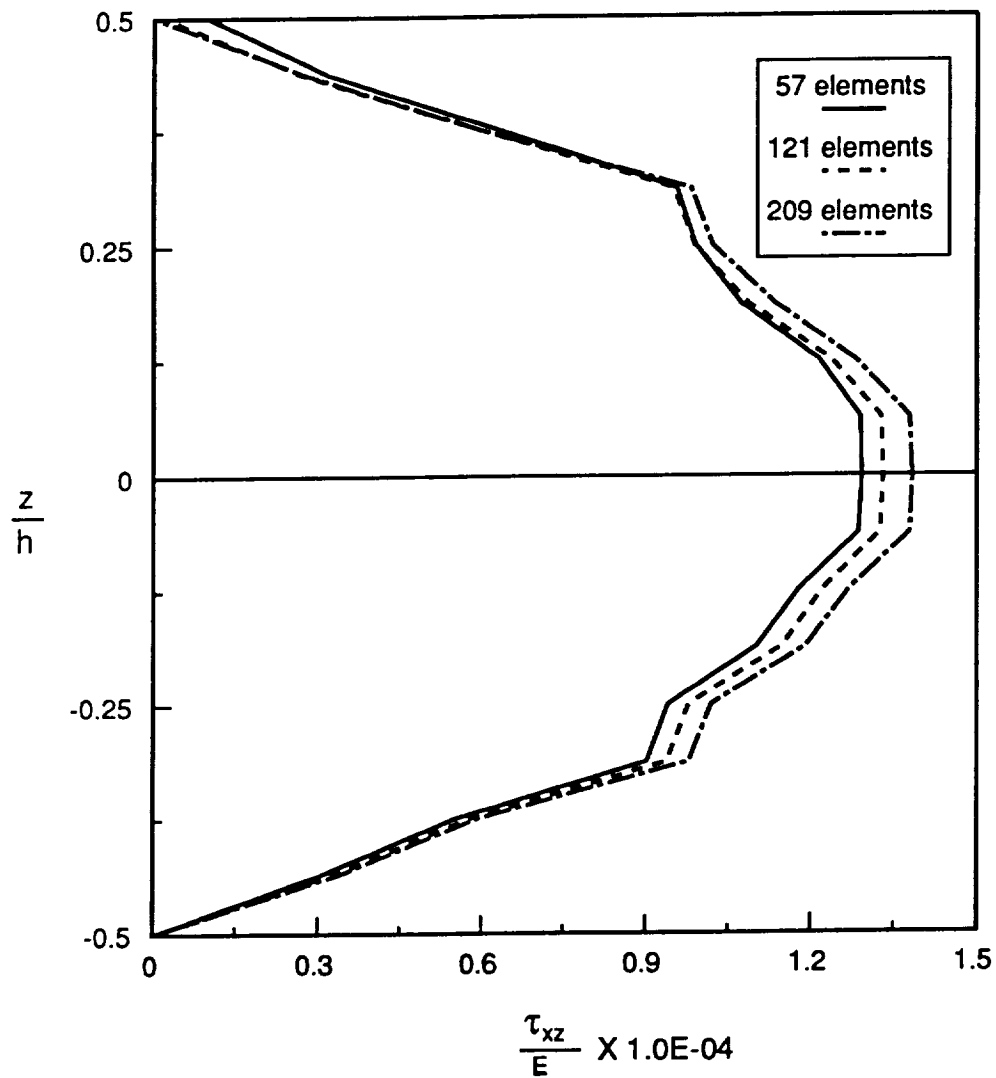
No. of elements	x	y
57	0.176	1.778
121	0.111	1.688
209	0.077	1.570

Fig. 4-8 Dependence of the distribution of τ_{xz} through the thickness on mesh size for a $[\pm 45/0/90]_{2s}$ laminate at $P/EA = 0.00152$ at net-section hole edge (Two half-waves in the loading direction).

equivalent Young's modulus of the laminate in the x direction. This modulus is listed in Table 2-4. In this comparison, since the centers of the elements at the net-section hole edge for each mesh refinement do not coincide with each other, the stresses are not computed at exactly the same point. However, some aspects of the stress calculations can be observed from this figure. As discussed with eqs. (4.6)-(4.8), the redundant traction free condition on the top surface in the derivation of eq. (4.4) and eq. (4.5) must be satisfied. Figure 4-8 shows that this condition is satisfied at the net-section hole edge with just 57 elements in the mesh. Also, it is clear that τ_{xz} calculated on the midplane with the 57 element mesh is quite different than τ_{xz} calculated with the 209 element mesh. As the mesh is refined, the observation point approaches the net-section hole edge. With a small movement toward the hole edge τ_{xz} on the midplane calculated with the 209 element mesh is about 4 times bigger than that calculated with the 57 element mesh. This shows that τ_{xz} at this region changes very rapidly. Using only a small number of elements could result in missing this rapid change of interlaminar shear stresses near the hole boundary.

As a next observation location, the region between the hole edge and the simple support along the net-section was selected. The through-the-thickness distribution of τ_{xz} at this location is shown in Fig. 4-9 for each mesh refinement. This figure shows that as the number of elements is increased, τ_{xz} on the top surface approaches zero. Also, the figure shows that at this point τ_{xz} on the midplane is about one-third of the value at the net-section hole edge.

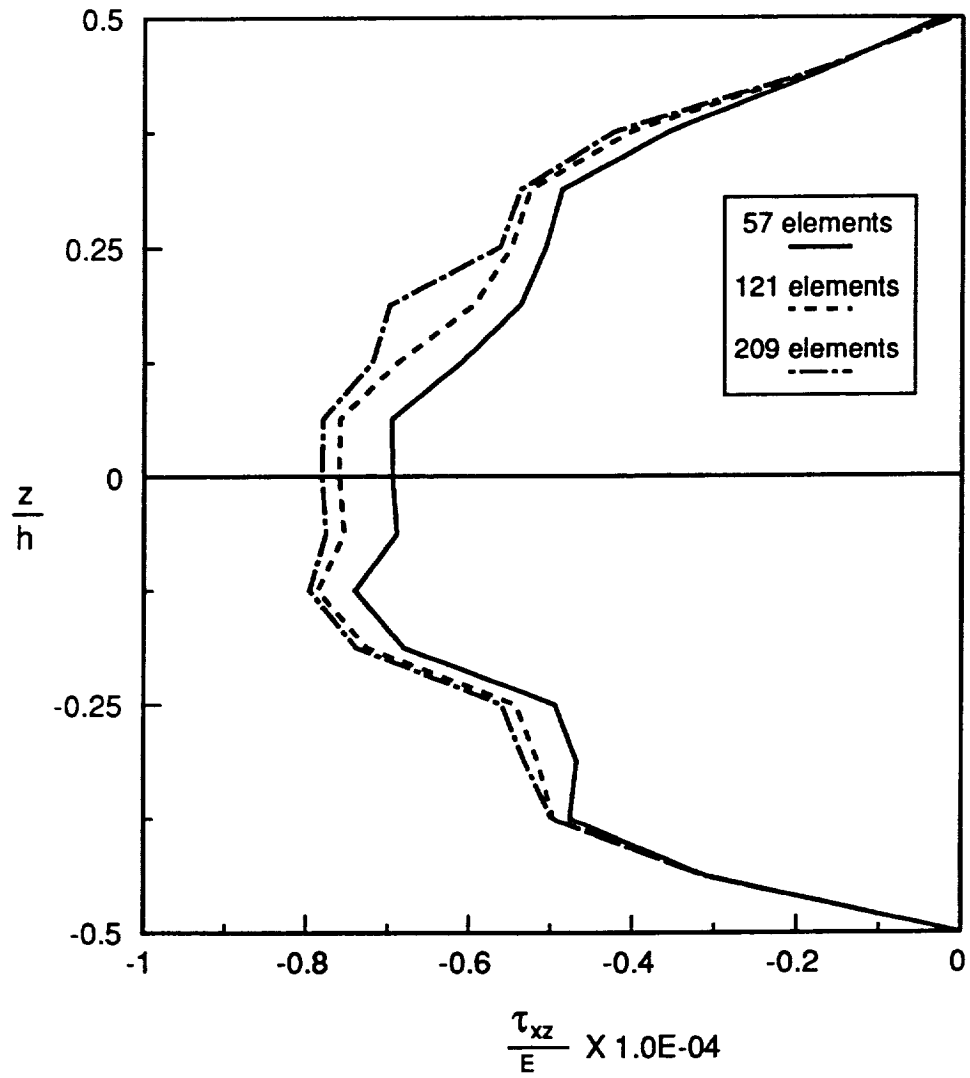
One more location of interest is the extension region outside the simple support. The element at this region is marked by dots in Fig. 4-7 and is labeled as the net-section extension region. Through the thickness distribution of τ_{xz} at this location is



Observation point

No. of elements	x	y
57	0.351	3.536
121	0.214	3.636
209	0.160	3.540

Fig. 4-9 Dependence of the distribution of τ_{xz} through the thickness on mesh size for a $[\pm 45/0/90]_{2s}$ laminate at $P/EA=0.00152$ between the net-section hole edge and the simple support (Two half-waves in the loading direction).



Observation point

No. of elements	x	y
57	0.497	5.25
121	0.329	5.25
209	0.246	5.25

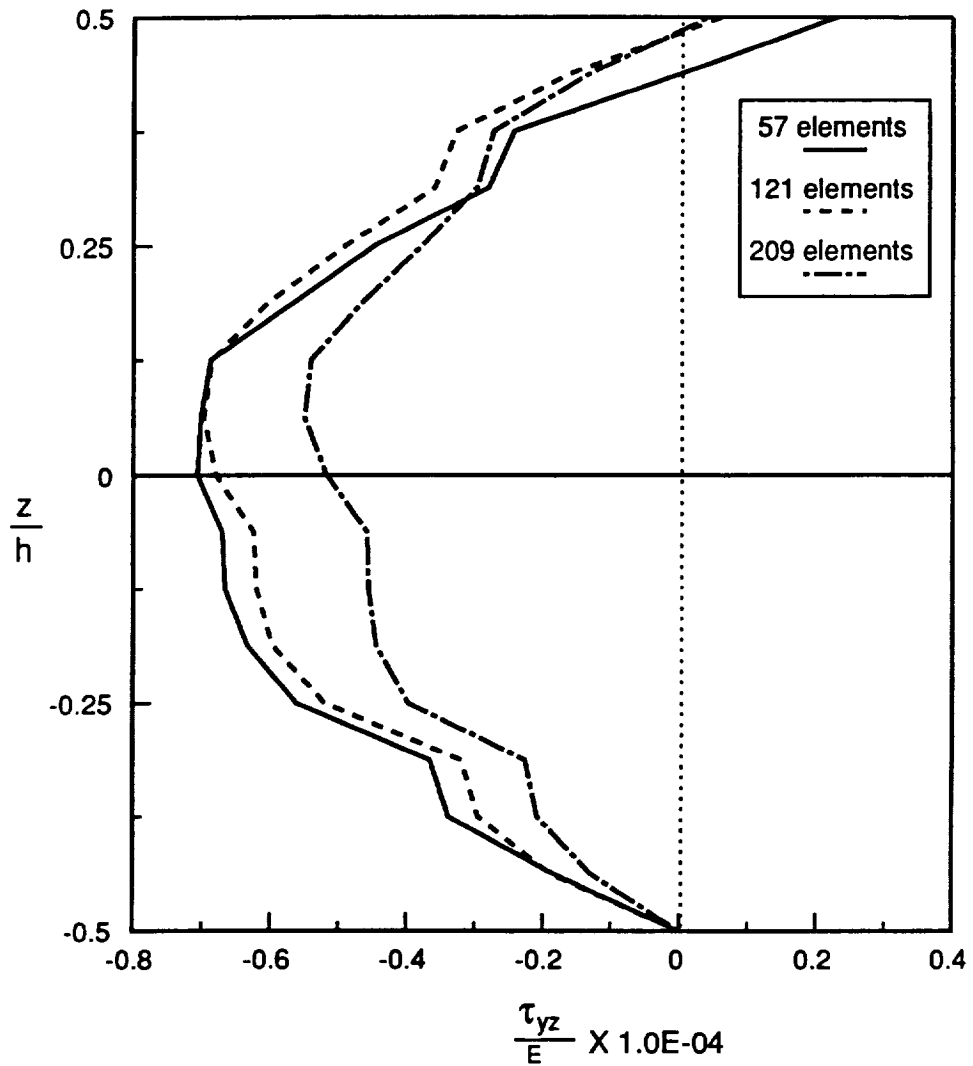
Fig. 4-10 Dependence of the distribution of τ_{xz} through the thickness on mesh size for a $[\pm 45/0/90]_{2s}$ laminate at $P/EA = 0.00152$ at the net-section extension region outside the simple support (Two half-waves in the loading direction).

shown in Fig. 4-10. The value of τ_{xz} at this location is relatively small, and the sign is opposite to the sign at the other two locations.

As a convergence test for τ_{yz} , the center of the element just inside the simple support, a region marked by a single hatch in Fig. 4-7, was selected. The distribution of τ_{yz} in the thickness direction at this location is shown in Fig. 4-11. The 57 element mesh shows poor convergence. As the number of elements is increased, the convergence is improved as indicated by the shear stress going to zero at the top surface. The value of τ_{yz} at this location is also relatively small compared to τ_{xz} at the net-section hole edge.

From this convergence study, it is shown that the convergence of interlaminar shear stresses is good at the locations where the interlaminar shear stresses are large. The convergence is not good at the location where the shear stress is small. However, the locations of interest for failure study are the areas where the stresses are indeed large. Thus, with the above results, it can be expected that by using a 209 element mesh an accurate and realistic study of failure can be achieved.

In order to learn more about the interlaminar shear stresses within the plate, the interlaminar shear stress on the geometric midplane is computed as a function of location along several loci. In particular, the variation of τ_{xz} and τ_{yz} along the centers of the elements at the net-section and along the centers of the elements on the hole boundary is examined. In Fig. 4-12 the variation of interlaminar shear stresses along the centroids of the elements at the net-section is shown. The y coordinate of the center of the elements is normalized by the plate width W, and the interlaminar shear stresses are again normalized by the equivalent Young's modulus of a $[\pm 45/0/90]_{2s}$



Observation point

No. of elements	x	y
57	0.468	4.707
121	0.316	4.805
209	0.235	4.780

Fig. 4-11 Dependence of the distribution of τ_{yz} through the thickness on mesh size for a $[\pm 45/0/90]_{2s}$ laminate at $P/EA=0.00152$ at the net-section just inside the simple support (Two half-waves in the loading direction).

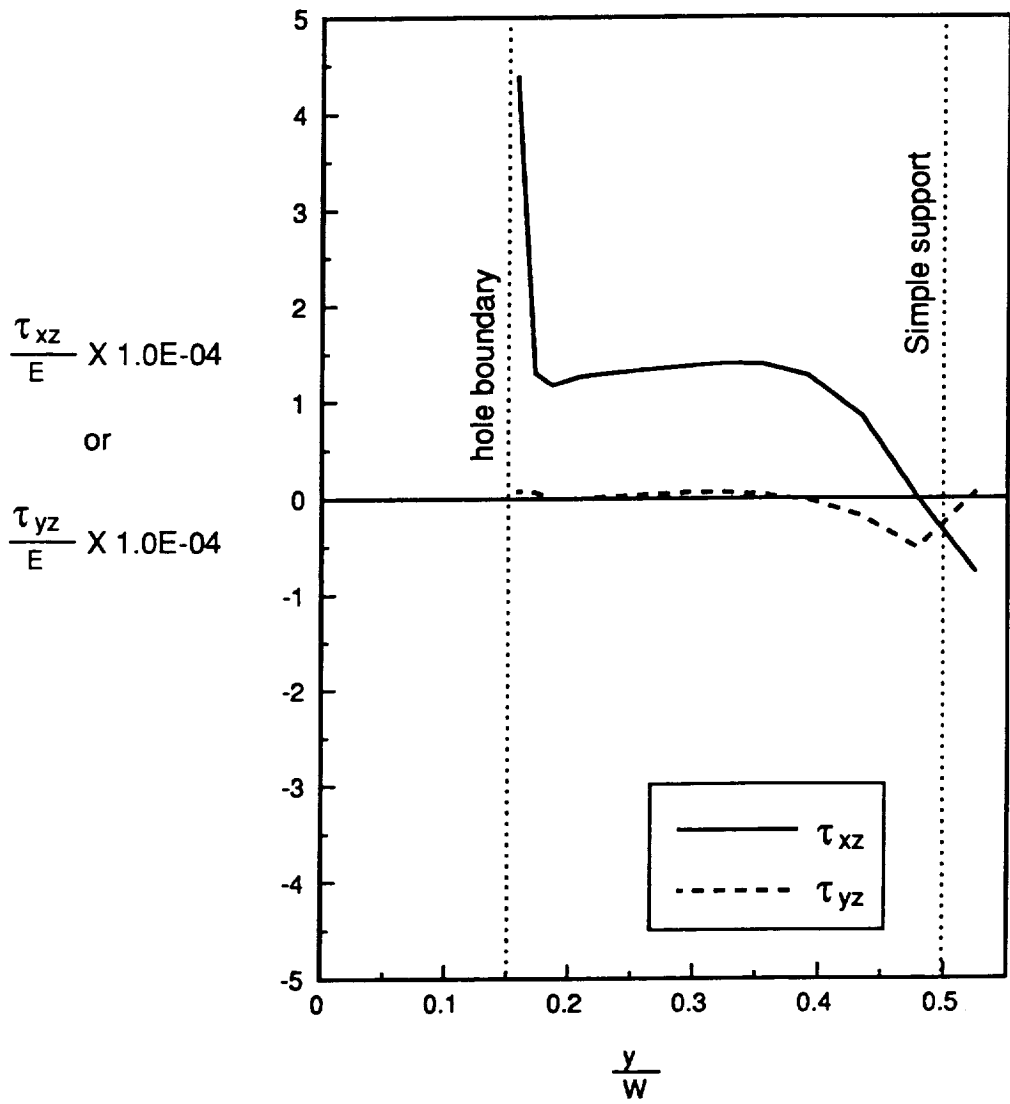


Fig. 4-12 Distribution of Interlaminar shear stresses on the midplane of $[\pm 45/0/90]_{2s}$ along the center of the elements at net-section.

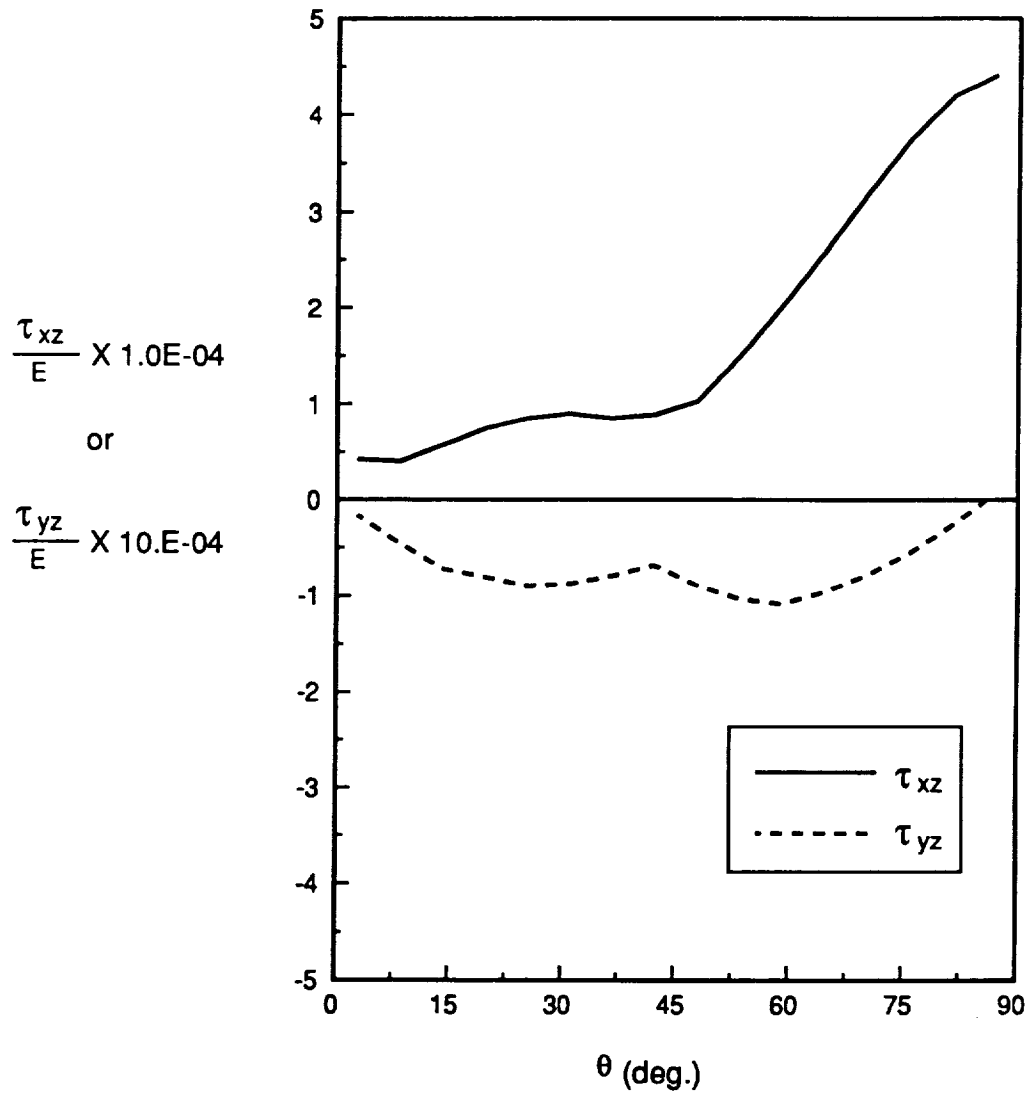
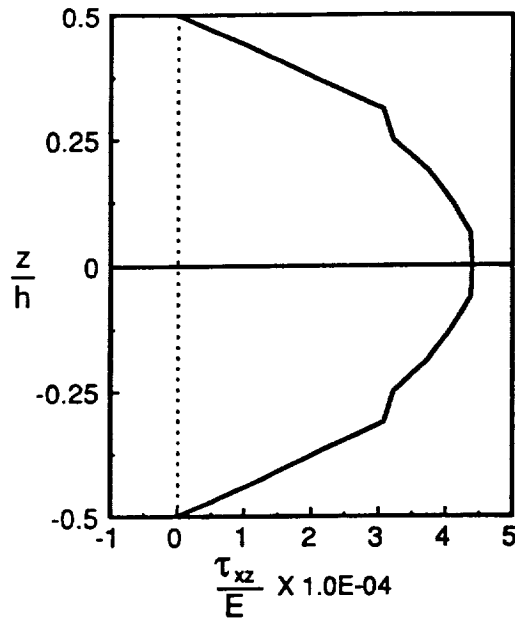


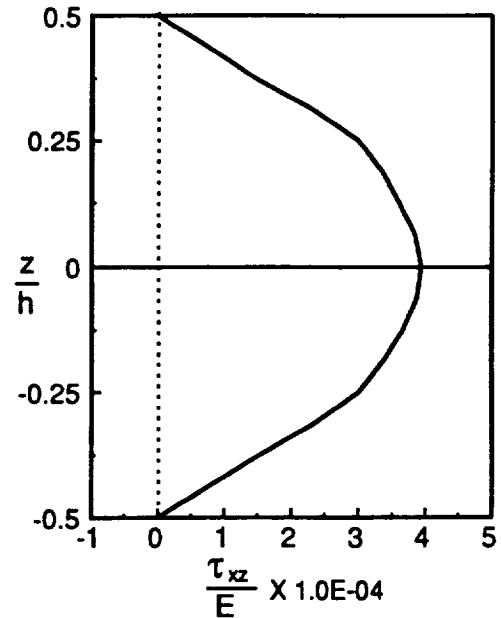
Fig. 4-13 Distribution of interlaminar shear stresses on the midplane of $[\pm 45/0/90]_{2s}$ along the center of the elements on hole boundary.

plate in the x direction. In Fig. 4-12 it is clearly shown that τ_{xz} increases very rapidly as the hole boundary is approached, as discussed at the beginning of this section. On the other hand, τ_{yz} is negligibly small. As expected, τ_{yz} is largest at the simple support. In Fig. 4-13 the variation of interlaminar shear stresses along the centers of the elements on the hole boundary is shown. The stresses are shown as a function of θ , where $\theta = 90^\circ$ is the net-section location. It can be seen that up to $\theta = 45^\circ$ the value of τ_{xz} is small, but for $\theta > 45^\circ$ τ_{xz} increases very rapidly and reaches its highest value at net section hole edge. Along the hole boundary τ_{yz} has relatively small values compared to τ_{xz} at the net-section hole edge. The distribution of τ_{yz} around the hole boundary is roughly symmetric with respect to $\theta = 45^\circ$.

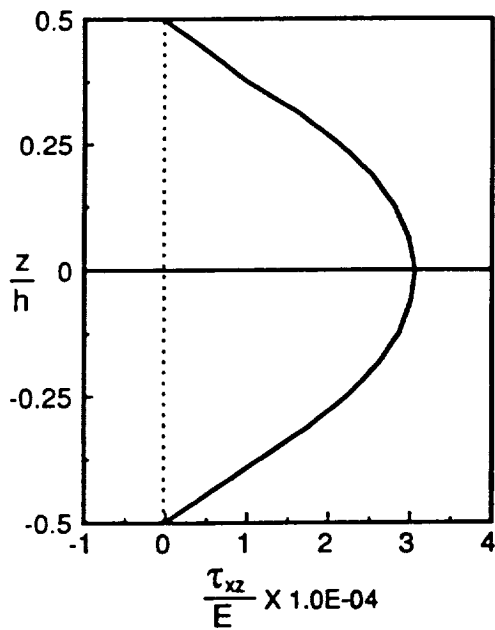
In Fig. 4-14 the through-the-thickness distribution of interlaminar shear stress τ_{xz} for the different laminates in this study is shown. The stress was calculated at the net-section hole edge. The 209 element mesh was used in this calculation. Note that the equivalent Young's moduli used to normalize the stresses are different from plate to plate. Also, the load levels are different from plate to plate. However, the load level was selected so that it represents the postbuckling range where the maximum out-of-deflection is approximately two plate thicknesses. From Fig. 4-14 it can be observed that τ_{xz} changes rapidly in the 0° and $\pm 45^\circ$ layers, and less rapidly in the 90° layers. Each figure shows symmetry with respect to the midplane. In the $[\pm 45/0]_s$ laminate the inner 12 layers have the same fiber orientation. In Fig. 4-14 (c) it can be seen that the distribution of τ_{xz} in these grouped 0° layers results in almost a parabolic distribution, as can be observed in an isotropic material. In Fig. 4-14 (d) the distribution of τ_{xz} in the $[\pm 45]_{4s}$ laminate does exhibit a parabolic shape.



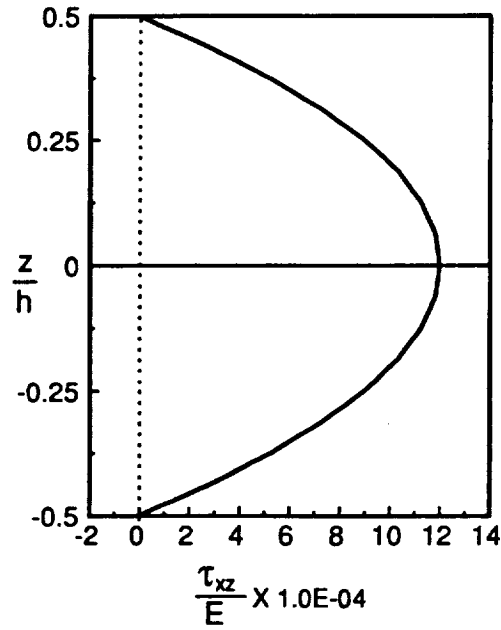
(a) $[\pm 45/0/90]_{2s}$ plate at $P/EA=0.00152$.



(b) $[\pm 45/0_2]_{2s}$ plate at $P/EA=0.00143$

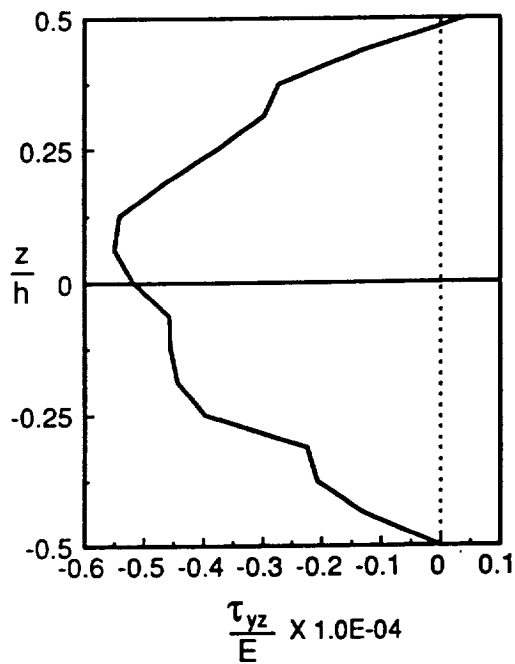


(c) $[\pm 45/0_6]_s$ plate at $P/EA=0.00117$.

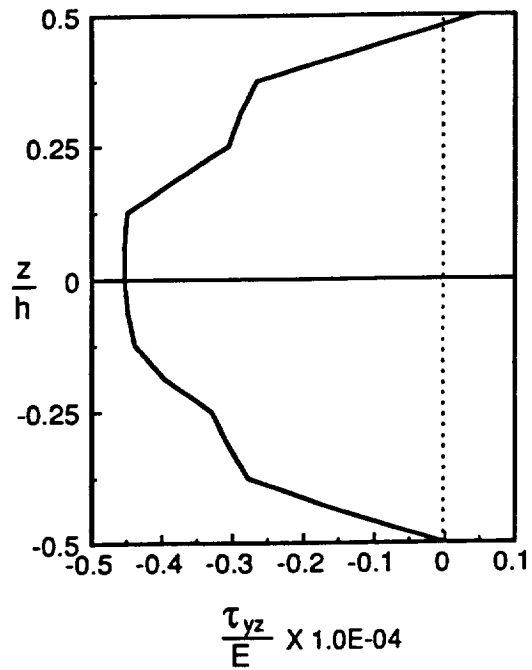


(d) $[\pm 45]_{4s}$ plate at $P/EA=0.00240$.

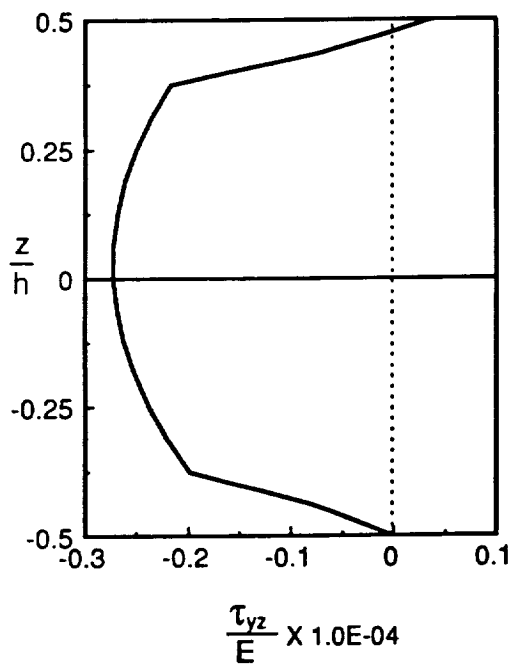
Fig. 4-14 Through the thickness distribution of τ_{xz} for each plate at the net-section hole edge.



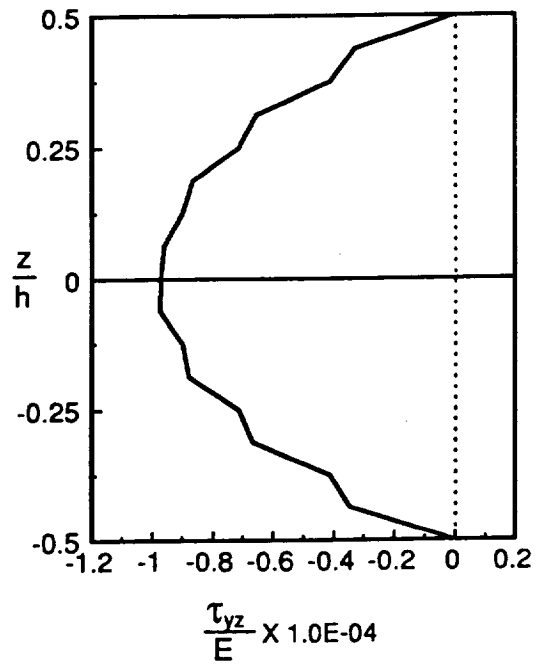
(a) $[\pm 45/0/90]_{2s}$ plate at $P/EA=0.00152$.



(b) $[\pm 45/0_2]_{2s}$ plate at $P/EA=0.00143$.



(c) $[\pm 45/0_6]_s$ plate at $P/EA=0.00117$.



(d) $[\pm 45]_{4s}$ plate at $P/EA=0.00240$.

Fig. 4-15 Through the thickness distribution of τ_{yz} for each plate at the net-section simple support.

The through-the-thickness distribution of τ_{yz} was observed at the center of the element at the net-section simple support for the laminates in this study. Their distribution with thickness is shown in Fig. 4-15. In general τ_{yz} on the top surface is not zero. This means that τ_{yz} is not fully converged. However, the value of τ_{yz} at this location is an order of magnitude smaller than τ_{xz} at the net-section hole edge. It can also be observed that the distribution of τ_{yz} is not symmetric about the midplane. In keeping with the results of Fig. 4-14, it is seen that for the 0° layers τ_{yz} does not vary significantly with z . In terms of actual value of interlaminar shear stress, the $[\pm 45/0_2]_{2S}$ and $[\pm 45/0_6]_S$ laminates experience the largest values of τ_{xz} and the $[\pm 45/0/90]_{2S}$ and $[\pm 45]_{4S}$ laminates experience about 25% less than these two laminates. As regards interlaminar stress τ_{yz} , the $[\pm 45/0/90]_{2S}$, $[\pm 45/0_2]_{2S}$, and $[\pm 45/0_6]_S$ laminates experience the same level of τ_{yz} and the $[\pm 45]_{4S}$ laminate experiences less.

With the stresses being computed and the calculations being validated, attention turns to the prediction of failure using the stress calculation. This is the subject of the next chapter.

5.0 Numerical Failure Analysis

As has been frequently stated, the primary goal of this study is to predict failure. The load level, the location, and the mode of the failure are of interest. The first step in the analysis of failure requires an accurate determination of the stresses. The calculations for the stresses have been discussed in the previous chapter. The second step in a failure analysis is the selection of a failure criterion and the development of failure scenarios using the stresses and the failure criterion. Here the maximum stress failure criterion is used. This criterion is selected because it is easy to understand and easy to use. Complicating data regarding failure due to stress interaction, as is sometimes required in more complicated failure theories, such as the Tsai-Wu criterion, are not needed.

Because of the numerical nature of this study the failure analysis in this study is carried out layer-by-layer by examining the stresses at the centroid of each element. Recall from the last chapter that the interlaminar stress calculations at the centroid are more accurate than at other Gauss points. With the stresses in each element and each layer computed, the following failure parameters are defined and calculated :

$$R_1 = \frac{\sigma_1}{X_t}, \text{ when } \sigma_1 \geq 0, \text{ or } R_1 = \frac{\sigma_1}{X_c}, \text{ when } \sigma_1 < 0, \quad (5.1)$$

$$R_2 = \frac{\sigma_2}{Y_t}, \text{ when } \sigma_2 \geq 0, \text{ or } R_2 = \frac{\sigma_2}{Y_c}, \text{ when } \sigma_2 < 0, \quad (5.2)$$

$$R_{12} = \frac{|\tau_{12}|}{S_{12}}, \quad (5.3)$$

$$R_{13} = \frac{|\tau_{13}|}{S_{13}}, \quad (5.4)$$

$$R_{23} = \frac{|\tau_{23}|}{S_{23}}, \quad (5.5)$$

In eqs. (5.1)-(5.5) σ_1 is the normal stress in the fiber direction, σ_2 is the normal stress transverse to the fiber direction in the plane of the layer, i.e., the 1-2 plane, τ_{12} is the shear stress in the 1-2 plane, τ_{13} is the interlaminar shear stress in the 1-3 plane, and τ_{23} is the interlaminar shear stress in the 2-3 plane. In addition, X_t is the tensile strength in the fiber direction, X_c is the compression strength in the fiber direction, Y_t is the tension strength transverse to the fiber direction in the plane of the layer, Y_c is the compression strength transverse to the fiber direction in the plane of the layer, and S_{12} is the inplane shear strength. These strengths are defined in the material coordinate system, i.e., the 1-2-3 coordinate system. Also, S_{13} is the interlaminar shear strength in the 1-3 plane, and S_{23} is the interlaminar shear strength in the 2-3 plane. The values of these strength parameters for AS4/3502 used in this study are listed in Table 5-1. These values are taken from reference [53, 54]. Note that S_{12} and S_{13} are assumed equal. This is a reasonable assumption. From the numerical analysis formulated in earlier chapters the stresses are calculated in x-y-z coordinates. These stresses are then transformed into the stresses in the material coordinate system for failure analysis with the maximum stress criterion. The stress transfor-

Table 5-1 Strengths of AS4/3502 used in this study.

Strength parameter	Strength (Ksi)
tensile strength in fiber direction (X_t)	200
compressive strength in fiber direction (X_c)	-200
tensile strength transverse to fiber direction (Y_t)	7
compressive strength transverse to fiber direction (Y_c)	-35
shear strength in 1-2 or 1-3 plane (S_{12}, S_{13})	9.4
shear strength in 2-3 plane (S_{23})	8

mation rule can be found in any book dealing with mechanics of composite materials, as an example, in reference [55, 56]

The ratios R_1 , R_2 , R_{12} , R_{13} , and R_{23} are used as indicators of failure. When R_1 is equal to 1.0, it is judged that fiber failure occurs due to normal stress in the fiber direction. In this study it is called fiber failure. In the same fashion, when R_2 and R_{12} are equal to 1.0, it is called transverse failure and inplane shear failure, respectively. There are three stress components that can contribute to fiber failure. They are σ_1 , σ_{12} , and σ_{13} . Even though fiber failure can be enhanced by the stresses σ_{12} and σ_{13} , fiber failure in this study means the failure of a layer in the fiber direction due to σ_1 .

To follow is a considerable amount of information regarding predictions of failure in the plates. As mentioned in chapter 3, a plate loaded in the postbuckling range can experience unexpected mode shape changes. For the laminates in this study failure loads, failure modes, and failure locations are predicted for both the one half-wave configuration and the two half-wave configuration. For plates with holes the failure analysis results are presented in Table 5-2 for the one half-wave configuration and Table 5-3 for the two half-wave configuration. For plates without holes, i.e., solid plates, failure analysis results are presented in Table 5-4 for the one half-wave configuration and Table 5-5 for the two half-wave configuration. The tables are based on a first-ply failure analysis. In these tables the element number and the layer number of the failed layer are given, where layer number is counted from the bottom concave surface of the plate. The element numbering scheme can be found in Fig. 5-1 for the plates with holes and Fig. 5-2 for the solid plates. Since the initial deflection due to the imperfection is assumed to be in the positive z direction, the plate deflects further in the positive z direction when loaded. Thus here the bottom surface is on the op-

Table 5-2 Failure loads, failure modes, and failure locations for plates with holes for the one half-wave configuration.

Laminate	Failure mode	$\overline{N_x}$ (lb/in)	$\frac{P}{EA}$	Failure location *
[± 45/0/90] _{2S}	R ₁	1605	0.00256	element 197 3-rd layer (0°)
	R ₂	1239	0.00197	element 189 16-th layer (45°)
	R ₁₂	1140	0.00182	element 197 1-st layer (45°)
[± 45/0 ₂] _{2S}	R ₁	1989	0.00217	element 169 2-nd layer (-45°)
	R ₂	1231	0.00134	element 205 14-th layer (0°)
	R ₁₂	1342	0.00146	element 197 1-st layer (45°)
[± 45/0 ₆] _{2S}	R ₁	2030	0.00163	element 169 2-nd layer (-45°)
	R ₂	1247	0.00100	element 205 14-th layer (0°)
	R ₁₂	1613	0.00129	element 197 1-st layer (45°)
[± 45] _{4S}	R ₁	1447	0.00592	element 129 2-nd layer (45°)
	R ₂	1132	0.00463	element 140 16-th layer (45°)
	R ₁₂	461	0.00189	element 197 1-st layer (45°)

* Layer no. is counted from concave side.

Table 5-3 Failure loads, failure modes, and failure locations for plates with holes for the two half-wave configuration.

Laminate	Failure mode	\bar{N}_x (lb/in)	$\frac{P}{EA}$	Failure location *
[± 45/0/90] _{2s}	R ₁	1532	0.00244	element 208 1-st layer (45°)
	R ₂	1168	0.00186	element 79 16-th layer (45°)
	R ₁₂	1536	0.00245	element 170 16-th layer (45°)
[± 45/0 ₂] _{2s}	R ₁	1892	0.00206	element 208 1-st layer (45°)
	R ₂	1232	0.00134	element 154 14-th layer (0°)
	R ₁₂	1681	0.00183	element 170 16-th layer (45°)
[± 45/0 _s] _s	R ₁	1953	0.00156	element 208 1-st layer (45°)
	R ₂	1318	0.00106	element 154 14-th layer (0°)
	R ₁₂	1894	0.00152	element 208 3-rd layer (0°)
[± 45] _{4s}	R ₁	1260	0.00515	element 207 1-st layer (45°)
	R ₂	716	0.00293	element 79 16-th layer (45°)
	R ₁₂	631	0.00258	element 158 1-st layer (45°)

* Layer no. is counted from concave side.

Table 5-4 Failure loads, failure modes, and failure locations for solid plates for the one half-wave configuration.

Laminate	Failure mode	\bar{N}_x (lb/in)	$\frac{P}{EA}$	Failure location
[$\pm 45/0/90$] _{2S}	R ₁	1758	0.00280	element 69 2-nd layer (-45°)
	R ₂	1544	0.00246	element 50 16-th layer (45°)
	R ₁₂	1710	0.00273	element 62 16-th layer (45°)
[$\pm 45/0_2$] _{2S}	R ₁	2060	0.00225	element 69 2-nd layer (-45°)
	R ₂	1468	0.0016	element 48 14-th layer (0°)
	R ₁₂	1859	0.00203	element 73 1-st layer (45°)
[$\pm 45/0_6$] _S	R ₁	2076	0.00166	element 68 2-nd layer (-45°)
	R ₂	1425	0.00114	element 46 14-th layer (0°)
	R ₁₂	1919	0.00154	element 68 3-rd layer (0°)
[± 45] _{4S}	R ₁	1443	0.00590	element 60 2-nd layer (-45°)
	R ₂	1080	0.00442	element 50 16-th layer (45°)
	R ₁₂	738	0.00302	element 73 1-st layer (45°)

* Layer no. is counted from concave side.

Table 5-5 Failure loads, failure modes, and failure locations for solid plates for the two half-wave configuration.

Laminate	Failure mode	\bar{N}_x (lb/in)	$\frac{P}{EA}$	Failure location
[$\pm 45/0/90$] _{2S}	R ₁	1606	0.00256	element 64 1-st layer (45°)
	R ₂	1546	0.00246	element 48 15-th layer (-45°)
	R ₁₂	1568	0.00250	element 76 16-th layer (45°)
[$\pm 45/0_2$] _{2S}	R ₁	1990	0.00217	element 64 1-st layer (45°)
	R ₂	1340	0.00146	element 58 14-th layer (0°)
	R ₁₂	1748	0.00191	element 76 16-th layer (45°)
[$\pm 45/0_6$] _{2S}	R ₁	2096	0.00168	element 64 1-st layer (45°)
	R ₂	1426	0.00114	element 58 14-th layer (0°)
	R ₁₂	1990	0.00159	element 67 16-th layer (45°)
[± 45] _{4S}	R ₁	1347	0.00551	element 64 1-st layer (45°)
	R ₂	1117	0.00457	element 39 15-th layer (-45°)
	R ₁₂	745	0.00305	element 66 1-st layer (45°)

* Layer no. is counted from concave side.

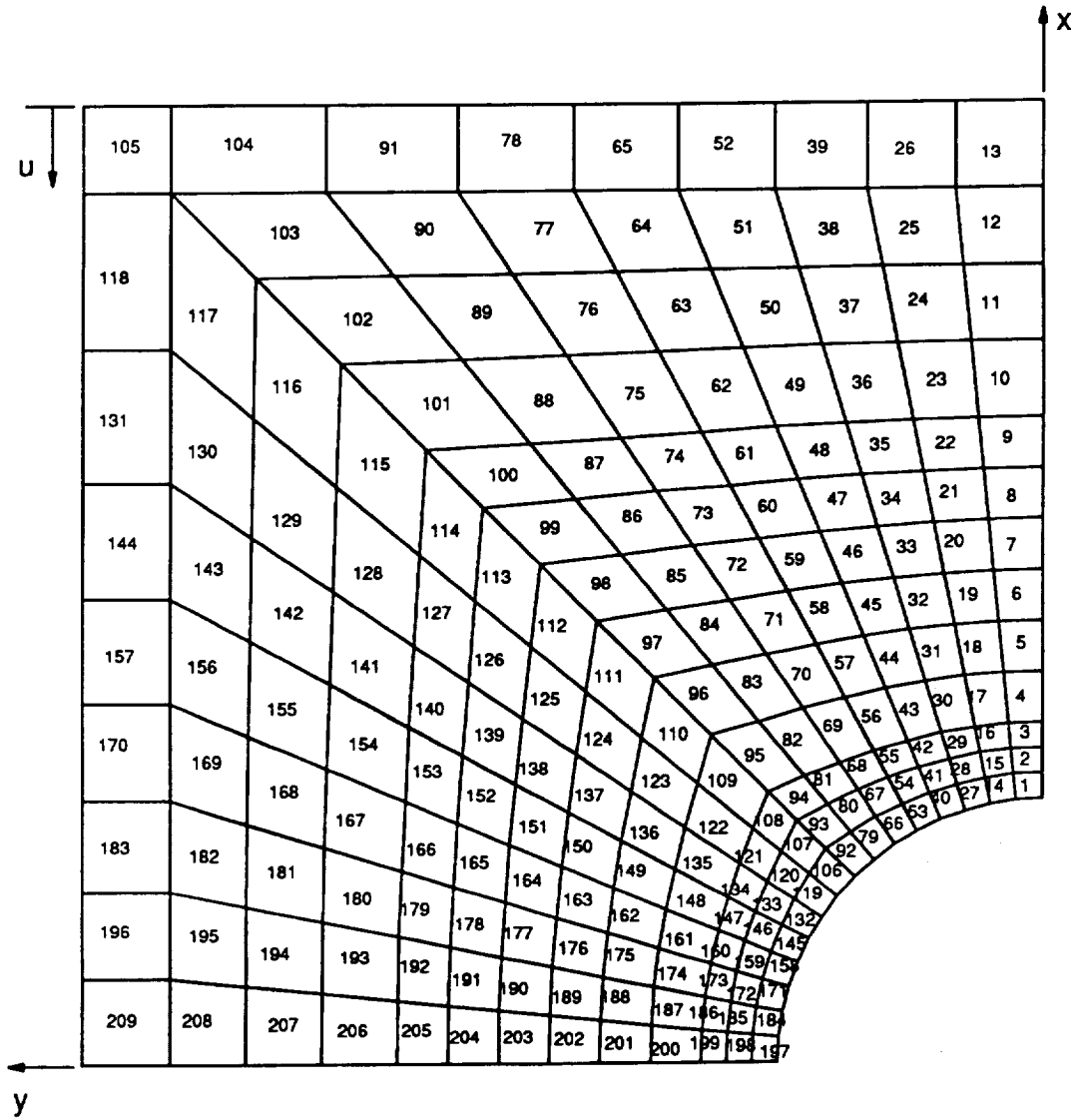


Fig. 5-1 Element numbering for a square plate with hole with a 209 element mesh.

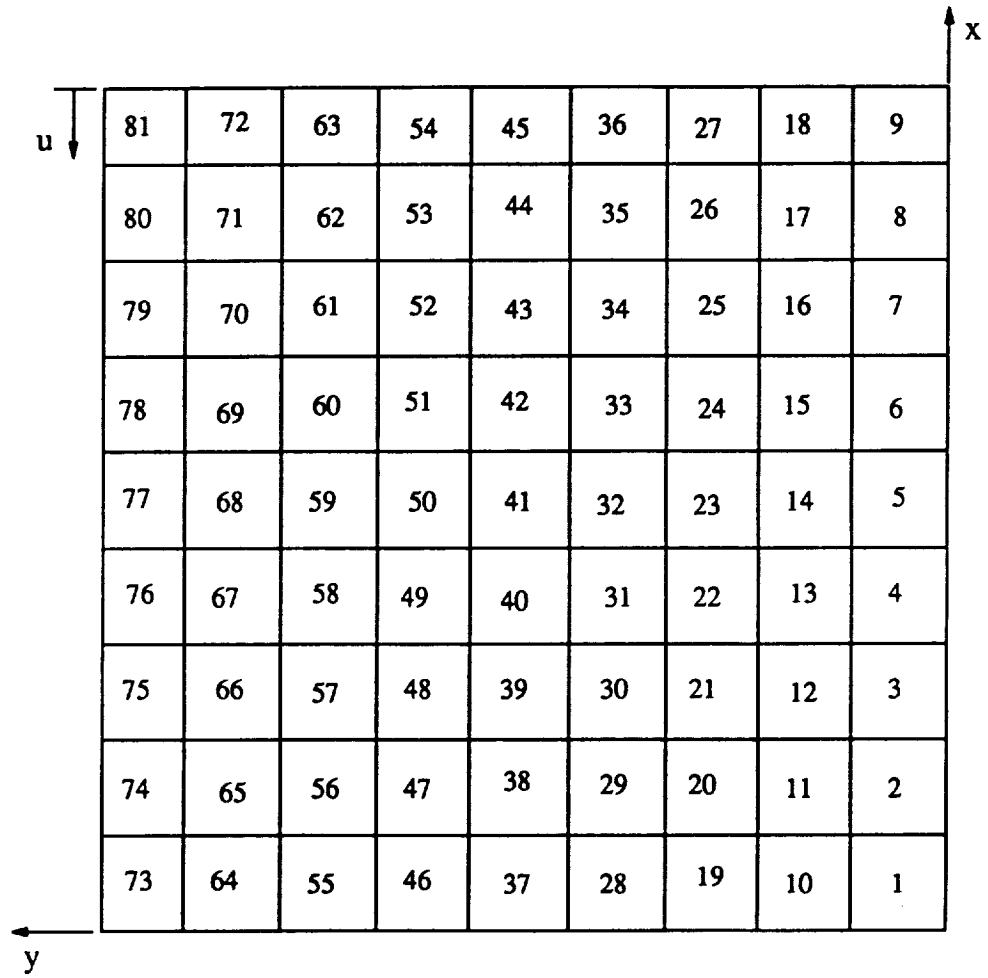


Fig. 5-2 Element numbering for a square solid plate with an 81 element mesh.

posite side to the direction of the plate deflection, i.e., on the concave side. These tables mean that if the plates remain in the one half-wave configuration without a mode shape change, failure occurs in the manner predicted in Table 5-2 for plates with holes and Table 5-4 for solid plates. If the plates have a mode shape change, failure occurs in the manner predicted in Table 5-3 for plates with holes and Table 5-5 for solid plates. In Tables 5-2 through 5-5 failure loads are presented in terms of average applied end force resultant as defined in eq. (2.21). The nondimensionalized values of these failure loads in the form of P/EA are also shown in these tables. As an example of the deflected shapes, the three-dimensional surface drawings of the deformed shape of the quasi-isotropic plate are presented for plates with and without holes for both the one half-wave and two half-wave configurations.

In figures to follow the predicted failure loads for each plate are marked on the load vs. end shortening relations for each deformation configuration. Following the load vs. end shortening relations for each plate, figures which show the failure locations, failure modes at that location, and the number of failed layers at that location are presented. These figures go beyond a first-ply failure analysis and provide information on multiple-ply failures, or interpreted differently, damage accumulation. These multiple-ply failures are assumed to occur after the first-ply failure and the calculations are done for loads greater than the first-ply failure loads. The analysis for the multiple-ply failure is not altogether correct, however. If first failure occurs in a certain mode and at a certain location in the plate, after this first-ply failure plate stiffnesses are no longer the same as before the first-ply failure. The stiffness change due to the first failure must be taken into account in the analysis for further ply failures. This makes the analysis much more complicated. In the damage accumulation scenario here, the stiffness changes due to the first failure are neglected. Except for

the $[\pm 45]_{4s}$ plates, the load level used for the damage accumulation scenarios is slightly above the first fiber failure load. For the $[\pm 45]_{4s}$ plates the fiber failure load is quite high compared to other failure loads. It is obvious that the final failure of the $[\pm 45]_{4s}$ plates will occur at much lower load than the fiber failure load. Therefore, a load level slightly above the first transverse failure load is selected to show the damage scenarios of these plates.

In chapter 7 the applicability of the first-ply failure theory will be examined by comparing the numerical results from the first-ply failure theory with the experimental results. Extensive comparisons for load-end shortening relations, load-deflection relations, strains, failure locations, failure loads, and failure modes will be presented in chapter 7. It will be noted in advance that contrary to the previous investigators' experimental results for rectangular plates [34, 36, 37], interlaminar shear failure is not predicted in this failure analysis for square plates. This will be discussed more in chapter 7.

5.1 Failure of Plates with Holes

5.1.1 The $[\pm 45/0/90]_{2s}$ Plate with a Hole

Figure 5-3 shows the deflected shape of the $[\pm 45/0/90]_{2s}$ plate with a hole in the one half-wave configuration. The load level is $P/EA = 0.00258$. Referring to Table 2-3 it is seen that this level is about 6 times the first buckling load. The lines where the

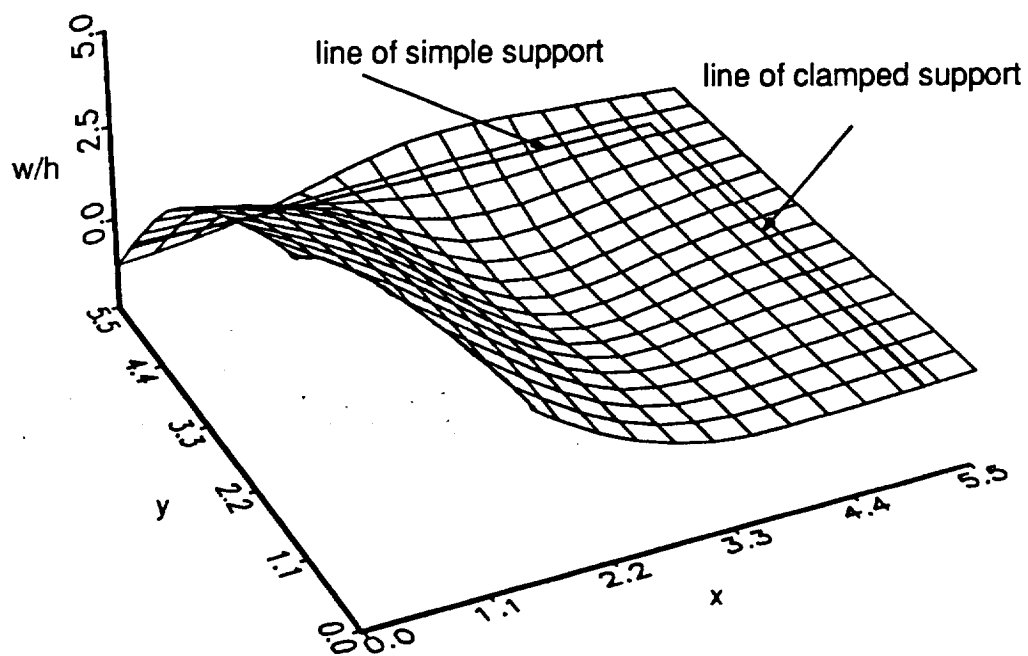


Fig. 5-3 Shape of the $[\pm 45/0/90]_{2s}$ plate with a hole deflected in the one half-wave configuration at $P/EA=0.00258$.

supports are assumed to act are shown. It can be observed that a curvature opposite to the curvature at the center of the plate occurs near the corner of the clamped support and simple support. The deflected shape of a quarter-plate in the two half-wave configuration is shown in Fig. 5-4. The load level used is about 4 times the buckling load corresponding to the two half-wave configuration in the loading direction. Figure 5-5 shows the predicted failures superimposed on the load vs. end shortening relations for the $[\pm 45/0/90]_{2s}$ plate with a hole. For the one half-wave configuration, the solid line, as the load is increased, inplane shear failure is predicted to occur first and it is predicted to occur at the net-section hole edge, element 197, in the bottom layer. Continuing to load in the one half-wave configuration, transverse failure in the top layer of element 189 follows the inplane shear failure. Fiber failure finally occurs at the net-section hole edge, in element 197, at a much higher load than the loads of the other two failure modes. Table 5-2 summarizes these findings and it records that first inplane shear failure and first fiber failure occur at the net-section hole edge. From this it can be deduced that the net-section hole edge is under severe stress. Figure 5-6, which is one of the aforementioned damage accumulation scenarios, shows clearly that the net-section hole edge is severely damaged in the postbuckling loading of quasi-isotropic plate responding in the one half-wave configuration. The load level used in the scenario is $P/EA=0.00258$, slightly above the fiber failure load of $P/EA=0.00256$. The scenario shows that all three failure modes appear in that area, and it shows that a number of layers at that location fail. Figure 5-6 also shows that at the hole edge on the x axis 5 or 6 layers are damaged by transverse failure. This is because of the high value of N_y at this location. Up to the load level of first fiber failure no interlaminar shear failure is predicted. At the load level of $P/EA=0.00258$ the highest value of R_{13} is 0.3, and the highest value of R_{23} is 0.34.

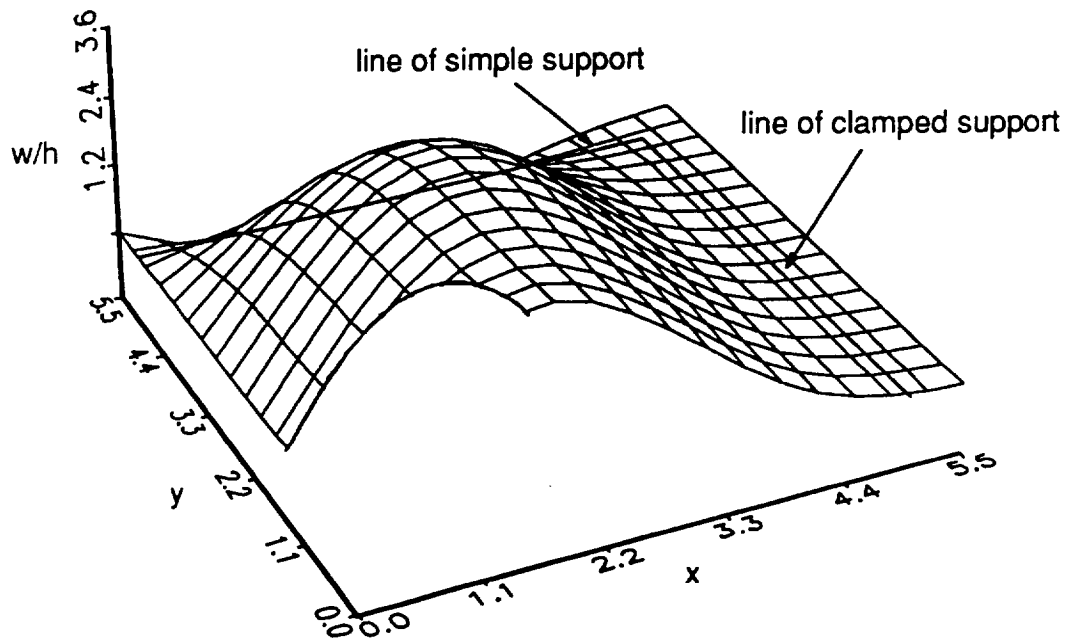


Fig. 5-4 Shape of the $[\pm 45/90]_{2s}$ plate with a hole deflected in the two half-wave configuration at $P/EA = 0.00255$.

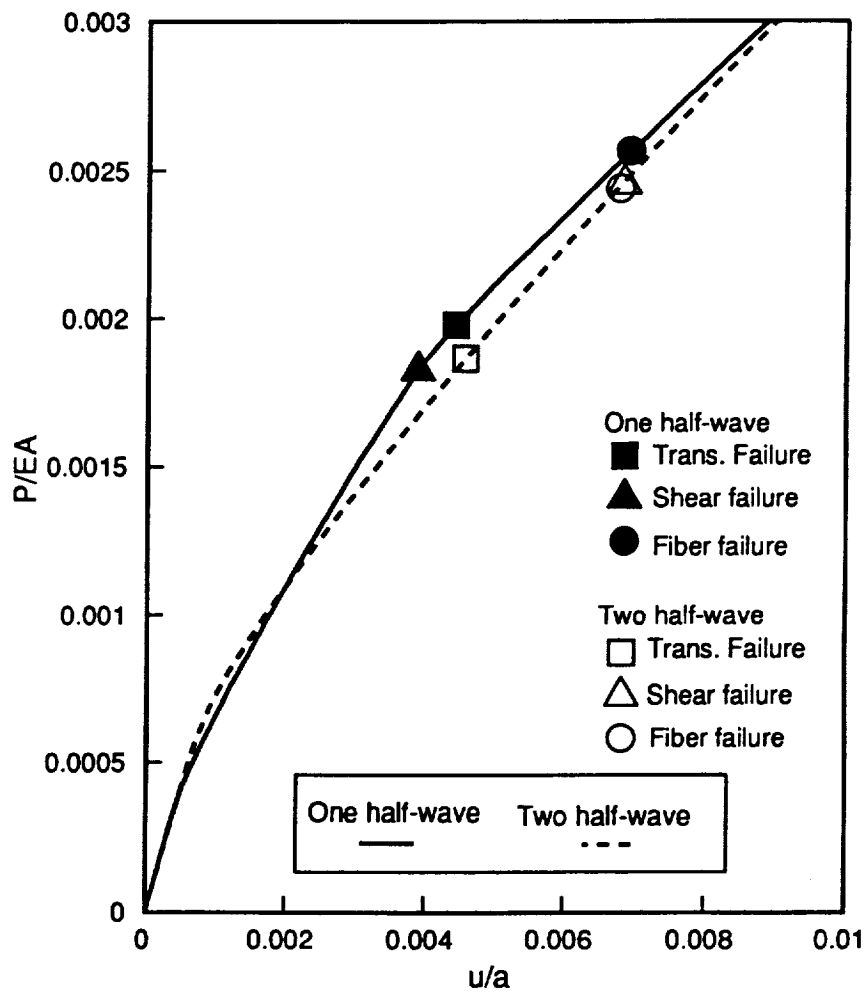
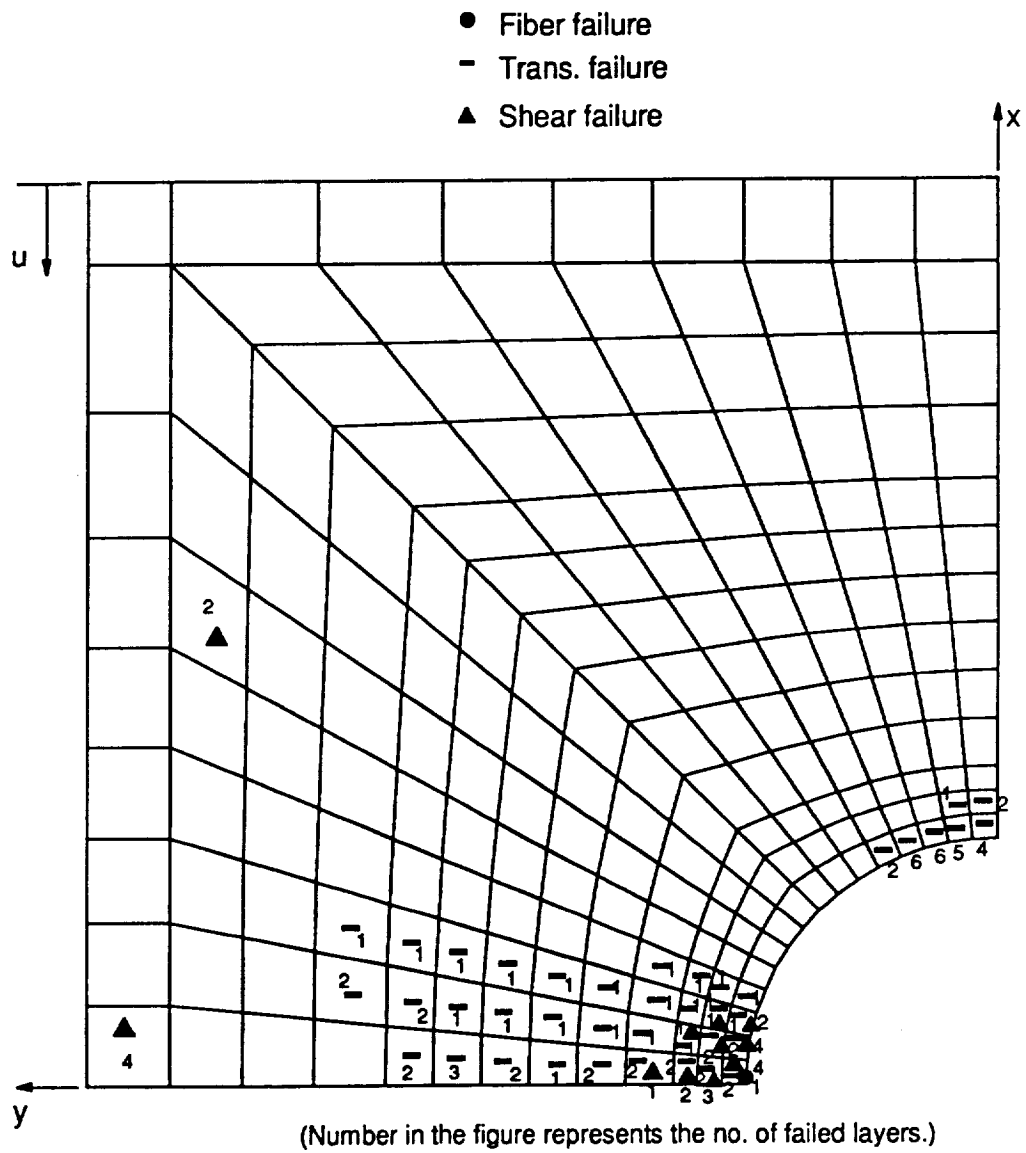


Fig. 5-5 Failures and load-end shortening relations for $[\pm 45/0/90]_{2s}$ plate with a hole.

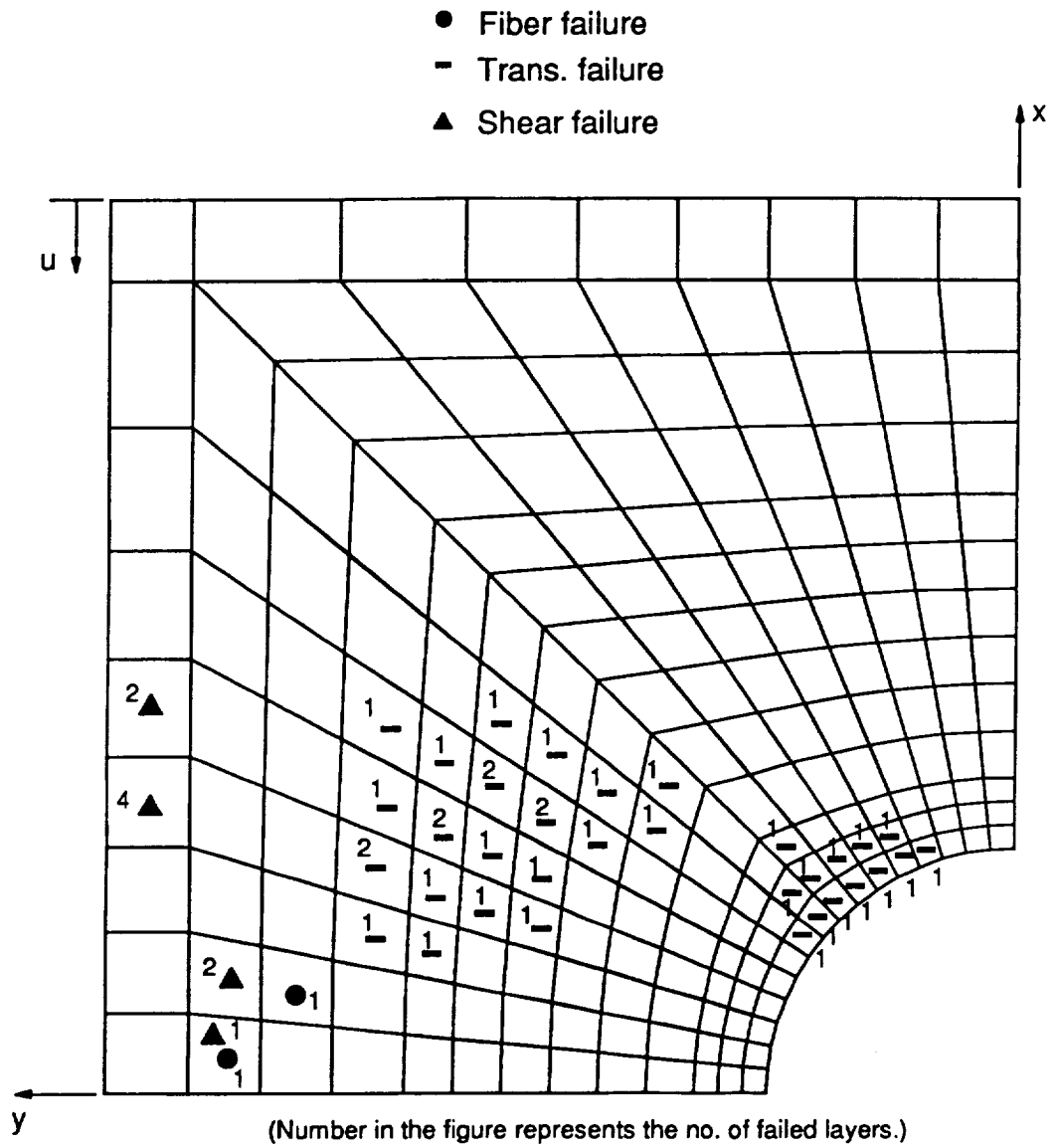


$$\text{Load} : \frac{P}{EA} = 0.00258$$

Fig. 5-6 Predicted failure locations and failure modes of the $[\pm 45/0/90]_{2s}$ plate with a hole in the one half-wave configuration.

Referring to Fig. 5-5 and Table 5-3 for the two half-wave configuration, the dashed line, as the load is increased, transverse failure is predicted to occur first and it is predicted to occur at the hole edge about half way between the net-section and the x axis, in the element 79. Inplane shear failure and fiber failure are predicted to occur at similar load levels, but at a level much higher than the transverse failure load. The first inplane shear failure is predicted to occur in the element 170, in the extension area away from the net-section. The first fiber failure occurs at element 208, just inside the simple support along the net-section. This is a significantly different location than for the one half-wave case. However, the fiber failure load of the two half-wave configuration is only slightly lower than the fiber failure load of the one half-wave configuration.

Considering the damage accumulation scenario of Fig. 5-7, at a load level slightly greater than first fiber or first inplane shear failure, transverse failure appears rather widespread over an area on the hole edge, near where the first transverse failure was predicted (element 79), and also over an area away from the net-section and simple support, in the central region of the quarter-plate. Inplane shear failure occurs outside the simple support, slightly away from the net-section. Interlaminar shear failure is not predicted in the two half-wave configuration at loads as high as the first fiber failure load. At $P/EA = 0.00255$ the highest value of the failure parameter R_{13} is 0.44, and the highest value of R_{23} is 0.54. These values are higher than those for the one half-wave configuration, but far from failure values. As mentioned at the beginning of this chapter, inplane shear failure can contribute to fiber failure. Therefore, inplane shear failure in addition to fiber failure can be a major factor of final failure of the



$$\text{Load : } \frac{P}{EA} = 0.00255$$

Fig. 5-7 Predicted failure locations and failure modes of the $[\pm 45/0/90]_{2s}$ plate with a hole in the two half-wave configuration.

plate. It is expected that the final failure of the plate may even occur outside the simple support, a location where severe inplane shear stresses, though not the maximum values, are predicted to occur.

5.1.2 The $[\pm 45/0_2]_{2s}$ Plate with a Hole

Figure 5-8 shows the load vs. end shortening relation for the $[\pm 45/0_2]_{2s}$ plate with a hole and with the failure loads and modes indicated. As can be seen, for both the one half-wave and two half-wave configuration, transverse failure occurs first as the plate is loaded from zero load. Figures 5-9 and 5-10 show the damage accumulation scenarios for the one and two half-wave configurations, respectively.

Referring to Table 5-2, for the one half-wave configuration transverse failure occurs first and it occurs in the middle of the net-section between the net-section hole edge and simple support in element 205. Shortly after the first transverse failure the first inplane shear failure follows at the net-section hole edge in element 197. Fiber failure occurs at a load higher than the other two failure loads just inside the simple support, slightly away from the net-section. The fiber failure load for this plate in the one half-wave configuration is higher than the fiber failure load of the quasi-isotropic plate in the one half-wave configuration.

Considering the damage accumulation scenario at a load of $P/EA = 0.00222$, just above the first fiber failure load of $P/EA = 0.00217$, as shown in Fig. 5-9 the transverse failure develops along the net-section line and also on the hole edge near the x axis.

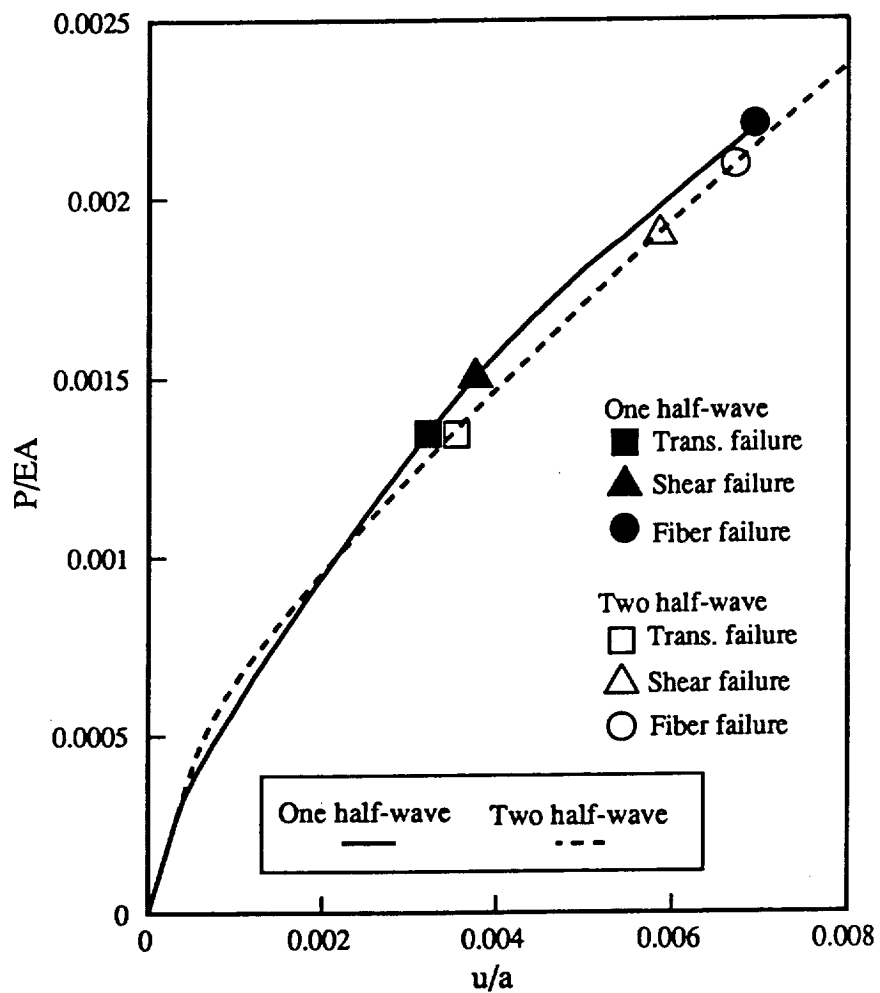
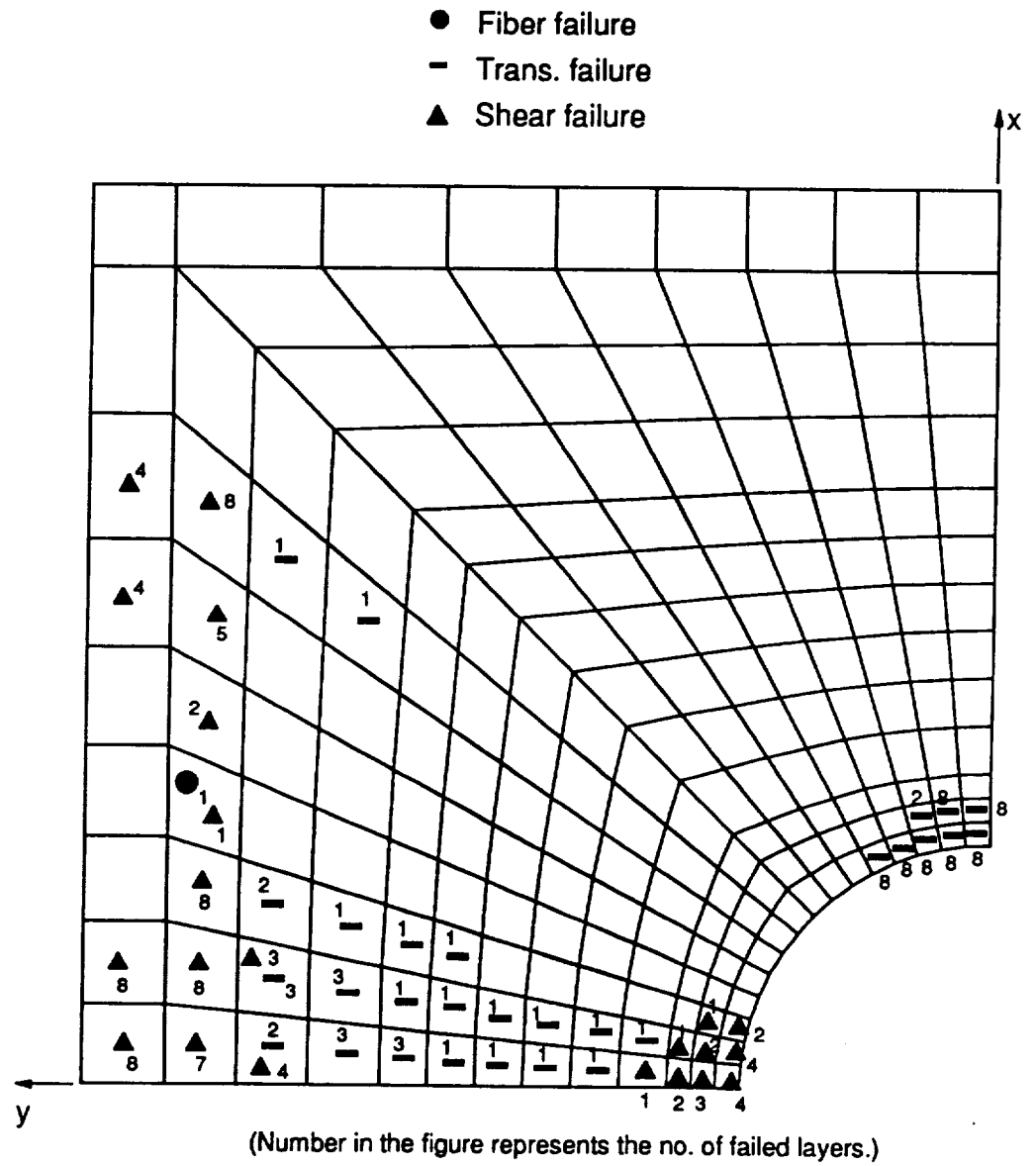
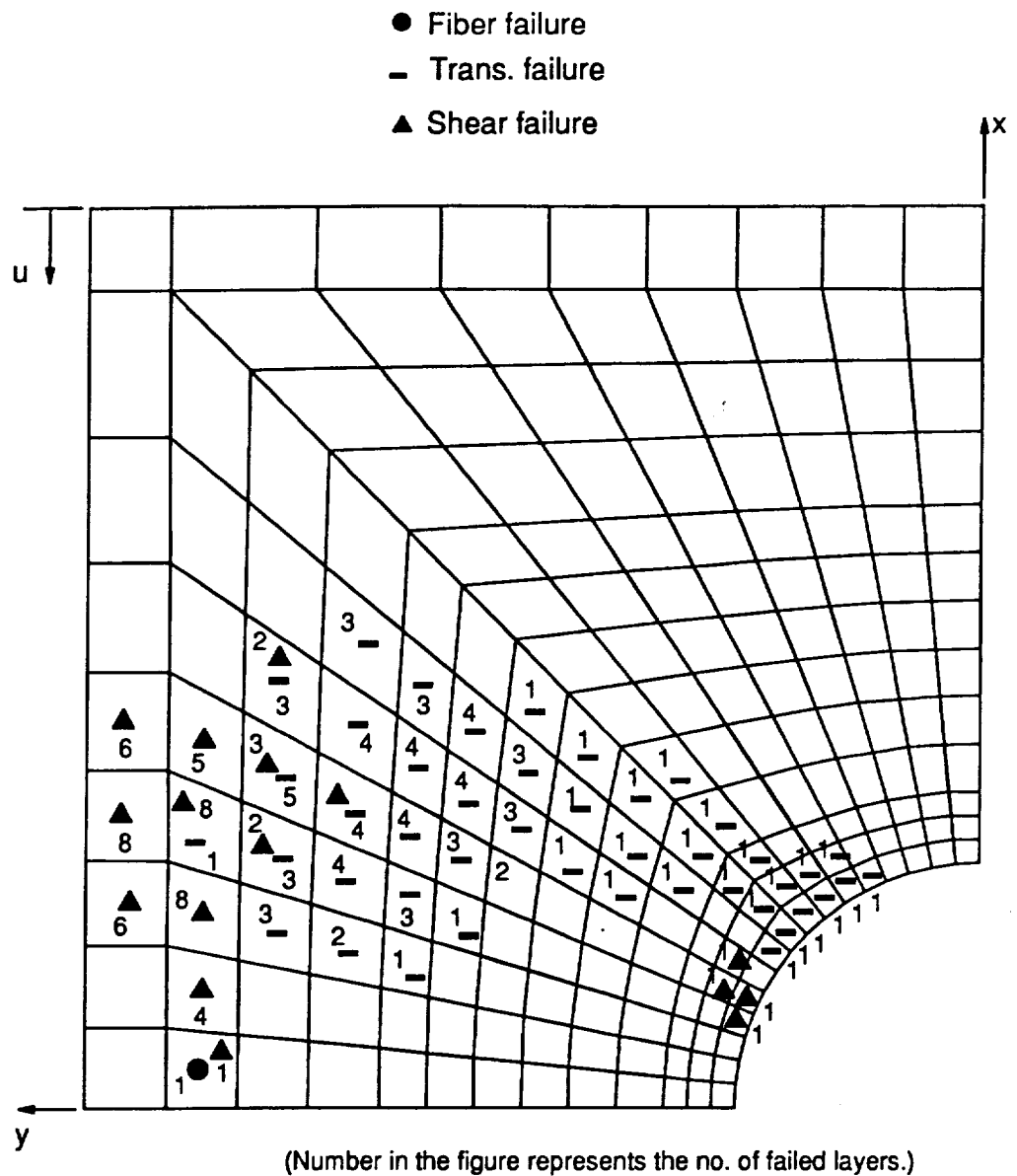


Fig. 5-8 Failures and load-end shortening relations for the $[\pm 45/0_2]_{2s}$ plate with a hole.



$$\text{Load} : \frac{P}{EA} = 0.00222$$

Fig. 5-9 Predicted failure locations and failure modes of the $[\pm 45/0_2]_{2s}$ plate with a hole in the one half-wave configuration.



Load : $\frac{P}{EA} = 0.00206$

Fig. 5-10 Predicted failure locations and failure modes of the $[\pm 45/0_2]_{2s}$ plate with a hole in the two half-wave configuration.

It is predicted that half of the laminate, i.e., 8 layers, is damaged on the hole edge near the x axis at this load just above the first fiber failure load. Inplane shear failure develops on the net-section hole edge and also along the simple support. The extension area outside the simple support on the net-section, and the area just inside the simple support on the net-section are damaged by inplane shear stress. Fiber failure occurs just inside the simple support away from the net-section. Compared with the quasi-isotropic plate deformed in the one half-wave configuration, the net-section hole edge of this $[\pm 45/0_2]_{2s}$ laminate is under a less severe stress state. Again, interlaminar shear stresses are low. At slightly above the first fiber failure load of $P/EA = 0.00222$ the highest value of R_{13} is 0.35, and the highest value of R_{23} is 0.40. It is expected that the final failure will occur along the net-section.

For the two half-wave configuration, as the load is increased failure occurs in the sequence of transverse failure, then inplane shear failure, and then fiber failure, as in the one half-wave configuration. However, from Table 5-3 it can be seen that the locations of these failure modes are quite different than the locations of failure for the one half-wave configuration, and the load level for the transverse failure is different. The first transverse failure occurs between the simple support and the hole edge, away from the net-section, in element 154. The first inplane shear failure occurs in element 170, the extension area away from the net-section. First fiber failure occurs just inside the simple support on the net-section, element 208. The location of the first fiber failure is the same location of first fiber failure of the $[\pm 45/0/90]_{2s}$ plate in the two half-wave configuration. As seen from Fig. 5-8, transverse failure occurs at about the same load level as for the one half-wave configuration. In the one half-wave configuration, inplane shear failure occurs shortly after transverse failure. However, in the two half-wave configuration the inplane shear failure load is much

higher than the transverse failure load. The fiber failure load for the $[\pm 45/0_2]_{2s}$ plate in the two half-wave configuration is slightly lower than the fiber failure load of the one half-wave configuration, but it is considerably higher than the failure load of the quasi-isotropic plate in the two half-wave configuration. Referring to the damage accumulation scenario for the two half-wave configuration at the first fiber failure load, Fig. 5-10, like the quasi-isotropic plate in the two half-wave configuration, Fig. 5-7, transverse failure is widespread in the region between the simple support and hole edge, but away from the net-section. Severe inplane shear failure occurs near the simple support but slightly away from the net-section. No interlaminar shear failure is predicted at the first fiber failure load. At the fiber failure load, $P/EA = 0.00206$, the highest value of R_{13} is 0.58, and the highest value of R_{23} is 0.44.

From Fig. 5-10, it is expected that the final failure of the plate will occur at the simple support at or slightly away from the net-section. Considering that the inplane shear failure load and fiber failure load are higher than those of the quasi-isotropic plate in the two half-wave configuration, the final failure load of this plate in the two half-wave configuration is expected to be greater than the final failure load of the quasi-isotropic plate in the two half-wave configuration.

5.1.3 The $[\pm 45/0_6]_s$ Plate with a Hole

The load vs. end shortening relation for the $[\pm 45/0_6]_s$ plate with hole is shown in Fig. 5-11. For the one half-wave configuration the failure sequence is transverse failure, followed by inplane shear failure, followed by fiber failure. The inplane shear

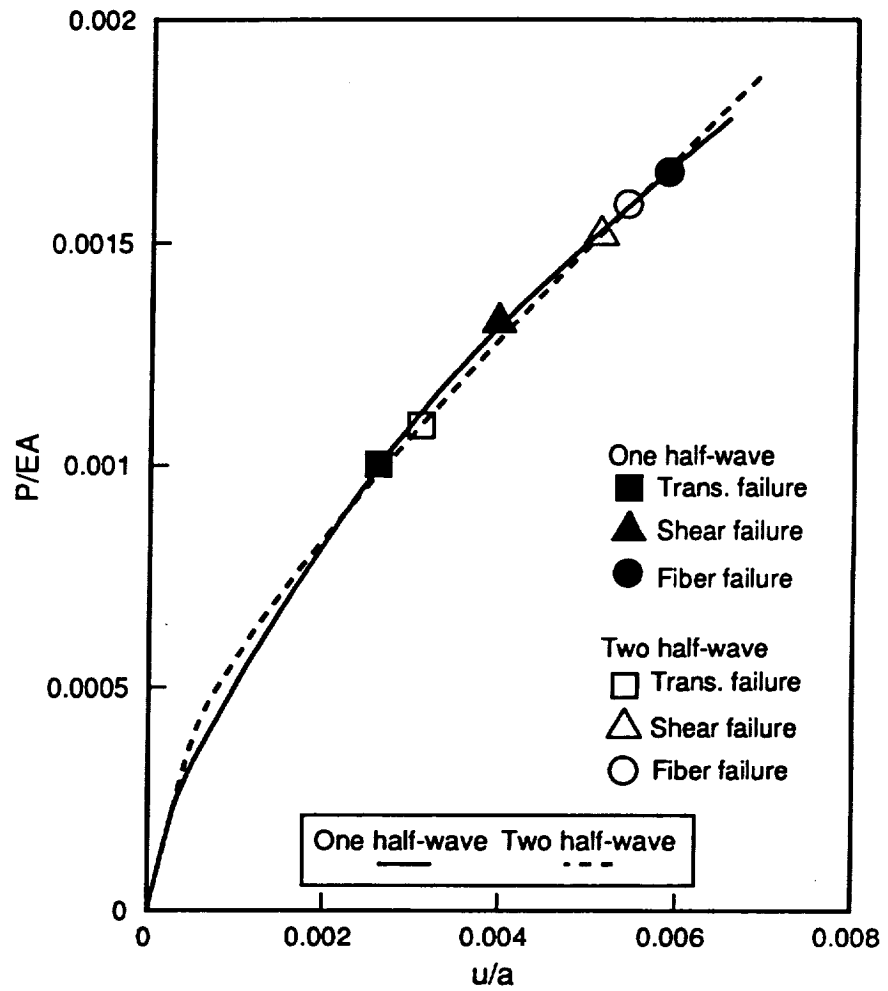
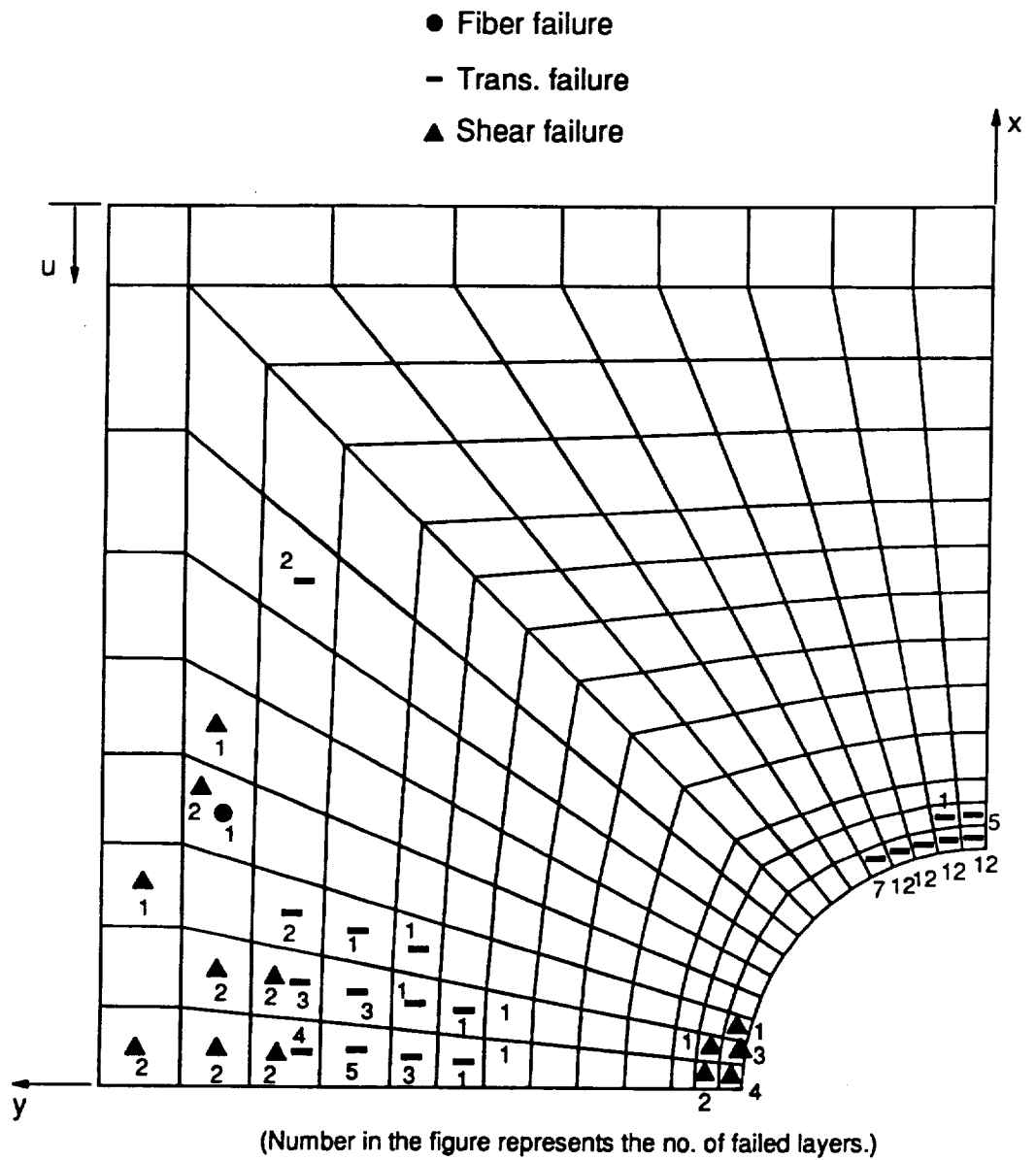


Fig. 5-11 Failures and load-end shortening relations for the $[\pm 45/0_e]_s$ plate with a hole.

failure load and fiber failure load are both higher than for the $[\pm 45/0_2]_{2s}$ plate, which, as has been seen, are higher than these failure loads for the quasi-isotropic plate. Table 5-2 shows that the first transverse failure occurs at the center of the net-section, element 205. First inplane shear failure occurs at the net-section hole edge, element 197, and first fiber failure occurs at the same location as the first fiber failure of the $[\pm 45/0_2]_{2s}$ plate in the one half-wave configuration, element 169, along the simple support but away from the net-section.

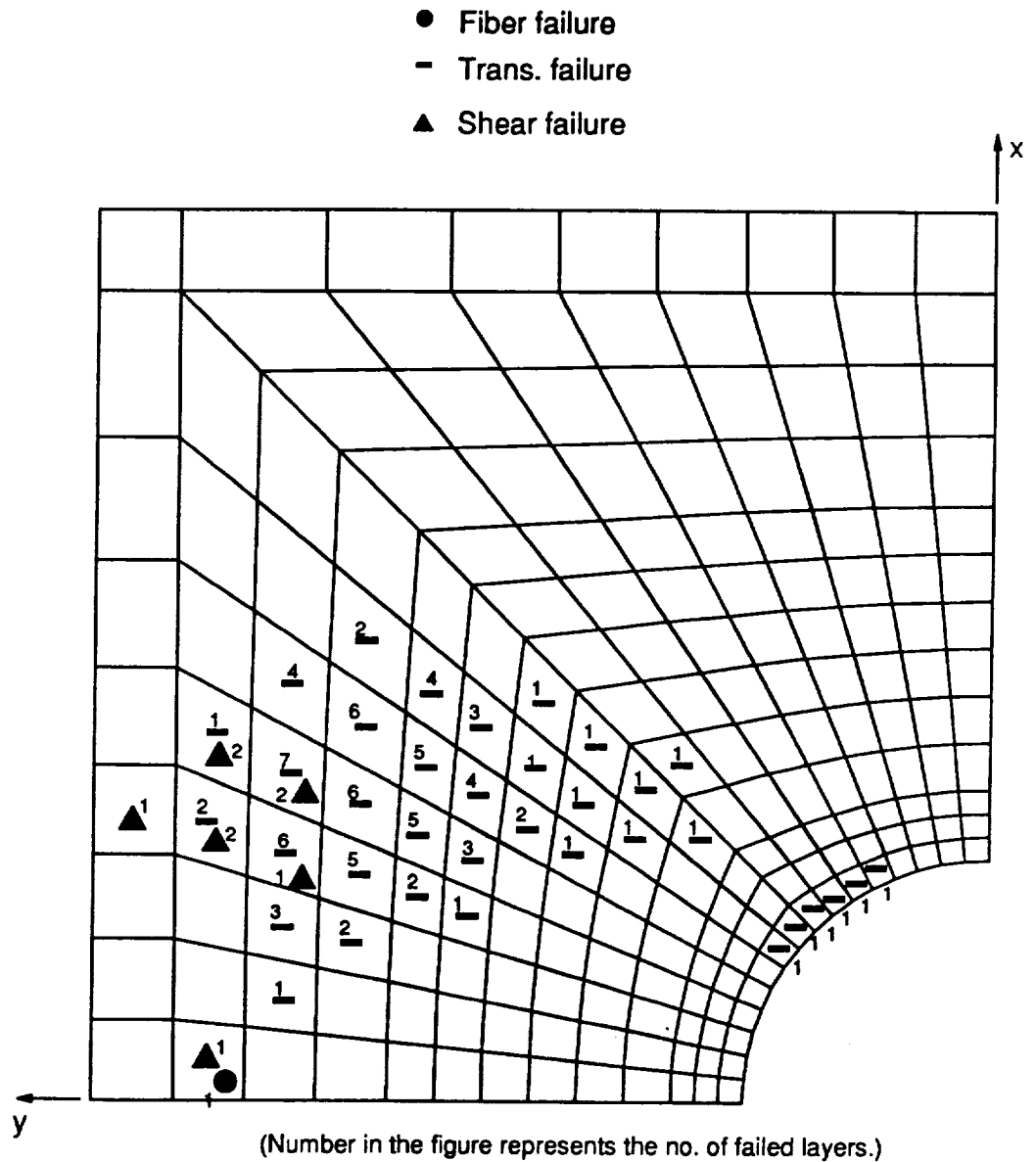
Figure 5-12 illustrates the damage accumulation scenario for the $[\pm 45/0_6]_s$ plate in the one half-wave configuration. Like the $[\pm 45/0_2]_{2s}$ plate in the one half-wave configuration, Fig. 5-9, transverse failure develops along the net-section line and at the hole edge on the x axis. However, by comparing Fig. 5-12, Fig. 5-9, and Fig. 5-6 it can be seen that as the number of 0° layers are increased, the location of transverse failure on the net-section moves toward the simple support. Also, since a larger number of layers have failed, it can be seen that the transverse failure at the hole edge on the x axis is more severe for the $[\pm 45/0_6]_s$ laminate than for the $[\pm 45/0_2]_{2s}$ laminate and for the $[\pm 45/0/90]_{2s}$. For the $[\pm 45/0_6]_s$ laminate all 12 0° layers on the hole edge on the x axis have failed in the transverse failure mode. For the $[\pm 45/0_2]_{2s}$ laminate all 8 0° layers on the hole edge at the x axis have failed in the transverse failure mode. For the $[\pm 45/0_6]_s$ plate at the fiber failure load, inplane shear failure develops on the net-section hole edge and net-section simple support. The net-section hole edge is under concentrated inplane shear failure. However, the inplane shear failure on the net-section simple support is spread out. The interlaminar shear failure parameters are far lower than the inplane failure parameters. The highest value of R_{13} is 0.35, and the highest value of R_{23} is 0.31, both computed at $P/EA = 0.00167$.



$$\text{Load : } \frac{P}{EA} = 0.00169$$

Fig. 5-12 Predicted failure locations and failure modes of the $[\pm 45/0_6]_s$ plate with a hole in the one half-wave configuration.

From Fig. 5-11 and Table 5-3 it can be seen that as the plate is loaded, for the two half-wave configuration transverse failure begins to develop at a slightly higher load than the transverse failure load of the one half-wave configuration. The location is element 154, the same location as the first transverse failure location of the $[\pm 45/0_2]_{2s}$ plate in the two half-wave configuration. The inplane shear failure load is higher than the transverse failure load, and the inplane shear failure occurs just inside the net-section simple support, element 208. Shortly after the inplane shear failure occurs, fiber failure occurs at just inside the simple support on the net-section, also at element 208. Thus at element 208 both inplane shear failure and fiber failure occur. This is the same location as the fiber failure location of the $[\pm 45/0/90]_{2s}$ and $[\pm 45/0_2]_{2s}$ plates with a hole in the two half-wave configuration. Compared to the $[\pm 45/0/90]_{2s}$ and $[\pm 45/0_2]_{2s}$ laminates, the fiber failure and inplane shear failure loads of the two half-wave configuration are higher for the $[\pm 45/0_s]_s$ laminate. Considering the damage accumulation scenario, Fig. 5-13, it can be seen that like the $[\pm 45/0/90]_{2s}$ and $[\pm 45/0_2]_{2s}$ plates, Figs. 5-7 and 5-10, respectively, transverse failure occurs in the central region of the quarter plate, away from the net-section. The area just inside the simple support is damaged by transverse failure and inplane shear failure. This is similar to the previous two plates. The highest value of failure parameter R_{13} is 0.61, and the highest value of R_{23} is 0.28 at the load level of $P/EA = 0.00161$, a level slightly greater than the first fiber failure load.



$$\text{Load : } \frac{P}{EA} = 0.00161$$

Fig. 5-13 Predicted failure locations and failure modes of the $[\pm 45/0]_s$ plate with a hole in the two half-wave configuration.

5.1.4 The $[\pm 45]_{4S}$ Plate with a Hole

The load vs. end shortening relation for the $[\pm 45]_{4S}$ plate with hole is shown in Fig. 5-14. In the one half-wave configuration inplane shear failure occurs at a very low load level. Table 5-2 shows that the first inplane shear failure occurs at the net-section hole edge, element 197. For the other plates failure begins about at least 3.5 times the buckling load. For this plate, however, failure begins at less than 2 times the buckling load. For this plate the transverse failure load is considerably greater than the inplane shear failure load. This has not been the case with the other plates. The first transverse failure occurs in the central region of the quarter plate, away from the net-section, in element 140. First fiber failure occurs in element 129, near the clamped end and near the simple support. This is the first plate to experience fiber failure in this location.

The damage accumulation scenario, Fig. 5-15, shows that at a load slightly above the inplane shear failure load the plate is damaged severely by inplane shear failure. In the area outside the simple support and near the net-section all 16 layers have failed. Table 5-2 showed that the first inplane shear failure occurred at the net-section hole edge. But in Fig. 5-15 failure marks for inplane shear do not appear there. This means that even though the first inplane shear failure occurred at the net-section hole edge, the location of severe inplane shear moved to the simply supported area near the net-section. That is, even though the value of R_{12} at the net-section hole edge is greater than 1.0 for a single layer, the value at the net-section simple support is greater than 1.0 for many more layers, i.e., 16 layers. The highest values of the interlaminar shear failure parameters are $R_{13} = 0.19$ and $R_{23} = 0.22$ at the

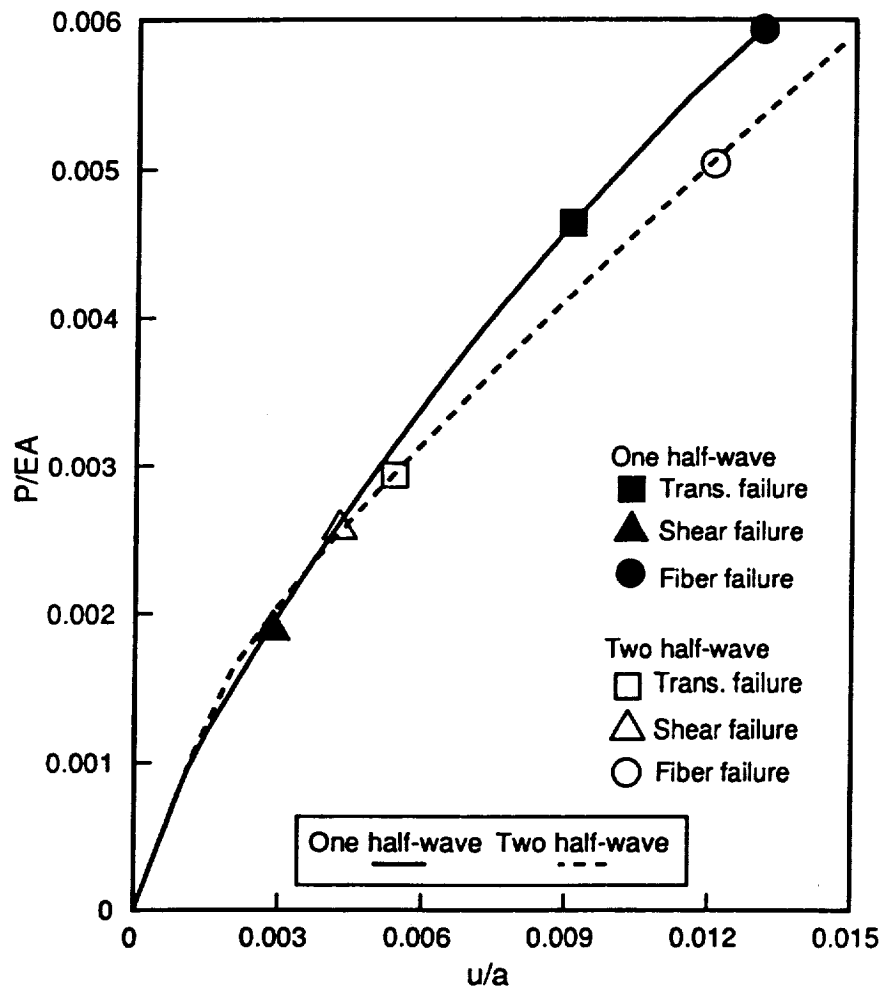
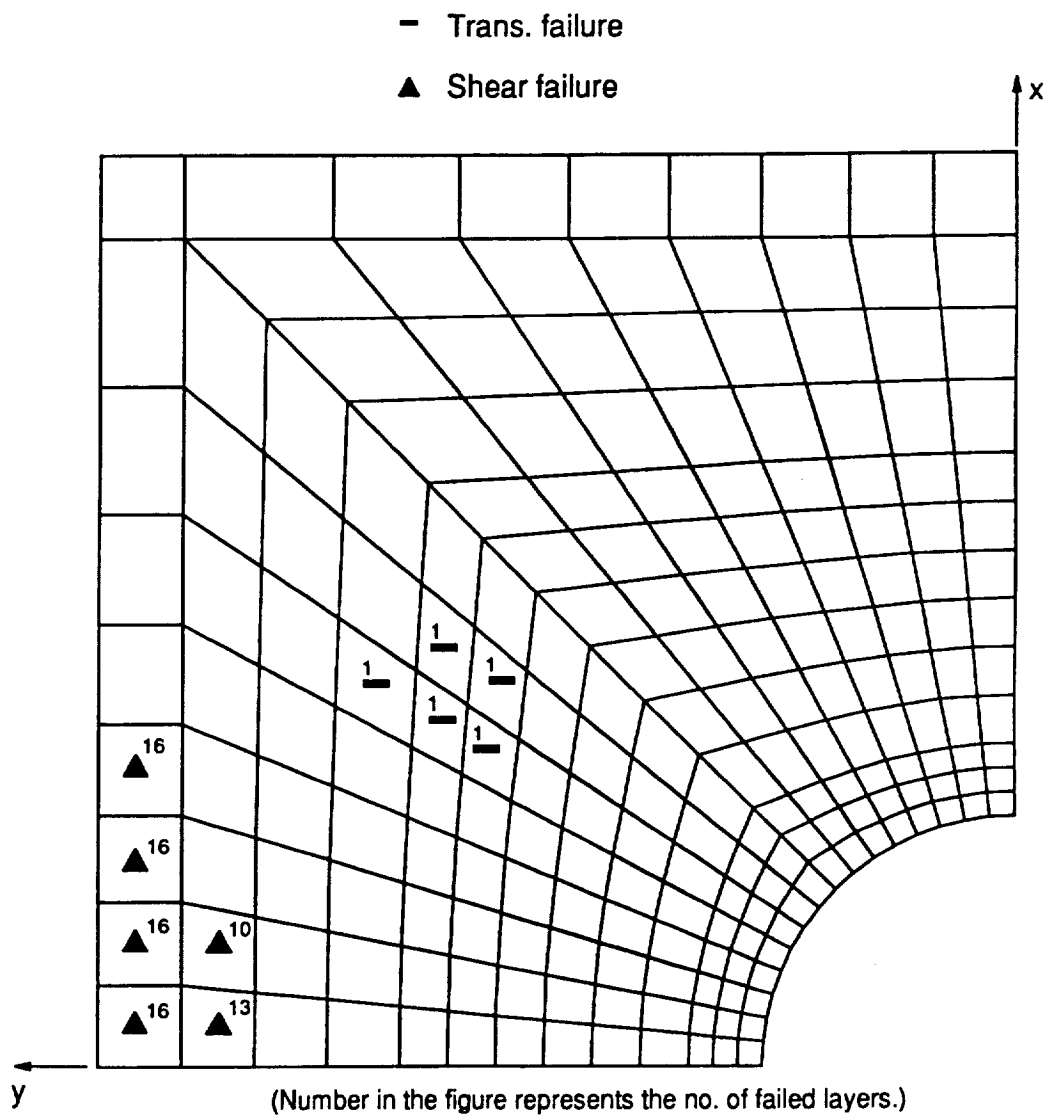


Fig. 5-14 Failures and load-end shortening relations for the $[\pm 45]_{4s}$ plate with a hole.

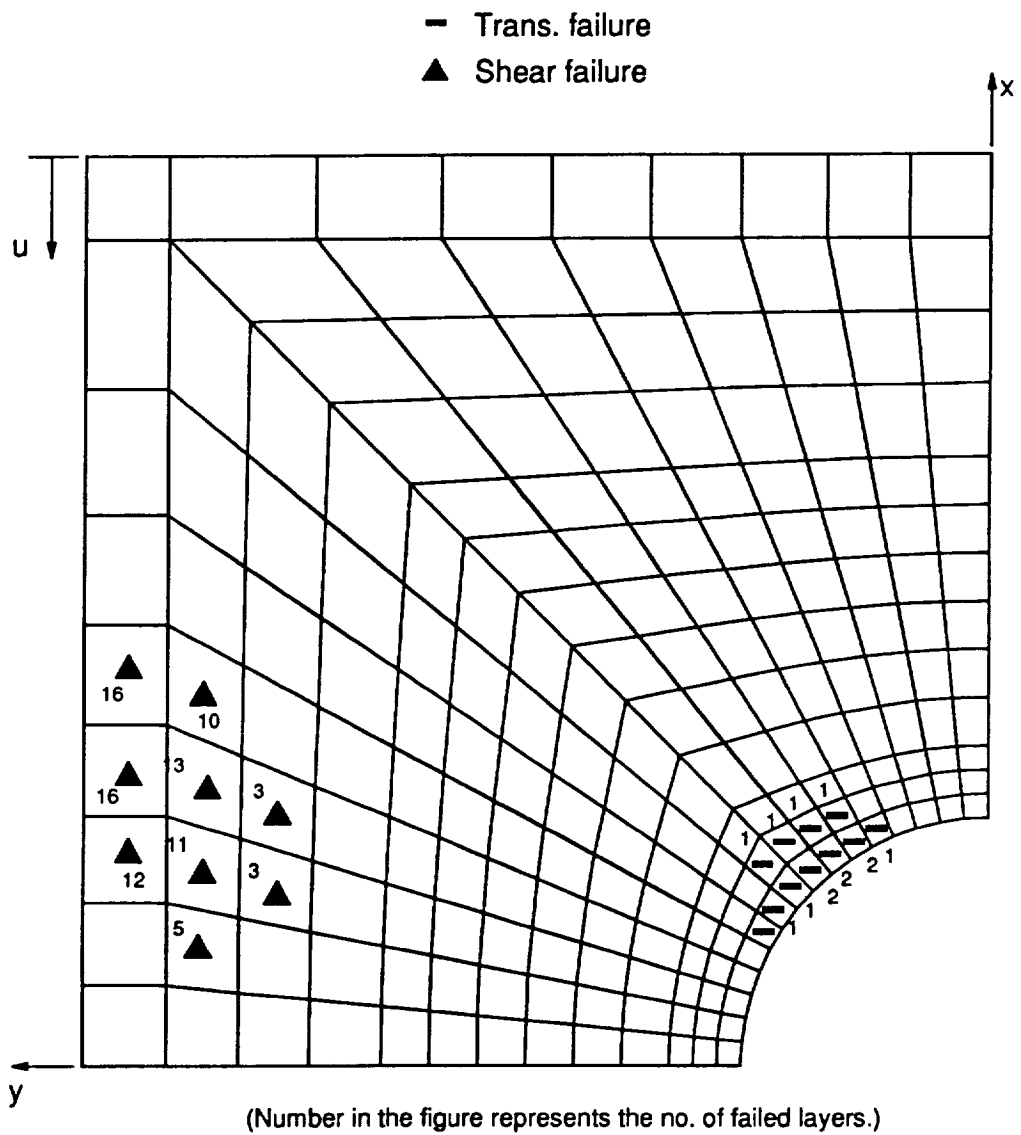


$$\text{Load} : \frac{P}{EA} = 0.00485$$

Fig. 5-15 Predicted failure locations and failure modes of the $[\pm 45]_{4s}$ plate with a hole in the one half-wave configuration.

load level slightly above the first inplane shear failure load. It is expected that failure begins outside the simple support near the net-section and propagates into the plate along the net-section.

Referring to Fig. 5-14 and Table 5-3, as the plate is loaded from zero load, inplane shear failure appears first in the two half-wave configuration for this case also. The first inplane shear failure is predicted to occur at the net-section hole edge, element 158. Compared to the other three plates, that is a slightly different location. The inplane shear failure load in the two half-wave configuration is higher than the inplane shear failure load in the one half-wave configuration. Transverse failure begins at a considerably lower load for the two half-wave configuration than for the one half-wave configuration. It occurs at the hole edge half way between the net-section hole edge and x axis, element 79. Fiber failure occurs near the net-section simple support in element 207. Figure 5-16 shows the damage accumulation at a load level between the transverse failure load and the fiber failure load, i.e., at $P/EA = 0.00394$. It shows severe inplane shear failure along the simple support slightly away from the net-section. Sixteen layers have failed. It also shows transverse failure along the hole edge partway between the net-section and x axis. Because of the large number of layers failed it is expected that inplane shear failure dominates in the two half-wave configuration as it did in the one half-wave configuration, Fig. 5-15. The highest value of the interlaminar shear failure parameters are $R_{13} = 0.35$ and $R_{23} = 0.42$ at the load level of $P/EA = 0.00394$. The final failure is expected to begin at the area outside the simple support slightly away from the net-section, and propagate into the plate toward the net-section and hole edge.



$$\text{Load: } \frac{P}{EA} = 0.00394$$

Fig. 5-16 Predicted failure locations and failure modes of the $[\pm 45]_{4s}$ plate with a hole in the two half-wave configuration.

5.2 Failure of Solid Plates

5.2.1 The Solid $[\pm 45/0/90]_{2S}$ Plate

As an example of the characteristics of the solid plates, the deflected shapes of the solid quasi-isotropic plate for one half-wave and two half-wave configurations are shown in Fig. 5-17 and Fig. 5-18, respectively. The load levels used in the figure are about a factor of 6 and a factor of 4 times the first and the second buckling loads, respectively. Comparing the deflected shape of the one half-wave configuration for the solid plate with the deflected shape of the one half-wave configuration of a plate with a hole, Fig. 5-3, no reverse curvature appears in the solid plate. It is felt that the stiffness at the center of the plate, for the case of no hole, is responsible for preventing this reverse curvature. For the cases of the two half-wave configuration, the plate with a hole, Fig. 5-4, and the plate without a hole are quite similar.

Figure 5-19 shows the load-end shortening relations of the solid $[\pm 45/0/90]_{2S}$ plate. As before, the failure load of each failure mode is marked on the load-end shortening relation for the one half-wave and two half-wave configurations. It can be seen that for both one half-wave and two half-wave configurations all three failure modes occur at almost the same load level of about 6 times the lowest buckling load. Considering that for the plate without a hole all of three failure loads are close each other, the failure process is expected to be sudden and catastrophic. Referring to Table 5-4 and Fig. 5-2, for the one half-wave configuration as the plate is loaded from zero load, the first transverse failure occurs in element 50 in the center of a quarter

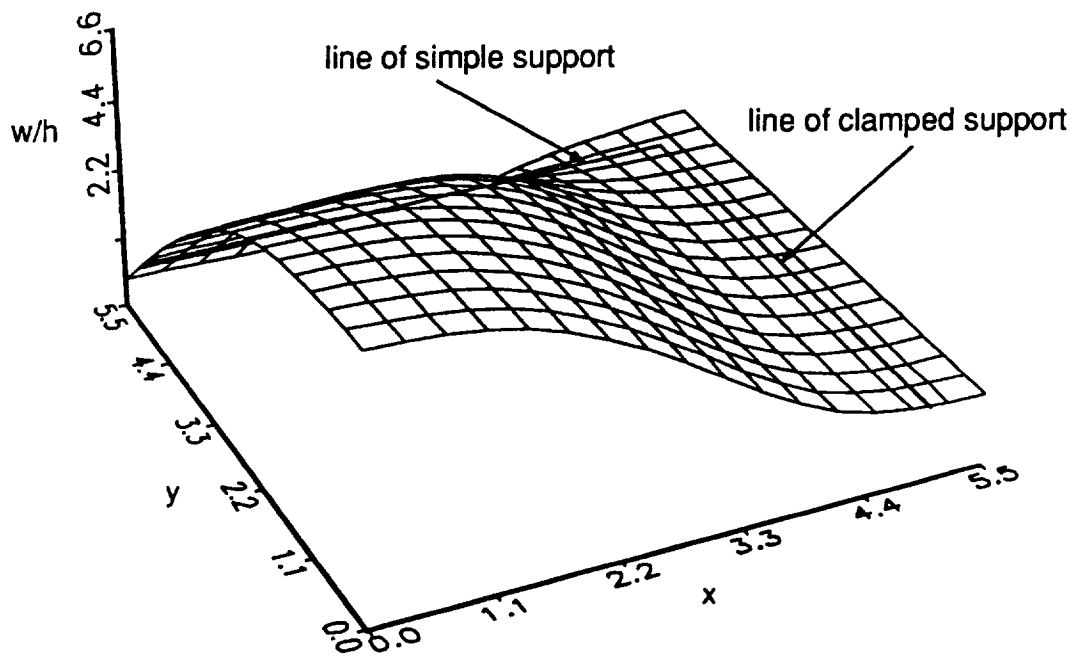


Fig. 5-17 Shape of $[\pm 45/90]_{2s}$ solid plate deflected in the one half-wave configuration at $P/EA = 0.00289$.

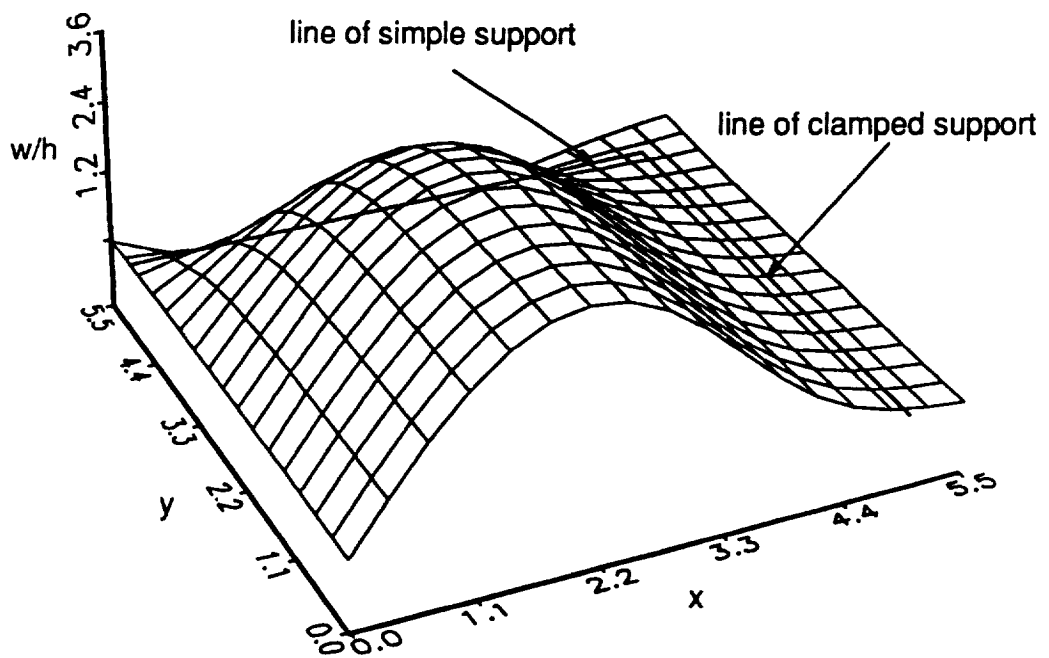


Fig. 5-18 Shape of $[\pm 45/0/90]_{2s}$ solid plate deflected in the two half-wave configuration at $P/EA = 0.00269$.

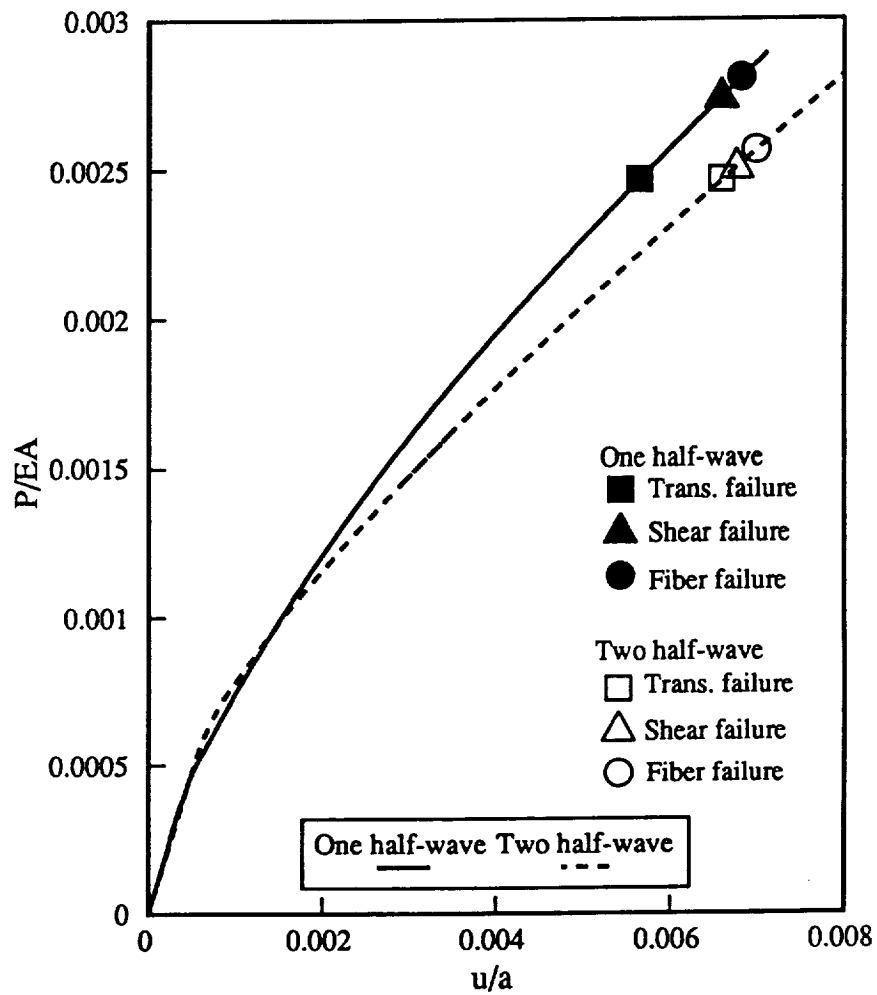
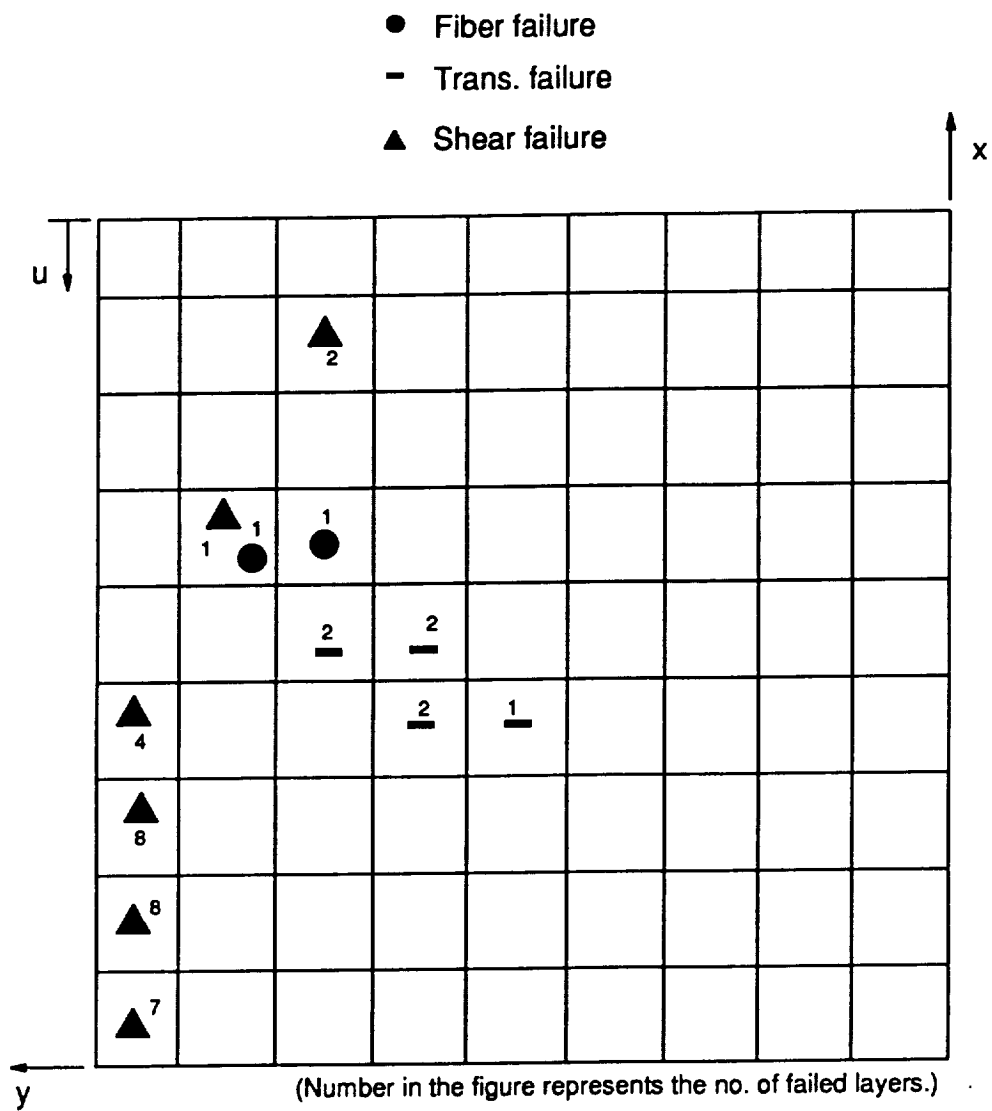


Fig. 5-19 Failures and load-end shortening relations for the solid $[\pm 45/0/90]_{2s}$ plate.

plate. The first inplane shear failure then occurs at the corner of the clamped edge and simple support, element 62. Fiber failure occurs just inside the simple support toward the clamped end, element 69. This is a location where curvatures begin to develop in the x direction. The fiber failure loads for one half-wave and two half-wave configurations are greater than the fiber failure loads of corresponding configurations of the quasi-isotropic plate with a hole. It is interesting to note that the first fiber failure load for a plate without a hole deformed in the two half-wave configuration is the same as the first fiber failure load of the plate with a hole deformed in the one half-wave configuration, namely $P/EA = 0.00256$. The failure locations, however, are different.

Figure 5-20 shows the damage accumulation scenario in the solid plate at a load level slightly above the first fiber failure load. The extension area near the net-section outside the simple support experiences severe inplane shear stress. From the figure it can be seen that half of the layers of the laminate are damaged there. Recalling that the quasi-isotropic plate with a hole shows severe failure at the net-section hole edge and along the net-section, Fig. 5-6, it is expected that for the one half-wave configuration the failure pattern of the solid plate will be different from the failure pattern for the plate with a hole. Regarding interlaminar stress, for the solid plate in the one half-wave configuration the highest values of interlaminar shear failure parameters at the load level of $P/EA = 0.00289$ are $R_{13} = 0.33$ and $R_{23} = 0.37$. These values show that the interlaminar shear stresses are low in the solid plate which is deformed in the one half-wave configuration.

For the two half-wave configuration failure first occurs as transverse failure at roughly the center of the quarter plate, specifically in element 48. Inplane shear fail-



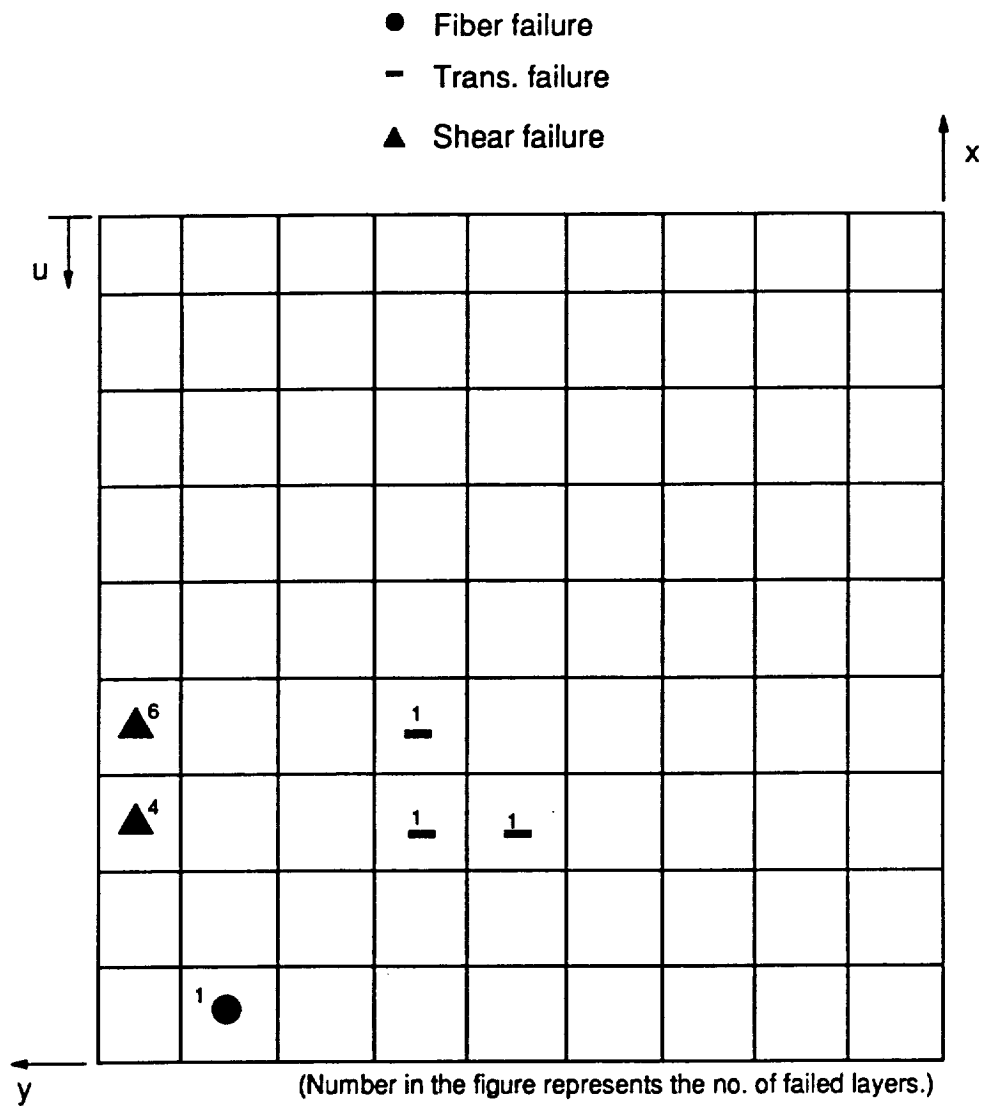
$$\text{Load} : \frac{P}{EA} = 0.00289$$

Fig. 5-20 Predicted failure locations and failure modes of the solid $[\pm 45/0/90]_{2s}$ plate in the one half-wave configuration.

ure then follows in the element 76, outside the simple support and slightly away from the net-section. Fiber failure then occurs at the net-section just inside the simple support. As shown in the damage scenario in Fig. 5-21, the extension area outside the simple support slightly away from the net-section experiences inplane shear stress. The location of the first fiber failure in this solid plate in the two half-wave configuration is the same location as first fiber failure of plate with a hole in the two half-wave configuration, namely at the simple support "net-section", net-section being in quotes since it does not really apply to the plate without a hole. For both the one half-wave and two half-wave configurations of the solid plate it is expected that the final failure will occur in the extension area due to severe inplane shear. The center of the plate remains intact for both the one half-wave and two half-wave configurations. The interlaminar shear stresses are low for the two half-wave configuration. The highest values of R_{13} and R_{23} are 0.29 and 0.34 at the load level slightly above the first fiber failure load, respectively.

5.2.2 The Solid $[\pm 45/0_2]_{2S}$ Plate

In Fig. 5-22 the load-end shortening relations for the solid $[\pm 45/0_2]_{2S}$ plate for both one half-wave and two half-wave configurations are shown. For both the one half-wave and the two half-wave configurations failure occurs in the sequence of transverse failure, inplane shear failure, and then fiber failure. Between the two configurations the failure loads of each failure mode are about the same. However, for the one half-wave configuration failure loads are slightly higher. In general, trans-



$$\text{Load} : \frac{P}{EA} = 0.00269$$

Fig. 5-21 Predicted failure locations and failure modes of the solid $[\pm 45/0/90]_{2s}$ plate in the two half-wave configuration.

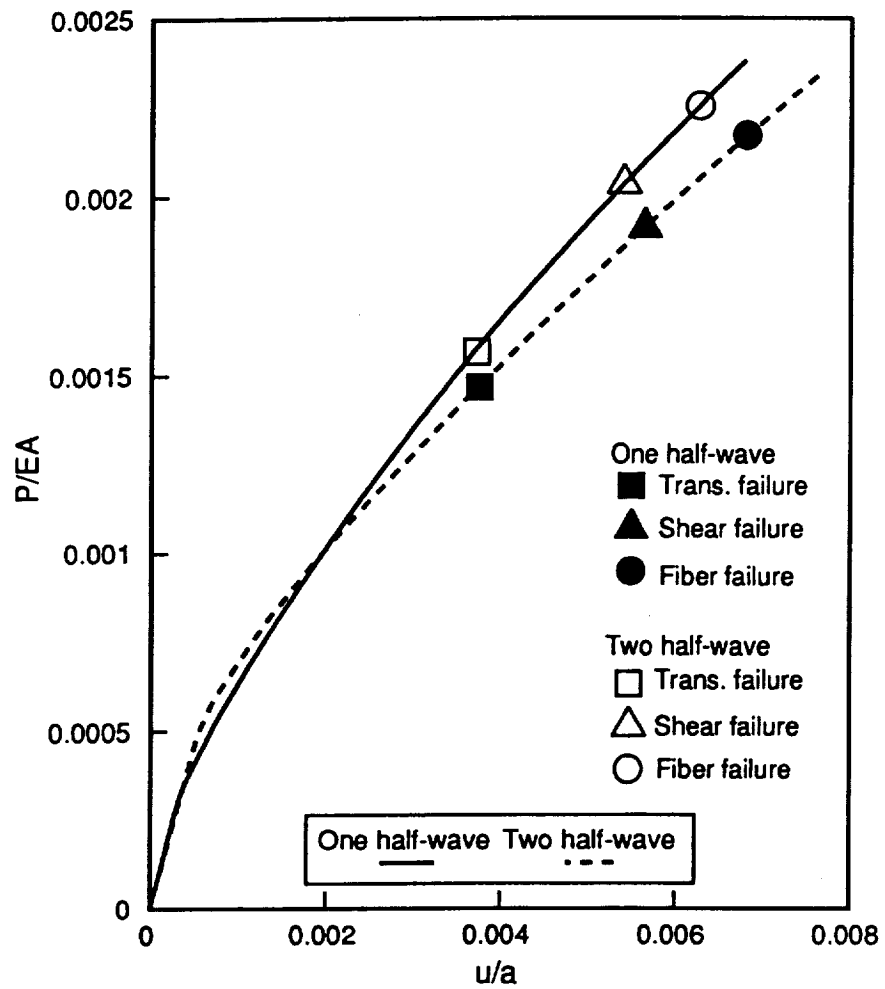
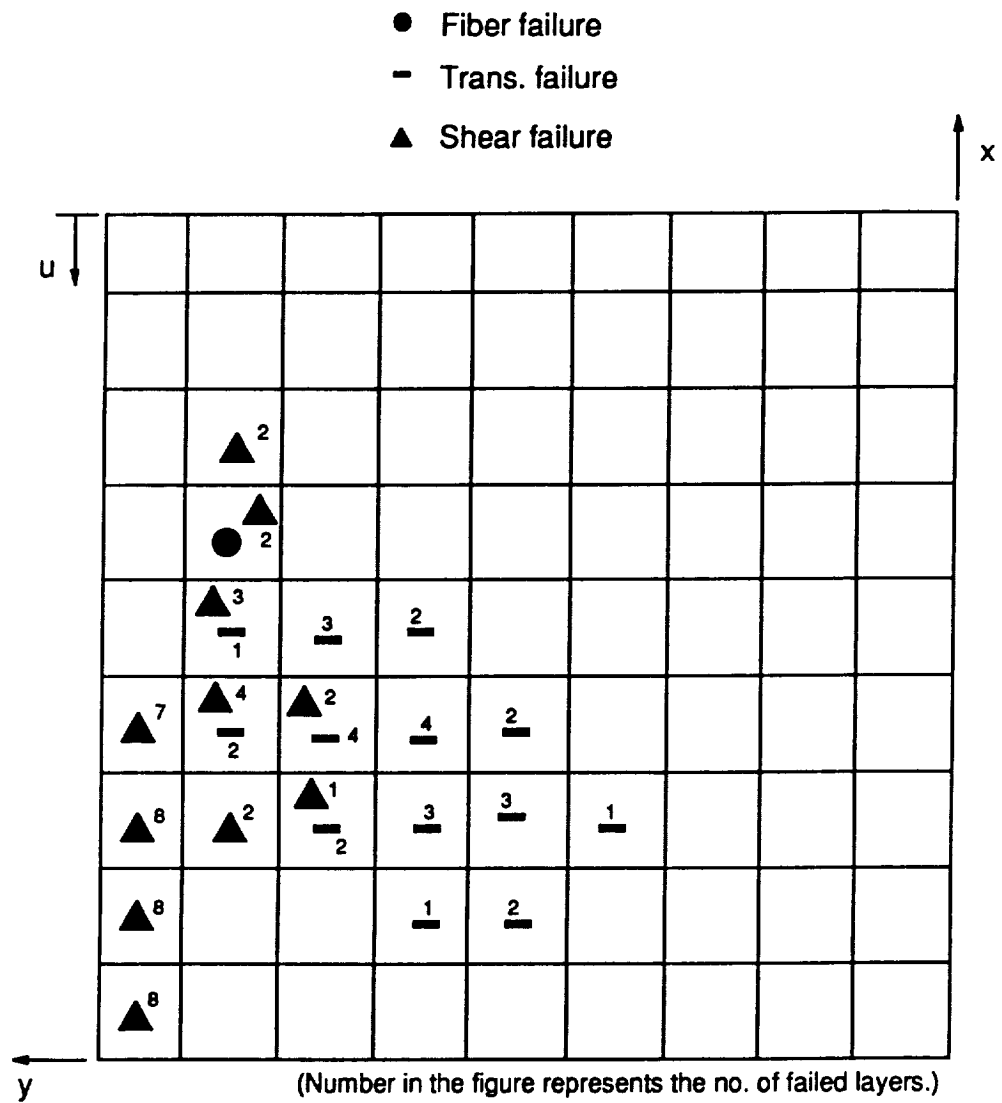


Fig. 5-22 Failures and load-end shortening relations for the solid $[\pm 45/0_2]_{2s}$ plate.

verse failure occurs at about 4 times the buckling load, inplane shear failure occurs at about 6 times the buckling load, and fiber failure occurs at about 6 times the buckling load.

For the one half-wave configuration transverse failure first occurs in element 48, near the center of the quarter-plate planform. First shear failure occurs at the net-section outside the simple support, element 73. First fiber failure occurs near the clamped edge but along the simple support, element 69. First fiber failure occurs at the same location as the solid quasi-isotropic plate in the one half-wave configuration. Figure 5-23, the damage accumulation scenario, shows that the solid $[\pm 45/0_2]_{2s}$ plate in the one half-wave configuration experiences inplane shear failure in the extension area near the net-section at the load level slightly greater than the first fiber failure load. Inside the simple support rather widespread inplane shear failure appears but it is less severe than that in the extension area near the net-section, i.e., less layers are failed. Transverse failure is widespread in the center of the quarter plate. The interlaminar shear failure parameters at the load level of $P/EA = 0.00229$, slightly above the first fiber failure load, are $R_{13} = 0.39$ and $R_{23} = 0.37$.

For the two half-wave configuration first fiber failure occurs at the same location as with the quasi-isotropic solid plate deformed in two half-waves, i.e., in element 64, just inside the simple support on the net-section. This first fiber failure follows transverse failure in element 58 and inplane shear failure in element 76, the latter location being outside the simple support. Figure 5-24 shows that at a load level slightly above the first fiber failure the area on both sides of the simple support and slightly away from the net-section has significant damage accumulation due to inplane shear failure. The interlaminar shear failure parameters at the load level



$$\text{Load} : \frac{P}{EA} = 0.00229$$

Fig. 5-23 Predicted failure locations and failure modes of the solid $[\pm 45/0_2]_{2s}$ plate in the one half-wave configuration.

$P/EA = 0.0023$, slightly above the first fiber failure load, are $R_{13} = 0.30$ and $R_{23} = 0.32$. From Fig. 5-24 it can be deduced that the final failure of this plate in two half-waves will occur slightly away from the net-section and along the simple support.

5.2.3 The Solid $[\pm 45/0_6]_S$ Plate

The load-end shortening relations for the $[\pm 45/0_6]_S$ plate are shown in Fig. 5-25. The failure load for each mode is very close to being the same for both the one half-wave and two half-wave configurations. In general, transverse failure occurs at about 4 times the buckling load and inplane shear failure and fiber failure occur at about 6 times the buckling load for both configurations. For the one half-wave configuration transverse failure first occurs at the net-section away from the simple support, in element 46. Inplane shear failure occurs along the simple support in element 68, between the net-section and the clamped edge. First fiber failure also occurs at exactly the same location. This is obviously a location of severe stress. Figure 5-26 shows the damage accumulation at a load just above the first fiber failure load in the one half-wave configuration. It shows that the transverse failure has developed near the net-section. The inplane shear failure and fiber failure continue to develop in the same location where the first failure for each mode is predicted. The interlaminar shear failure parameters at just above the fiber failure load are $R_{13} = 0.35$ and $R_{23} = 0.26$.

For the two half-wave configuration transverse failure first occurs toward the center of the quarter plate, in element 58. Inplane shear failure first occurs along the

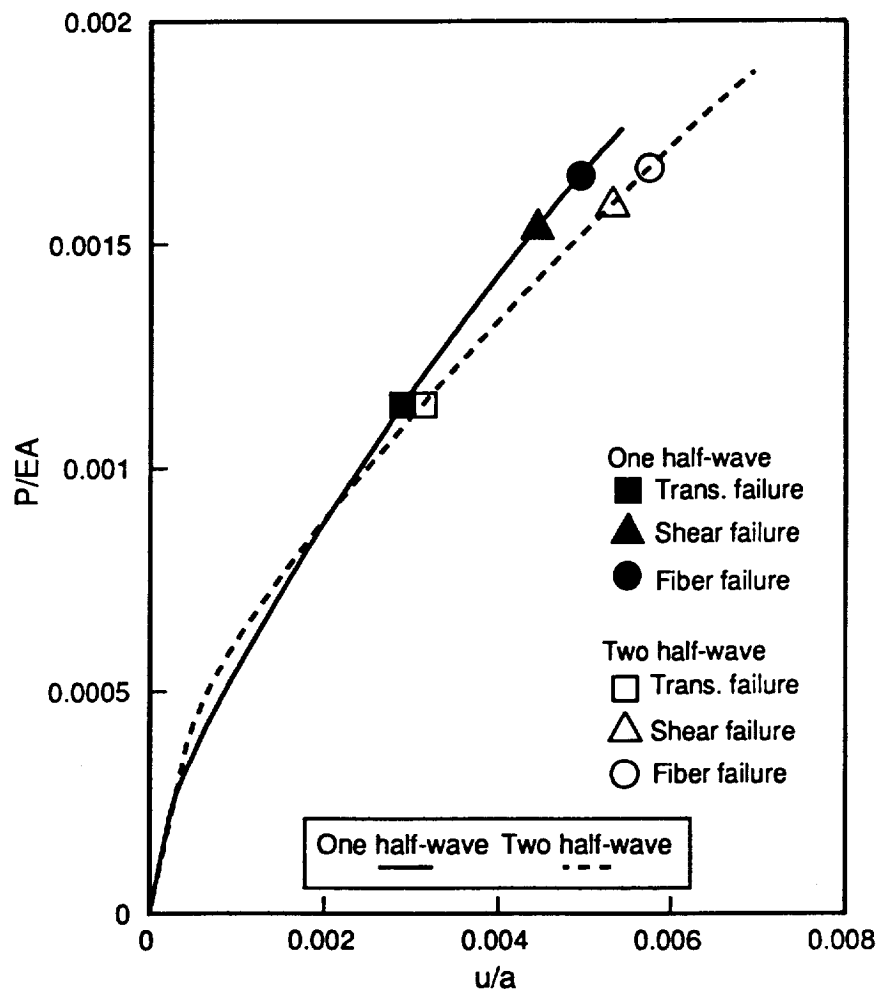
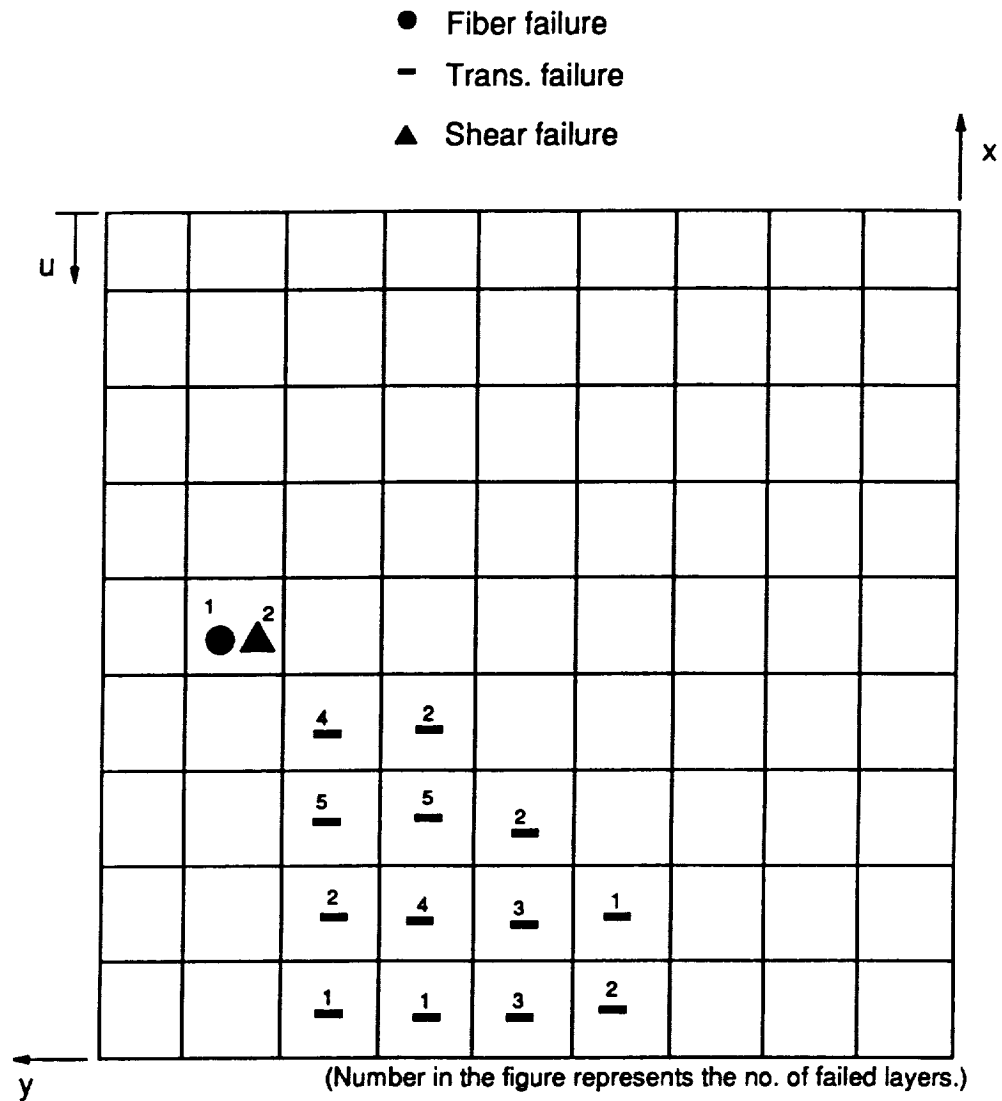


Fig. 5-25 Failures and load-end shortening relations for the solid $[\pm 45/0]_s$ plate.



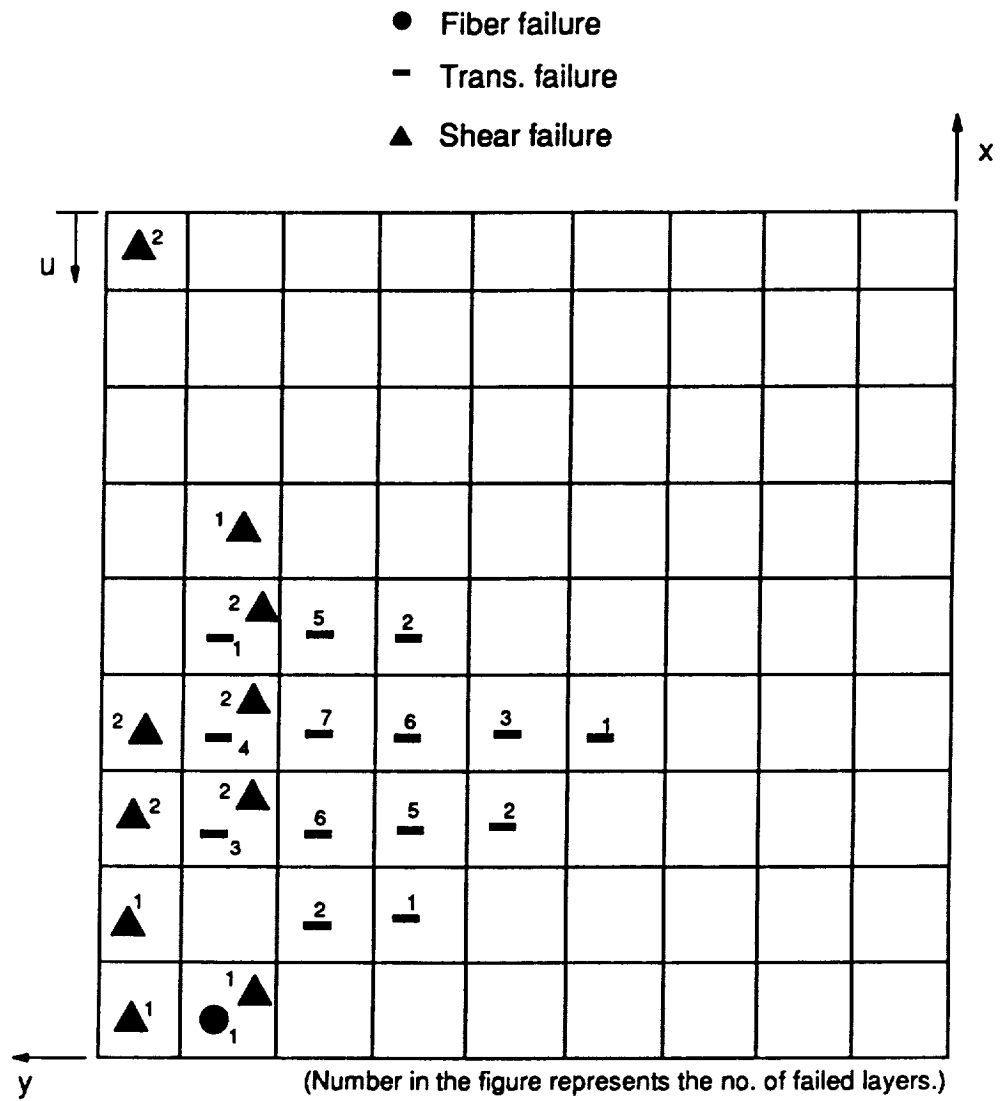
$$\text{Load} : \frac{P}{EA} = 0.00169$$

Fig. 5-26 Predicted failure locations and failure modes of the solid $[\pm 45/0_s]_s$ plate in the one half-wave configuration.

simple support half-way between the net-section and the clamped edge, element 67. First fiber failure occurs at the net-section near the simple support, element 64. Damage accumulation for the two half-wave configuration is shown in Fig. 5-27. It shows that at a load slightly greater than the first fiber failure load the transverse failure occurs from the center of the quarter-plate to the simply-supported edge. Where there is transverse failure, about a quarter of the layers are failed. Figure 5-27 shows that inplane shear failure also develops along the simple support in the two half-wave configuration. It is expected that the final failure will occur along the simple support for $[\pm 45/0_8]_s$ solid plate in the two half-wave configuration. The failure could begin at the net-section. The interlaminar shear failure parameters at the load level above the first fiber failure load are $R_{13} = 0.49$ and $R_{23} = 0.29$. It should be noted that the solid $[\pm 45/0_8]_s$ plate, in either configuration, is the strongest plate studied so far.

5.2.4 The Solid $[\pm 45]_{4s}$ Plate

Figure 5-28 shows the load-end shortening relations for the solid $[\pm 45]_{4s}$ plate for both the one half-wave and two half-wave configurations. For a given failure mode the failure load is practically independent of the deformed configuration. The inplane shear failure occurs at about 2.5 times the buckling load, transverse failure occurs at about 4 times the buckling load, and fiber failure occurs at about 5 times the buckling load. For the one half-wave configuration, as the load is increased, inplane shear failure first occurs outside the simple support on the net-section, element 73. With increasing load transverse failure occurs near the center of the quarter plate, in element 50. First fiber failure occurs closer to the clamped support and just away



$$\text{Load} : \frac{P}{EA} = 0.00177$$

Fig. 5-27 Predicted failure locations and failure modes of the solid $[\pm 45/0]_s$ plate in the two half-wave configuration.

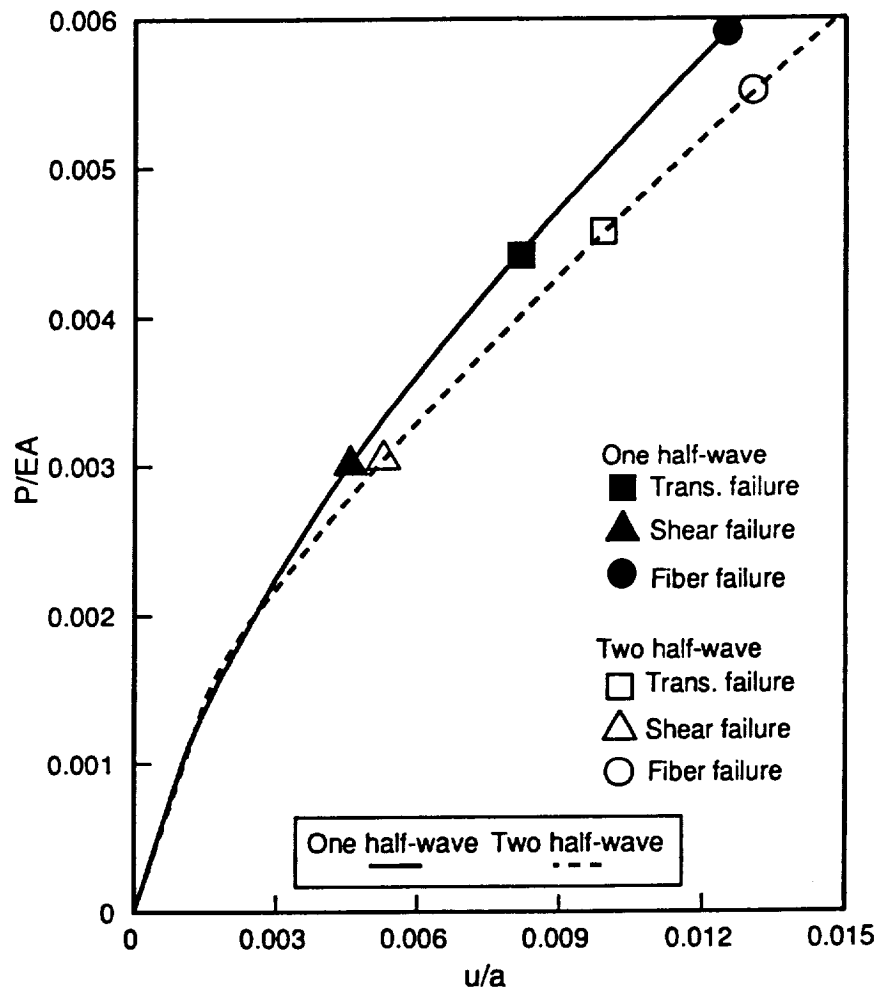
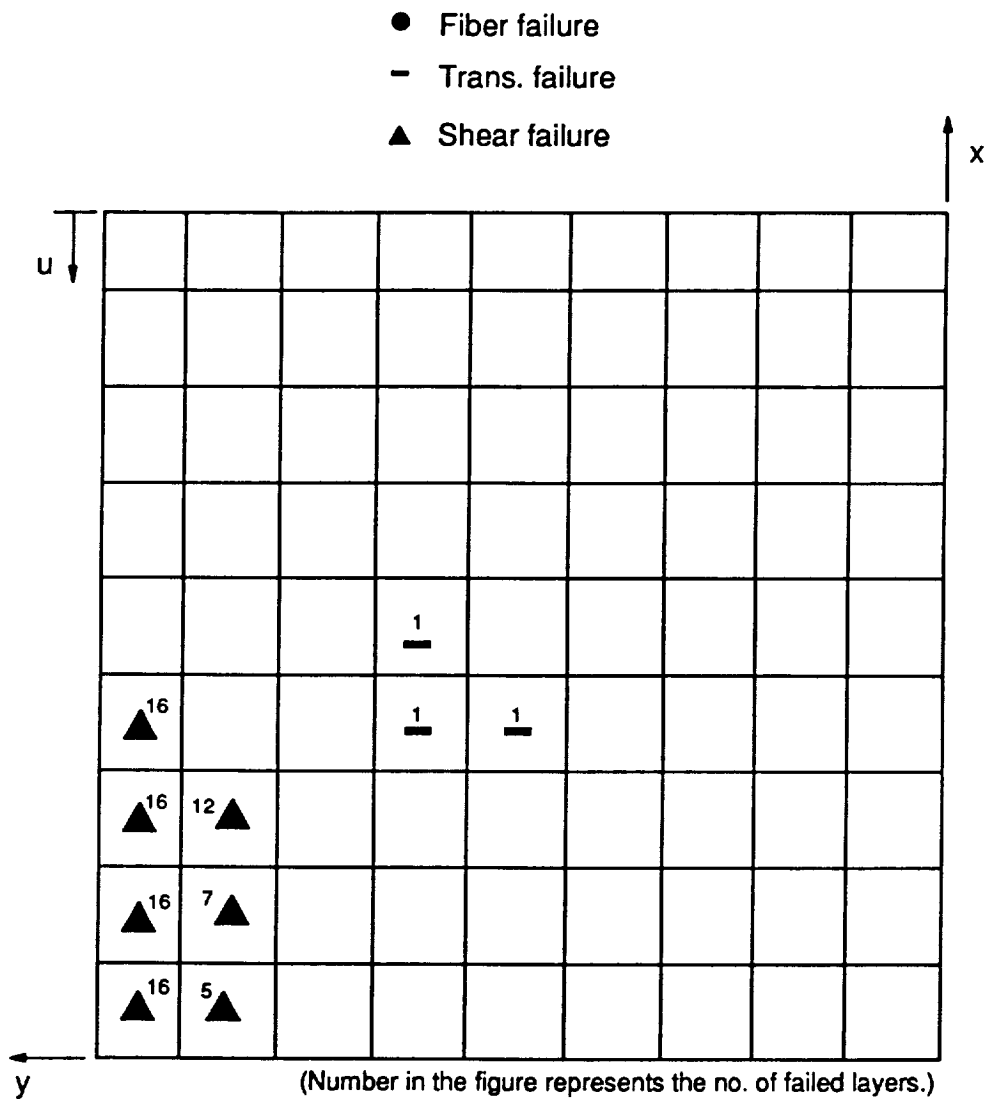


Fig. 5-28 Failures and load-end shortening relations for the solid $[\pm 45]_{4s}$ plate.

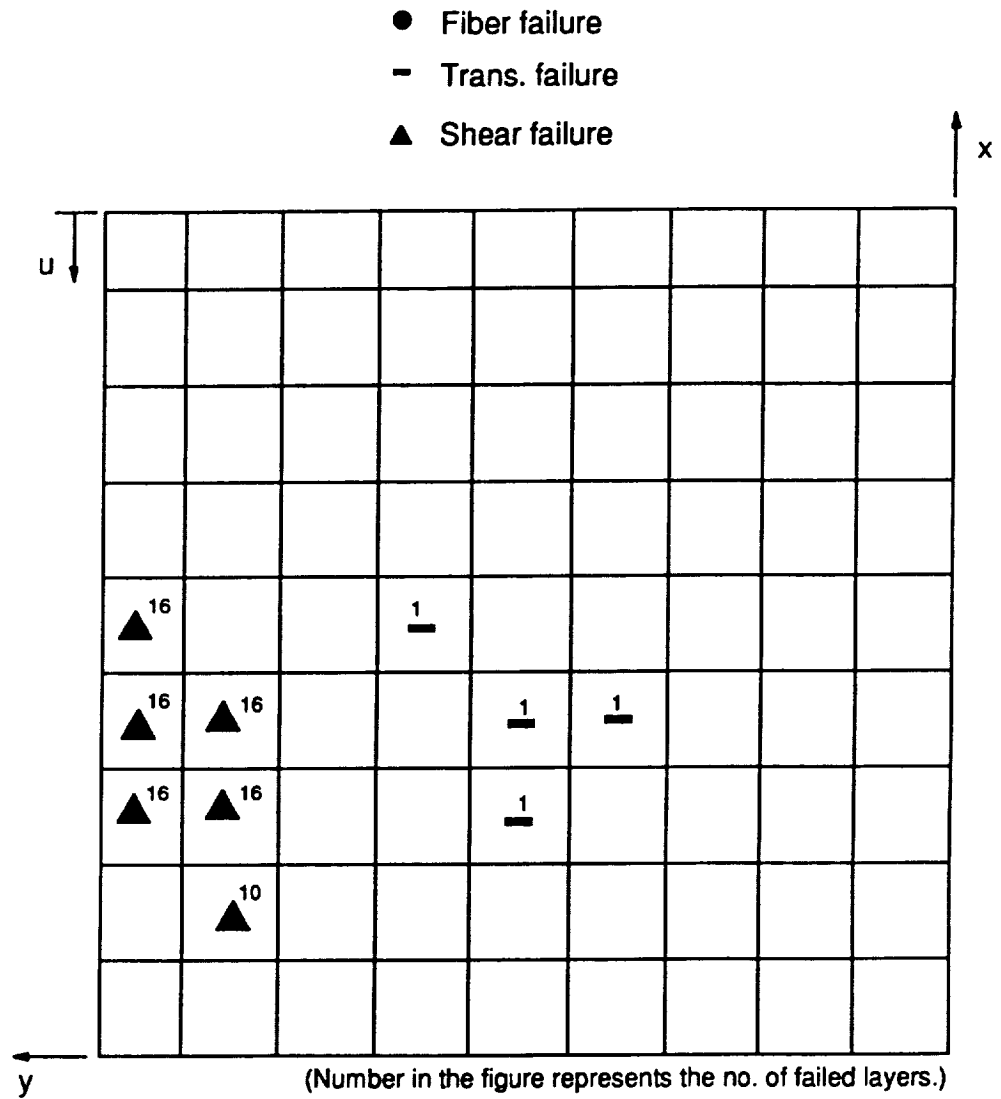
from the simple support, in element 60. This location of first fiber failure being nearer the clamped support than with the other three solid plates is quite similar to the case of the $[\pm 45]_{4s}$ plate with a hole. The $[\pm 45]_{4s}$ plate with a hole experienced fiber failure nearer the clamped end than any other plate with a hole. Like the plate with a hole, it is expected that inplane shear failure will dominate the failure in this solid plate. This is supported by Fig. 5-29. Figure 5-29 shows the damage accumulation scenario at a load just above the first transverse failure load in the one half-wave configuration. It can be seen that the simply supported area near the net-section is severely damaged by inplane shear failure, all 16 layers having failed. Concentrated inplane shear failure can be observed outside the simple support and just inside the simple support.

For the two half-wave configuration the situation is similar. Figure 5-30 shows the damage accumulation in the two half-wave configuration at slightly above the first transverse failure load. Transverse failure is minor. However, significant inplane shear failure is predicted near the simple support near the net-section. It can be seen that all of 16 layers are failed in the area outside the simple support and just inside the simple support. Comparing with the one half-wave configuration, the location of inplane shear failure is moved slightly away from the net-section. The interlaminar shear failure parameters are very small. For the one half-wave configuration the highest values of R_{13} and R_{23} are 0.17 and 0.20, respectively, at the load level slightly above the first transverse failure load. For the two half-wave configuration R_{13} is 0.18, and R_{23} is 0.22.



$$\text{Load} : \frac{P}{EA} = 0.00469$$

Fig. 5-29 Predicted failure locations and failure modes of the solid $[\pm 45]_{4s}$ plate in the one half-wave configuration.



$$\text{Load} : \frac{P}{EA} = 0.00479$$

Fig. 5-30 Predicted failure locations and failure modes of the solid $[\pm 45]_{4S}$ plate in the two half-wave configuration.

5.3 Summary

One of the most important conclusions from the analysis of failure in this chapter is that it appears as though the failure load may be independent of whether the plate deforms in the one half-wave configuration or the two half-wave configuration. An examination of the results presented shows this to be the case.

In this chapter no interlaminar shear failure is predicted for either the one half-wave or two half-wave configuration in any plate. Bringing forward the results from Ch. 4 and the results from this chapter, another important conclusion can be made. In Fig. 4-12 it was shown that the interlaminar stress component τ_{xz} was much larger at the net-section hole edge than at the net-section simple support region. This figure was for the case of the two half-wave configuration and the quasi-isotropic laminate but the findings are general. As a result, it can be concluded that if the plate is deformed in the two half-wave configuration and if failure is due to a high interlaminar shear stress component τ_{xz} , failure will begin at the hole edge, not elsewhere. This conclusion should be useful when observing the location of failure in the experiments. It is tempting to say that if failure begins at any location other than the hole edge, interlaminar failure due to τ_{xz} is not involved. However, the plate could fail at the hole edge due to the other mechanisms, e.g., fiber failure when the plate is deformed in the one half-wave configuration as predicted in this chapter (see Table 5-2 and Fig. 5-6).

Finally, the failure load of the $[\pm 45/0_6]_s$ plate is expected to be the highest, the failure load of the $[\pm 45/0_2]_{2s}$ plate next, and the failure load of the $[\pm 45/0/90]_{2s}$ plate

next. The failure load of the $[\pm 45]_{4s}$ plate is expected to be the lowest. This ordering of failure loads is true for both solid plates and plates with holes. Only the $[\pm 45/0/90]_{2s}$ plate with hole deforming in the one half-wave configuration is expected to fail at the net-section hole edge. For the other plates failure is predicted to occur near the simple support. The postbuckling failure loads of solid plates are expected to be higher than the postbuckling failure loads of the plates with holes with $D/W = 0.3$.

Attention now shifts to the experimental aspects of this study. Correlation of the predictions of this and past chapters with experimental observations and measurements is critical to providing credibility for the findings.

6.0 Description of Experiment

6.1 *Test Fixture*

Considerable effort has been put into developing a fixture to load composite plates in the manner discussed in the preceding chapters. The boundary conditions and other conditions used in the analysis, and described in Fig. 1-1, were actually idealizations of the conditions that could be most conveniently built into an experimental set-up. It is more difficult to enforce a specified stress resultant distribution on the loaded edge than to enforce a specified displacement distribution. Hence the uniformly displaced edge is used. In addition, it is easier to clamp this displaced edge than to allow it to be simply supported. Similarly, as has been mentioned, it is impossible to not have the plate width exceed the supported width. The extra width outside the supports is necessary to accommodate the plate width decrease when the plate buckles. As has been shown, the extra width must be included in the analysis. The extensions of the plate outside the supports provide extra stiffness and are a site of high inplane stresses.

The detail drawings of the fixture are shown from Fig. 6-1 to Fig. 6-9, and a photograph of the fixture in the displacement-controlled Tinius-Olsen load frame is shown in Fig. 6-10. When placed in the fixture the two opposite simply-supported edges of the composite plate specimen are vertical, the displaced clamped edge is at the top, and the stationary clamped edge is at the bottom.

The fully assembled fixture with the composite plate specimen is depicted in Fig. 6-1. The fixture consists of a top assembly, a bottom assembly, a stiffback steel bar, and a steel ball. The majorities of both the top and bottom assemblies are made of aluminum and the top assembly moves vertically relative to the bottom assembly through the four linear bearings.

The top assembly, shown in Fig. 6-2, includes a top plate, four hardened linear bearing shafts, of steel, for alignment of the top assembly with the bottom assembly, and the supports for clamping the top edge of the composite plate specimen. The steel shafts are 0.75 in. in diameter. Other dimensions are shown on the figure.

The bottom assembly, illustrated in Fig. 6-3, consists of a bottom frame (which consists of a bottom plate, side gussets, and side plates) four linear bearings, four knife edges to effect the vertical simply supported edges, brackets for holding the two linear variable differential transducers (LVDT's), and clamped supports for the bottom edge of the composite plate specimen. More details of the bottom assembly are shown in Fig. 6-4, an illustration of the bottom frame.

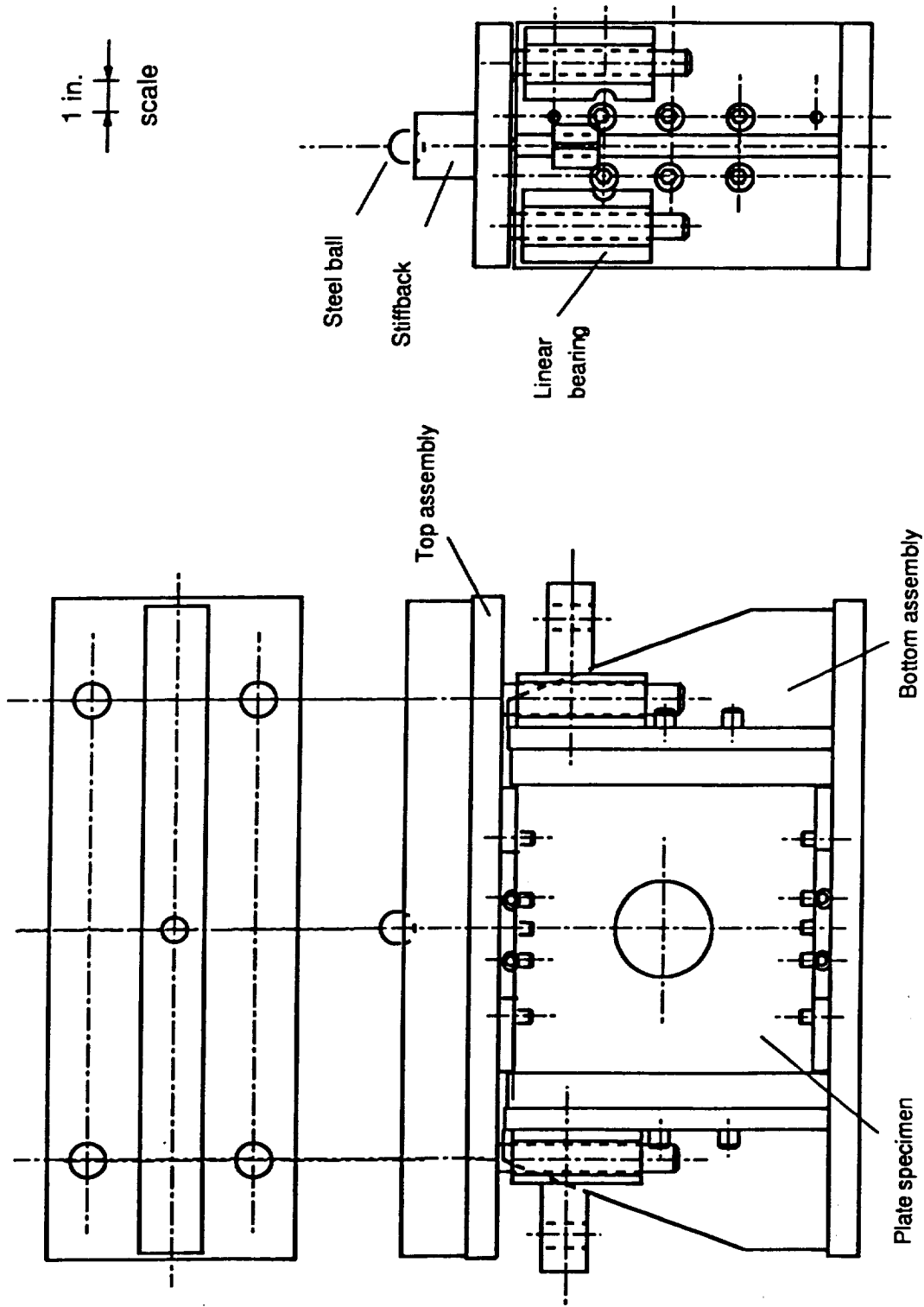
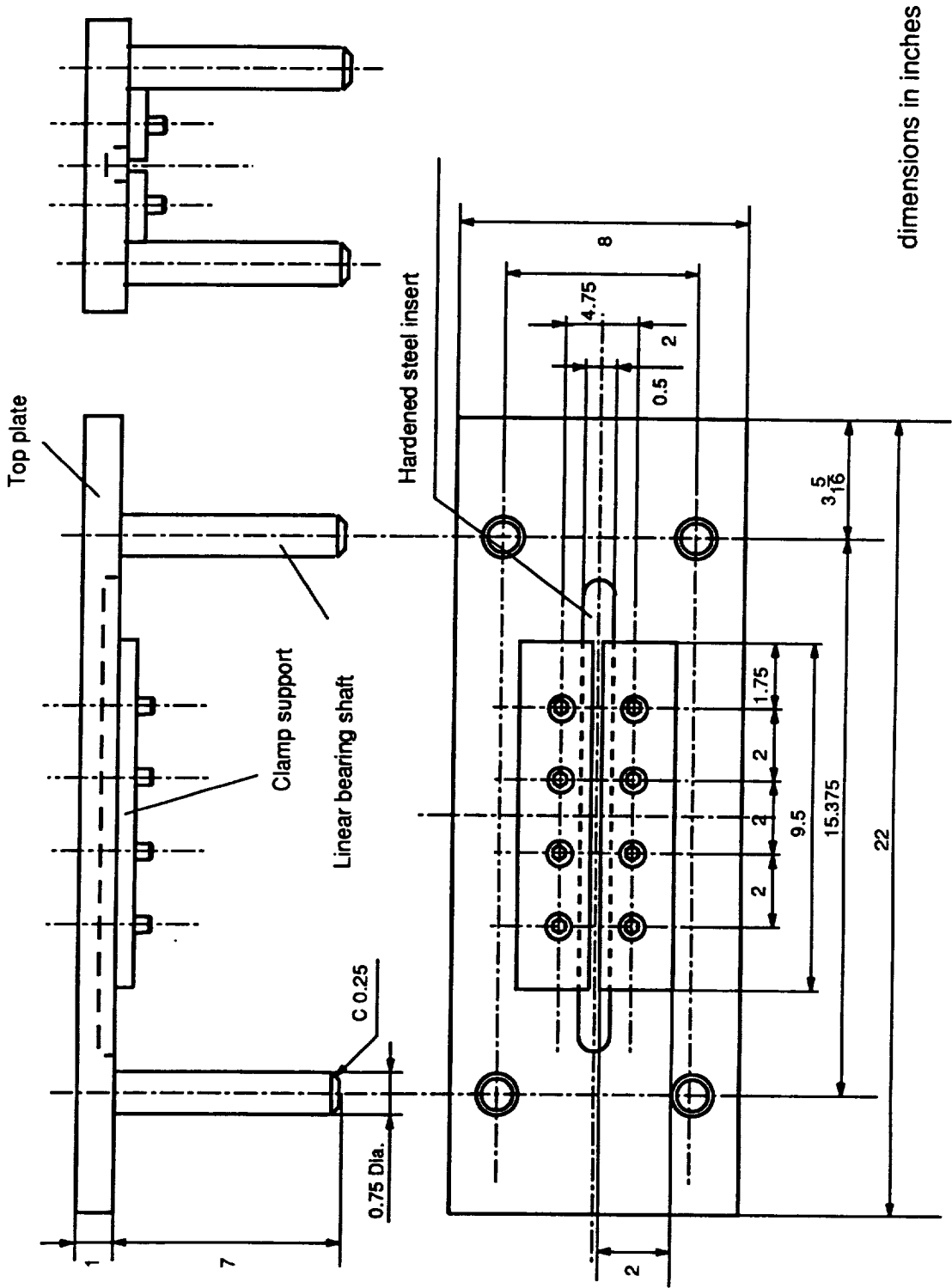


Fig. 6-1 Full assembly of the fixture with plate specimen.



dimensions in inches

Fig. 6-2 Top assembly of the fixture.

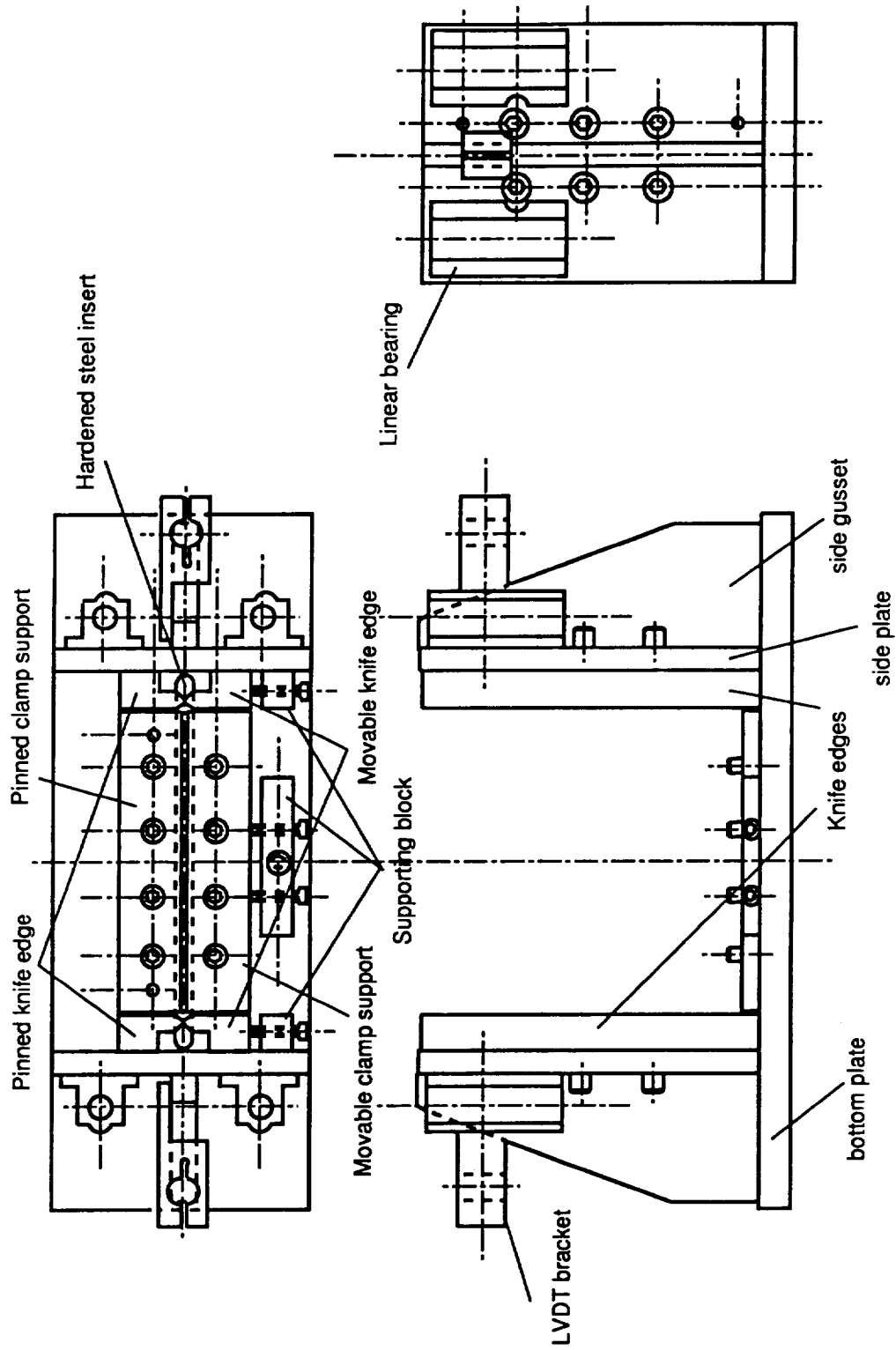


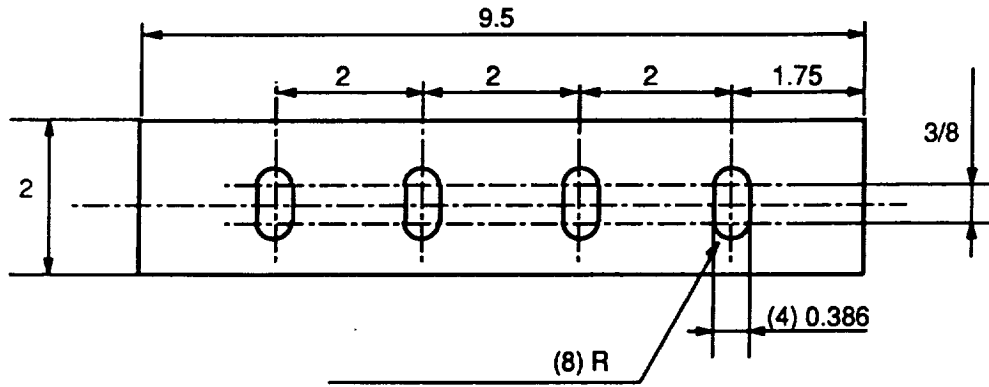
Fig. 6-3 Bottom assembly of the fixture.

Included in the top and bottom assembly are machined hardened steel inserts. The hardened steel inserts are actually what the top and bottom machined edges of the composite plate specimen bear against in the top and bottom assemblies. These inserts are flat to within close tolerances (less than 0.0005 in.) so as uniform as possible edge displacements are imposed on the top and bottom edges of the composite plate specimen, the bottom edge displacement, of course, being zero. In addition to maintaining flatness, the hardened inserts prevent the sharp edges of the composite plates from deforming the softer aluminum at high load levels.

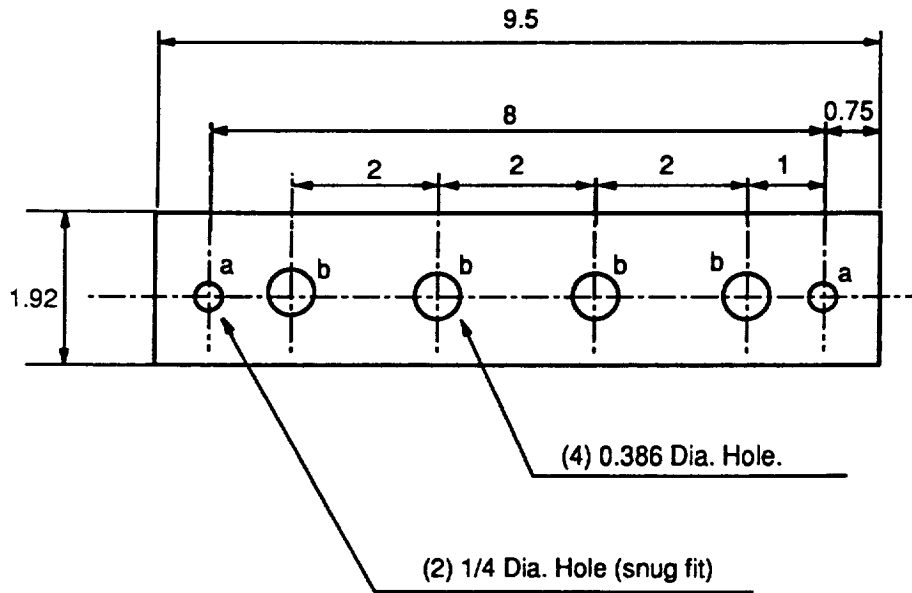
With the bottom assembly, though not shown in detail, but illustrated to some degree in Fig. 6-5, one of the clamped supports is afixed to the bottom plate with pins and Allen bolts. The other clamped support contained slotted holes so it can move in a horizontal plane on the bottom plate. This sliding clamp support is forced against the composite plate, which is, in turn, forced against the fixed clamp support. The sliding clamp support is forced against the composite plate by screws which is threaded into a supporting block attached to the bottom plate. The supporting block is shown in Fig. 6-6. In essence, the sliding clamp support squeezes the composite plate, in the thickness direction, against the fixed clamp support to enforce the clamped boundary condition. Once the plate is sufficiently "squeezed", both clamp supports are secured to the bottom plate with Allen bolts.

Referring to Fig. 6-3, knife-edges are fastened to the side plates, the side plates also serving to hold the linear bearings that guide the hardened steel shafts from the top assembly. Though the horizontal forces, either left-right or fore-aft, are expected to be small, the side plates are reinforced with side gussets. Brackets for the LVDT's are fastened to the side gussets. The scheme for forcing the composite plate against

dimensions in inches



(a) Sliding clamped support.



(b) stationary clamped support.

Fig. 6-5 Clamped supports.

dimensions in inches

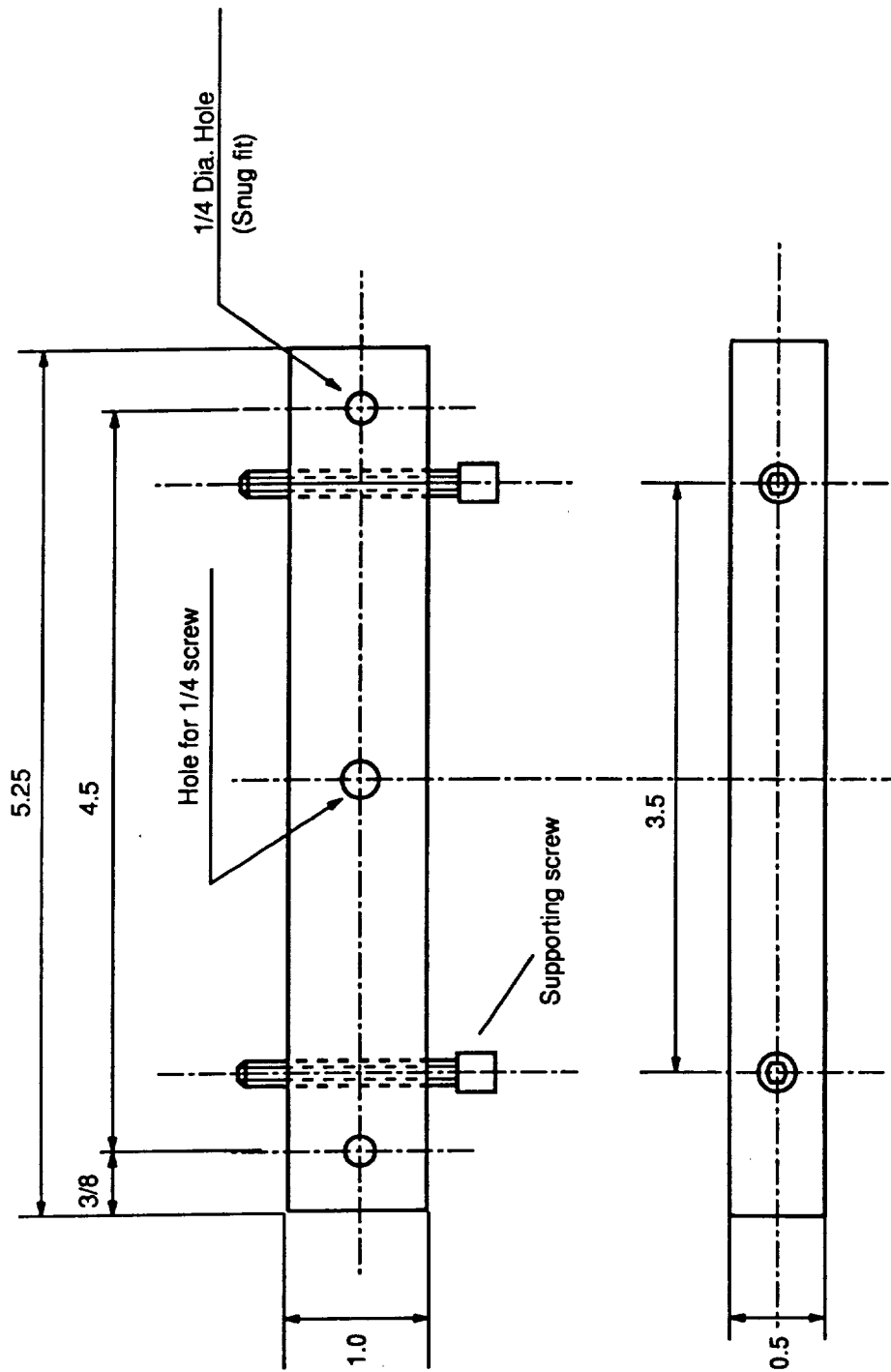


Fig. 6-6 Supporting block for clamped supports.

the vertical knife-edges is similar to the scheme for clamping it on the bottom edge. A schematic of a knife-edge is shown in Fig. 6-7. On both the left and right sides of the composite plate one knife-edge is fixed in place while the other is movable and can slide against the composite plate, in the thickness direction. The sliding knife edge is forced against the plate by another supporting block and Allen screw assembly, this supporting block component being shown in Fig. 6-8.

The fixture is designed so the bottom fixed clamp support and the two fixed knife edge supports form a boundaries in a plane against which the composite plate is forced. That the plate is forced against three boundaries all lying in a plane minimizes eccentricities or misalignments of the plate with respect to the loading.

The clamp supports on the top edge, supports that are part of the top assembly, are both sliding, much like the one bottom clamp support. One sliding support is positioned, by hand, against the composite plate which is already forced against the three other planar boundaries. This sliding support is secured with Allen screws. The other sliding boundary is forced against the composite plate, as at the bottom edge, by a screw which is threaded into the supporting block attached to the top plate.

The LVDT bracket, shown in Fig. 6-9, clamps the round barrel of the LVDT and prevents motion of the LVDT relative to the bottom assembly. The clamping action is such that the LVDT can easily be moved vertically to balance the LVDT voltage output. The LVDT's are a vital part of the experiment. The average of the left and right LVDT's is used as a measure of the displacement of the loaded edge of the

dimensions in inches

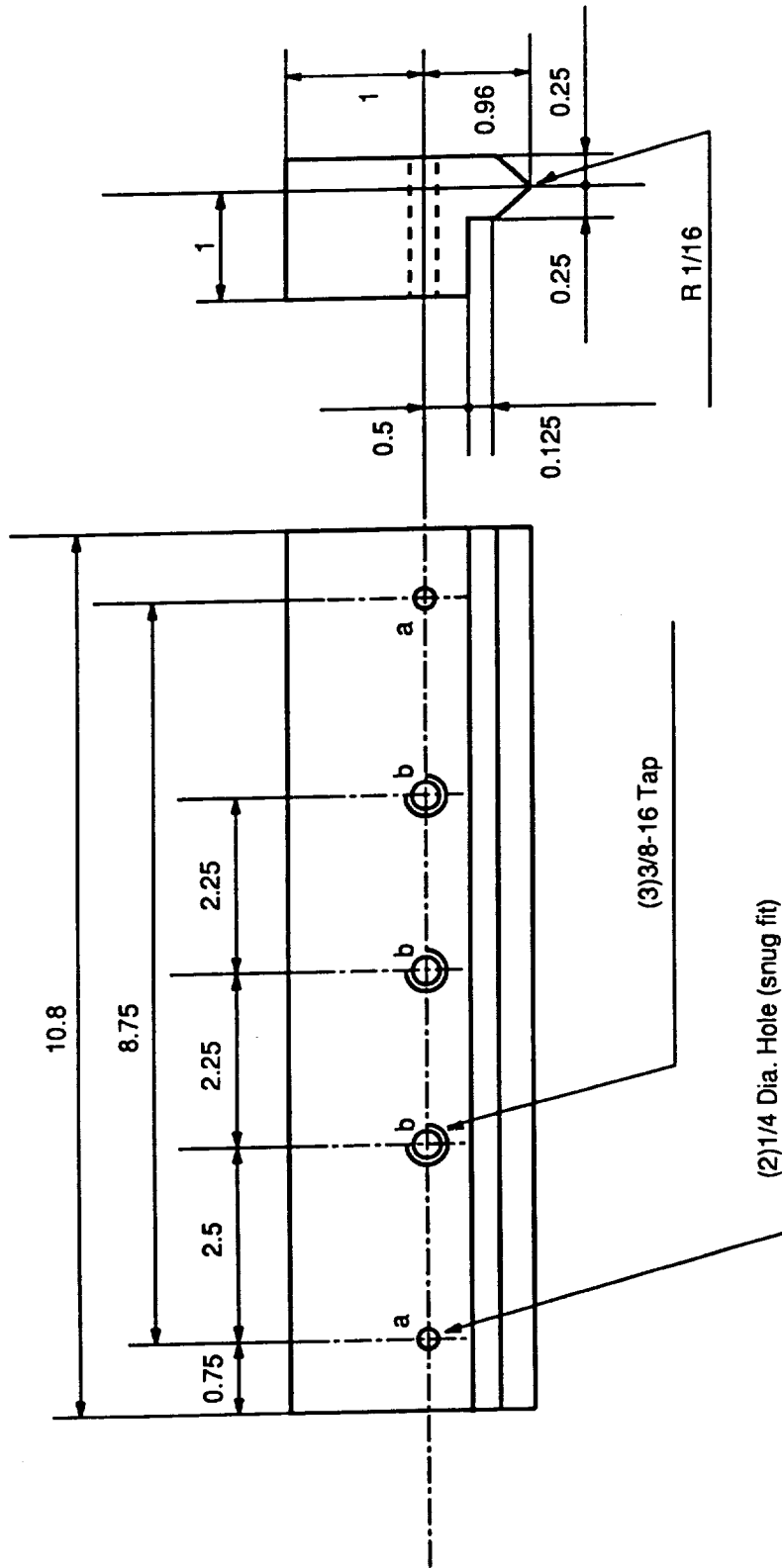


Fig. 6-7 Knife edge.

dimensions in inches

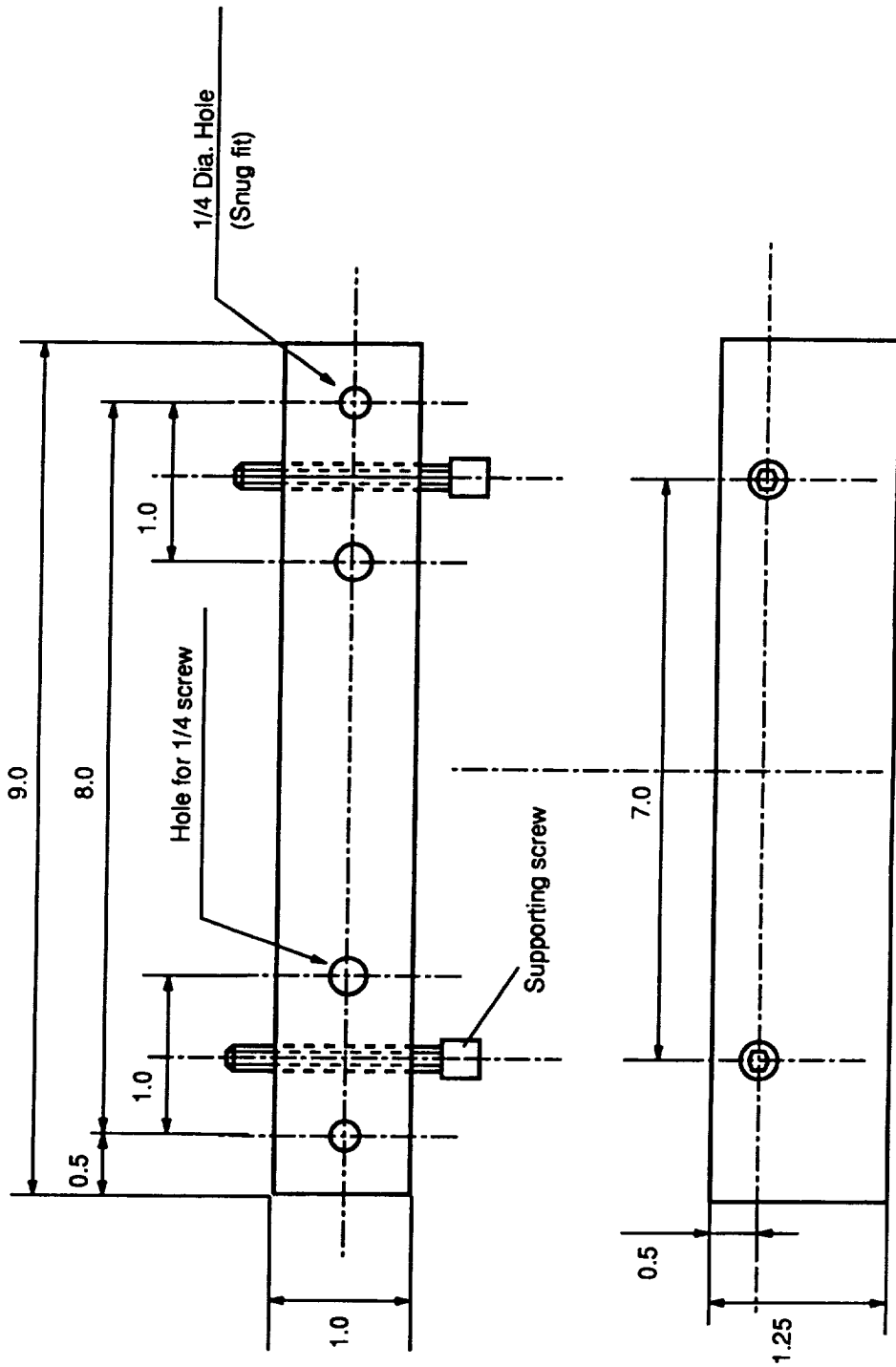


Fig. 6-8 Supporting block for knife edge.

dimensions in inches

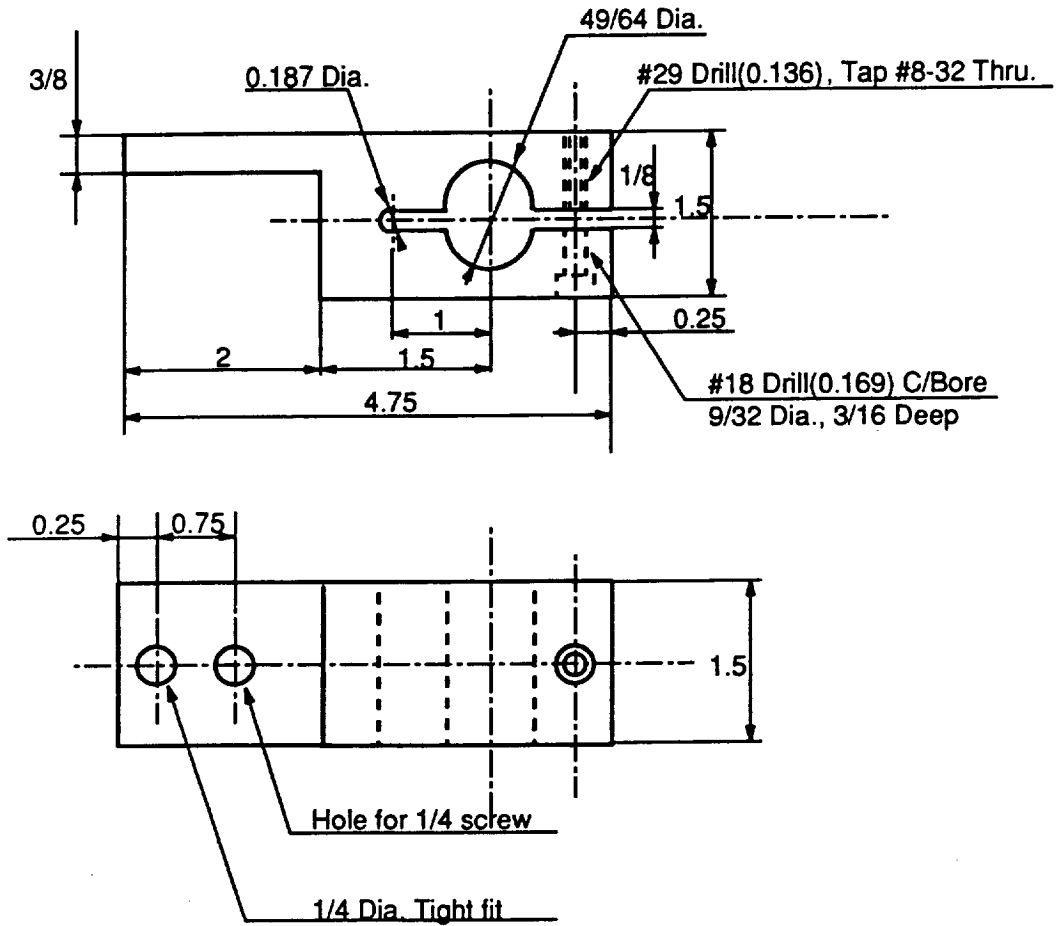


Fig. 6-9 LVDT bracket.

composite plate. A comparison of the left and right displacement readings is a direct measure of how uniformly the edge is being displaced.

The load from the load frame is transmitted to the fixture through a spherical steel ball on the top assembly. A thick stiffback steel bar between the ball and the top plate of the top assembly provides additional stiffness and helps enforce the condition of uniform inplane displacement. The steel ball provides a decoupling of any misalignments of the fixture relative to the Tinius-Olsen load frame, though any misalignments were expected to be slight. The linear bearings restrains all but vertical motions of the top assembly relative to the bottom assembly. Replacing a specimen is relatively easy. The pinned clamp support on the bottom edge and the pinned knife edge do not have to be loosened, nor does the one movable clamp support on the top edge. Only the movable components needed to be loosened to accomodate a new specimen.

The fixture is designed to accomodate an 11 in. by 11 in. square plate with 0.08 in. thickness. One-half inch of the plate on each edge is used for the various boundary conditions. Thus the analysis region is 10 in. by 10 in.. The 0.5 in. on the left and right edges of the plate, outside the knife-edges, are simply free. The 0.5 in. at the top and bottom are under clamps. The 10 in. by 10 in. dimensions were somewhat dictated by the size of the load frame available. Also, the dimensions coincide with the dimensions used by the other investigator [31] and hence results could be compared. The loaded edges of the laminates are machined precisely to achieve uniform contact with the loading surface of the fixture, namely the hardened steel inserts. In Fig. 6-10 the fixure with a composite plate is shown within the Tinius-Olsen load frame. The LVDT's are in place in their brackets. Wires from strain gauges (to be discussed next)

ORIGINAL PAGE
BLACK AND WHITE PHOTOGRAPH

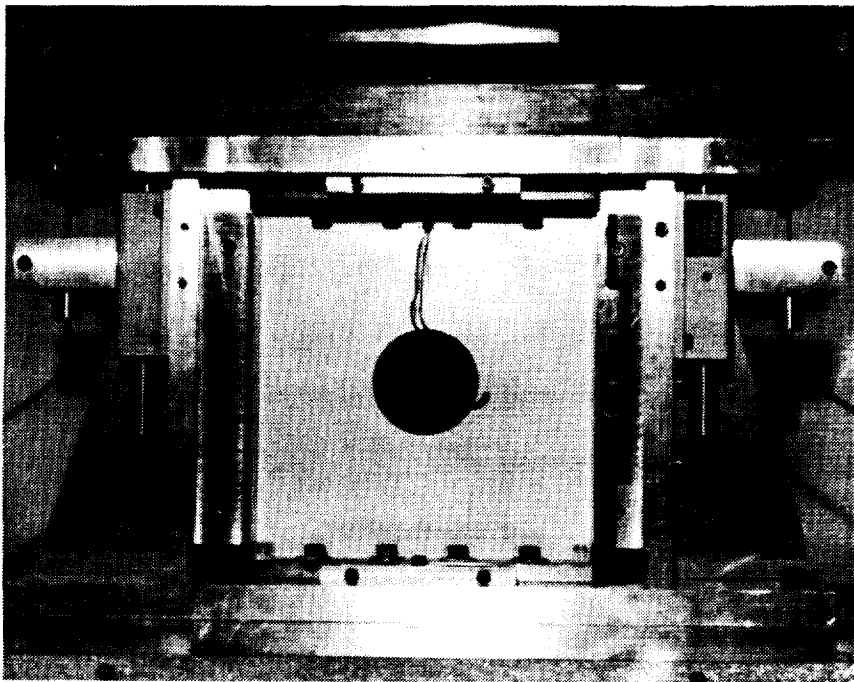


Fig. 6-10 Close-up of the flixture in load frame.

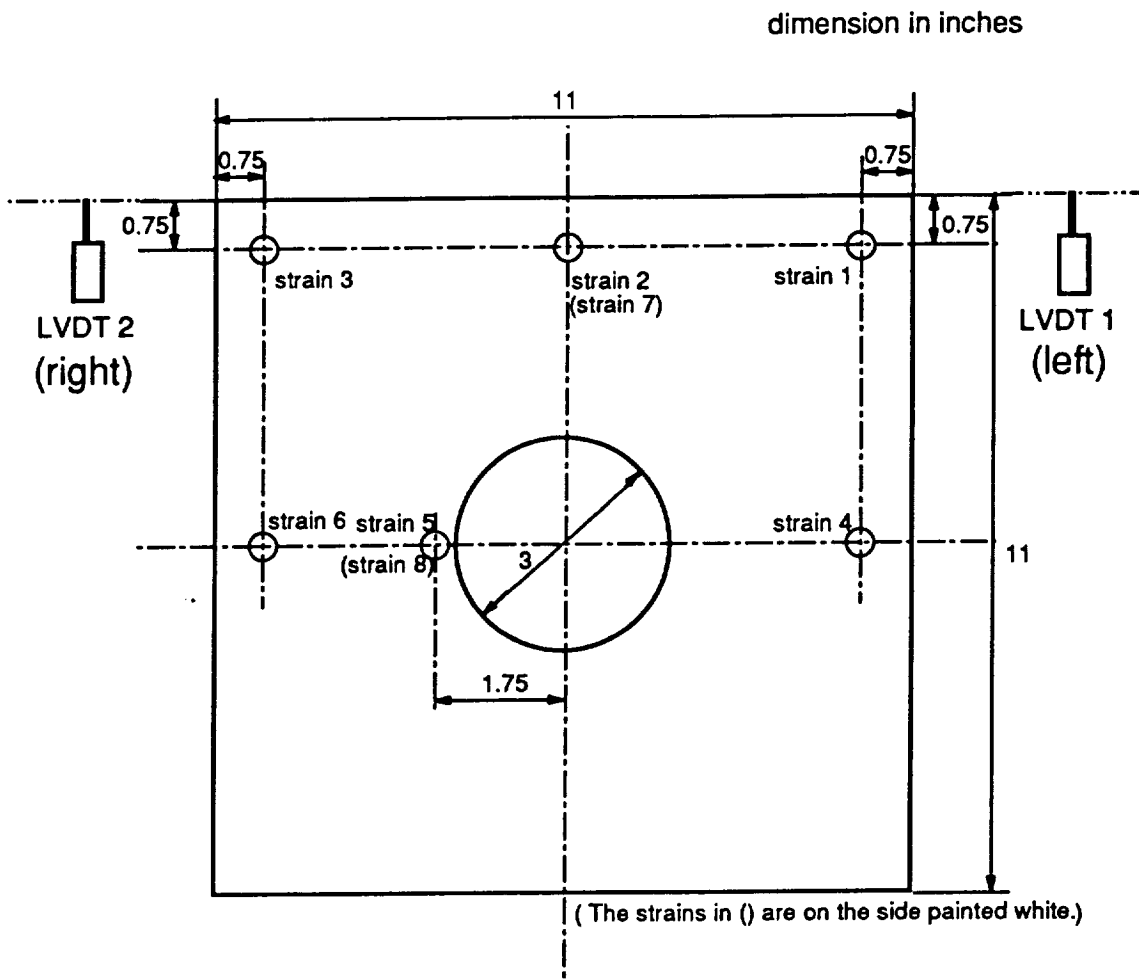
are visible. As will be discussed, the composite plate specimen is painted white on one side to enhance moire interferometry.

6.2 Test Set-up

As has been discussed, LVDT's are used to measure the inplane movement of the top end of the composite plate. The LVDT's used had sensitivity of 195 volts per inch and were manufactured by Schaeitz.

Strain gauges are bonded at a number of points on the composite plate specimen to measure local response. The strain gauge response could be used to examine plate behavior, and also evaluate the validity of the test by identifying lack of symmetry, unusual strain response, etc.

The locations where the strains are measured are depicted in Fig. 6-11. Strains are measured at six locations on one side of the plate, gauges 1-6, and two locations on the other side, gauges 7 and 8. Gauges 7 and 8, along with gauges 2 and 5, respectively, provide back-to-back strain measurement. Gauges 1 and 3 are placed to measure left-right uniformity of the response at the clamped end, gauges 2 and 7 are used to measure bending at the clamped end. Gauges 4 and 6 are also used to measure left-right uniformity. Gauges 5 and 8 are used to measure bending effects at the hole edge.



View toward the black side

Fig. 6-11 Strain gauging locations on the plate specimen.

After strain gauging, the side of the composite plate which has only two strain gauges is painted white for use with the shadow moire measurements. The shadow moire [57] is a technique used to observe the overall out-of-plane displacement pattern of plates. For shadow moire measurements a clean white surface gives better results. Thus the side with less strain gauges is chosen for painting white. For implementing the shadow moire technique a reference grid and light source are needed. Here the reference grid is a thin photographic film with 200 lines per inch mounted on a one-half inch thick piece of plexiglass. The plexiglass used has close tolerance on both its thickness and flatness. The lines of the grid are parallel with the simply supported edges (vertical). The shadow moire fringe pattern is recorded on video tape by means of a TV camera. Still photographs of the fringe patterns are also taken during the test. For the quantitative measurement of out-of-plane displacement at a specific point another LVDT is used. This LVDT is placed perpendicular to the surface of the plate. The simplified top view of the arrangement of the LVDT to measure the out-of-plane displacement and the shadow moire set-up is shown in Fig. 6-12. Finally, acoustic emission signals are recorded. An acoustic emission sensor is attached on the side of the composite plate with six strain gauges. The acoustic emission sensor needs to be attached securely so that it does not fall off during the test. Since the composite plate bends during loading, it is rather difficult to maintain a good contact between the sensor and the plate. When a mode shape changes during postbuckling, there is a sudden motion of the plate. If the sensor is not attached securely, it can fall off.

The voltages corresponding to composite plate end shortening, out-of-plane displacement, strain, and load are collected by a data acquisition system at regular time intervals. These voltages are converted to engineering units by being multiplied by

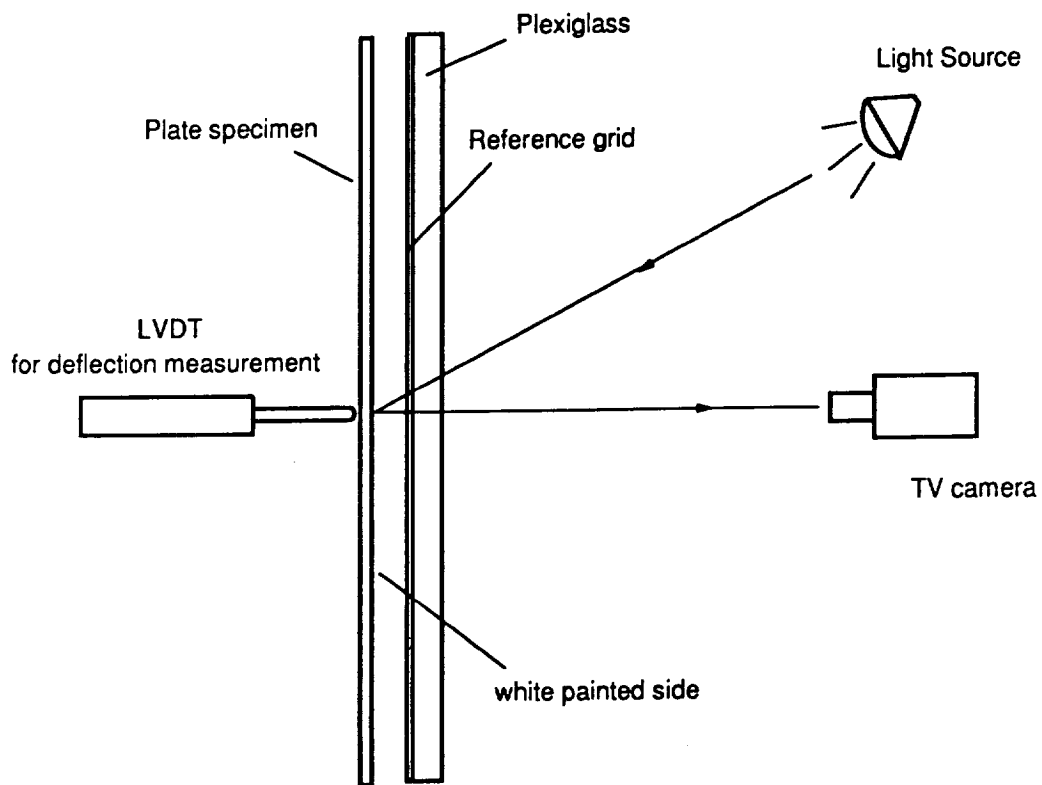


Fig. 6-12 Top view of arrangement of LVDT for out-of-plane displacement measurement and shadow moiré.

the appropriate scale factors, when the data are analyzed. A schematic drawing of the overall layout of the test equipment is shown in Fig. 6-13. A photograph of the overall set-up is shown in Fig. 6-14. The data acquisition system for strains and loads is in the foreground on the left in the upper photograph. The data acquisition system for acoustic emission is in the background on the left. The console on the right is the control unit for the Tinius-Olsen load frame. The VTR equipment, which is placed in front of the of the load frame during testing, is shown in the lower photograph. The next chapter discusses the results obtained with this experimental set-up and the comparison of the experimental results with numerical predictions.

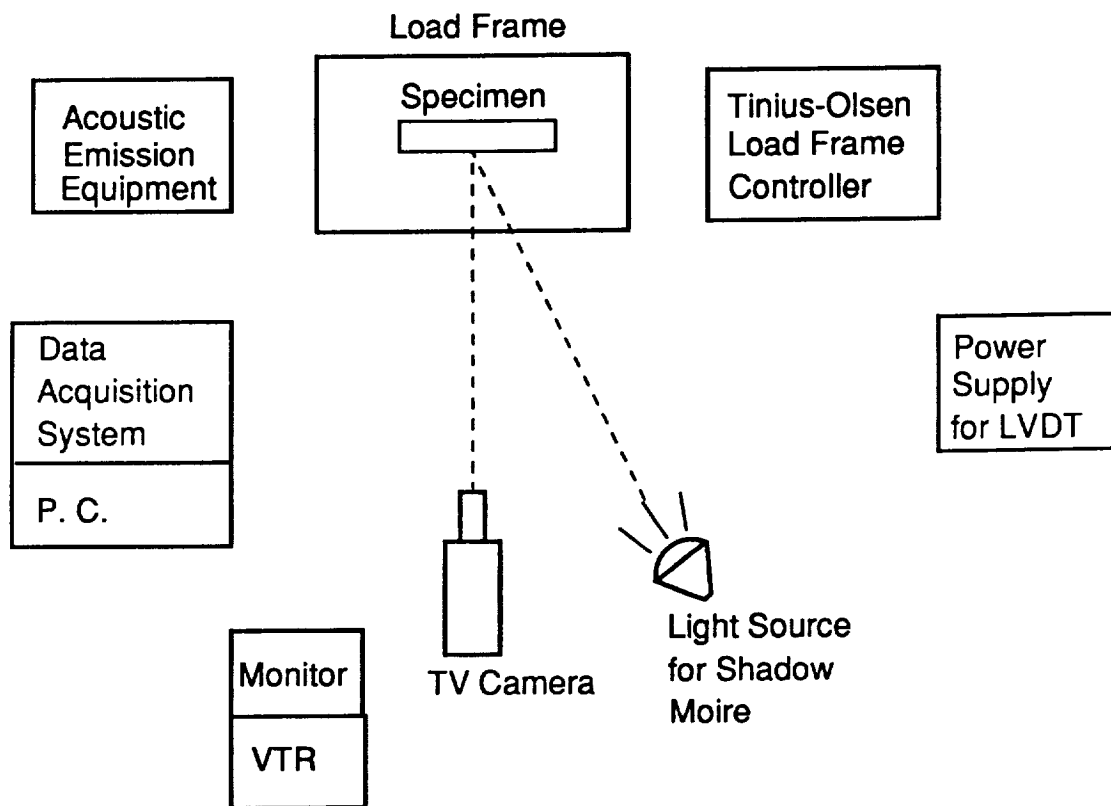
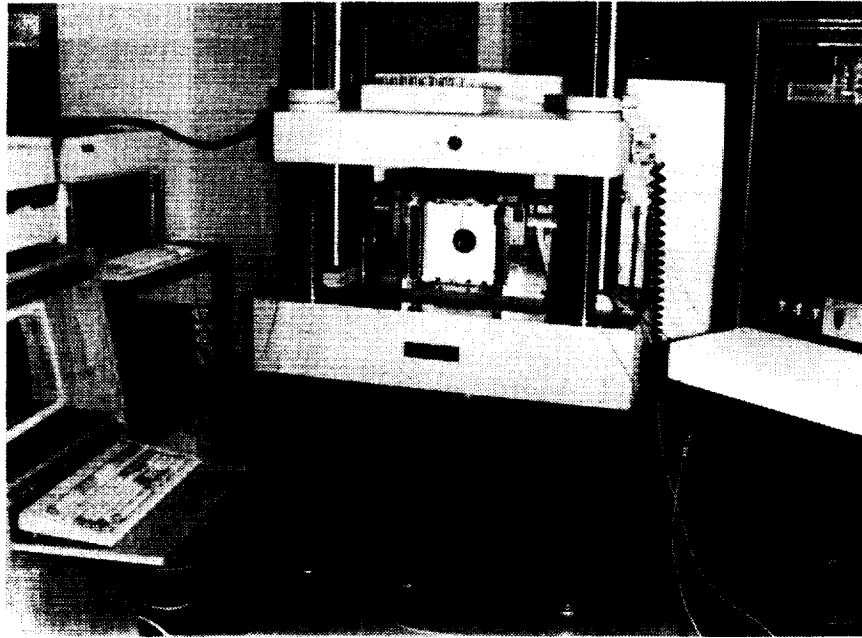
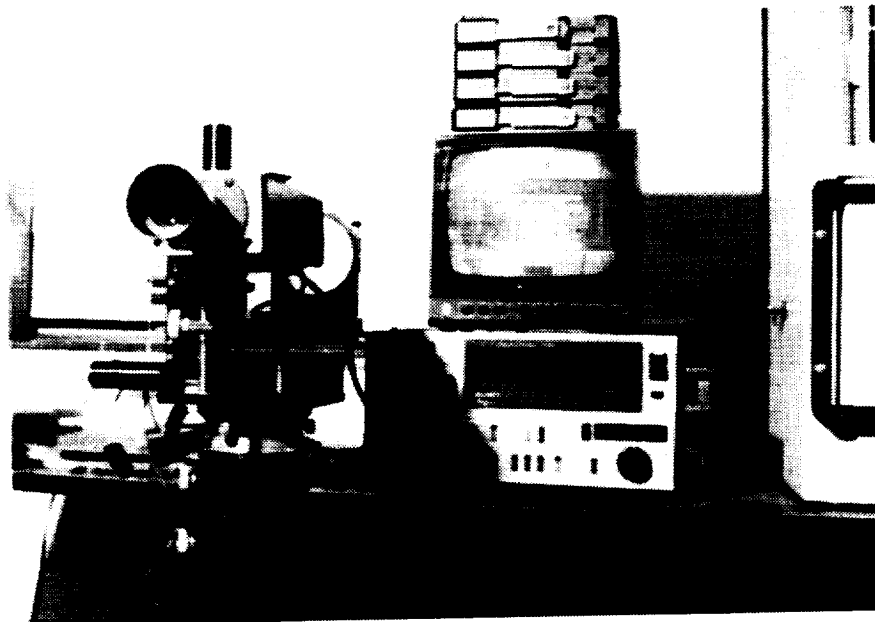


Fig. 6-13 Equipment layout for experimental test.

ORIGINAL PAGE
BLACK AND WHITE PHOTOGRAPH



(a) Test equipment -load frame, data acquisition system, A.E. equipment.



(b) Video recording equipment.

Fig. 6-14 Photograph for experimental set-up.

7.0 Experimental Results and Comparison with Numerical Results

As shown in Table 7-1, two plates for each laminate were tested to failure. With these plates the even numbered plates were tested first, and the odd numbered plates were tested second. For each test, plate end-shortening, the out-of-plane deflection of a point at net-section hole edge, strains at 8 locations on the plate, and the applied load were measured and recorded. Acoustic emission test and moire-interferometry measurements were also made. These measurements are discussed in this chapter, and they are compared with the predictions discussed earlier.

In order to check the uniformity of the loading on the edge of the plate, for each of the plates tested the inplane displacements on the left and right side of the plate, namely, the responses of LVDT 1 and LVDT 2 in Fig. 6-11, were compared. The displacements used in the load vs. end-shortening relations which are compared with numerical results are the averaged values of these left and right LVDT responses. In the load vs. out-of-plane deflection relations, since the out-of-plane deflection was

Table 7-1 Numbering of plates tested in this study.

Plate 1	$[\pm 45/0/90]_{2s}$
Plate 2	
Plate 3	$[\pm 45/0_2]_{2s}$
Plate 4	
Plate 5	$[\pm 45/0_6]_s$
Plate 6	
Plate 7	$[\pm 45]_{4s}$
Plate 8	

measured at the hole edge of the net-section, comparison with numerical results can be made only for one half-wave configuration. Because the net-section is the nodal line of deformed shape, for the two half-wave configuration the theoretical out-of-plane deflection at this point is zero. For both types of load vs. displacement relations discussed, the numerically predicted failure loads are marked on the relation.

For each laminate shadow moire patterns are compared with numerically calculated out-of-plane deflection contour drawings. Finally, acoustic emission results are plotted in the format of end-displacement vs. accumulated counts. In this manner the acoustic emission data can be compared easily with the load-end shortening relation by drawing the two relations on one figure. Numerically predicted failure loads are also marked on this figure. In the following discussions the comparison of experimental results with numerical prediction will be made on a laminate by laminate basis.

7.1 The $[\pm 45/0/90]_{2s}$ Plates

7.1.1 Load vs. Deflection Relations

Experimental load vs. end shortening relations for the $[\pm 45/0/90]_{2s}$ plates, plate 1 and plate 2, and a comparison of these relations with numerical predictions is shown in Fig. 7-1. Failure information, both experimental and numerically predicted,

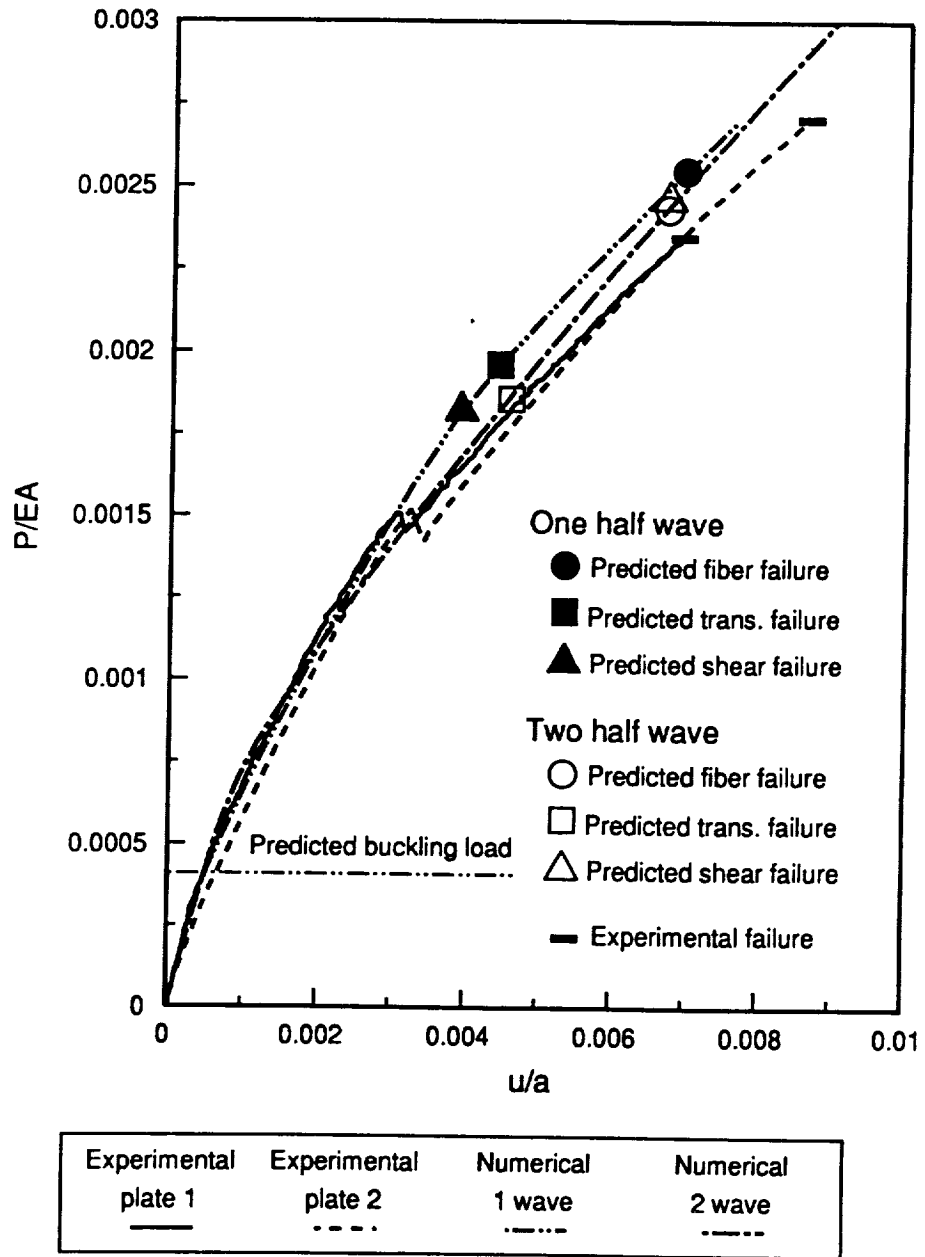


Fig. 7-1 Comparison of load vs. end shortening relations and failure loads for the $[\pm 45/0/90]_{2s}$ plates.

are shown, as is the level of the predicted buckling load. The predicted buckling load for this plate is, as was indicated in Table 2-3, $P_{cr}/EA = 0.000411$, or $\bar{N}_x^{cr} = 258$ lb/in.. The experimental buckling load was obtained from the experimental load vs. end shortening relations by drawing straight lines on the prebuckling and postbuckling path and finding the intersection of these two straight lines. The experimental buckling load of plate 1 was $P_{cr}/EA = 0.000375$, or $\bar{N}_x^{cr} = 235$ lb/in., and that of plate 2 was $P_{cr}/EA = 0.000364$, or $\bar{N}_x^{cr} = 228$ lb/in.. These loads are summarized in Table 8-1 along with similar information for plates to be discussed. Chapter 8 will further discuss the findings presented in this chapter. Referring to the figure, after the buckling load the experimental relations followed the initial postbuckling path characterized by one half-wave in both the x and y directions. At the load level of $P/EA = 0.0015$ ($\bar{N}_x = 940$ lb/in.) the mode shape in the x direction (the loading direction) suddenly changed to two half-waves, while the mode shape in the y direction remained in one half-wave. The experimental relations for both plate 1 and plate 2 showed mode transition from the one half-wave to the two half-wave configuration at similar load levels. As the load level approached the mode shape transition load, the mode transition began to develop from the bottom stationary clamped support. Suddenly, the mode shape transition occurred with a rather violent motion. With the first test for plate 2 the moire reference grating, which was placed in front of the plate without any support, was knocked out of the alignment by the violence of mode shape transition. The test had to be stopped and the plate unloaded. Upon repositioning of the moire reference grating with a support and reloading the plate, the mode shape transition occurred again at the same load level. The mode shape transition for the plate was quite surprising. The problem of predicting the mode shape transition is beyond the scope of this study. In this study the out-of-plane deformation shape before the mode shape transition is assumed to be in one half-wave in both the x and y directions, and

after the mode shape transition two half-waves in the x direction and one half-wave in the y direction. This assumption will be examined and justified in the following discussions by comparing the experimental results with numerical results in terms of load-end shortening relations, strains, and out-of-plane displacements.

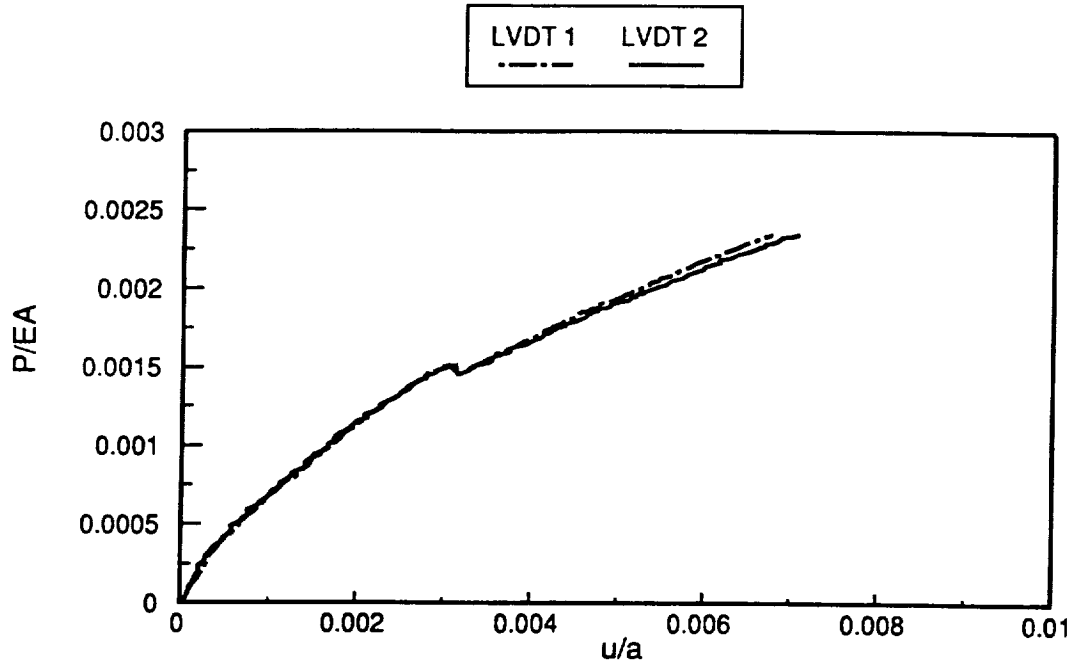
Referring to Fig. 7-1, the experimental results indicate that the stiffness after the mode shape transition was lower than the stiffness before the mode shape transition. The data for plate 2 showed slightly softer behavior as compared with plate 1, and as compared with numerical predictions. It was found that this was due to paint on the loaded edge of the plate. When the paint was sprayed onto the plate to enhance the shadow moire, the loaded edge was also sprayed. After a few tests it was realized that the excessive paint on the loaded edge affected the stiffness observed, and that when the paint was sprayed, masking the edges of a plate was necessary.

Until the mode shape change occurred, the numerical prediction for one half-wave configuration agreed quite well with the experimental results for plate 1. Just after the mode shape change the experimental results for plate 1 agreed with the numerical prediction for two half-waves. At higher load levels the numerical prediction began to deviate from the experimental results. The experimental relation showed softer behavior than the numerical prediction. It is felt that the plate became soft, because the plate began to fail. As the plate began to fail, it began to lose load bearing capability. However, from the relations in Fig. 7-1 it can be seen that until the final failure occurred, the load bearing capacity of the plate did not decrease substantially. Final failure occurred catastrophically for each plate at the load level marked by the horizontal bars. Plate 1 failed at a load of $P/EA = 0.00234$ ($\bar{N}_x = 1468$ lb/in.) and plate 2 failed at $P/EA = 0.00271$ ($\bar{N}_x = 1700$ lb/in.). The numerically pre-

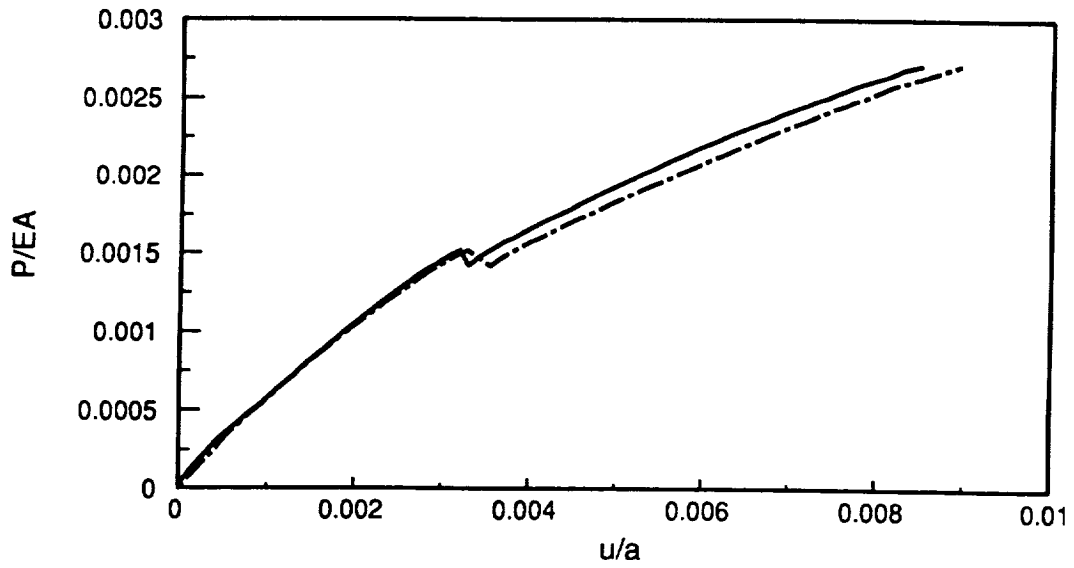
dicted failure loads are marked on the numerical load-end shortening curves. For the two half-wave configuration the numerically predicted inplane shear failure and fiber failure loads occur at $P/EA = 0.00244$. These failure loads are summarized in Table 8-2 along with similar information for plates to be discussed. It can be seen that the experimental failure load of plate 1 was close to the numerically predicted inplane shear and fiber failure loads, while the failure load of plate 2 was higher than that of plate 1. The average of the failure loads of plate 1 and plate 2 is $P/EA = 0.00253$. With the numerically predicted fiber failure load considered as the failure load, the deviation of the numerical prediction from the average of the experimental result is 3 %.

Figure 7-2 shows the degree of uniformity of the loading for plate 1 and plate 2. By comparing the displacements measured by LVDT 1 and LVDT 2, the left-right uniformity of loading was checked. It can be seen that until the mode shape change occurred, both plates 1 and 2 were loaded uniformly, the left and right displacements being identical. After the mode shape change there was a slight difference between the left and right displacements. With plate 1 the side of the plate with LVDT 2 displaced more, and with plate 2 the side of the plate with LVDT 1 displaced more. This shows that the fixture was not biased. The discrepancy between the two side displacements was worse for plate 2 than plate 1. However, considering the magnitude of the displacements, the discrepancy was not serious.

The experimentally measured and numerically predicted out-of-plane deflections of the plates at the net-section hole edge are shown in Fig. 7-3. The jump from the one half-wave configuration to the two half-wave configuration is very evident. Until the jump occurred, the experimental load vs. out-of-plane deflection relation agreed well with the numerically predicted relation. The almost flat part of the load vs. out-



(a) plate 1



(b) plate 2

Fig. 7-2 Comparison of displacements measured from LVDT 1 and LVDT 2 for plate 1 and plate 2.

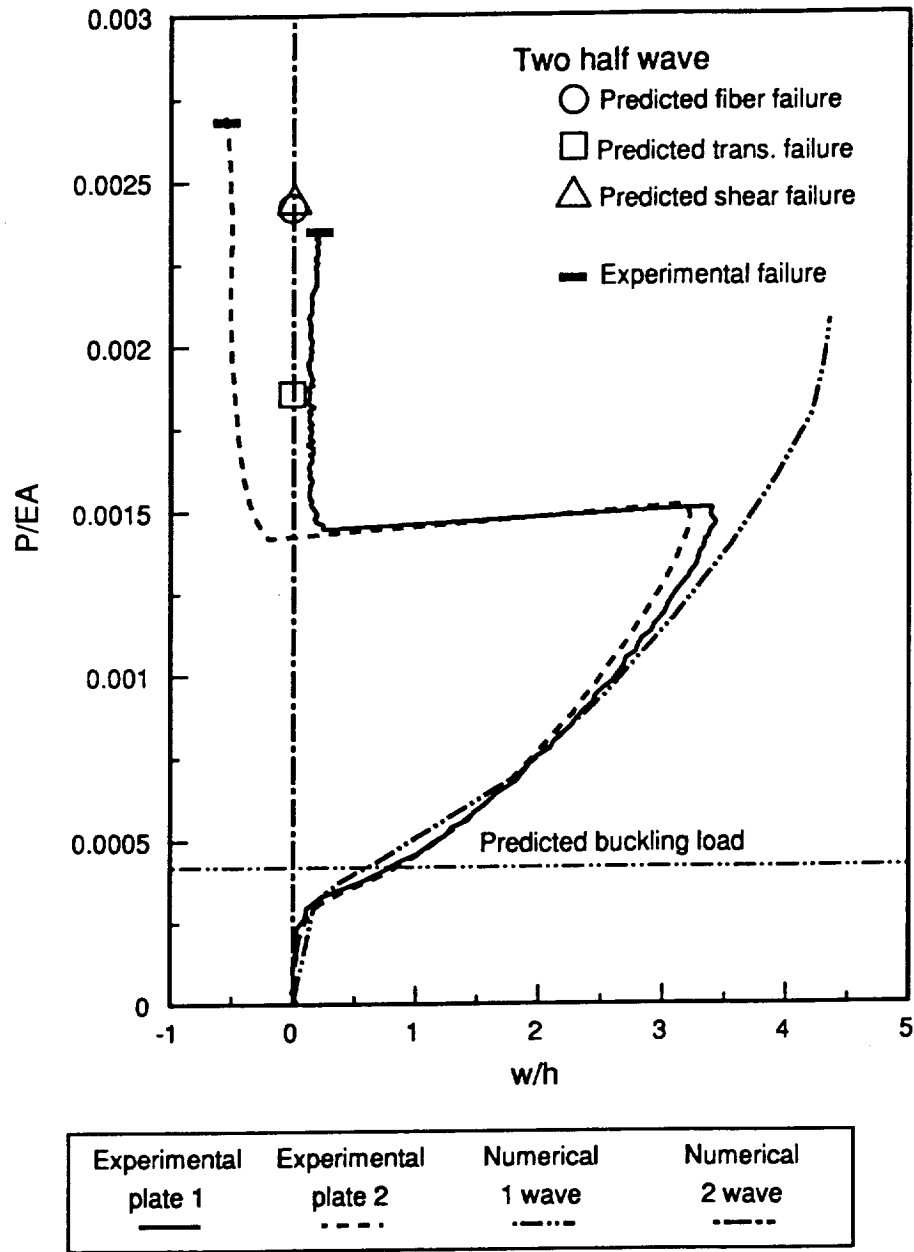


Fig. 7-3 Comparison of load vs. deflection relations and failure loads for $[\pm 45/0/90]_{2s}$ plates.

of-plane deflection curve representing the mode shape change shows that the change occurred in a very short period of time. Theoretically, the out-of-plane displacement at the net-section hole edge for two half-waves is zero. This is because the net-section hole edge is a node line for the two half-wave configuration. The experimental out-of-plane displacement after the mode shape change was close to zero, but it was not identically zero. There are a few reasons why it was not zero. First, the node line of the two half-wave configuration was not perfectly parallel to y axis. As shown in Fig. 7-2, it was impossible to load the plate in a perfectly uniform manner throughout the range of load. Second, with the sudden movements associated with the mode shape change, there is a risk that the LVDTs' may have shifted slightly when the change occurred.

7.1.2 Load vs. Strain Relations

Experimentally measured strains at the 8 locations on the plate 1 are shown in Fig. 7-4. The strain gauge locations were illustrated in Fig. 6-11, and the strain gauges are grouped in Fig. 7-4 by location on the plates. Gauges 1, 2, 3, and 7 are located at the clamped movable edge and gauges 4, 5, 6, and 8 are at the net-section. Examination of each group of gauges provides information on the symmetry of the loading, when buckling began, local bending effect, etc. In Fig. 7-4 it can be seen that the strains after the mode shape change increased faster with load than before the mode shape change. This reflects the sharper curvatures associated with the two half-wave configuration. Strains 1 and 3 were very close. This indicates good but not perfect left-right symmetry of loading, boundary conditions, and response near the movable

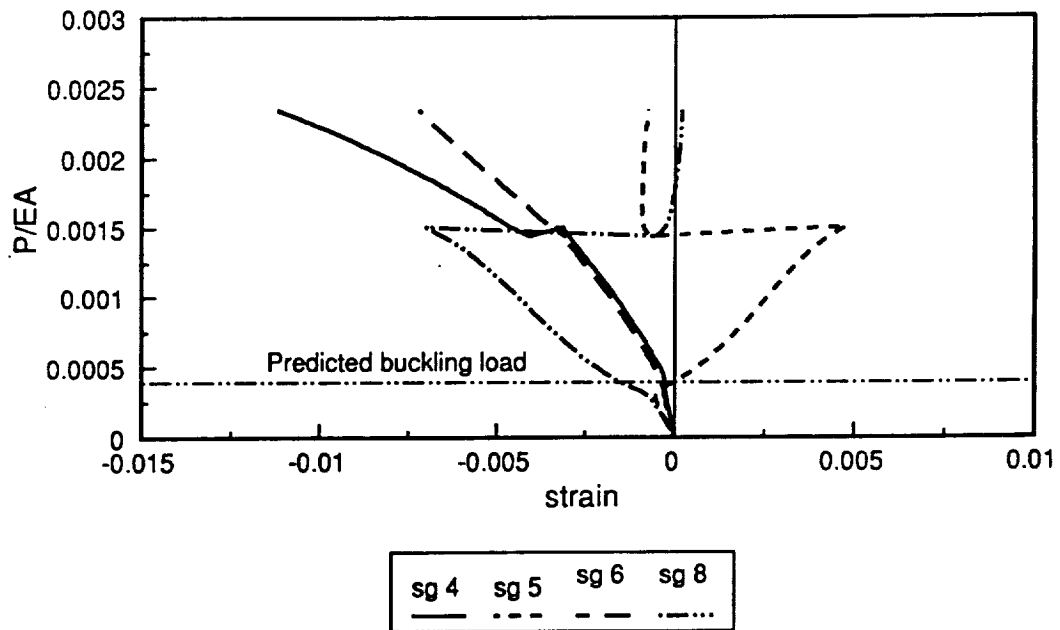
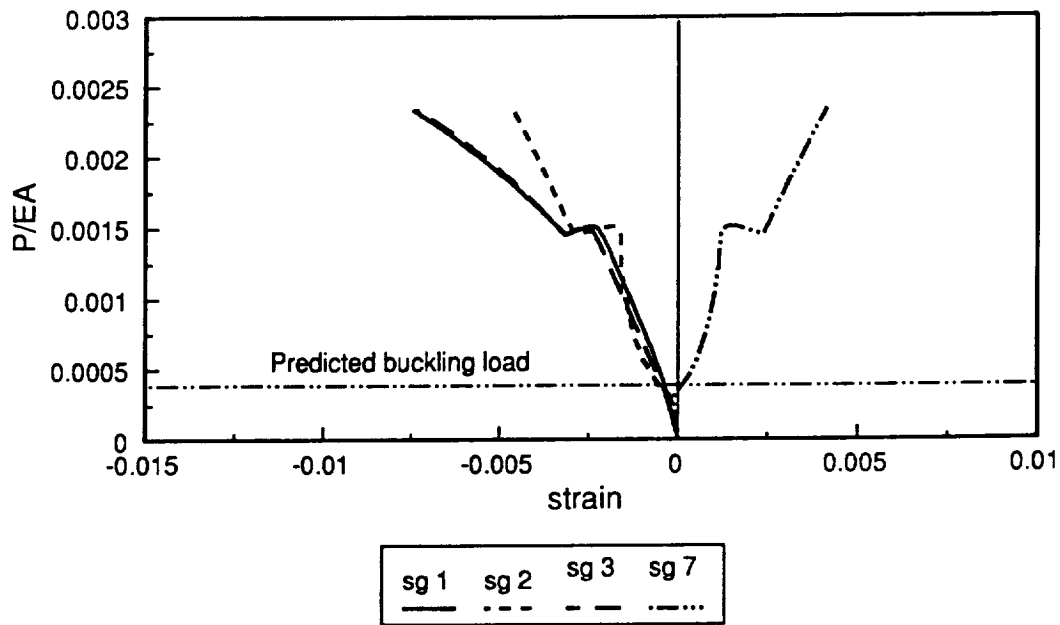


Fig. 7-4 Experimentally measured strains of plate 1.

clamped support. These strains look identical despite the fact that the inplane displacements on the left and right side of the plate had slight differences, i.e., see Fig. 7-2. Strain gauge 2 and strain gauge 7 were back-to-back gauges. Up to the buckling load both strain gauges registered compressive strains. After buckling the response of strain gauge 2 remained in compressive and continued to increase. However, the response of strain gauge 7 changed sign and became positive. Before explaining more on this, another back-to-back pair of strain gauges, strain gauge 5 and strain gauge 8, is examined. Until buckling occurred, they also both showed compressive strains. After buckling strain 8 remained in compression, but strain gauge 5 became tensile. The high level of compressive strain in strain gauge 8 reflects bending and strain concentration effects at the net-section hole edge. That strain 5 was positive indicates that the plate was deflected so that strain gauge 5 was on the convex surface of the plate, as in Fig. 7-5. Strain gauge 2 and strain gauge 5 were on the same side of the plate, and strain gauge 7 and strain gauge 8 are on the other side of the plate. It is interesting that strain 2 and strain 5 had signs opposite each other, and strain 7 and strain 8 had signs opposite each other. This can be explained by Fig. 7-5. Since the loaded edge was clamped, the curvature near the clamped edge was opposite in sign to the curvature at the center of the plate. This made the signs of strain 2 and strain 5, both being on the same side of the plate, opposite one another. The fact that the strains at location 5 and 8 dropped so dramatically after the mode shape change was due to the fact that these gauges were on the two half-wave configuration nodal line. With the two half-wave configuration there was not much strain for these gauges to register, whereas in the one half-wave configuration there were significant bending strains at the locations of gauges 5 and 8.

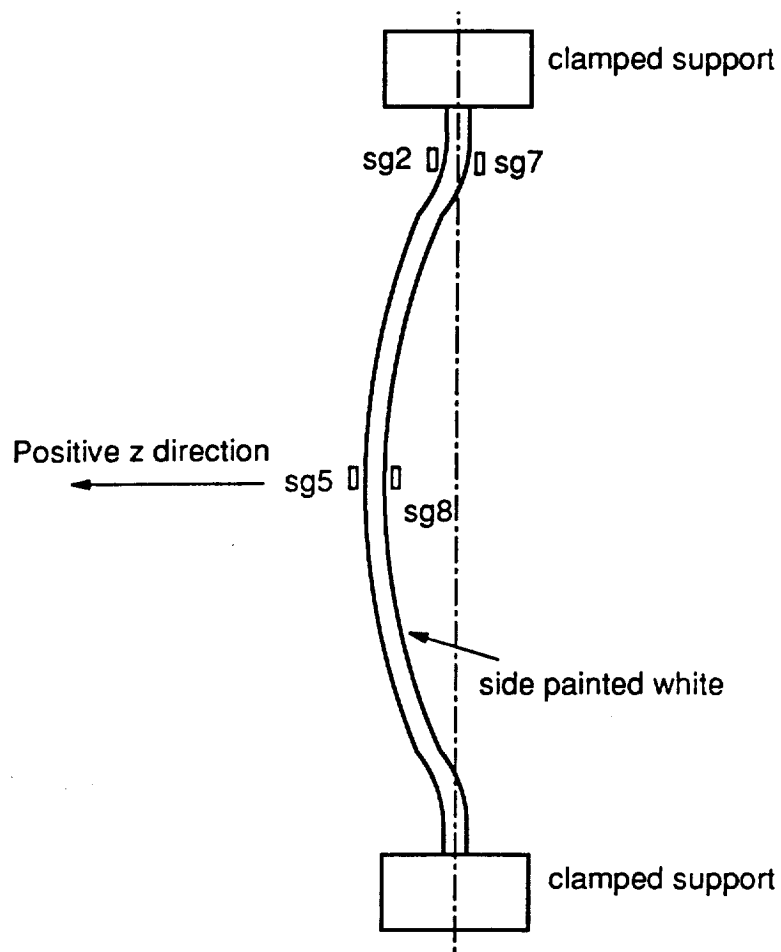


Fig. 7-5 Schematic drawing to explain the sign change of strains.

Like strain gauges 1 and 3, strain gauges 4 and 6 were not influenced much by bending, since the plate was held flat at those gauge locations by the simple supports. It should be mentioned that gauges 4 and 6 generally registered higher strains than gauges 1 and 3, even though they were essentially in line with each other and near the simple supports, the supports keeping the plate flat. The higher response of gauges 4 and 6 reflects the fact that the presence of the hole caused more load to be transferred through the material near the net-section simply supported area than near the clamped end simple support area. Finally, it can be seen that before the mode shape change strains 4 and 6 were almost the same, indicating symmetry of response. After the mode shape change the symmetry of left-right strains was not as good as before the mode shape change.

The strains of plate 2, shown in Fig. 7-6, show results similar to the results of plate 1, except that the left-right symmetry of the response after the mode shape change was not as good as it was for plate 1.

In the following figures comparisons between the experimentally measured strains and numerically predicted strains are shown. This, of course, is a critical comparison as it indicates whether or not the numerical analyses discussed in previous chapters accurately represent experiments. Figure 7-7 shows the comparison for strains 2 and 7 of plate 1. Overall, the figure shows very good agreement between experimental results and numerical predictions. Strain gauge 2 registered compressive strain and followed the one half-wave numerical prediction until the mode shape change. After the mode shape change the strain gauge response followed the numerical two half-wave prediction quite closely. Comparisons for strain gauge 7 are similar. Until the mode shape change strain gauge 7 followed the one

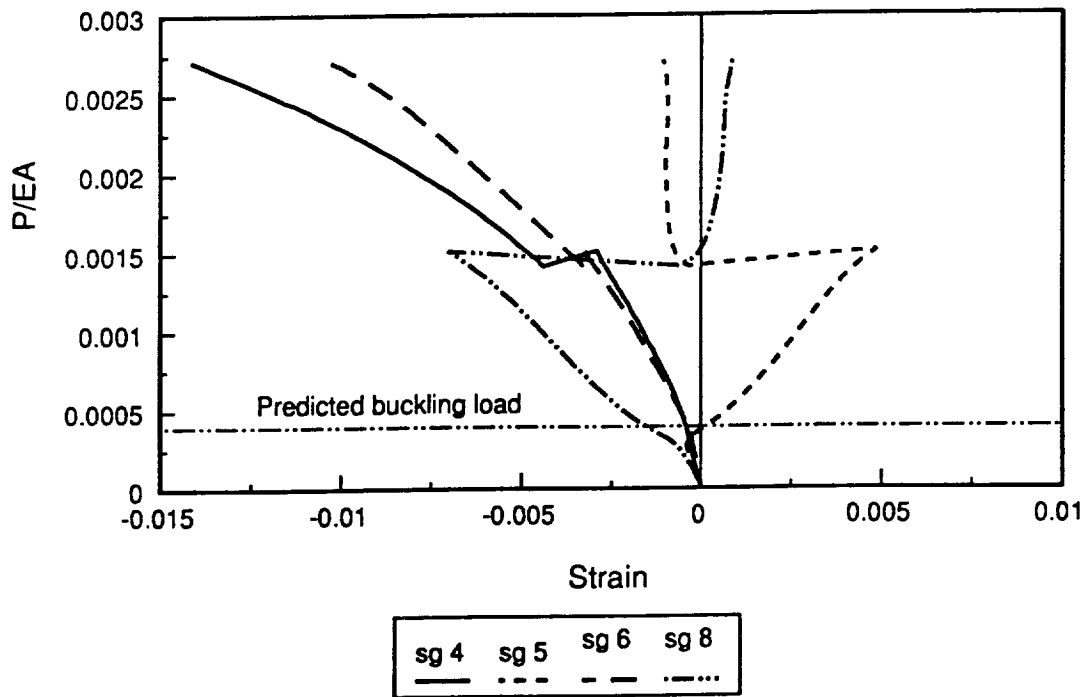
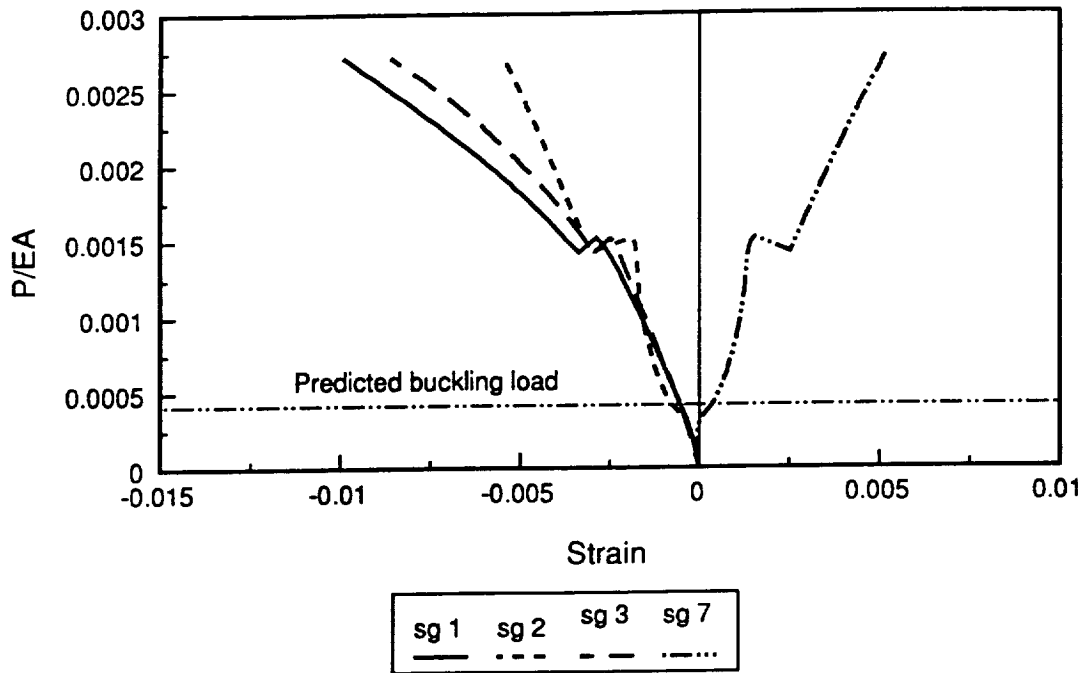


Fig. 7-6 Experimentally measured strains of plate 2.

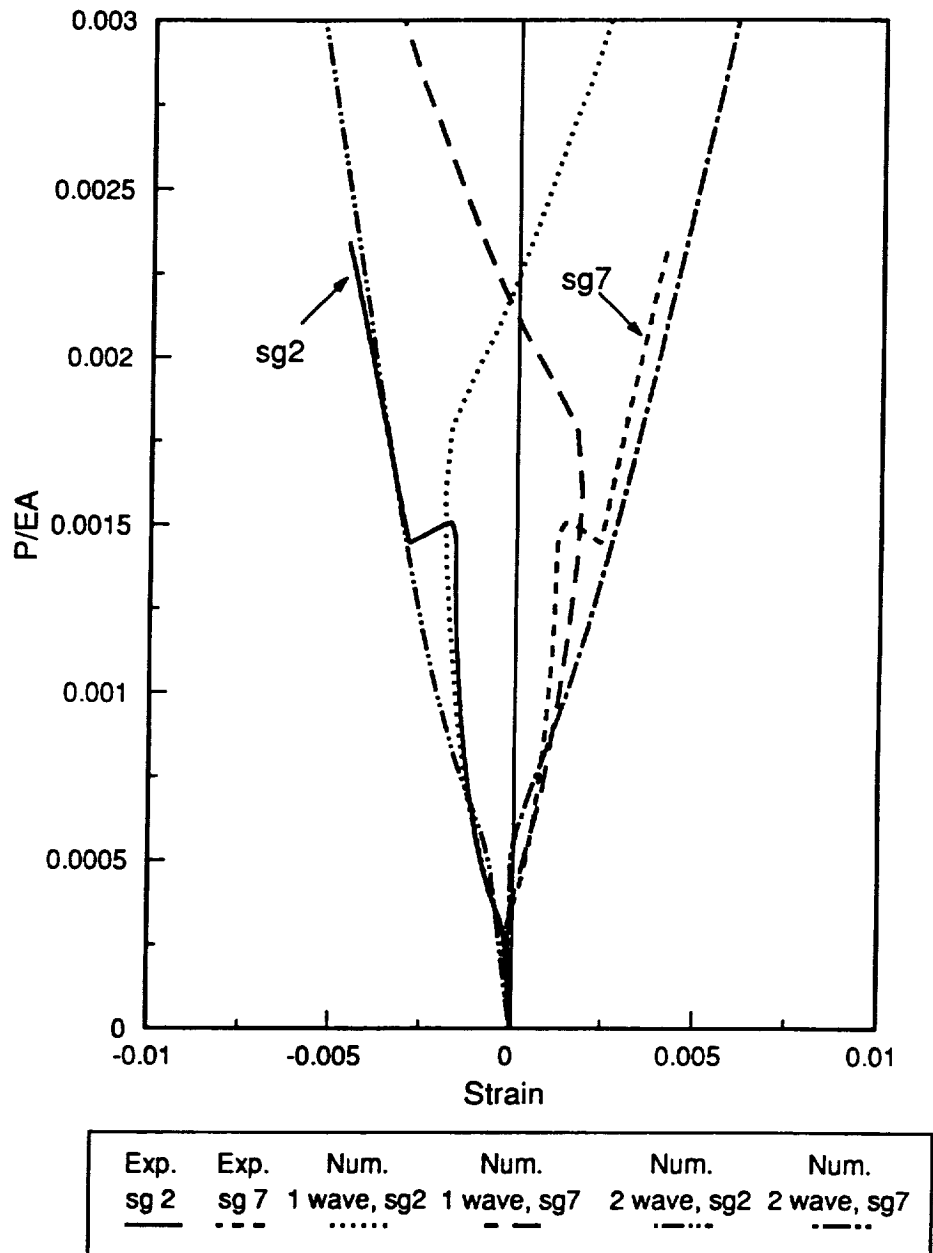


Fig. 7-7 Comparison of strains near the clamped support of plate 1.

half-wave prediction, then it followed the two half-wave prediction, the response being tension for the majority of the load range. The comparison for strain gauge 5 and strain gauge 8 are shown in Fig. 7-8. Comparisons between numerical prediction and experimental measurements for strain gauges 5 and 8 are remarkably close. Initially both strain gauges registered compression. After buckling strain gauge 5 registered tension, while strain gauge 8 continued to register compression. The gauge readings and the numerical predictions are almost in perfect correlation. After the mode shape change the gauges followed the two half-wave prediction. The comparisons for strain gauges near the simple support, strain gauges 1, 3, 4, and 6, are shown in Fig. 7-9. Before changing modes correlations between experimental results and numerical predictions are good. After the mode change the experimentally measured strains were higher than numerical predictions. After the mode shape change strain gauge 4 registered considerably higher strain than the numerical predictions. In general, though, the strain gauges followed the one half-wave prediction until the mode shape changed. Then they followed the two half-wave prediction. The comparisons of the strains for plate 2 are shown in Fig. 7-10 through Fig. 7-12. The trends are similar to plate 1. For strains 2 and 7 and 5 and 8 excellent correlation between observations and predictions can be observed. Again, strain gauge 4 registered considerably higher strain than the numerical prediction.

7.1.3 Shadow Moire Results

A shadow moire fringe pattern represents lines of equal out-of-plane displacement. In fig. 7-13 the fringe pattern at a load level before the mode shape change is

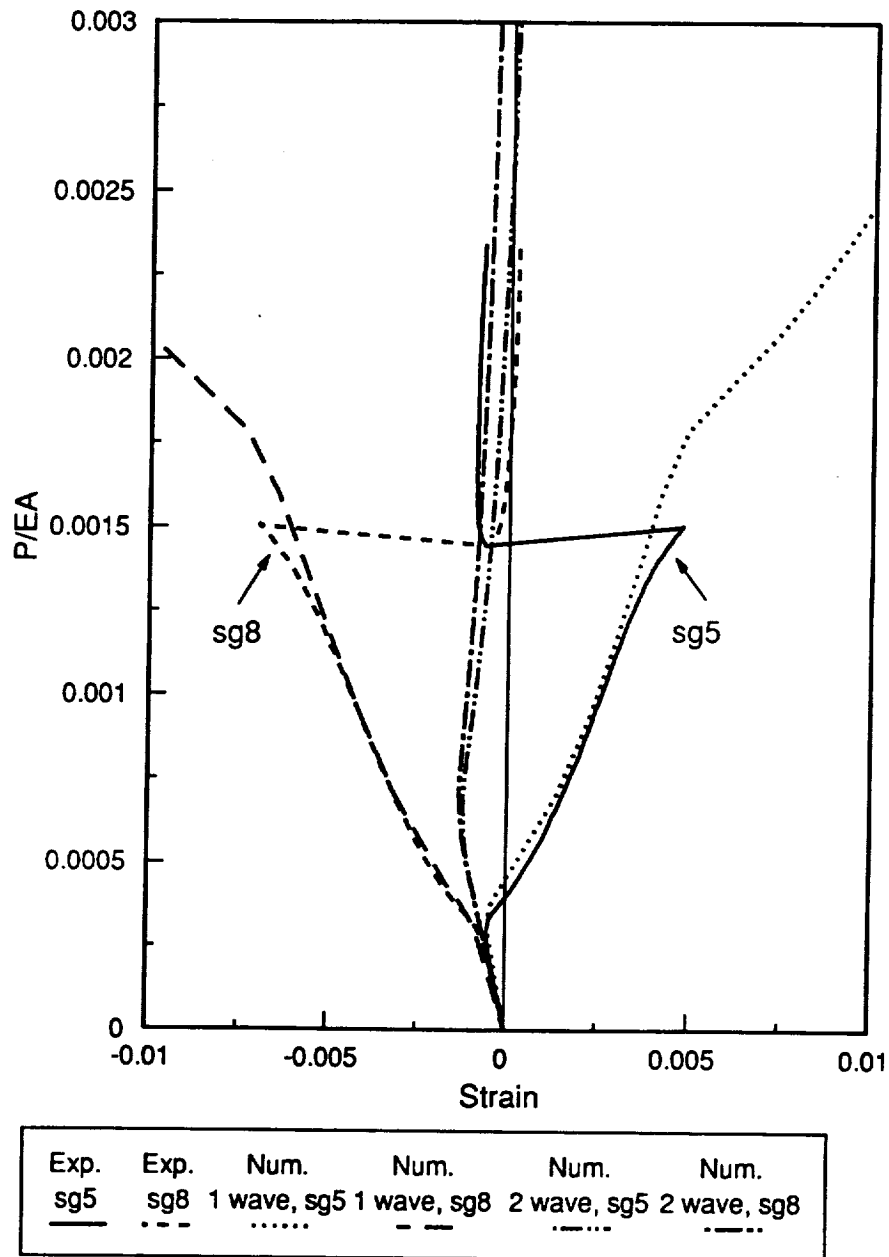
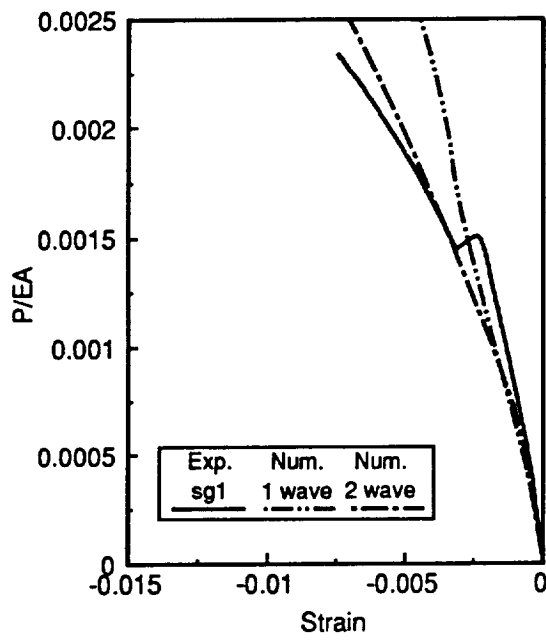
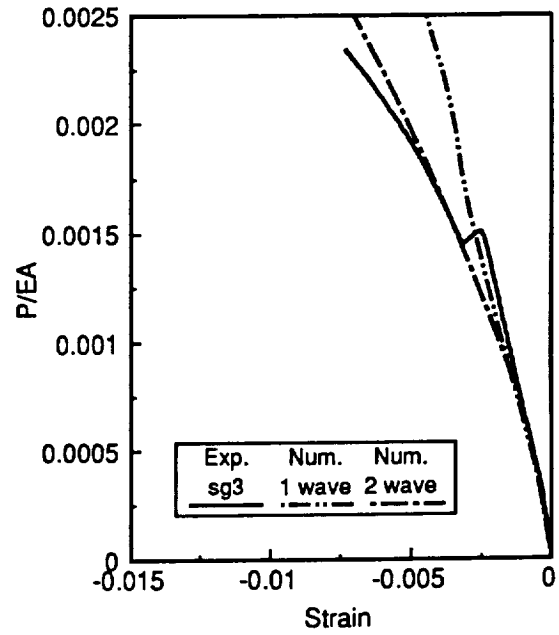


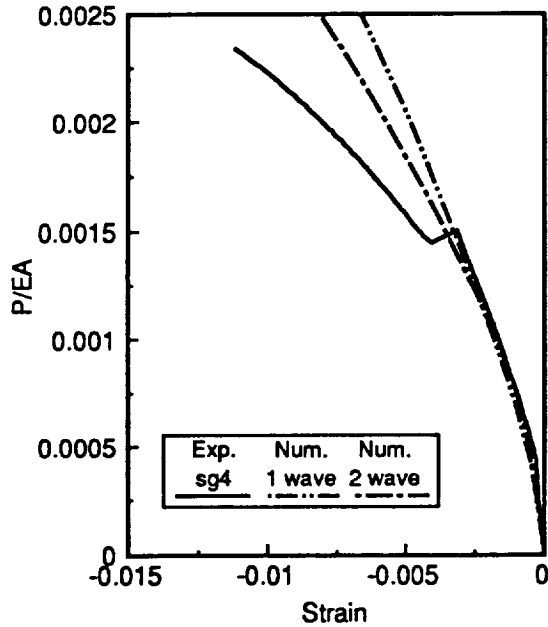
Fig. 7-8 Comparison of strains at the net-section hole edge of plate 1.



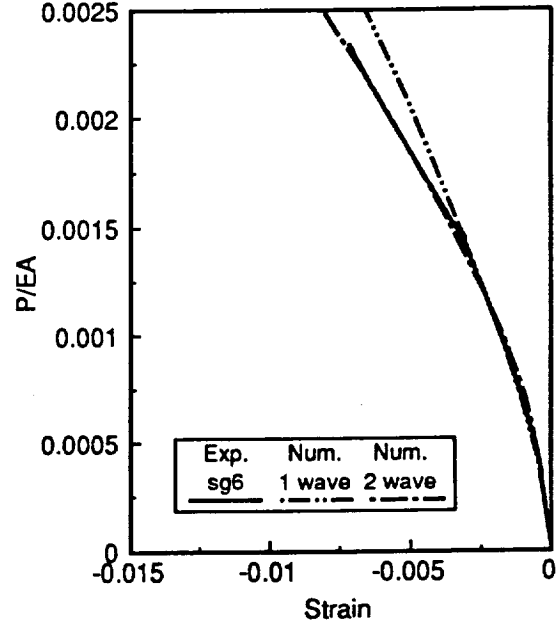
(a) strain gauge 1



(b) strain gauge 3



(c) strain gauge 4



(d) strain gauge 6

Fig. 7-9 Comparison of strains near the simple support of plate 1.

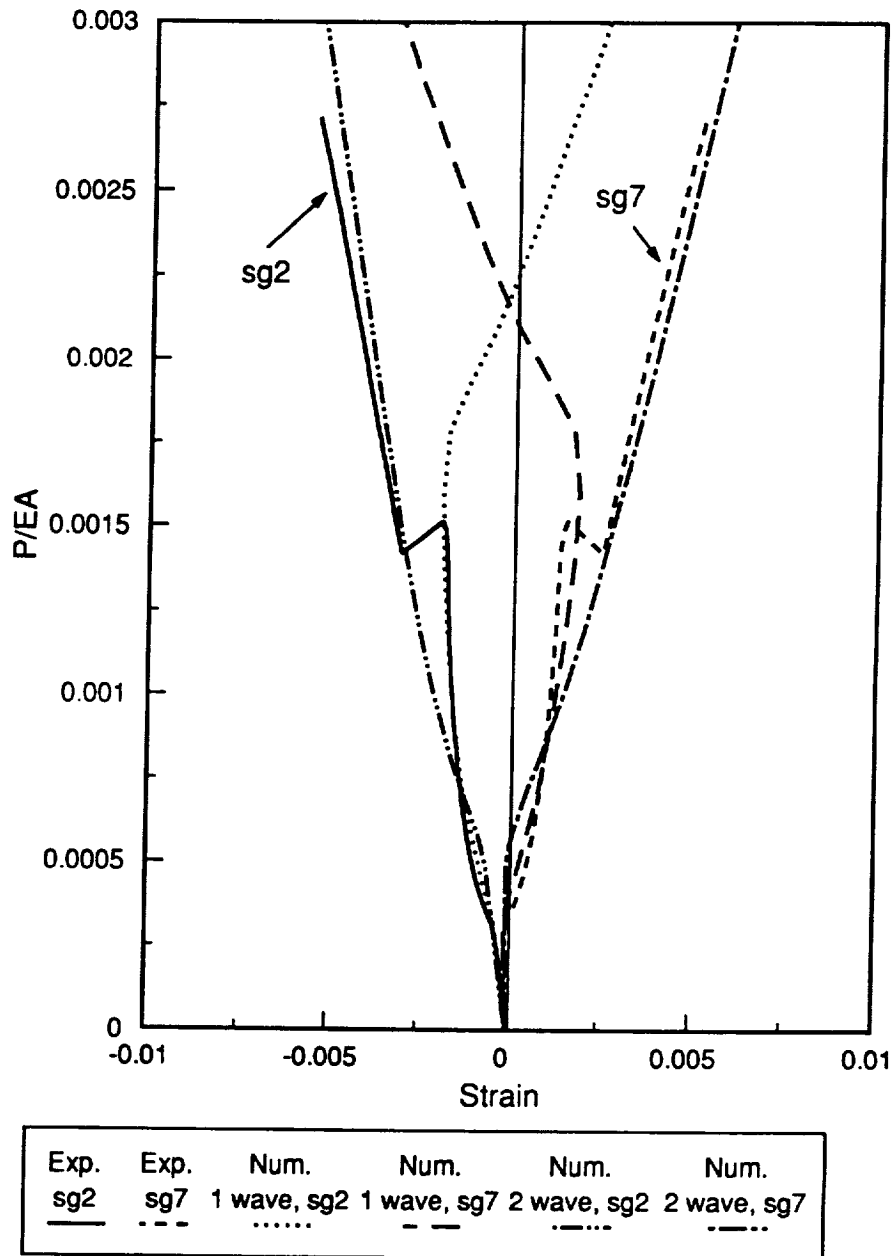


Fig. 7-10 Comparison of strains near the clamped support of plate 2.

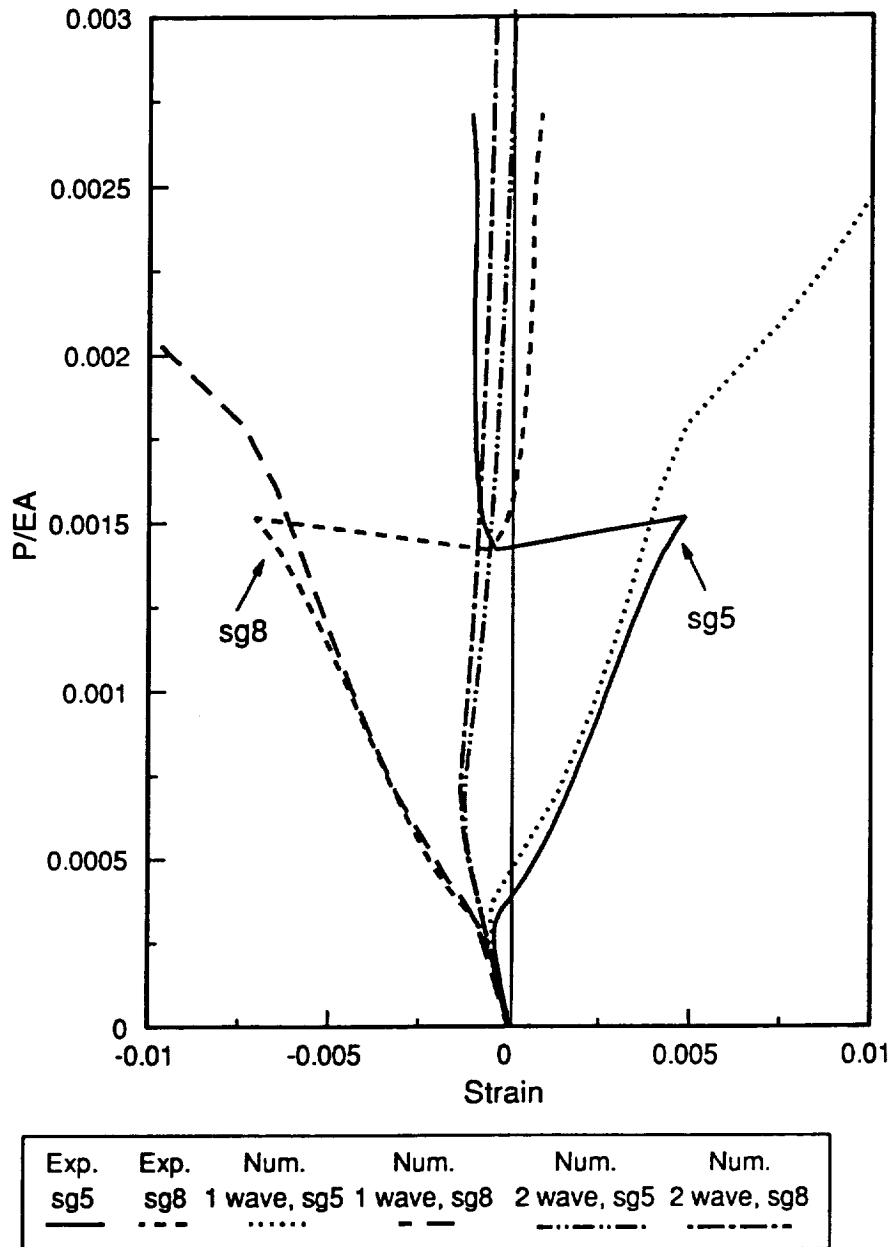
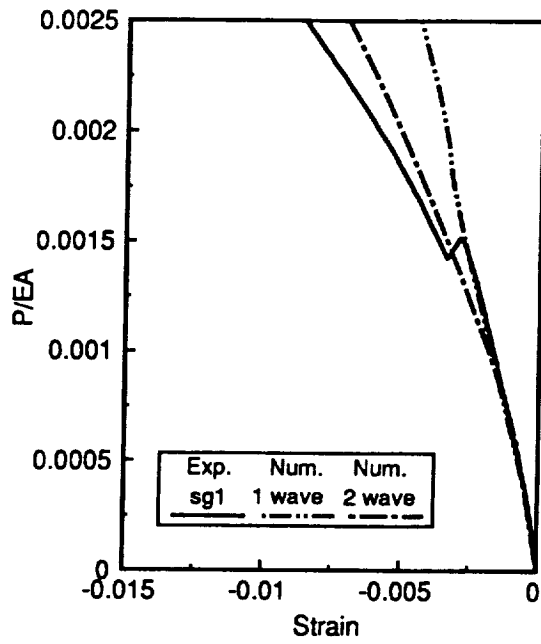
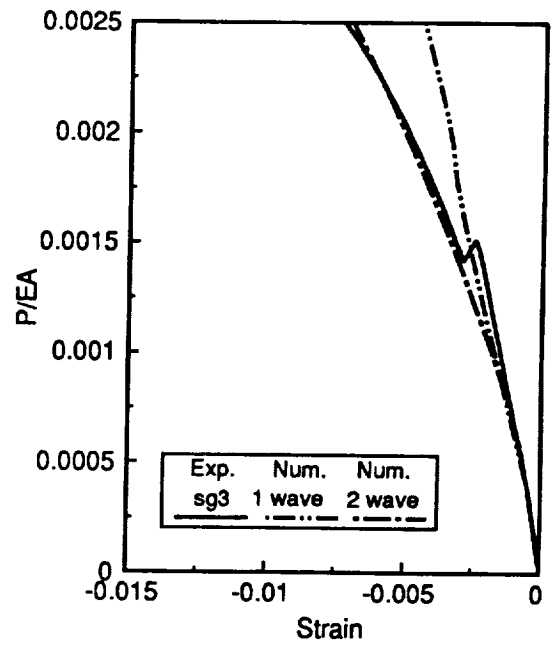


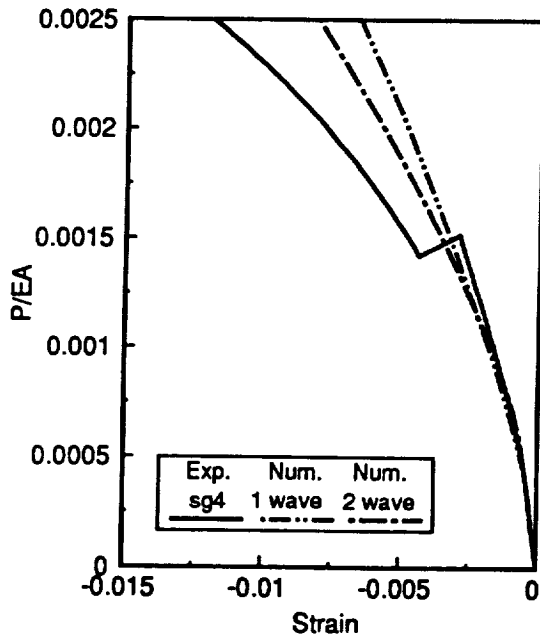
Fig. 7-11 Comparison of strains at the net-section hole edge of plate 2.



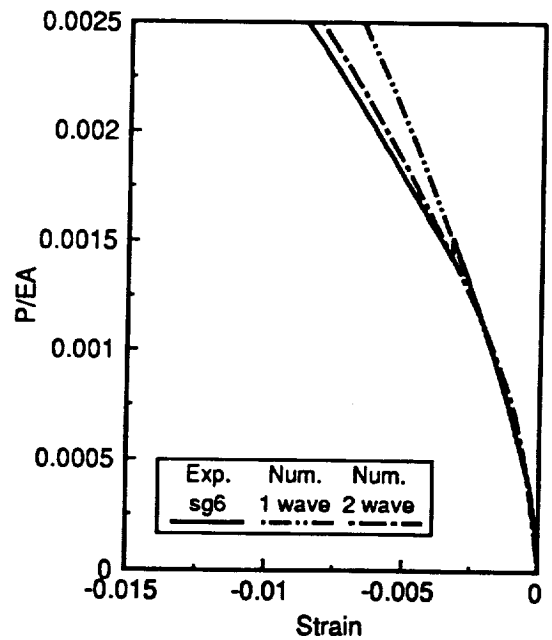
(a) strain gauge 1



(b) strain gauge 3



(c) strain gauge 4



(d) strain gauge 6

Fig. 7-12 Comparison of strains near the simple support of plate 2.

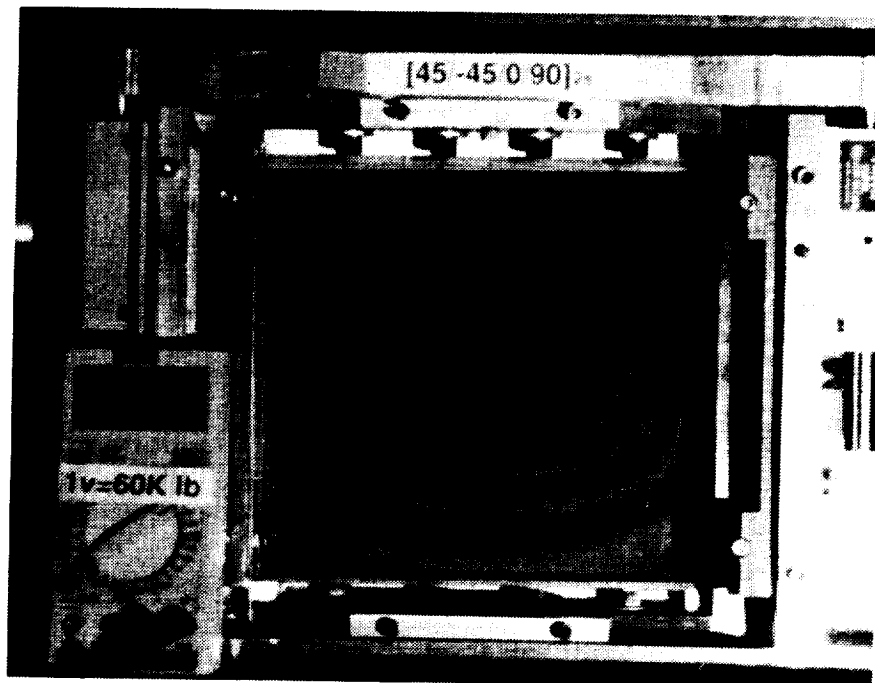
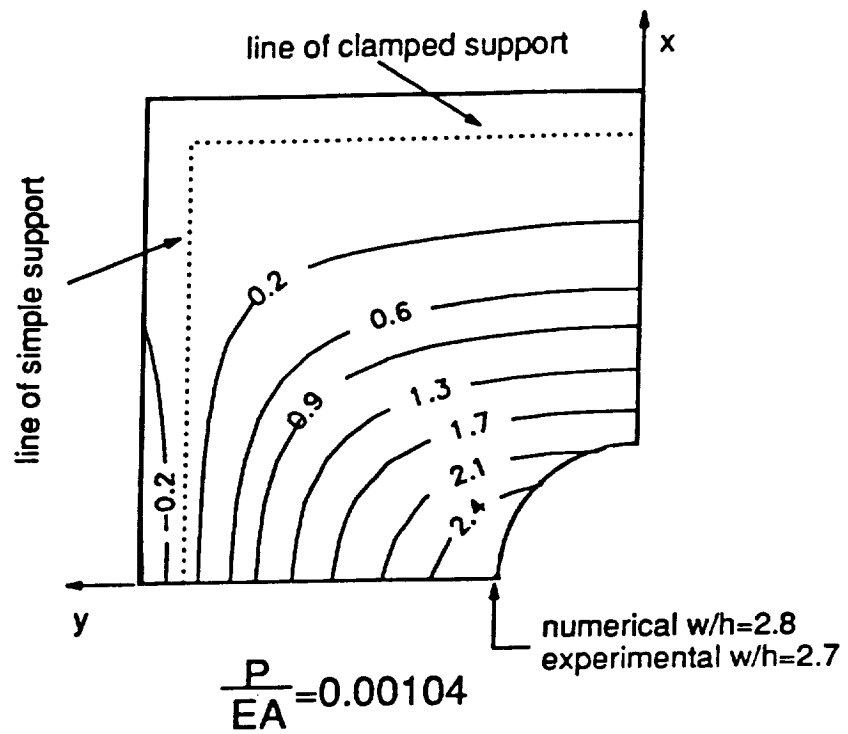
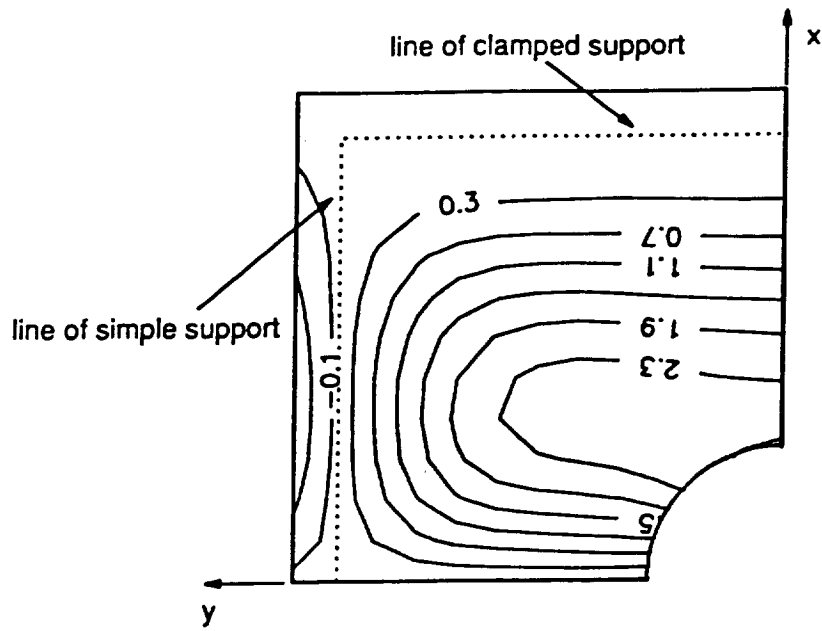
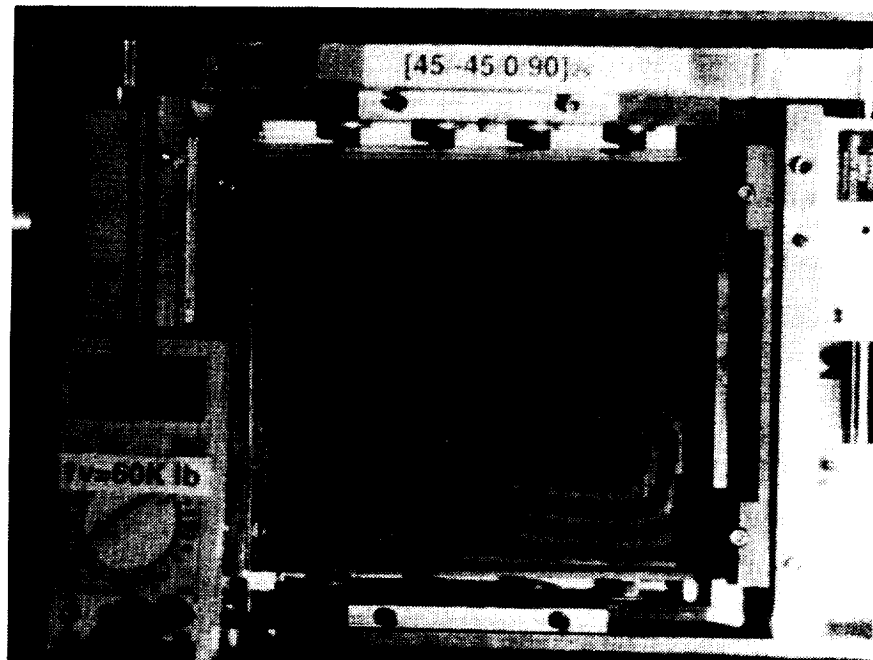


Fig. 7-13 Predicted and measured shadow moiré fringe pattern for a $[\pm 45/0/90]_{2s}$ plate with a one half-wave configuration.

compared with numerically predicted out-of-plane displacement contour plot for the one half-wave configuration at the same load. Note the voltmeter to the left in the lower photograph and the indication that 1 volt = 60,000 lbs. Given that the width of the plate was 11 in., this is interpreted to mean 1 volt corresponded to $\bar{N}_x = 5450$ lb/in. . In the figure the voltage reading, 0.12 volts, corresponded to $\bar{N}_x = 655$ lb/in. , and a nondimensionalized value of $P/EA = 0.00104$. This load level was well above the buckling load (see Table 2-2 and Fig. 7-3). The out-of-plane deformation shown in Fig. 7-13 is characterized by being predominantly a one half-wave configuration. This photo is from the testing of plate 1. Since the view is toward the white side of the plate (see Figs. 6-11 and 7-5), the plate in the photo is deflected into the page, the positive z direction. The experimentally measured out-of-plane deflection at the net-section hole edge at this load was $w/h = 2.7$. The numerically predicted out-of-plane deflection is $w/h = 2.8$. These comparisons are shown in the Fig. 7-13. As the plate was loaded, the mode switched from predominantly a one half-wave configuration to a two half-wave configuration. The fringe pattern after the mode shape change is compared with the numerically predicted out-of-plane displacement contour plot in Fig. 7-14. The voltage reading, 0.25 volts, corresponded to $\bar{N}_x = 1364$ lb/in. , and normalized value of $P/EA = 0.00217$. Because in the experiments the LVDT measuring out-of-plane displacements was placed on the node line, its response was minimal (see Fig. 7-3). Hence it was not possible to correlate displacements at a point for the two half-wave configuration as it was for the one half-wave configuration.



$$\frac{P}{EA} = 0.00217$$



$$\frac{P}{EA} = 0.00217$$

Fig. 7-14 Predicted and measured shadow moiré fringe pattern for a $[\pm 45/0/90]_{2s}$ plate with a two half-wave configuration.

7.1.4 Failure and Post-Mortem Analysis

A photo of a failed $[\pm 45/0/90]_{2s}$ plate is shown in Fig. 7-15. This is plate 1. The failure zone can be seen in the photo. It is clear that the failure propagated from the simply supported edge inward. The failure occurred near the node line. The left edge of the plate just above the node line failed, and the right edge of the plate just below the node line failed. For the 2 plates tested this failure pattern was the same. Compared with the numerically predicted failure locations in Fig. 5-7, the experimental results agreed well with the numerical predictions. In the numerical prediction no interlaminar shear failure was predicted. Failure was governed by inplane stresses at the net-section simple support. This was borne out by experimental observations.

Figure 7-16 shows the contour plots of the failure parameters defined in eqs.(5.1) - (5.5) at selected layers and for each of the five failure modes at the load level where the first fiber failure is predicted in two half-wave configuration. These figures are drawn with the a posteriori knowledge that the plates failed in the two half-wave configuration. The layer shown for each failure mode is the layer exhibiting the largest value of the failure parameter for that mode. Figure 7-16(a) shows the high fiber direction stresses near the net-section simple support region in the outer bottom layer, bottom referring to the negative-most z position. These stresses were responsible for failure. Figure 7-16(b) shows the transverse failure zone in the central region of the quarter plate. Figure 7-16(c) shows the inplane shear failure zone along the simple support away from the net-section. These could have contributed to failure. From Fig. 7-16(d) and (e) it can be seen that the failure parameters related to interlaminar shear stresses are very low, the maximum value being about 0.35. Fig-

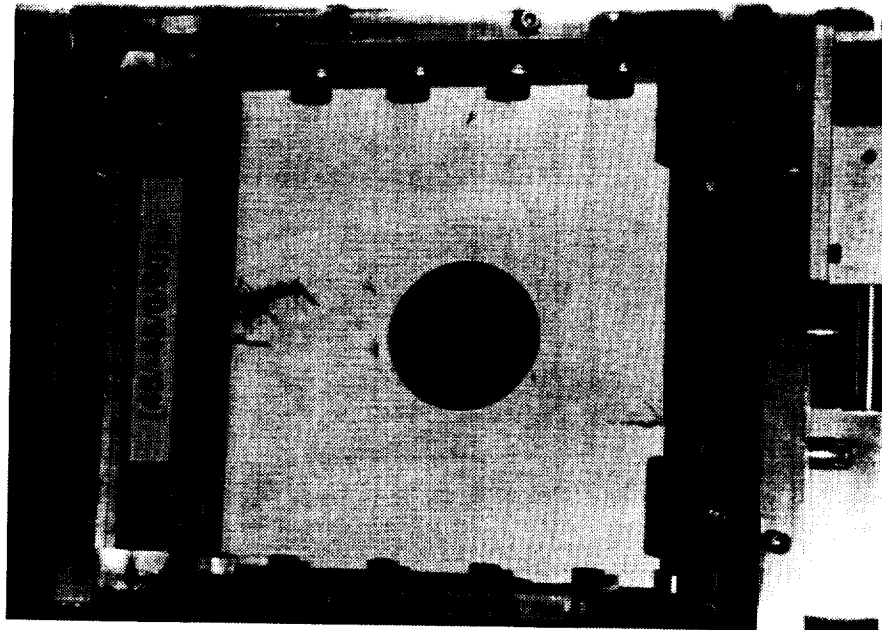
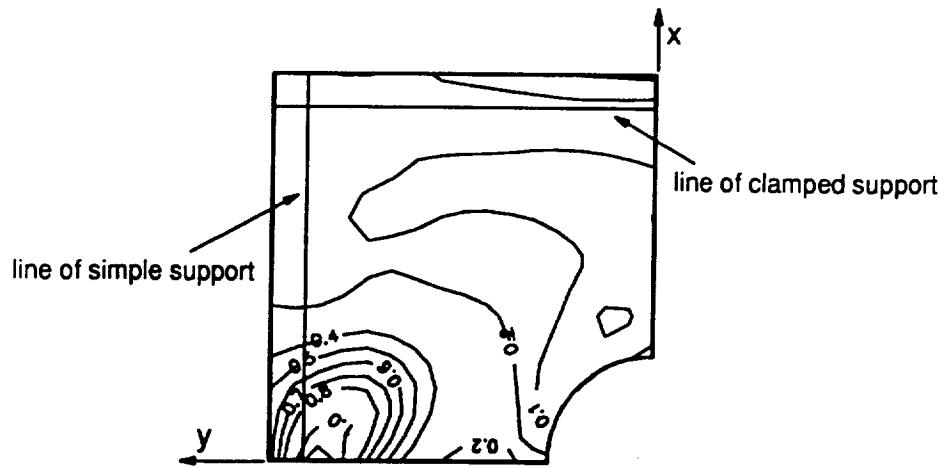
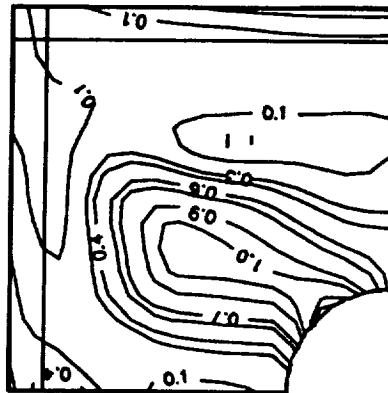


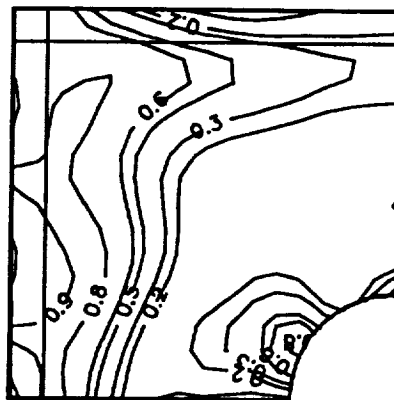
Fig. 7-15 Failed $[\pm 45/0/90]_{2s}$ plate in the fixture.



(a) Contour plot of R_1 on 1-st layer from bottom (45° layer).

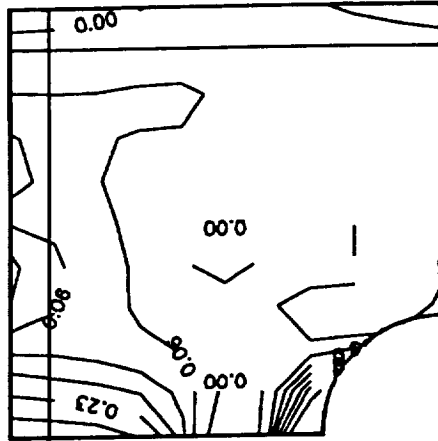


(b) Contour plot of R_2 on 16-th layer from bottom (45° layer).

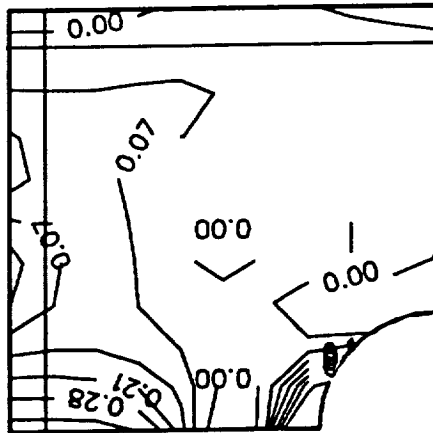


(c) Contour plot of R_{12} on 16-th layer from bottom (45° layer).

Fig. 7-16 Contour of failure parameters of the $[\pm 45/0/90]_{2s}$ plates at $P/EA=0.00255$ (continued).



(d) Contour plot of R_{13} on 10-th layer from bottom (0° layer).



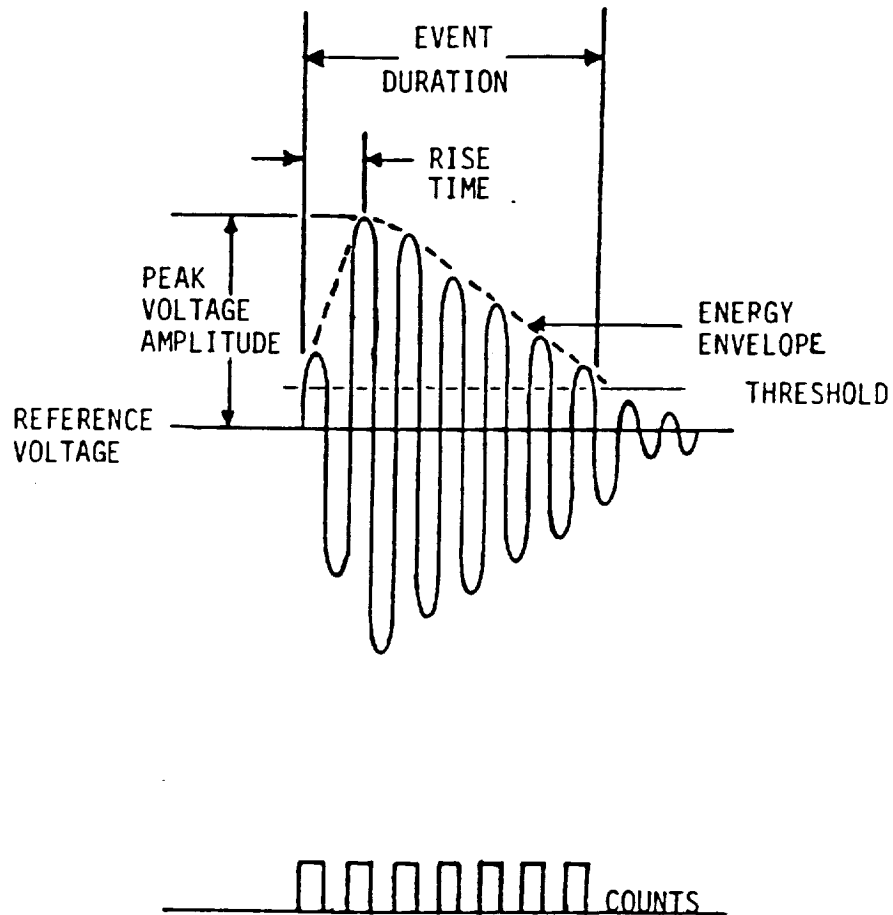
(e) Contour plot of R_{23} on 8-th layer from bottom (90° layer).

Fig. 7-16 Contour of failure parameters of the $[\pm 45/0/90]_{2s}$ plates at $P/EA=0.00255$ (concluded).

ure 7-16(d) and (e) also shows that the interlaminar shear stresses increase very rapidly on the hole boundary. The conclusion to be reached from Figs. 7-16(a)-(e) is that inplane not interlaminar stresses were responsible for failure. Interestingly enough, referring to Fig. 7-1, if the fiber failure load is considered as the failure load of the laminate, then for these quasi-isotropic laminates the numerically predicted failure load is about the same, independent of whether the plate is deformed into the one half-wave configuration or the two half-wave configuration.

7.1.5 Acoustic Emission Results

Finally, acoustic emission test results are shown. The results are presented in terms of accumulated counts. The definition of count can be understood from Fig. 7-17 [58]. Acoustic emission or stress wave emission is the phenomenon of transient wave generation due to a rapid release of strain energy caused by a structural alteration in a solid material [59]. The upper portion of Fig. 7-17 shows a typical example of an acoustic emission signal. Count is the number of waves which have a higher amplitude than a predetermined threshold amplitude. The acoustic emission test results for plate 1 and plate 2 are shown in Fig. 7-18 and Fig. 7-19. In an acoustic emission test keeping a good contact between the test specimen and acoustic emission transducer is important. Unfortunately, it is not easy in the testing of a large plate specimen. In the testing of plate 1 the good contact between the test specimen and transducer was lost. Figure 7-18 shows that acoustic emission signals were picked up only for the audible mode shape change and final failure. The data for damage accumulation between the mode transition and final failure was not collected cor-



EVENT WAVEFORM CHARACTERISTICS

COUNTS (EXAMPLE 7 COUNTS)
 AMPLITUDE (EXAMPLE 66 dB)
 DURATION (EXAMPLE 361 μ s)

Fig. 7-17 Definition of terms related to acoustic emission test [58].

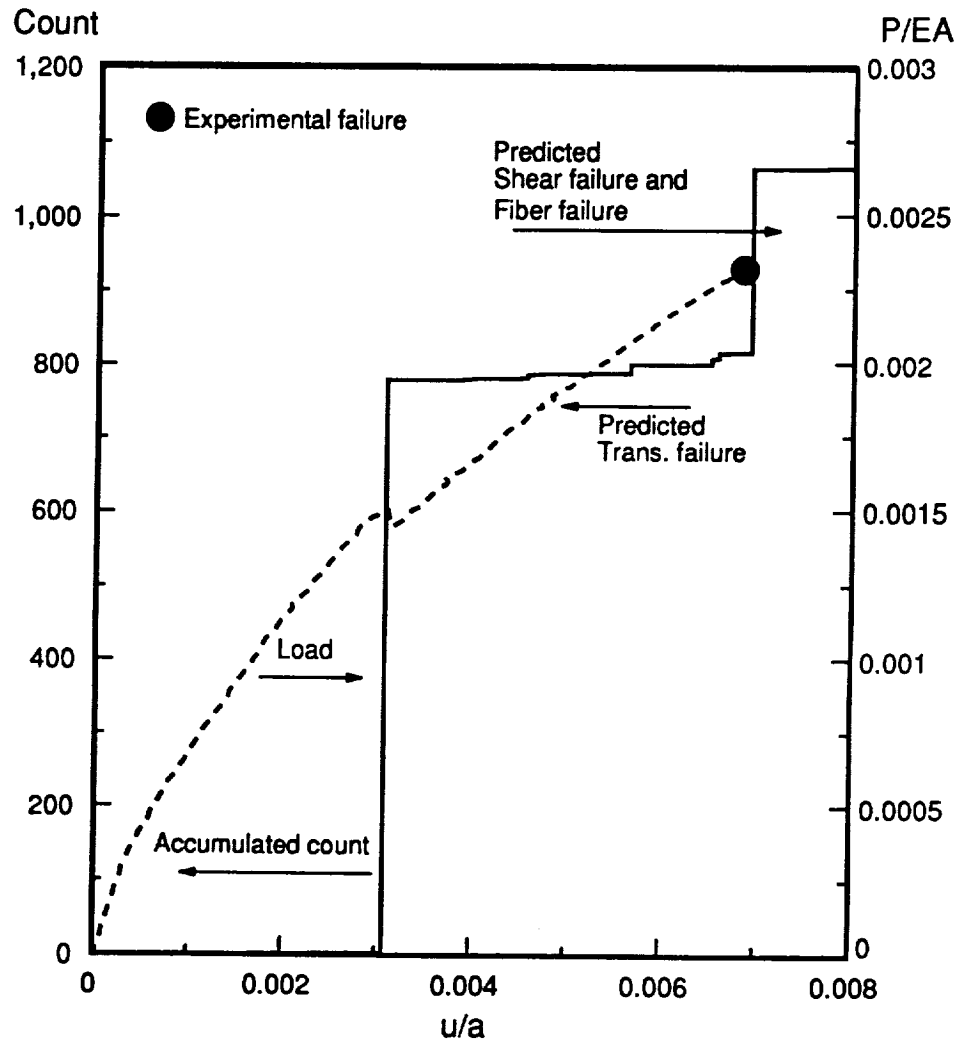


Fig. 7-18 Acoustic emission activity and load-end shortening relation for plate 1, $[\pm 45/0/90]_{2S}$.

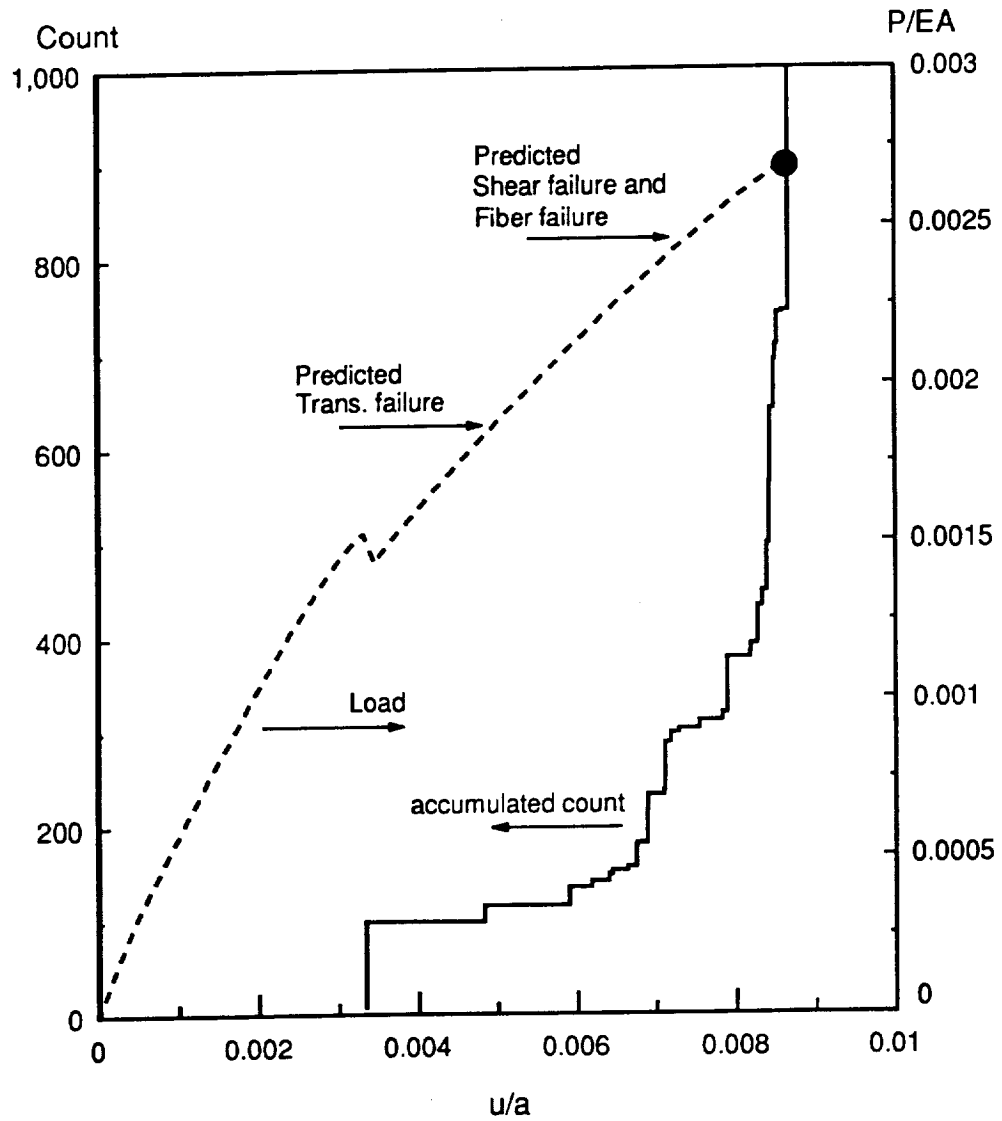


Fig. 7-19 Acoustic emission activity and load-end shortening relation for plate 2, $[\pm 45/0/90]_{2s}$.

rectly. Figure 7-19 shows good acoustic emission results. As well as the mode shape change and final failure, the damage accumulation can be observed qualitatively from the acoustic emission result. Immediately after the mode transition there was little acoustic emission. However, with increasing load, acoustic emission increased. This correlates with the numerical prediction that transverse failure occurred at a load level somewhat higher than the mode transition. However, since the acoustic emission results are only qualitative in the application here, the correlation can only be suggested. Shortly before failure the acoustic emission count increased dramatically. The high acoustic emission count can also be correlated with the numerical prediction that inplane shear failure and fiber failure was predicted to occur at similar load levels. This implies that the final failure would occur catastrophically. Practically speaking, the horizontal axis of Figs. 7-18 and 7-19, i.e., the end shortening, has the same meaning as time. Therefore, the solid circle on the load-end shortening relation representing the final failure falls on the portion of the rapid increase in acoustic emission at the final stage of count-end shortening relation.

7.2 The $[\pm 45/0_2]_{2S}$ Plates

7.2.1 Load vs. Deflection Relations

Experimental load vs. end shortening relations for the $[\pm 45/0_2]_{2S}$ plates, plates 3 and 4, and the comparison of these relations with numerical prediction are shown

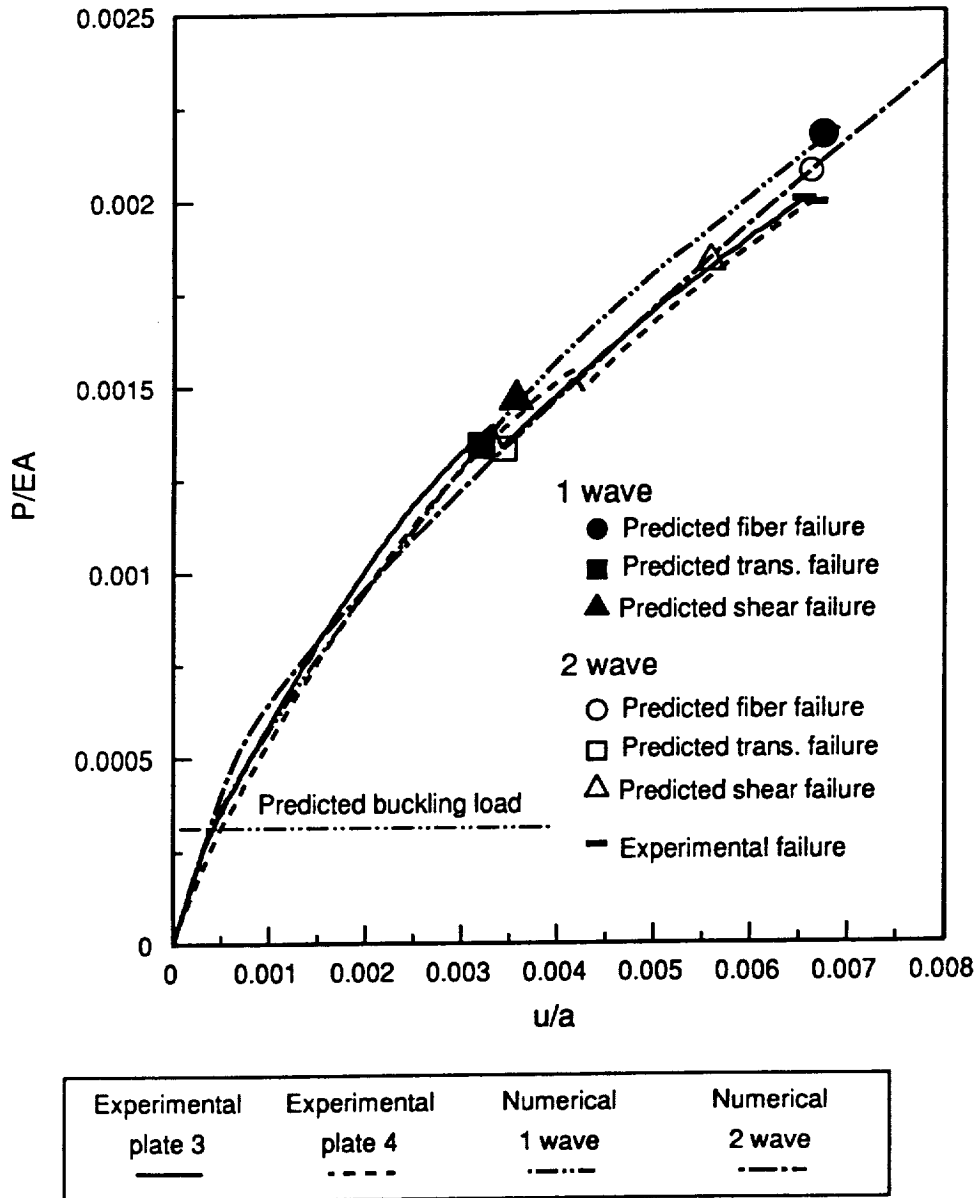


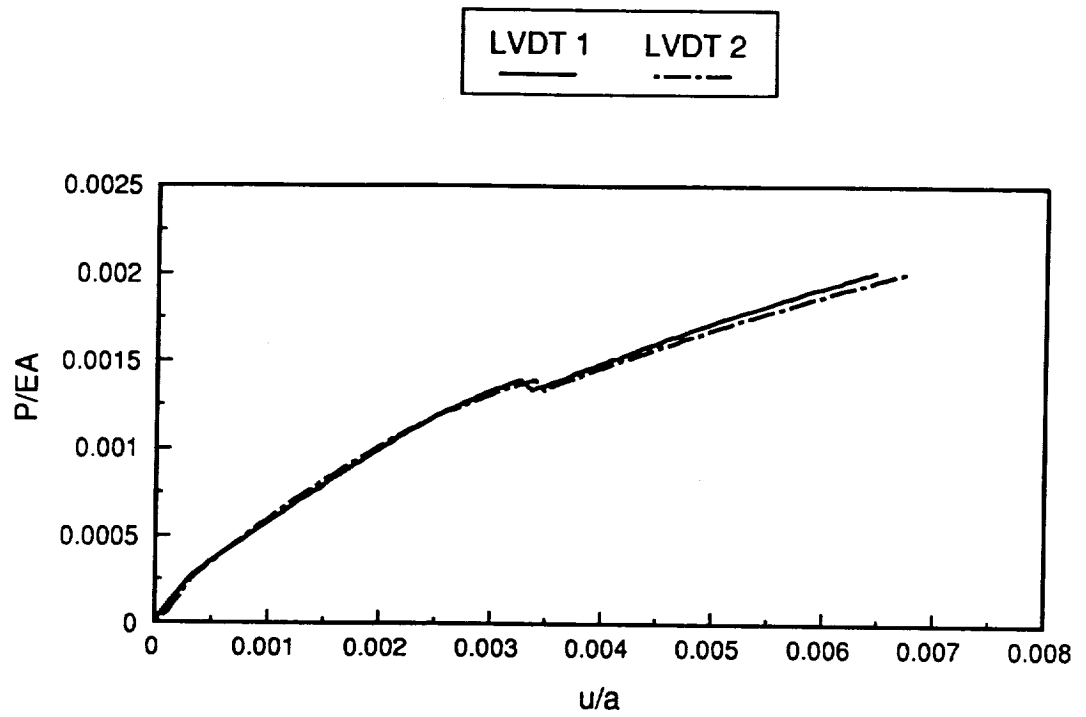
Fig. 7-20 Comparison of load vs. end shortening relations and failure loads for the $[\pm 45/0_2]_{2s}$ plates.

in Fig. 7-20. It can be seen that the results from plate 3 agree well with the numerical predictions for both the prebuckling and the postbuckling behavior. The predicted buckling load for this laminate was $P_{cr}/EA = 0.000321$, or $\bar{N}_x^{cr} = 294$ lb/in., as shown in Table 2-3. This load level is marked on Fig. 7-20. The experimental buckling loads obtained in the same way as for $[\pm 45/0/90]_{2s}$ plates were $P_{cr}/EA = 0.000300$, or $\bar{N}_x^{cr} = 275$ lb/in. for plate 3, and $P_{cr}/EA = 0.000309$, or $\bar{N}_x^{cr} = 283$ lb/in. for plate 4. Until the mode transition occurred at $P/EA = 0.00138$ ($\bar{N}_x = 1265$ lb/in.) in plate 3, the load vs. end shortening relation agreed well with the one half-wave configuration numerical prediction. Just after the mode transition, the load vs. end shortening relation agreed well with the two half-wave numerical prediction. At the final stages before failure the experimental relation became softer than the numerical prediction. This again is felt to occur because the plate began to fail and lose load bearing capability. In Fig. 7-20 plate 4 shows softer behavior than plate 3 and the numerical predictions. The reason is the same as it was with plate 2. Since plates 2 and 4 were tested first, the same mistake, excessive paint on the loaded edge, made this particular plate soft. As can be seen from Fig. 7-20, there was a difference in mode transition load between plates 3 and 4. The mode transition load of plate 4 was $P/EA = 0.00153$ ($\bar{N}_x = 1402$ lb/in.), while the mode transition load of plate 3 was $P/EA = 0.00138$, as said earlier. However, the failure loads of the two plates were nearly identical, $P/EA = 0.00201$ ($\bar{N}_x = 1842$ lb/in.) for plate 3 and $P/EA = 0.00199$ ($\bar{N}_x = 1824$ lb/in.) for plate 4. Numerically predicted failure loads for the one half-wave and the two half-wave configurations are marked on the load vs. end shortening relations. It can be seen that the experimental failure loads were very close to the predicted fiber failure load. Again it can be seen that the fiber failure load for this plate did not depend greatly on the deformed configuration. The numerically predicted fiber failure load is $P/EA = 0.00206$, the experimental failure load of plate 3 was $P/EA = 0.00201$, and ex-

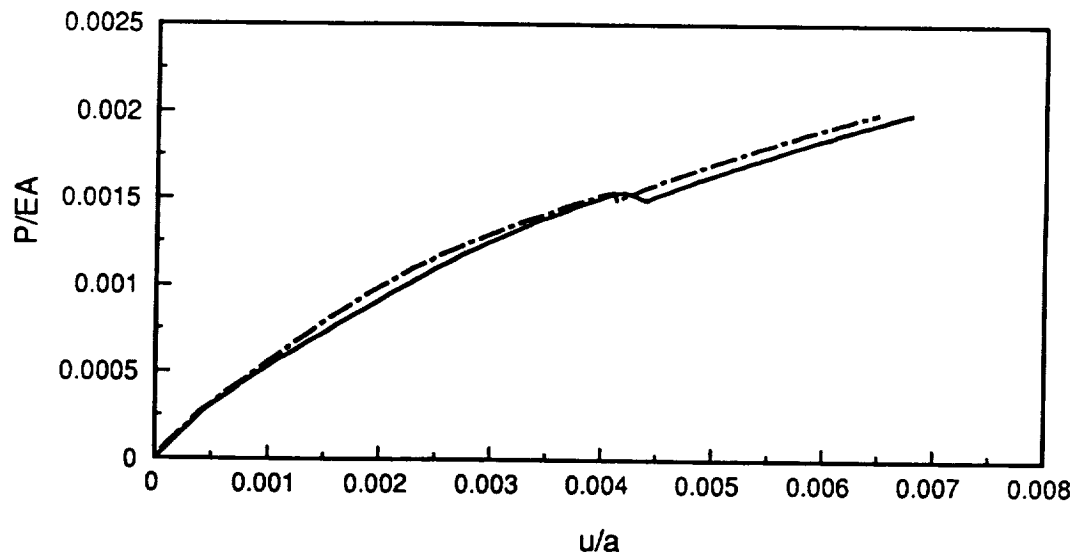
perimental failure load of plate 4 was $P/EA = 0.00199$. With the numerically predicted fiber failure load considered as the failure load of the laminate, the difference between the numerically predicted failure load and the average of the experimental failure loads is 3 %.

Figure 7-21 shows uniformity of end loading for plates 3 and 4. With plate 3 the uniformity of loading was excellent before the mode shape change. After the mode shape change the side with LVDT 2 was displaced inplane slightly more than the side with LVDT 1. With plate 4, throughout the test the side with LVDT 1 is displaced slightly more than the side with LVDT 2. Compared with the quasi-isotropic plates, after the mode transition the uniformity of loading of plate 3 was about the same as plate 1, and the uniformity of loading of plate 4 was about the same as plate 2, after the mode transition.

Load vs. out-of-plane deflection relations are shown in Fig. 7-22. It is noted that plate 4 deflected in the negative z direction. Correlations between experimental results and the one half-wave configuration are good until mode transition occurs. At the load level of the mode transition the experimental relation showed some deviation from the numerical prediction. That is because the deformed shape just before the mode transition was not predominantly one half-wave. As the load level approached the mode transition load, the deformed shape of the plate began to change from predominantly one half-wave to a mixture of one half-wave and two half-waves. As the load was increased, the deformed shape of the plate then changed rapidly to two half-waves. Numerically predicted failure loads for the two half-wave configuration are marked on the two half-wave relation. This relation corresponds to an iden-



(a) plate 3



(b) plate 4

Fig. 7-21 Comparison of displacements measured from LVDT 1 and LVDT 2 for plate 3 and plate 4.

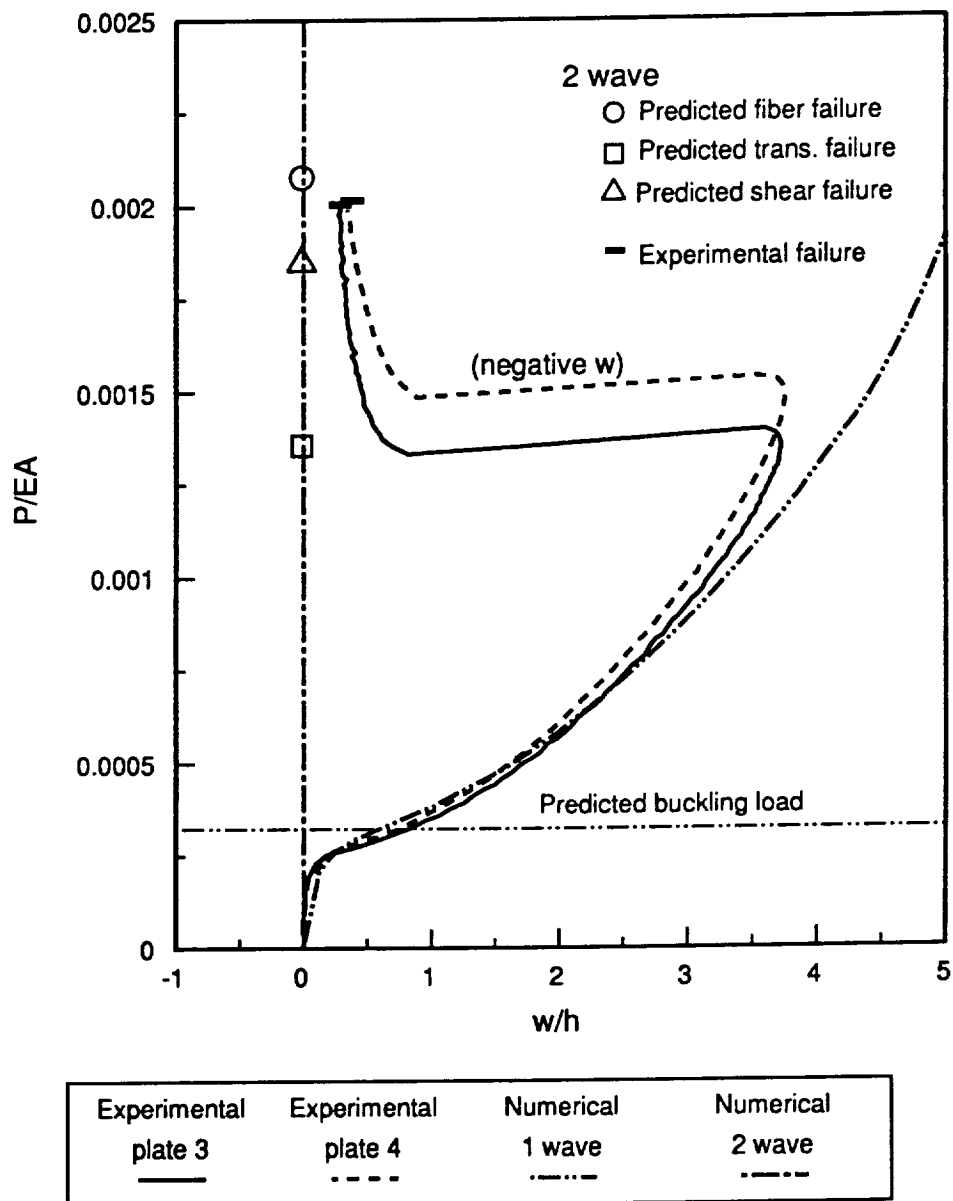


Fig. 7-22 Comparison of load vs. deflection relations and failure loads for the $[\pm 45/0_2]_{2s}$ plates.

tically zero deflection at the net-section hole edge. Again note the closeness of the failure loads for the two repeat tests.

7.2.2 Load vs. Strain Relations

Experimentally measured strains for plate 3 are shown in Fig. 7-23. Again, these grouping of strain gauges allow assessment of the overall as well as the detailed response of the plate. As with the quasi-isotropic plates, Fig. 7-4, strain gauge 1 and strain gauge 3 registered negative strains before and after the mode transition. However, the left-right symmetry of strains was not as good as it was with the quasi-isotropic plates. As was discussed for quasi-isotropic plates, by the fact that strain gauge 5 registered positive strain in the load range between the buckling load and the mode shape change load, it can be seen that before mode transition plate 3 was deformed so that strain gauge 5 was on the convex side of the deflected plate.

Experimentally measured strains for plate 4 are shown in Fig. 7-24. Strain gauge 5 in plate 4 registered negative strain all through the test. From this it can be seen that plate 4 deformed so that strain gauge 5 was on the concave side. That is, as said before, the deflected direction of plate 4 was opposite plate 3. Strain gauge 1 and strain gauge 3 registered negative strains, as with the previous plates. However, it can be seen that the responses of strain gauge 1 and strain gauge 3 of plate 4 after the mode transition were different than the responses of those gauges for other plates after mode transition. With plate 4 after the mode shape change the magnitudes of strains 1 and 3 were reduced, while in the other three plates the magnitudes

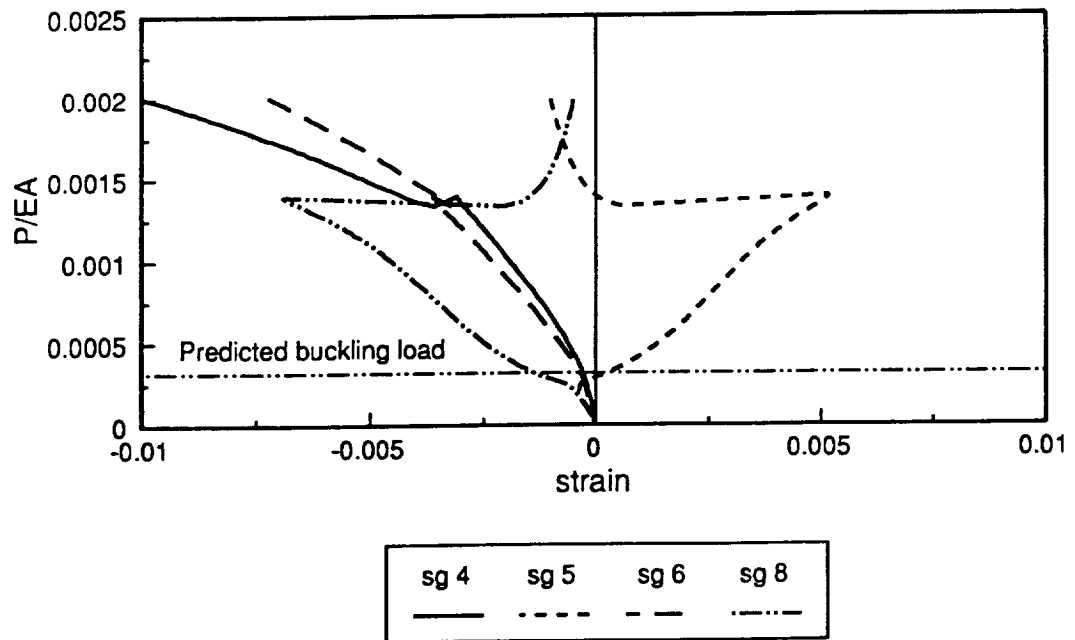
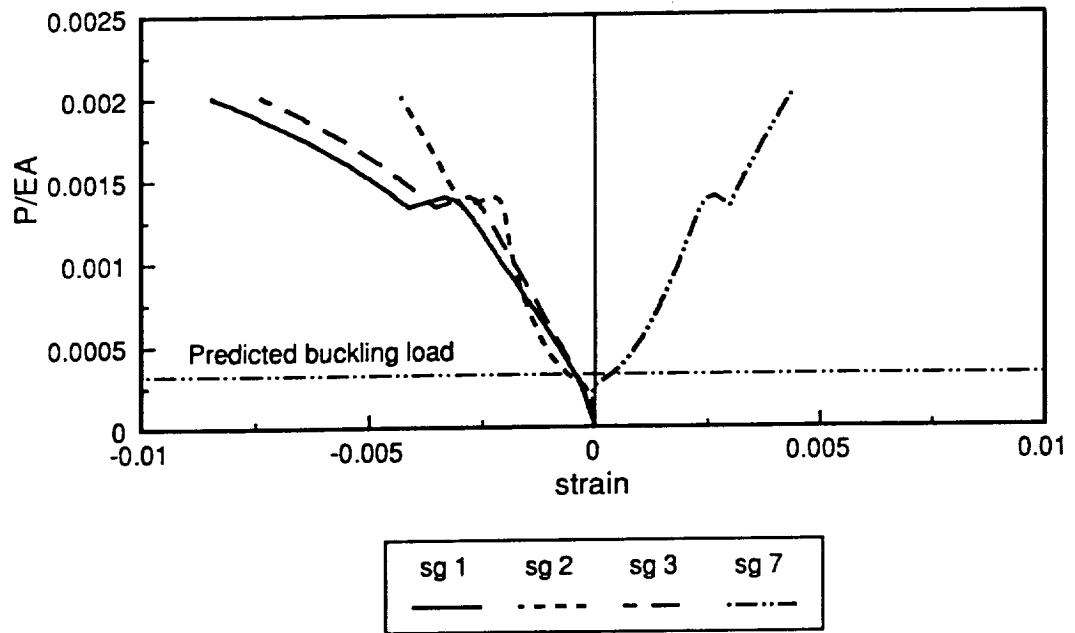


Fig. 7-23 Experimentally measured strains of plate 3.

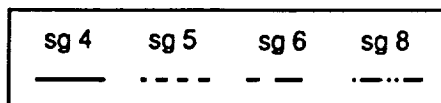
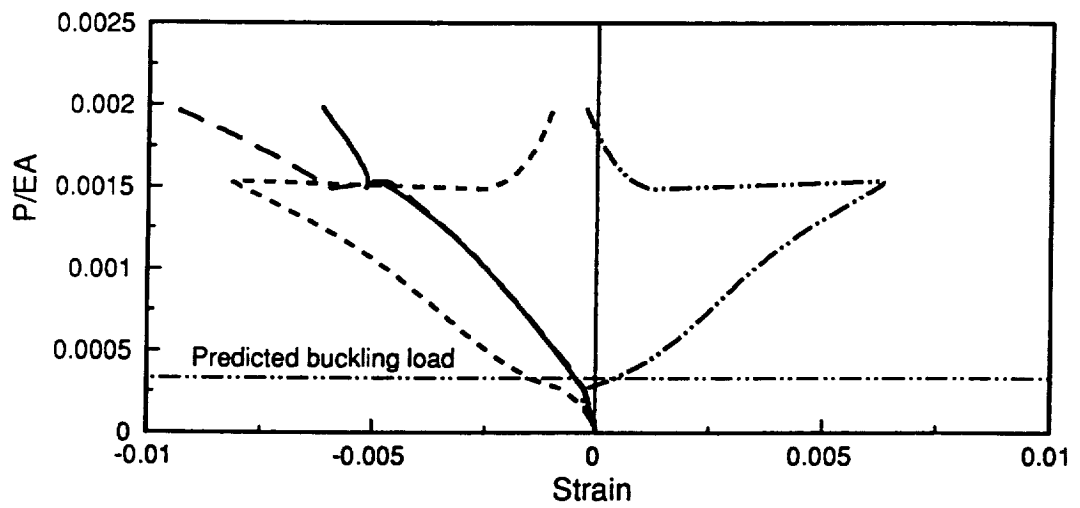
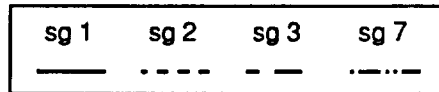
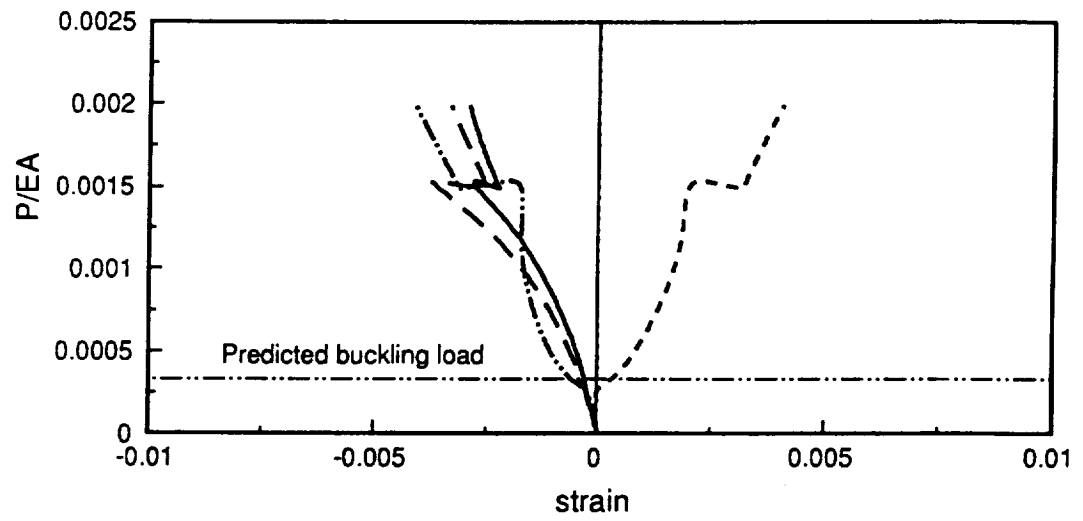
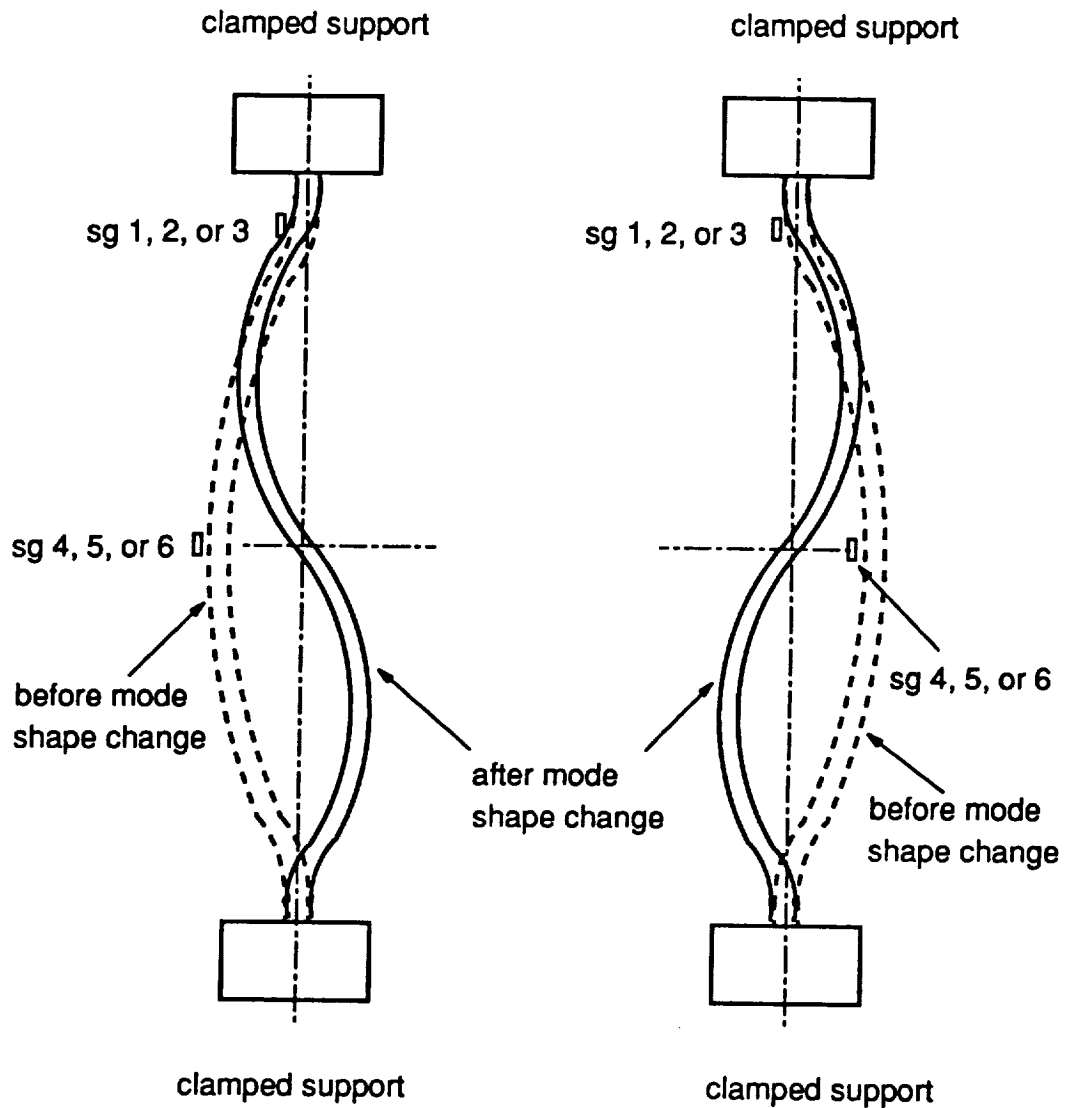


Fig. 7-24 Experimentally measured strains of plate 4.

of these strains increased. Figure 7-25 explains the mechanism related to the above strain variation. Figure 7-25(a) shows the cases of plate 1, 2, and 3. In these cases the locations of strain gauges 1 and 3 were on the locally concave side of the plate. At the locations of strain gauges 1 and 3 the out-of-plane deflections were very small. Therefore, the strains were determined predominantly by inplane compression. However, the curvature due to the out-of-plane deflection did contribute to these strains. From Fig. 7-25(a) it can be seen that the curvature at strain gauges 1 and 3 would increase, in magnitude, after the mode shape change. Therefore, strain gauges 1 and 3 became more compressive after the mode shape change. When the plate was deflected in opposite direction, as with plate 4 and as shown in Fig. 7-25(b), strain gauges 1 and 3 were on the locally convex side of the plate. After the mode transition the local curvature increased so as to produce tensile strain. Therefore, the negative strains at the locations of strain gauge 1 and 3 were relieved. In Fig. 7-24, for plate 4 strains in strain gauges 4 and 6 were identical before the mode shape change. After the mode shape change these strains showed a big difference.

Comparison of the experimentally measured and numerically predicted strains are shown in Fig. 7-26 - Fig. 7-28 for plate 3. In Fig. 7-26 the comparison of strains 2 and 7 show good correlation. Before the mode shape change the measured strains agree well with the one half-wave prediction, and after the mode shape change the measured strains agree well with the two half-wave prediction. The comparison of strains at the net-section hole edge, strains 5 and 8, show excellent correlation in Fig. 7-27. The comparisons for strain gauge 1, 3, 4, and 6 are shown in Fig. 7-28. It shows that the strains initially tended to follow the one half-wave prediction. After the mode shape change the strains generally followed the trends of the two half-wave prediction, though strain gauge 4 tended to be larger than the numerical prediction.



(a) deflection into positive z direction. (b) deflection into negative z direction.
 (plate 1, 2, and 3) (plate 4)

Fig. 7-25 Curvature change at the locations of sg1 and sg3 after mode shape change.

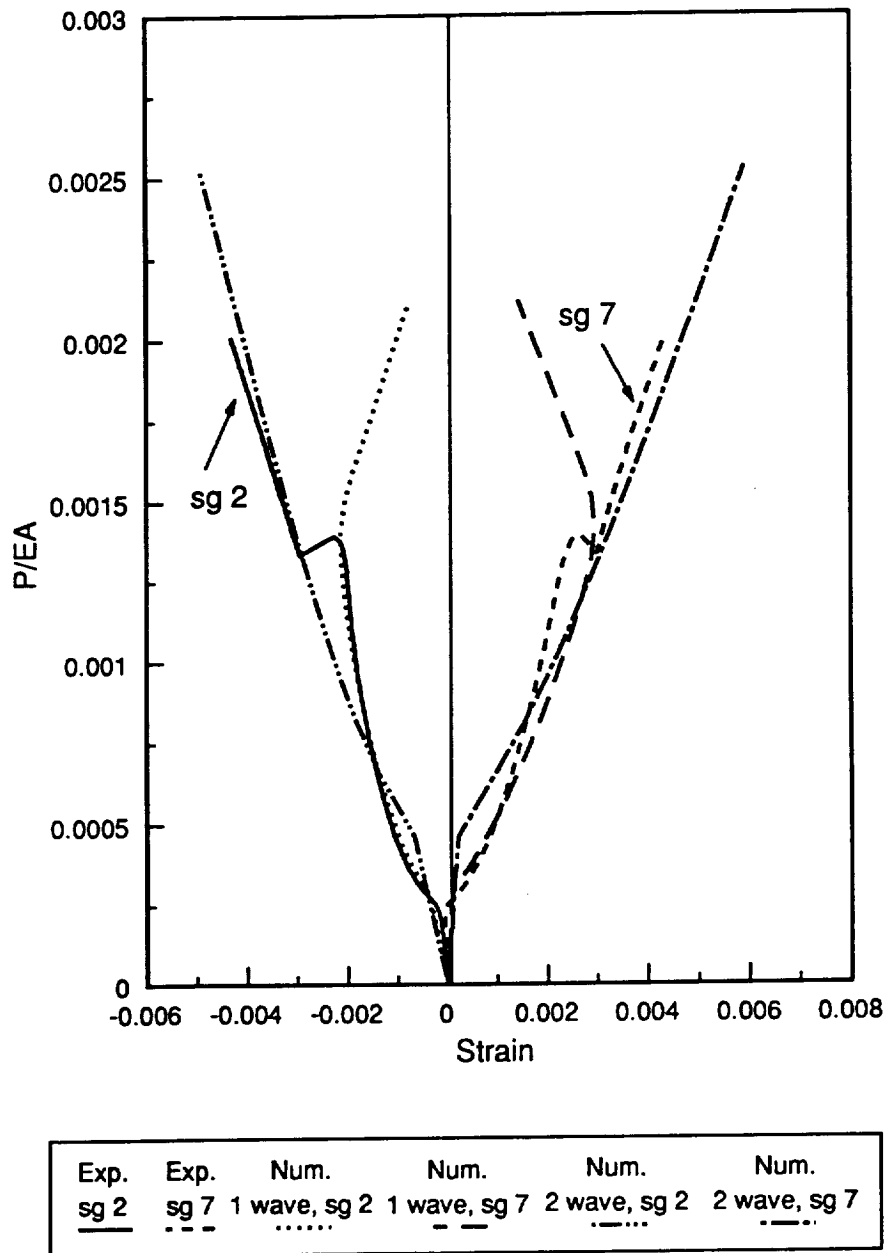


Fig. 7-26 Comparison of strains near the clamped support of plate 3.

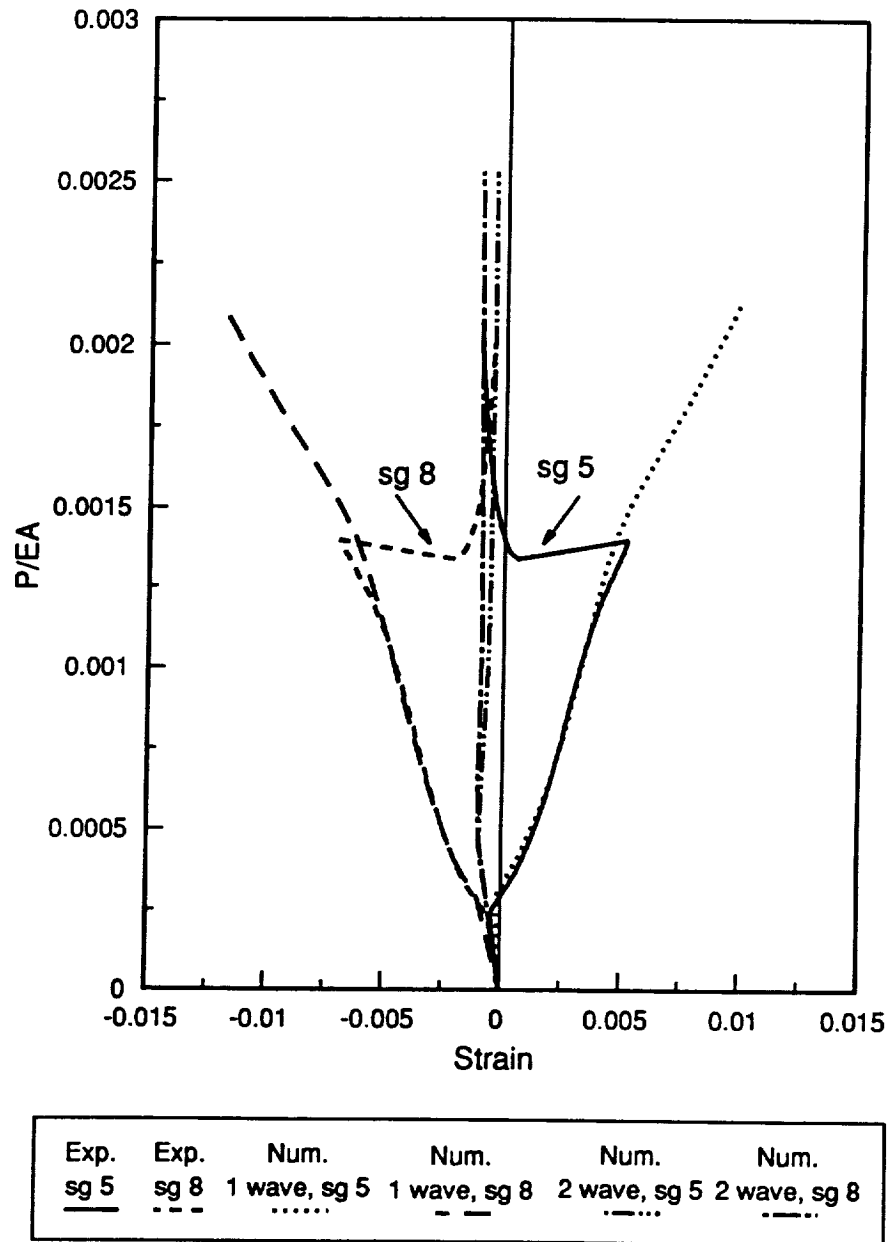


Fig. 7-27 Comparison of strains at the net-section hole edge of plate 3.

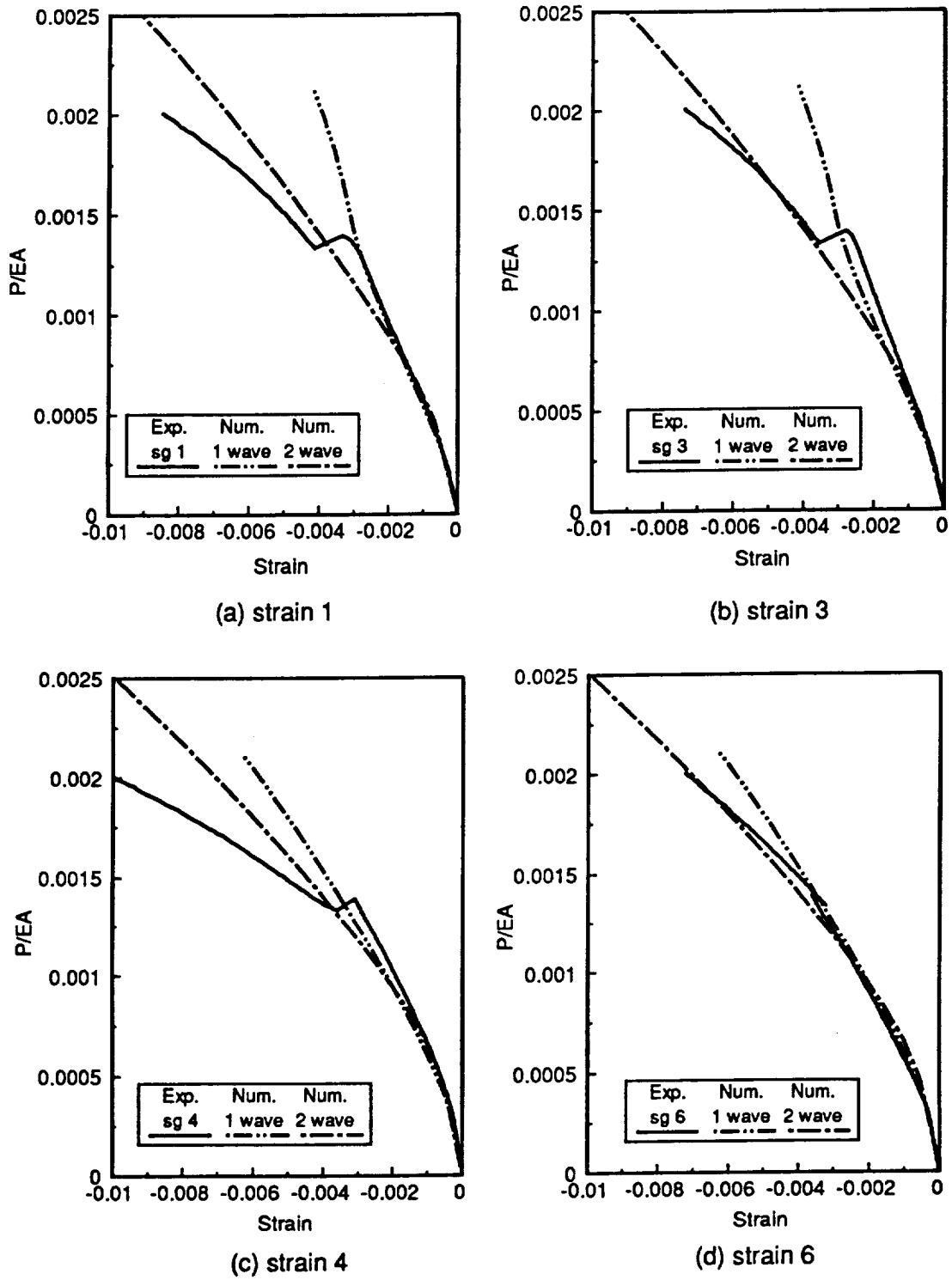
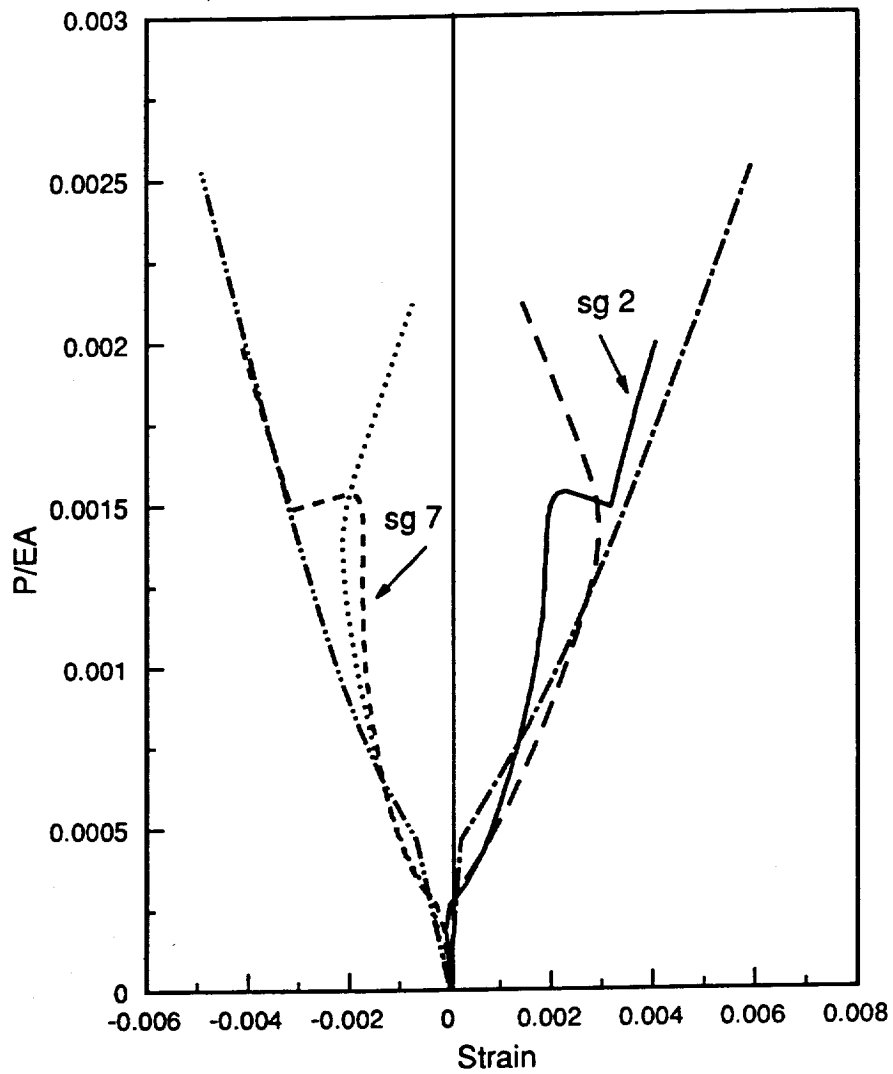


Fig. 7-28 Comparison of strains near the simple support of plate 3.

The comparison of strains for plate 4 is shown in Fig. 7-29 through Fig. 7-31. Recall that plate 4 deflected in the direction opposite to plate 3. In Fig. 7-29 the comparison of strains for strain gauge 2 and 7 show reasonable correlation. However, it can be seen in Fig. 7-30 that the strains at the net-section hole edge, strains 5 and 8, show excellent correlation with numerical prediction. Relative to Fig. 7-28 for plate 3, the load vs. strain relations for the one half-wave and two half-wave predictions for strain gauge 1 and strain gauge 3 are interchanged. Experimentally, the jump in the data for these gauges was opposite Fig. 7-28. Before the mode change the experimental data of gauges 1 and 3 followed the one half-wave prediction. After the mode change the data followed the two half-wave prediction.

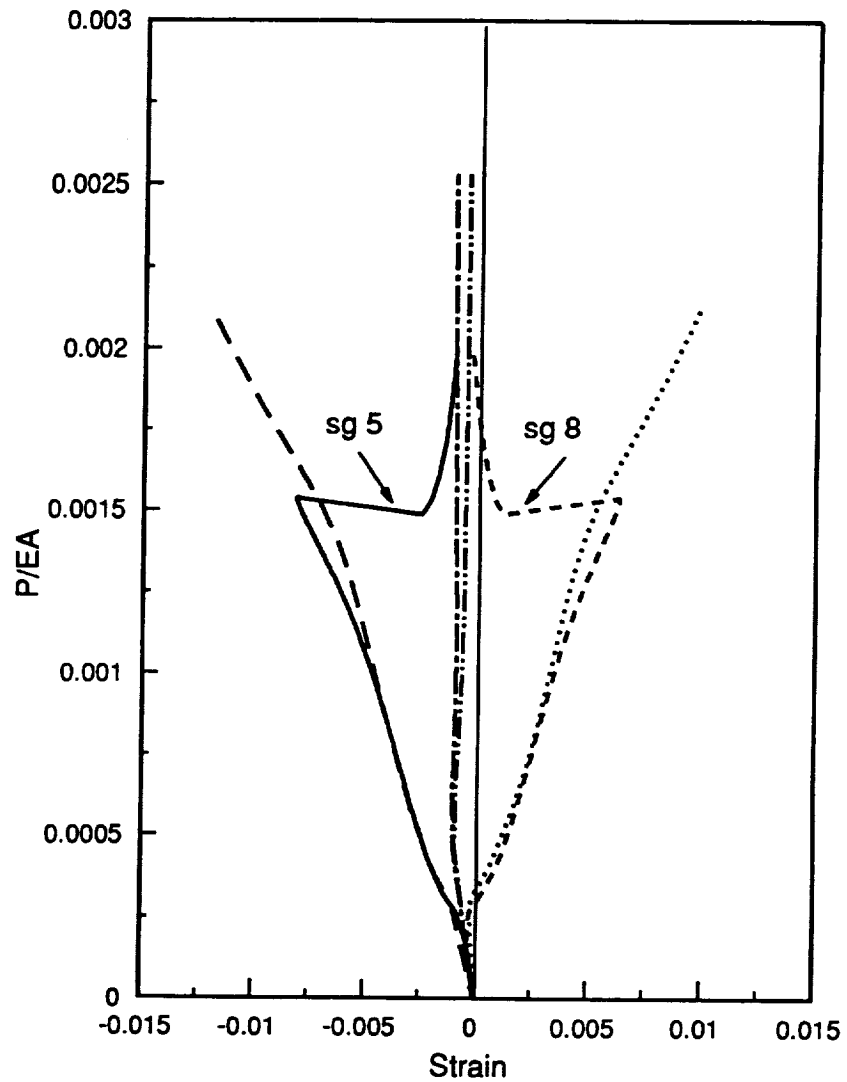
7.2.3 Shadow Moire Results

The comparisons of shadow moire fringe pattern and numerically predicted contour lines of out-of-plane displacement are shown in Fig. 7-32 for the one half-wave configuration and in Fig. 7-33 for the two half-wave configuration. The load level for the one half-wave configuration in Fig. 7-32 indicated at the volt meter, 0.151 v, corresponded to $\bar{N}_x = 824$ lb/in., and for the two half-wave configuration, 0.315 v corresponds to $\bar{N}_x = 1715$ lb/in.. For the one half-wave configuration experimental out-of-plane deflection at this load was $w/h = 3.0$, and the numerical out-of-plane deflection was $w/h = 3.1$.



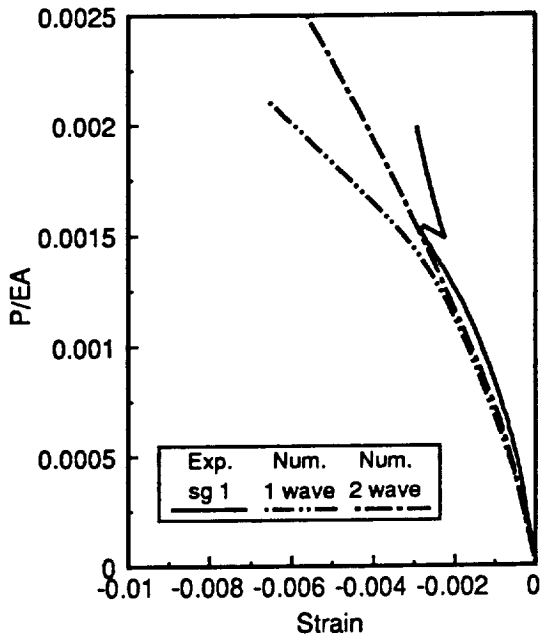
Exp.	Exp.	Num.	Num.	Num.	Num.
<u>sg 2</u>	<u>sg 7</u>	1 wave, <u>sg 7</u>	1 wave, <u>sg 2</u>	2 wave, <u>sg 7</u>	2 wave, <u>sg 2</u>

Fig. 7-29 Comparison of strains near the clamped support of plate 4.

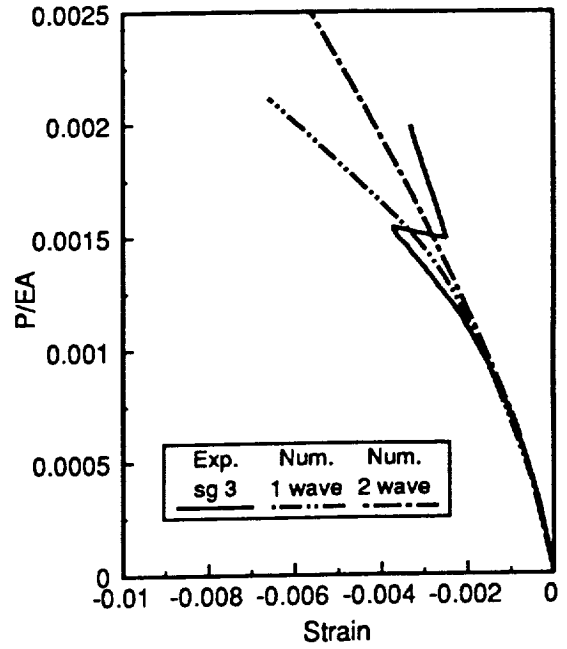


Exp.	Exp.	Num.	Num.	Num.	Num.
sg 5	sg 8	1 wave, sg 8	1 wave, sg 5	2 wave, sg 8	2 wave, sg 5
—	- - -	- . - .	-	- - - -

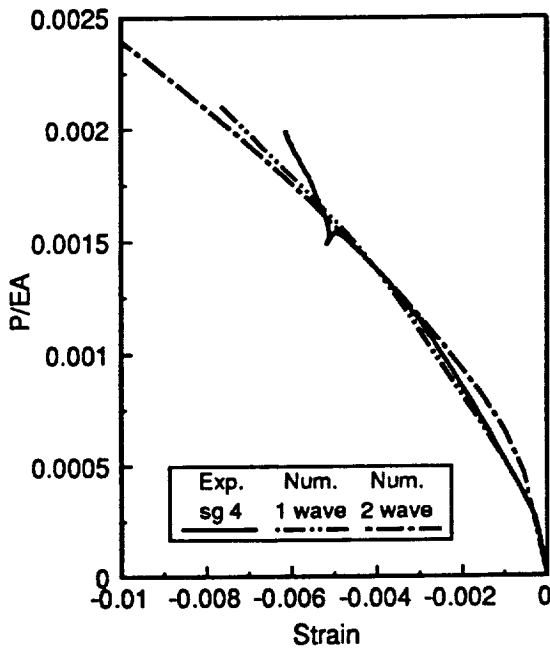
Fig. 7-30 Comparison of strains at the net-section hole edge of plate 4.



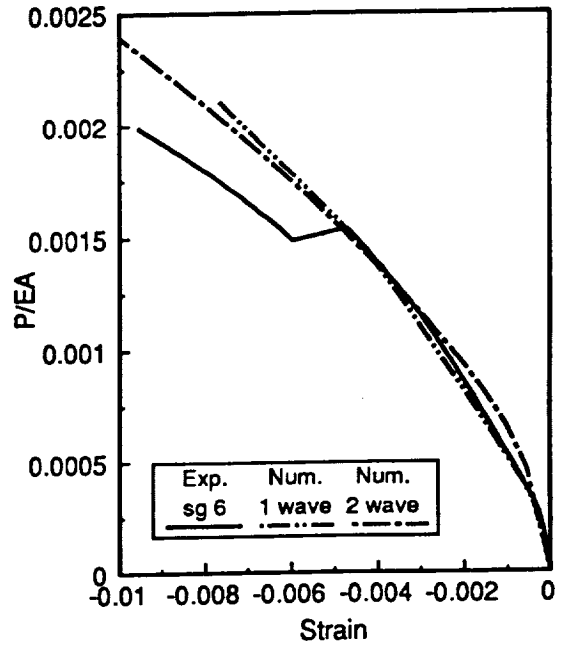
(a) strain 1



(b) strain 3



(c) strain 4



(d) strain 6

Fig. 7-31 Comparison of strains near the simple support of plate 4.

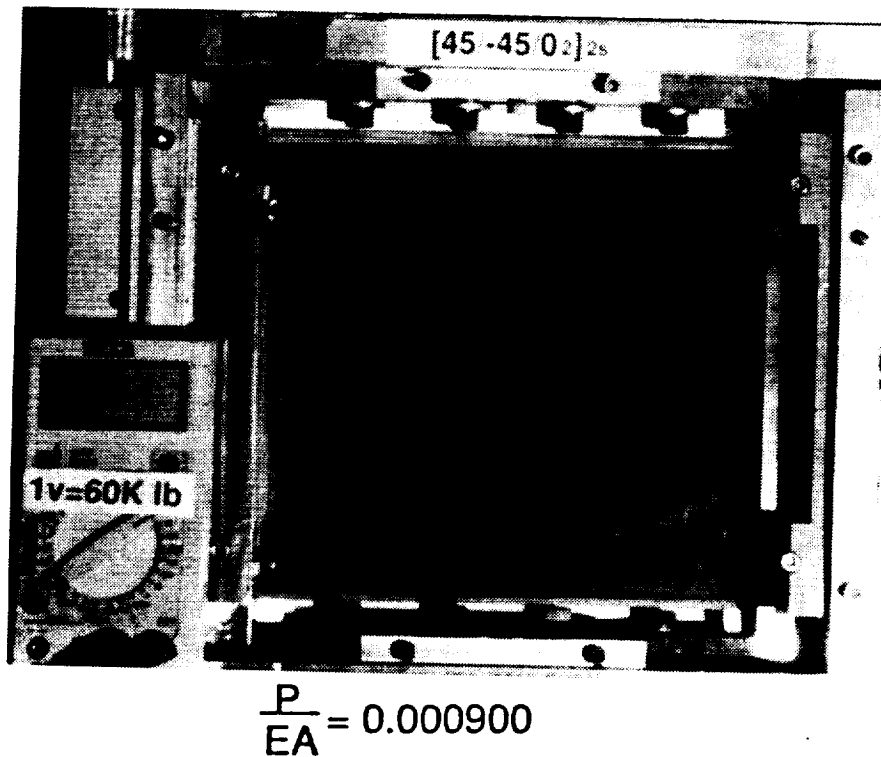
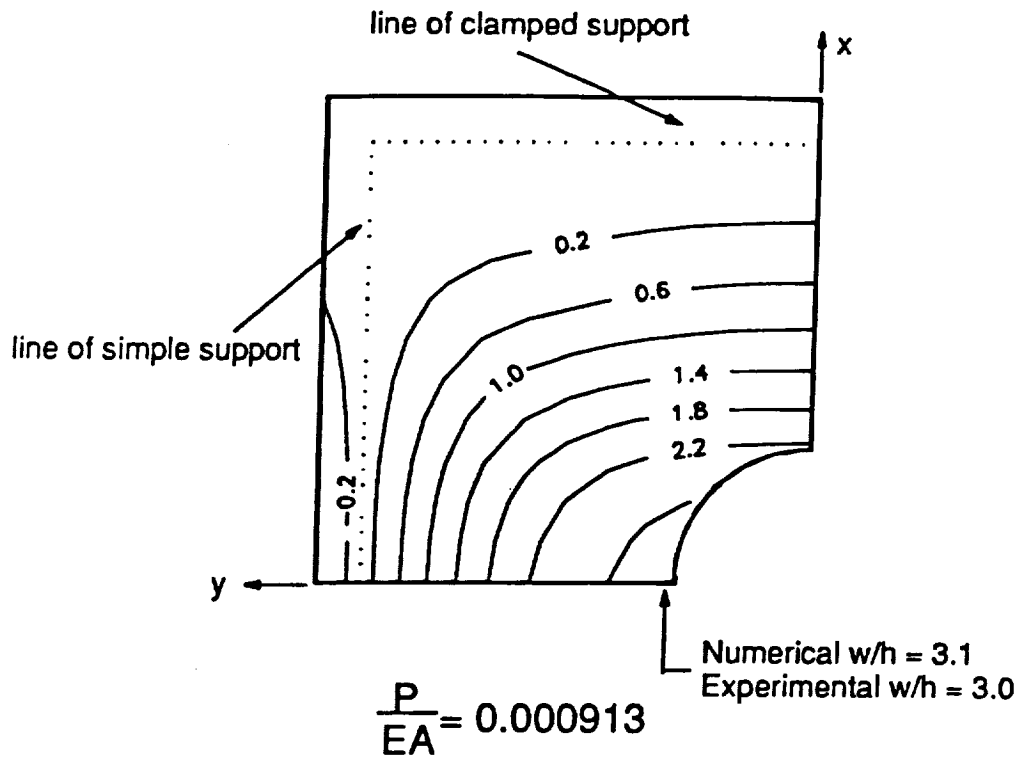
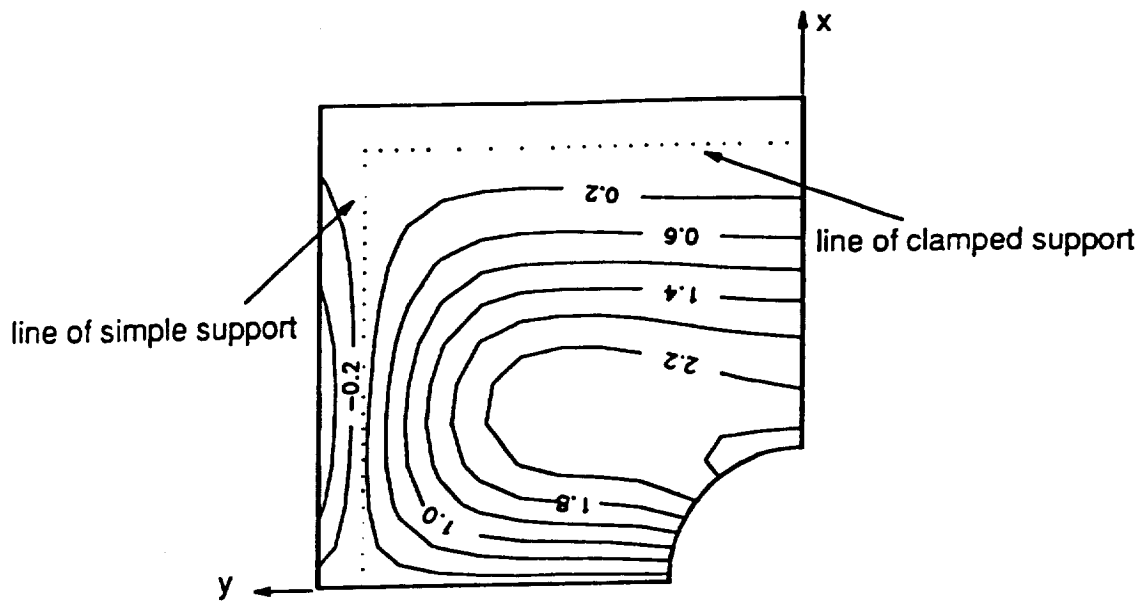
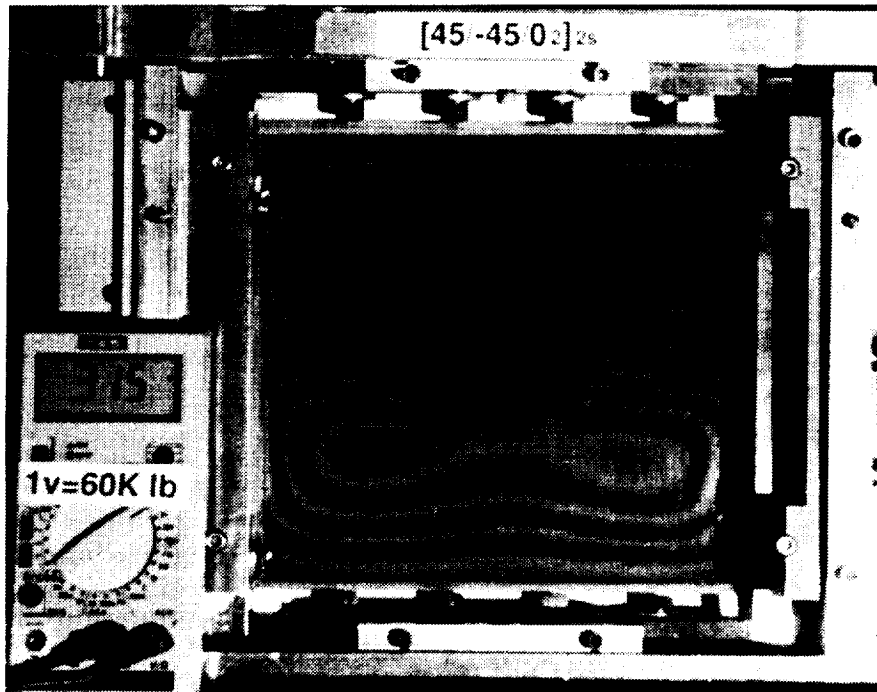


Fig. 7-32 Predicted and measured shadow moiré fringe pattern for a $[\pm 45/0_2]_{2s}$ plate with a one half-wave configuration.



$$\frac{P}{EA} = 0.00187$$



$$\frac{P}{EA} = 0.00187$$

Fig. 7-33 Predicted and measured shadow moiré fringe pattern for a $[\pm 45/0]_2$ plate with a two half-wave configuration.

7.2.4 Failure and Post-Mortem Analysis

The photograph for the failure of plate 3 is shown in Fig. 7-34. It shows that the failure occurred at the node line of the two half-wave configuration. It can be seen the failure occurred at the simply supported edge, not the hole edge. The failure for plate 4 also occurred at the simply supported edge. The contour plots of failure parameters at the load level of first fiber failure in the two half-wave configuration are shown in Fig. 7-35. From 7-35 (a) it can be seen that fiber failure is predicted at the net-section simple support. Figure 7-35(b) shows that the transverse failure region is wide spread in the center of the quarter-plate. From Fig. 7-35(c) it can be seen that inplane shear failure is predicted along the simple support and away from the net-section. From Fig. 7-35(d) and (e) it can be seen that the interlaminar shear failure parameters are very small over all of the plate. However, it can be seen that R_{13} and R_{23} are increasing rapidly at the net-section hole edge.

7.2.5 Acoustic Emission Results

The acoustic emission results are shown in Fig. 7-36 for plate 3 and in Fig. 7-37 for plate 4. These results also show clearly the audible mode shape change and the final failure event. Figures 7-36 and 7-37 show some acoustic emission activity occurred before the mode shape change. The activity correlates well with numerically predicted transverse failure just before the mode shape change. These figures also show increasing acoustic emission activity near the load level at which the inplane

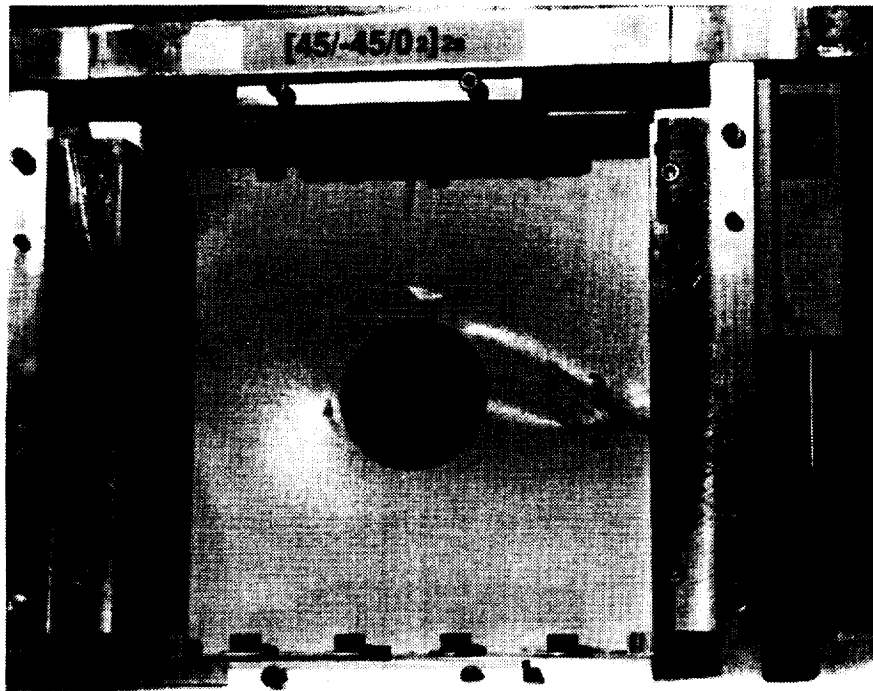
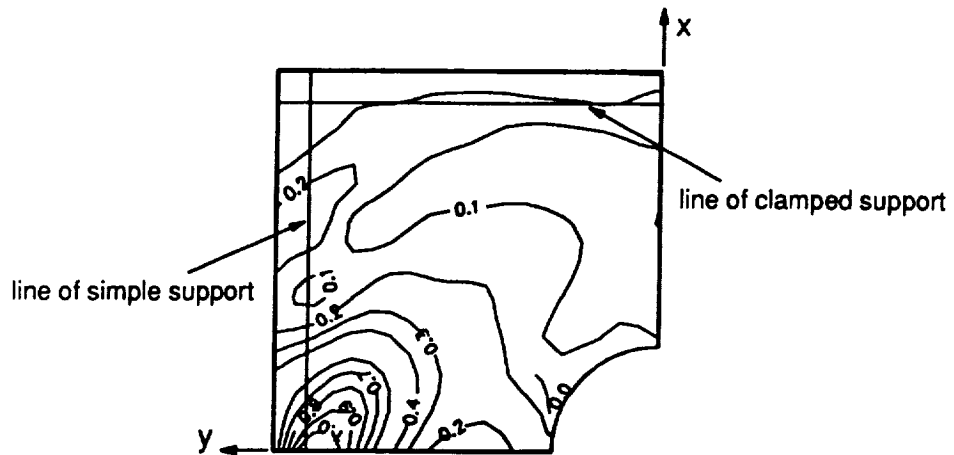
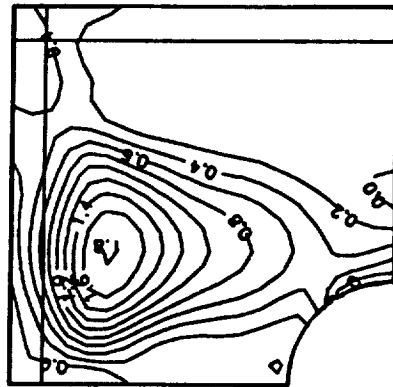


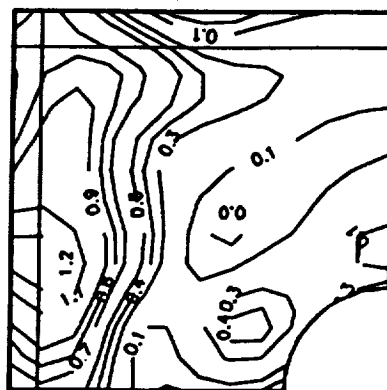
Fig. 7-34 Failed $[\pm 45/0]_{2s}$ plate in the fixture.



(a) Contour plot of R_1 on 1-st layer from bottom (45° layer).

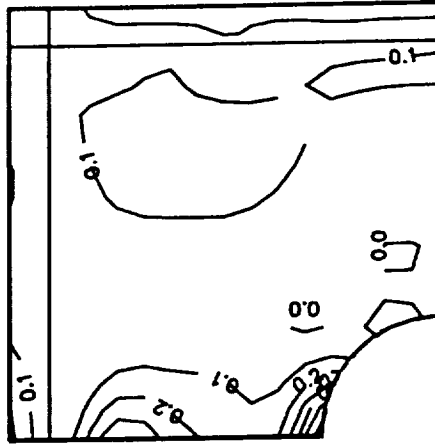


(b) Contour plot of R_2 on 14-th layer from bottom (0° layer).

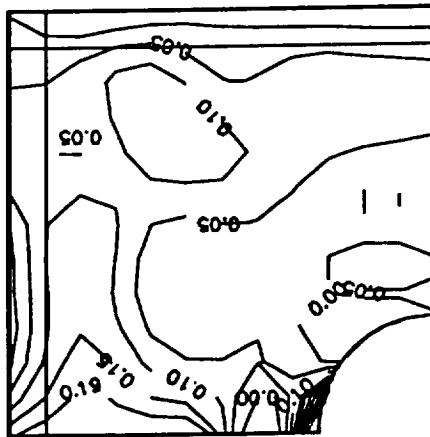


(c) Contour plot of R_{12} on 16-th layer from bottom (45° layer).

Fig. 7-35 Contour of failure parameters of the $[\pm 45/0_2]_{2s}$ plate at $P/EA=0.00206$ (continued).



(d) Contour plot of R_{13} on 8-th layer from bottom (0° layer).



(e) Contour plot of R_{23} on 6-th layer from bottom (-45° layer).

Fig. 7-35 Contour of failure parameters of the $[\pm 45/0_2]_{2s}$ plate at $P/EA = 0.00206$ (concluded).

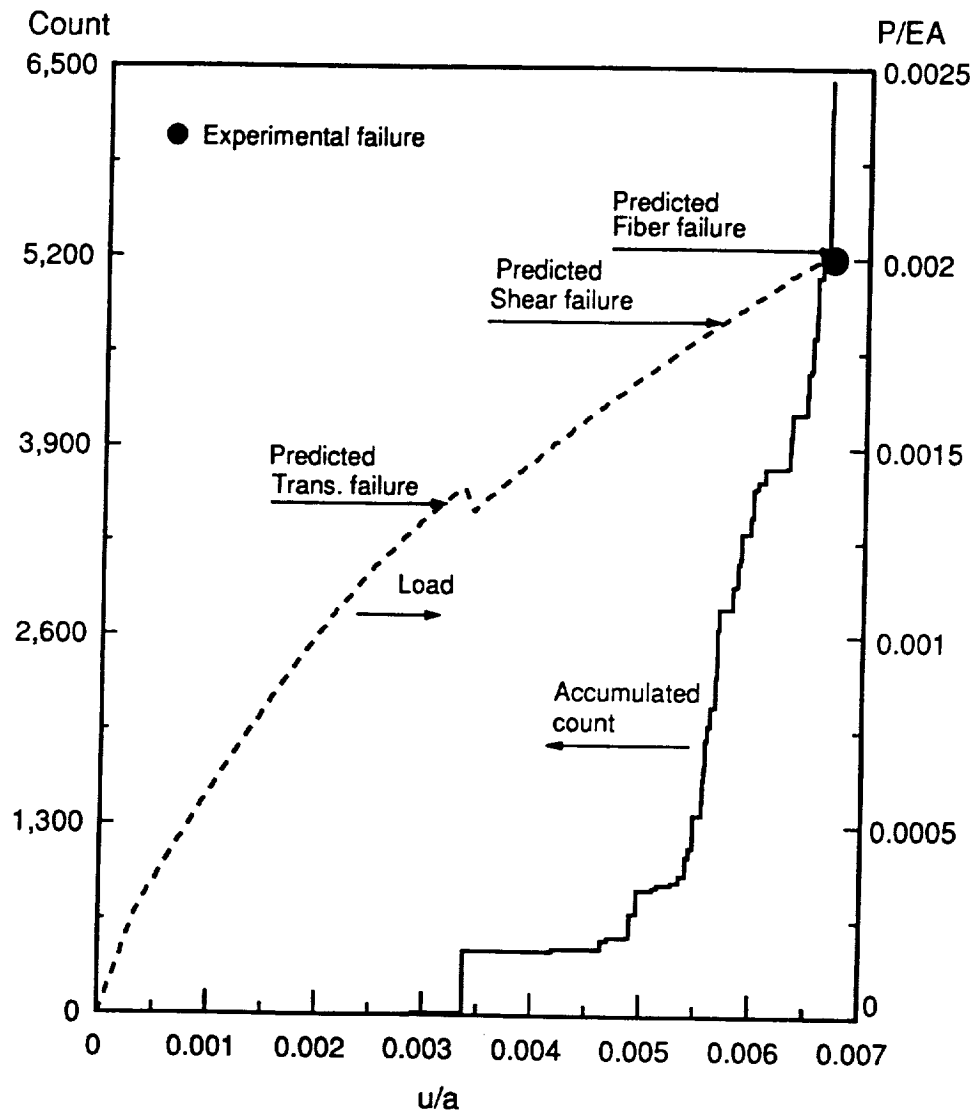


Fig. 7-36 Acoustic emission activity and load-end shortening relation for plate 3, $[\pm 45/0_2]_{2s}$.

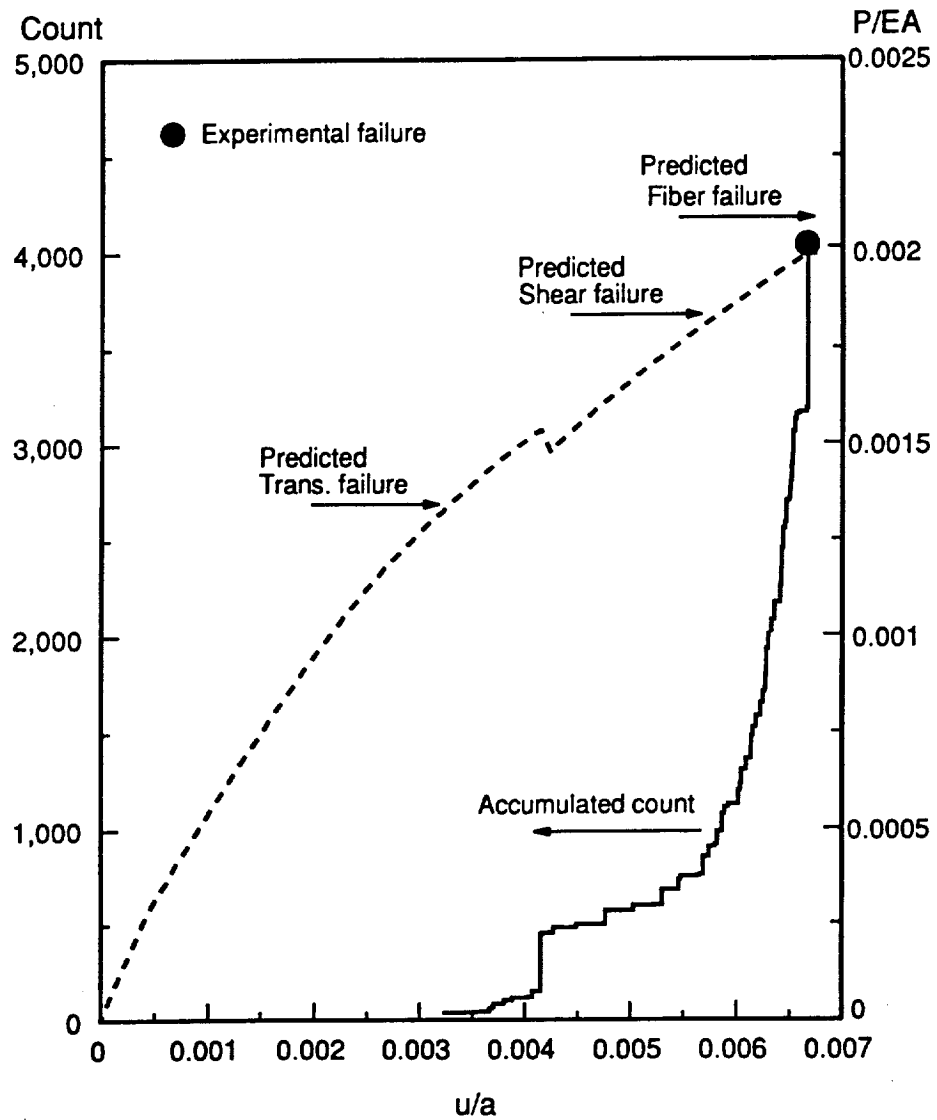


Fig. 7-37 Acoustic emission activity and load-end shortening relation for plate 4, $[\pm 45/0_2]_{2s}$.

shear failure is predicted. Qualitatively, the the numerical prediction for this plate agrees with the acoustic emission test results.

7.3 The $[\pm 45/0_6]_s$ Plates

7.3.1 Load vs. Deflection Relations

Figure 7-38 shows experimental load vs. end shortening relations for $[\pm 45/0_6]_{2s}$ plates, plate 5 and plate 6. With this laminate a mode shape change did not occur. Until the plate failed, the mode shape remained in the one half-wave configuration in both the loading and transverse directions. The figure shows the excellent repeatability of the load-end shortening relations for the plates. The numerically predicted buckling load shown in Table 2-3, $P_{cr}/EA = 0.000245$, or $\bar{N}_x^{cr} = 318$ lb/in., is marked on Fig. 7-38. Experimental buckling loads were $P_{cr}/EA = 0.000241$, or $\bar{N}_x^{cr} = 301$ lb/in. for plate 5, and $P_{cr}/EA = 0.000227$, or $\bar{N}_x^{cr} = 283$ lb/in. for plate 6. It can be seen that there was a difference in the experimental failure loads between plate 5 and plate 6. Plate 5 failed when $P/EA = 0.00143$ ($\bar{N}_x = 1786$ lb/in.), and plate 6 failed when $P/EA = 0.00162$ ($\bar{N}_x = 2023$ lb/in.). Figure 7-38 shows that the numerically predicted load-end shortening relation agrees very well with experimental results. The numerically predicted failure loads are marked on the numerical load-end shortening relation curve. The experimental average failure load of plate 5 and plate 6 was $P/EA = 0.00154$. The numerically predicted fiber failure load listed in Table 5-2 was

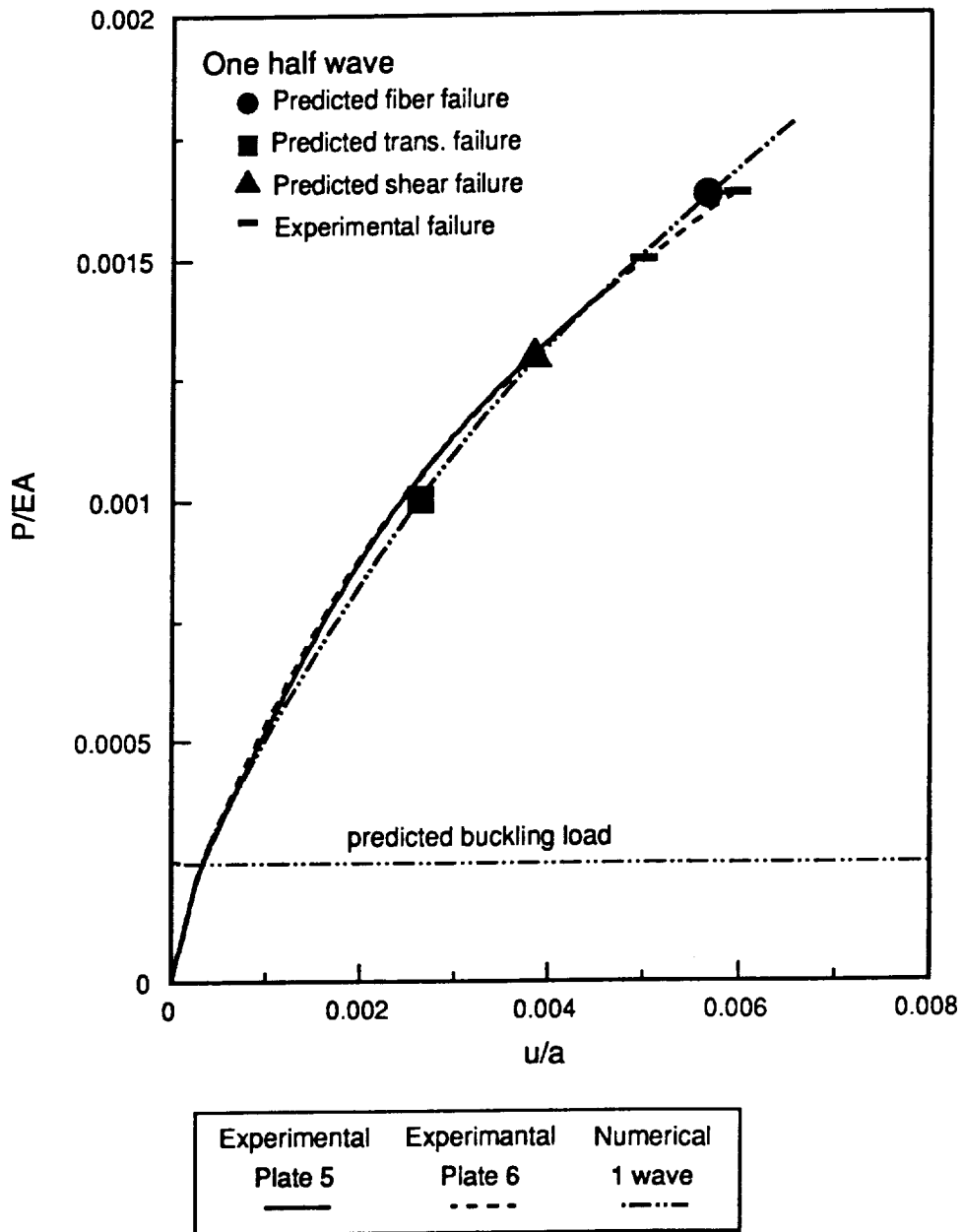
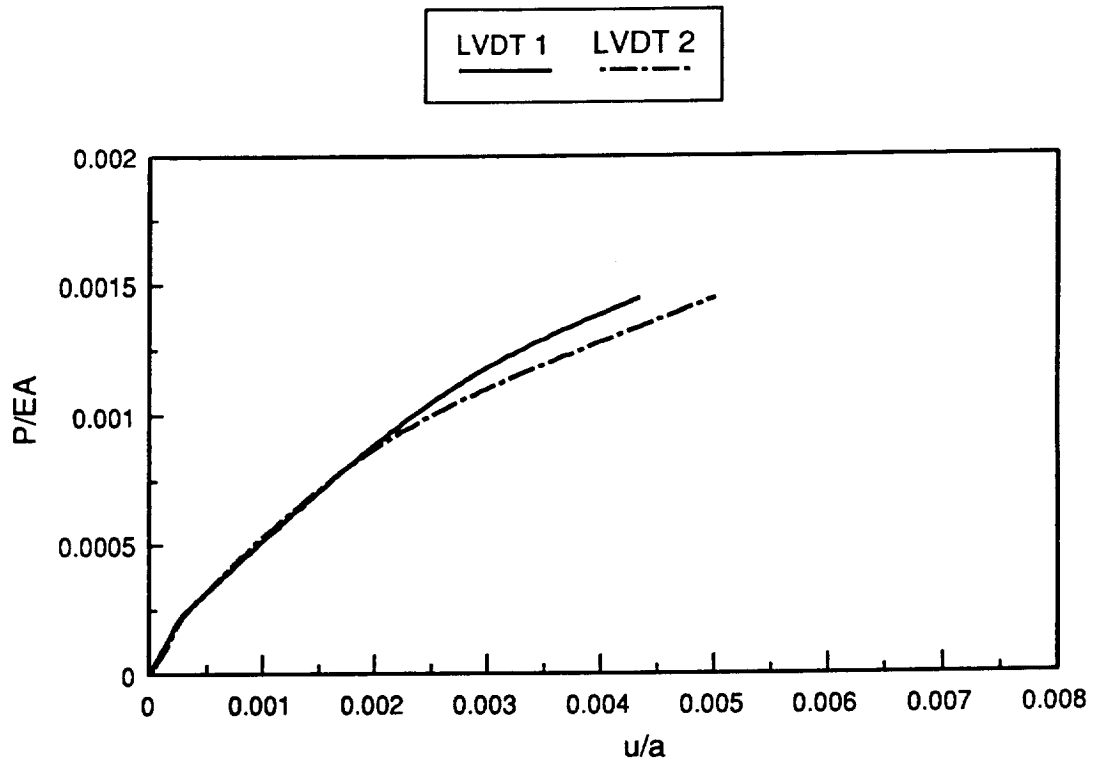


Fig. 7-38 Comparison of load vs. end shortening relations and failure loads for the $[\pm 45/0_8]_s$ plates.

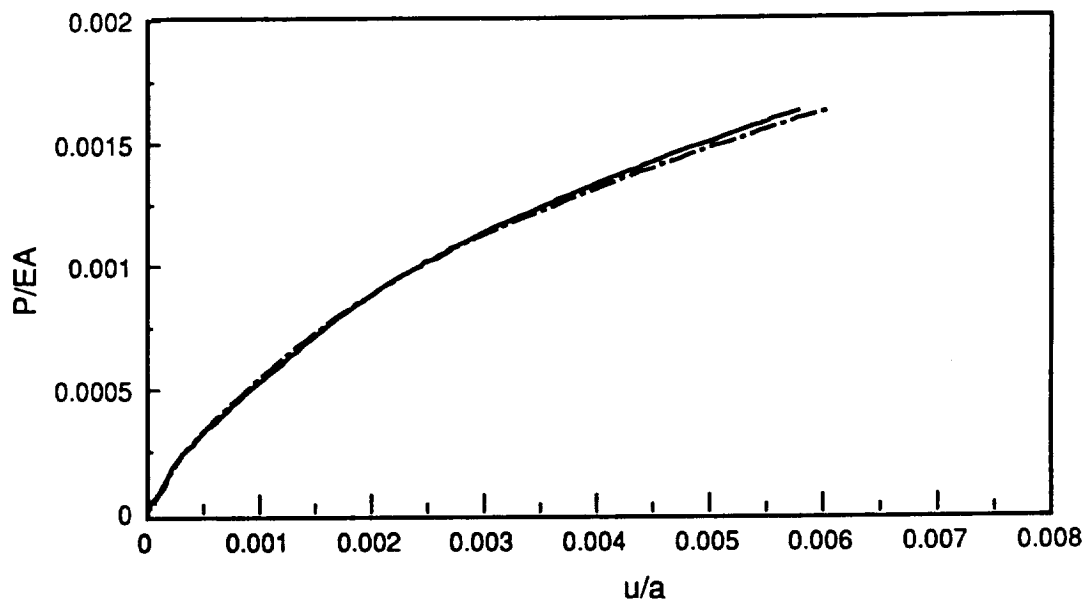
$P/EA = 0.00163$. With the fiber failure load considered as the final failure load, the numerical prediction is in error relative to the experimental result by 6 %.

Figure 7-39 shows the uniformity of loading for plate 5 and plate 6. It can be seen that the plate 6 was loaded with left-right uniformity to failure. However, with plate 5 the uniformity of the loading was not maintained for $P/EA > 0.001$. After the tests it was found that plate 6 failed with about equal damage on both the left and right sides. However, plate 5 failed on only one side. From Fig. 7-39 it can be deduced that the failure of plate 6 progressed equally on both sides, and the failure of plate 5 began on the side of LVDT 2 and the damage on the side of LVDT 2 increased as the load increased. As that side of the plate was damaged more and more, the displacement increased more and more relative to the other side. The difference between the LVDT 1 and LVDT 2 at the maximum load was 13 % of the average end displacement.

The comparison of experimental and numerically predicted load vs. out-of-plane deflection relations is shown in Fig. 7-40. It should be noted that both plates deflected in the negative z direction. As with the load vs. end shortening relation of Fig. 7-38, plate 5 and plate 6 followed exactly the same load vs. out-of-plane deflection relation. In addition, the relation showed good agreement with numerical prediction. From Fig. 7-40 it can be seen that plate 5 failed with a maximum deflection level of $w/h = 4.55$ at the center of the plate, and plate 6 failed with a maximum deflection level of $w/h = 5.0$. This is a rather large out-of-plane deflection. The previous four plates had relatively small maximum deflection when they failed, since those plates were deformed in the two half-wave configuration.



(a) plate 5



(b) plate 6

Fig. 7-39 Comparison of displacements measured from LVDT 1 and LVDT 2 for plate 5 and plate 6.

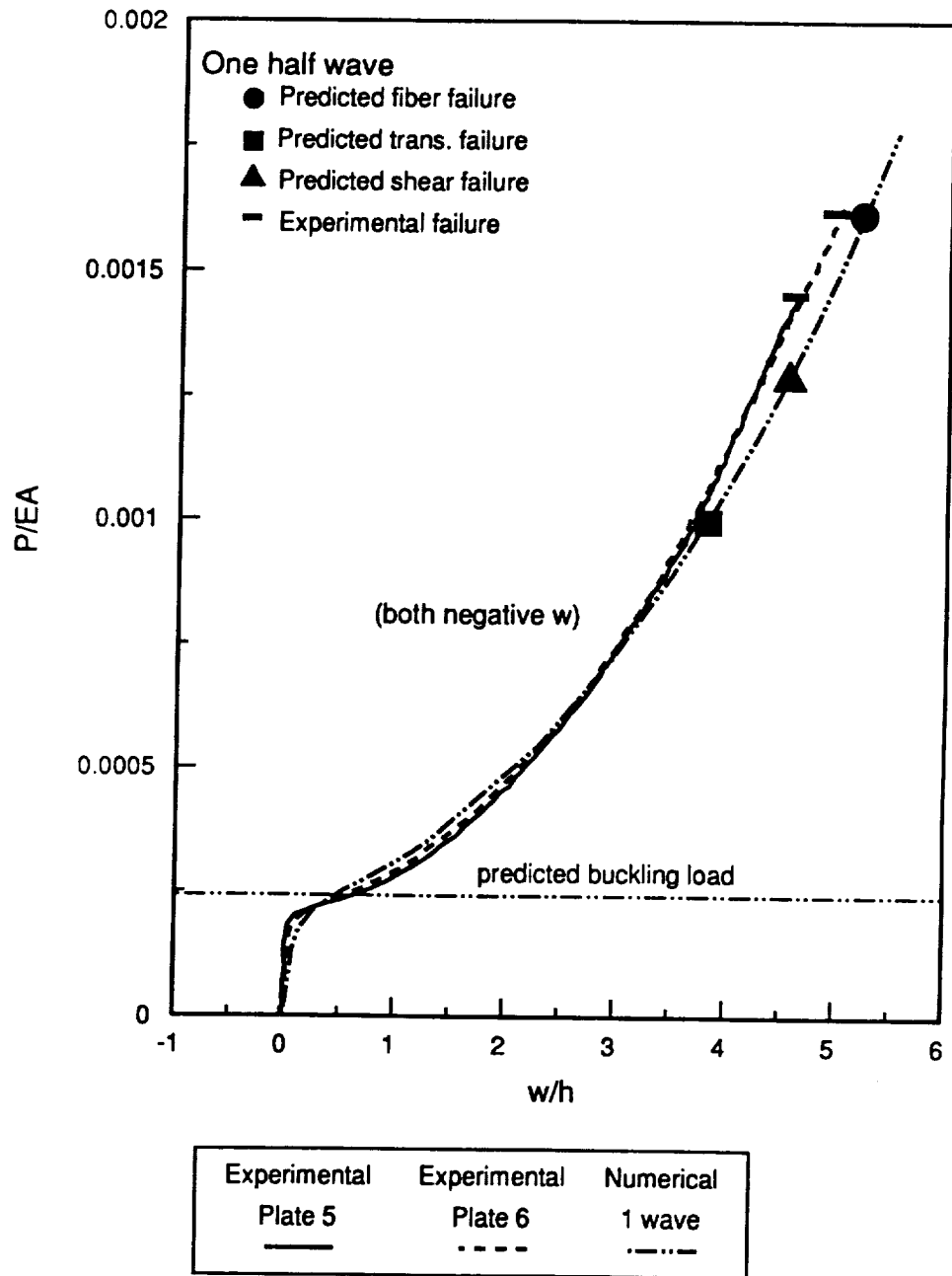


Fig. 7-40 Comparison of load vs. deflection relations and failure loads for the $[\pm 45/0]_s$ plates.

7.3.2 Load vs. Strain Relations

Figure 7-41 shows the experimentally measured strains for plate 5. It can be seen that the response of strain 1 and strain 3 agreed with the measurement of LVDT 1 and LVDT 2 shown in Fig. 7-39, the displacement of LVDT 2 being greater than LVDT 1. By the fact that strain gauge 5 registered negative strain until plate failed, it can be realized that the plate was bowed so that the strain gauge 5 was on the concave side of the deflected plate. The experimentally measured strains for plate 6 are shown in Fig. 7-42. From the response of strain gauges 1, 3, 4, and 6 it can again be seen that the response of plate 6 was more symmetrical than plate 5. Strain gauge 5 of plate 6 also registered compressive strain until the plate failed. Therefore, it can be understood that plate 6 also deflected in the same direction as plate 5.

The comparison of numerically predicted strains and experimentally measured strains are shown in Fig. 7-43 - Fig. 7-45 for plate 5 and in Fig. 7-46 - Fig. 7-48 for plate 6. Generally, plate 6 shows better experimental-numerical correlation than plate 5. In light of the lack of left-right symmetry of the response with plate 5, this was expected.

7.3.3 Shadow Moire Results

Figure 7-49 shows the moire fringe pattern at the load level of $P/EA = 0.0008$, or $\bar{N}_x = 993$ lb/in.. The pattern is compared with the numerically predicted out-of-plane displacement contour drawing. At this load level the experimental out-of-plane deflection at the net-section hole edge was $w/h = 3.17$, and numerically predicted out-

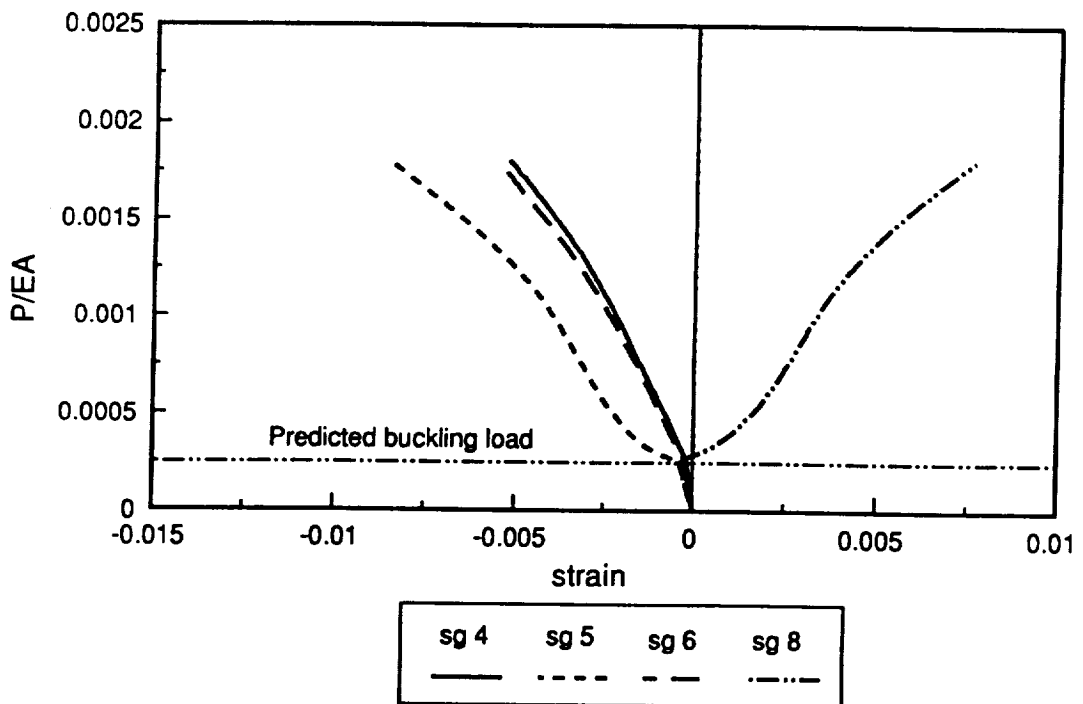
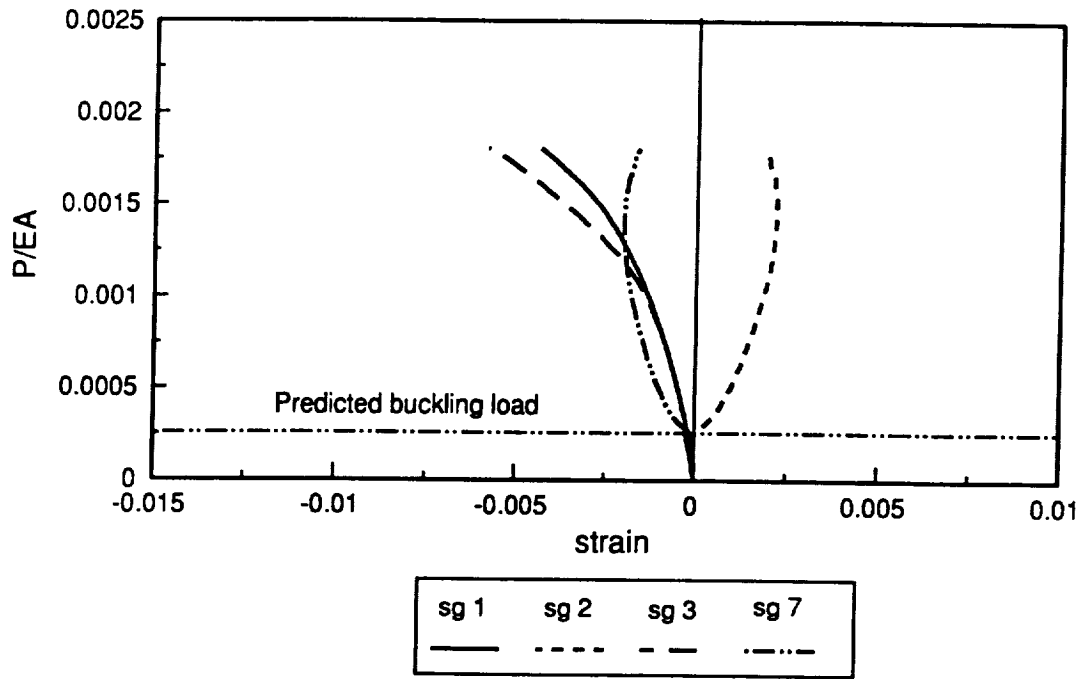


Fig. 7-41 Experimentally measured strains of plate 5.

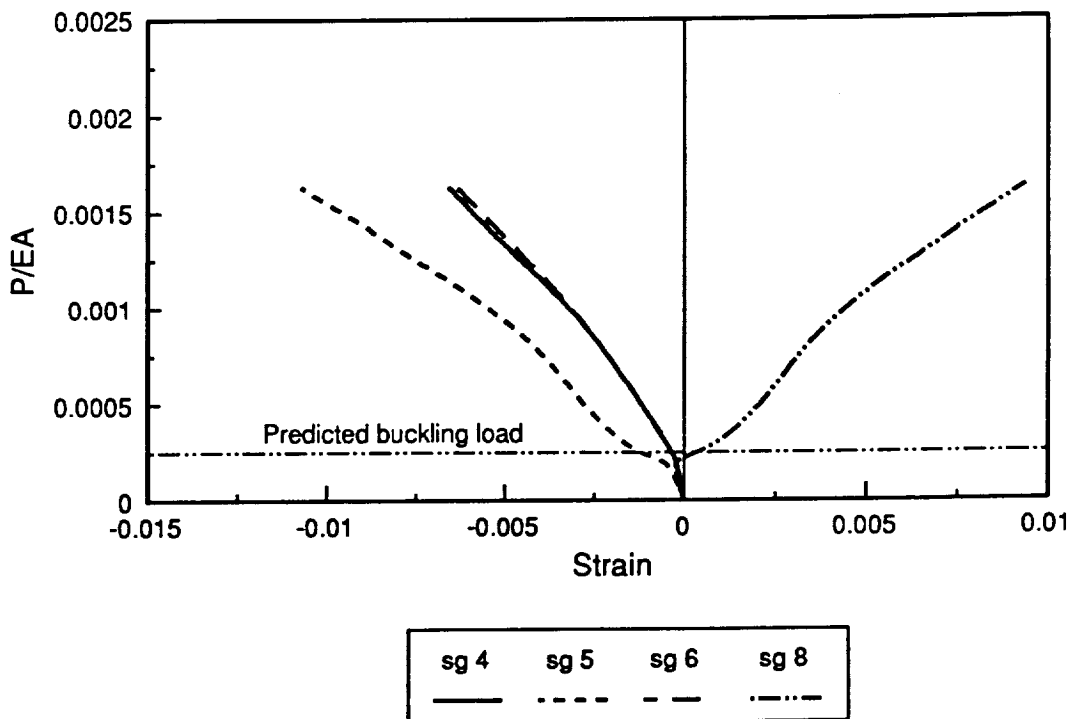
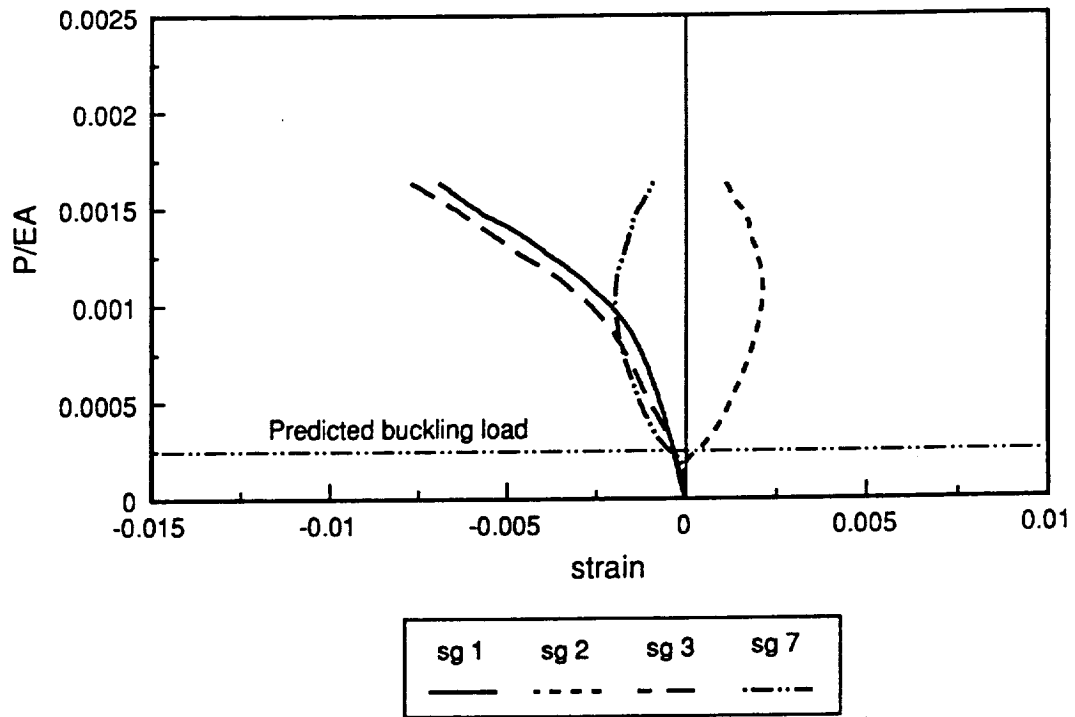


Fig. 7-42 Experimentally measured strains of plate 6.

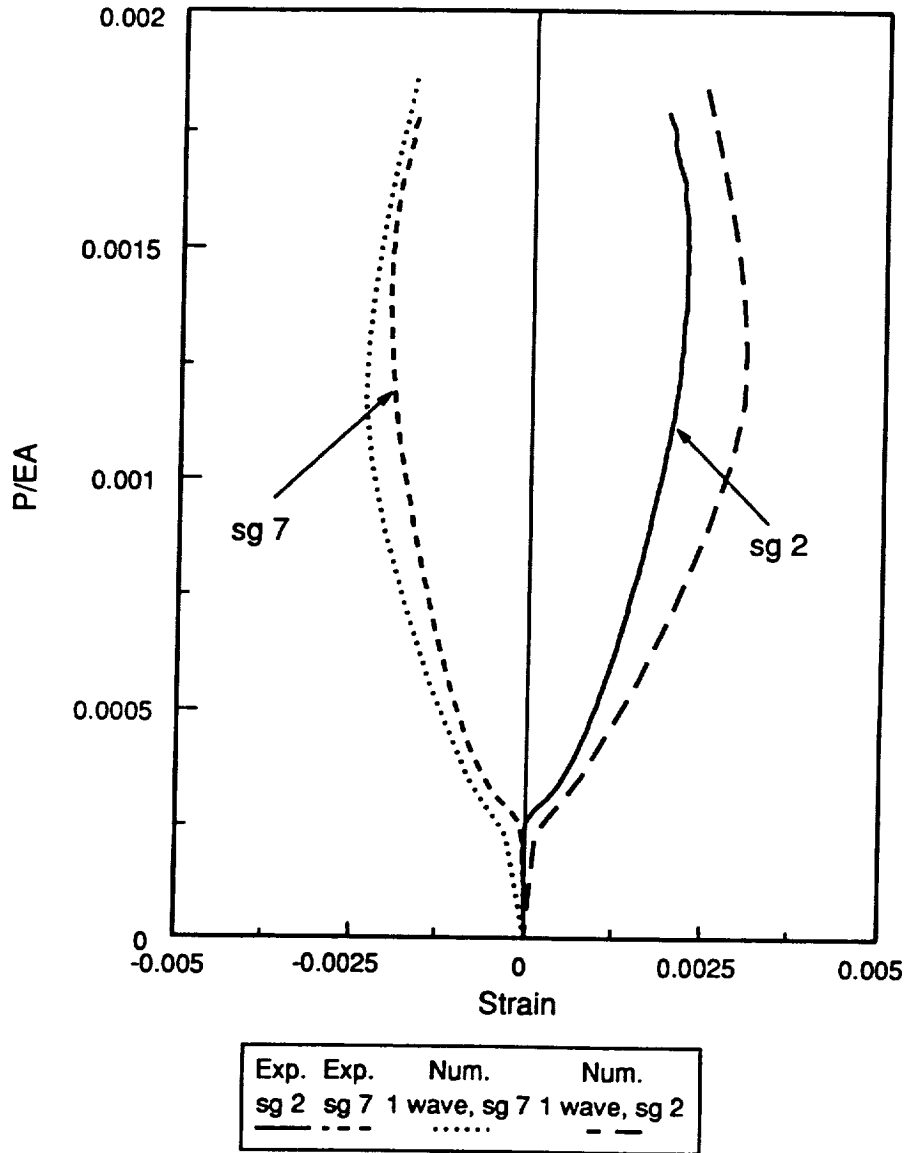


Fig. 7-43 Comparison of strains near the clamped support of plate 5.

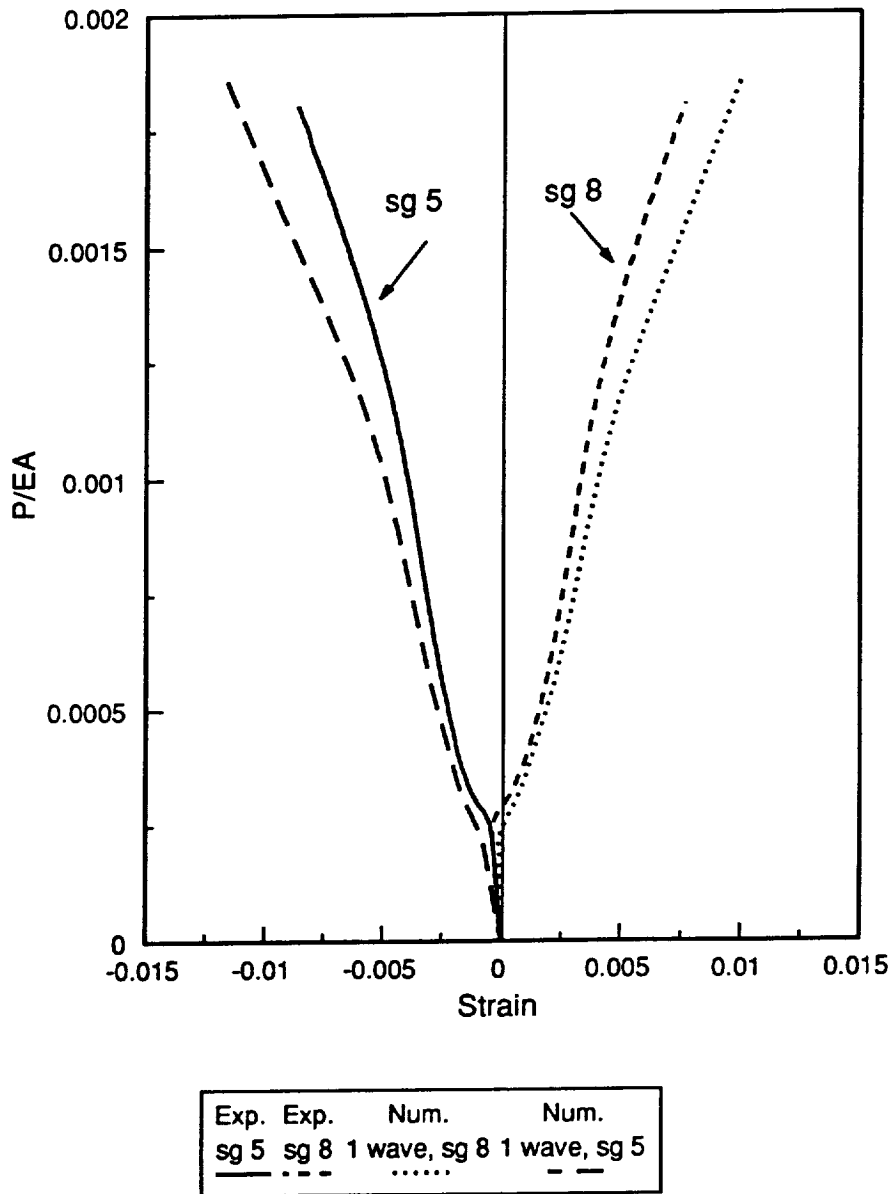
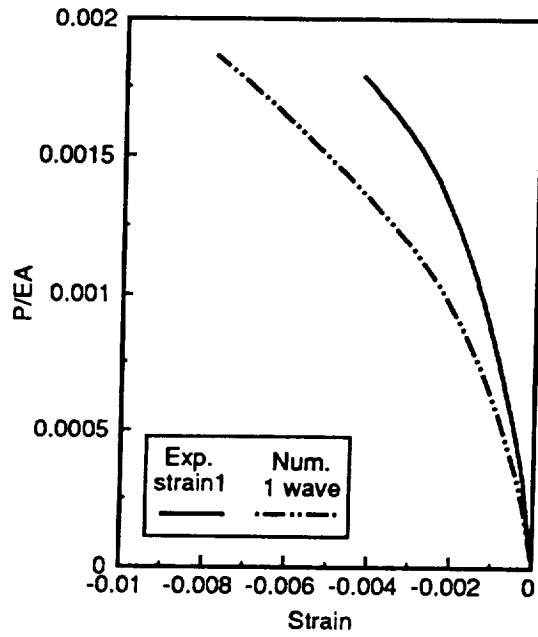
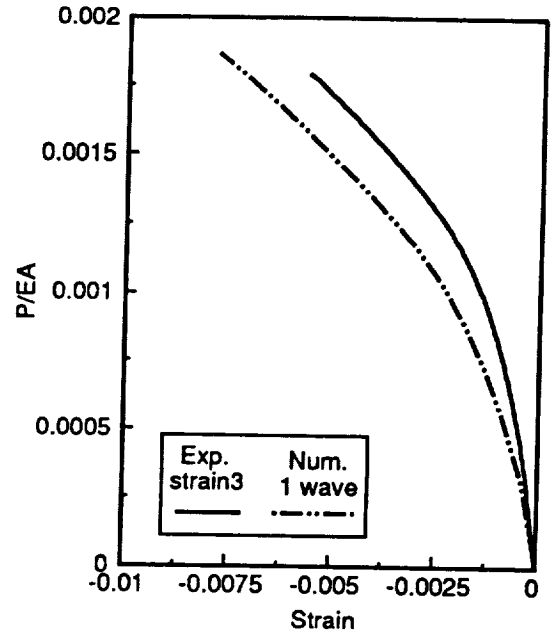


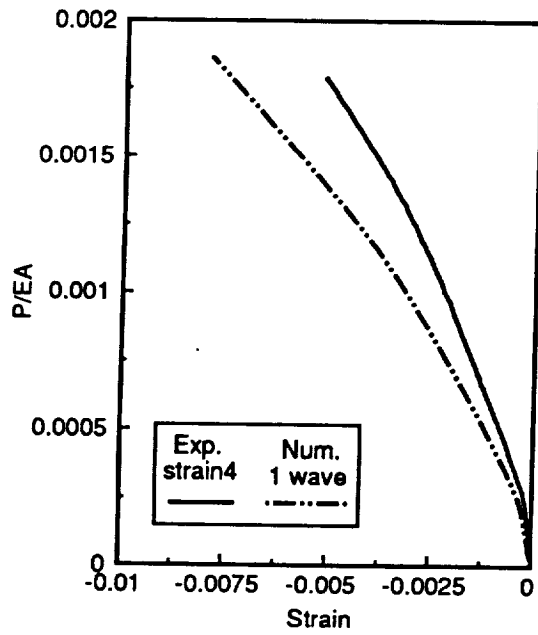
Fig. 7-44 Comparison of strains at the net-section hole edge of plate 5.



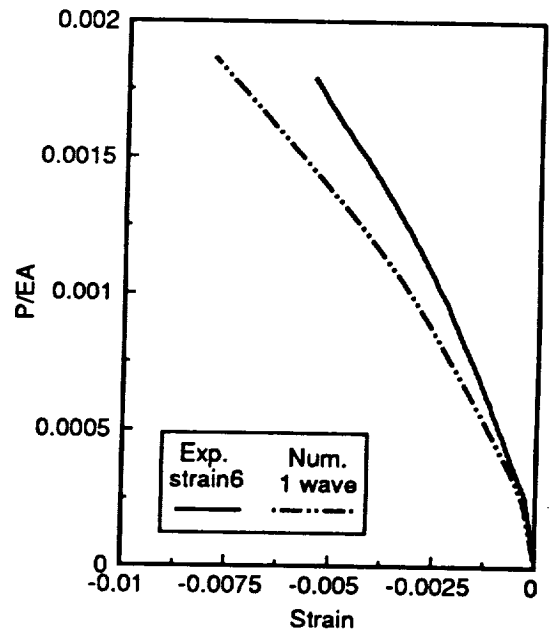
(a) strain 1



(b) strain 3



(c) strain 4



(d) strain 6

Fig. 7-45 Comparison of strains near the simple support of plate 5.

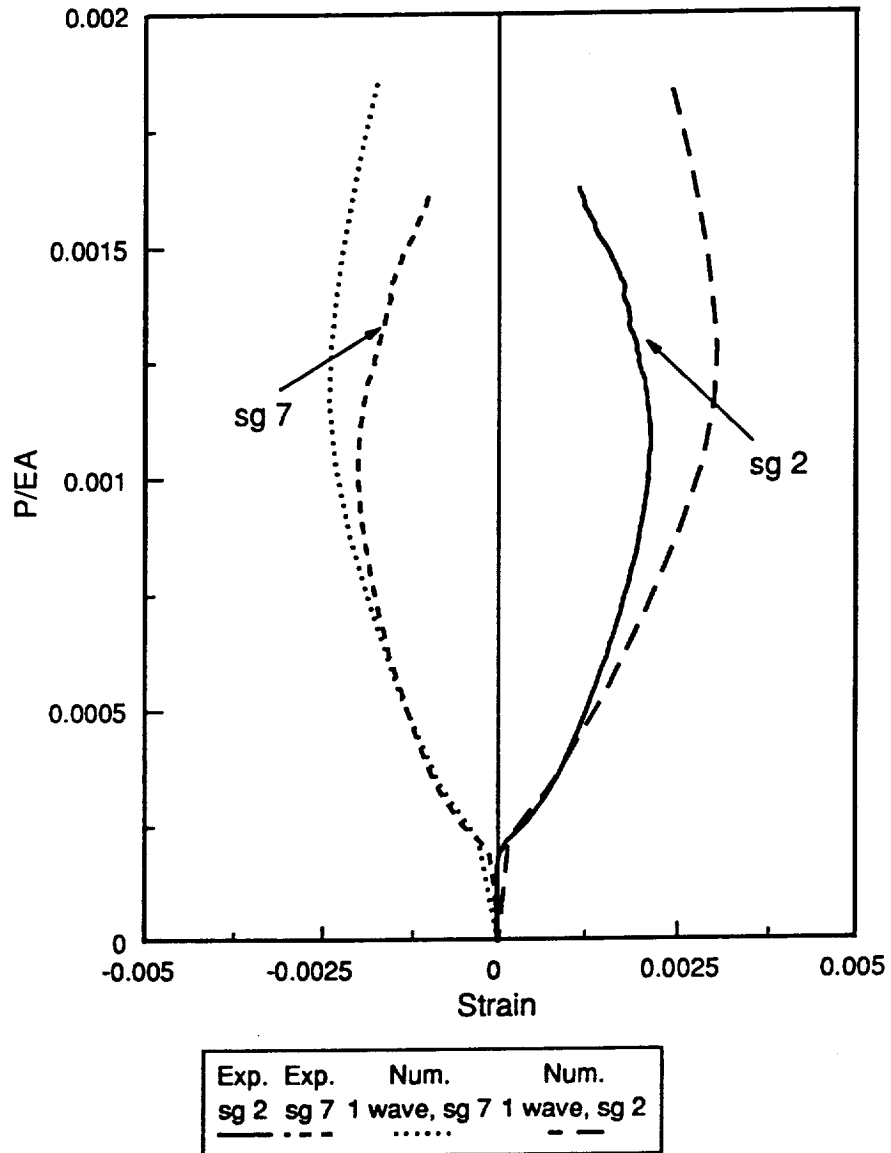


Fig. 7-46 Comparison of strains near the clamped support of plate 6.

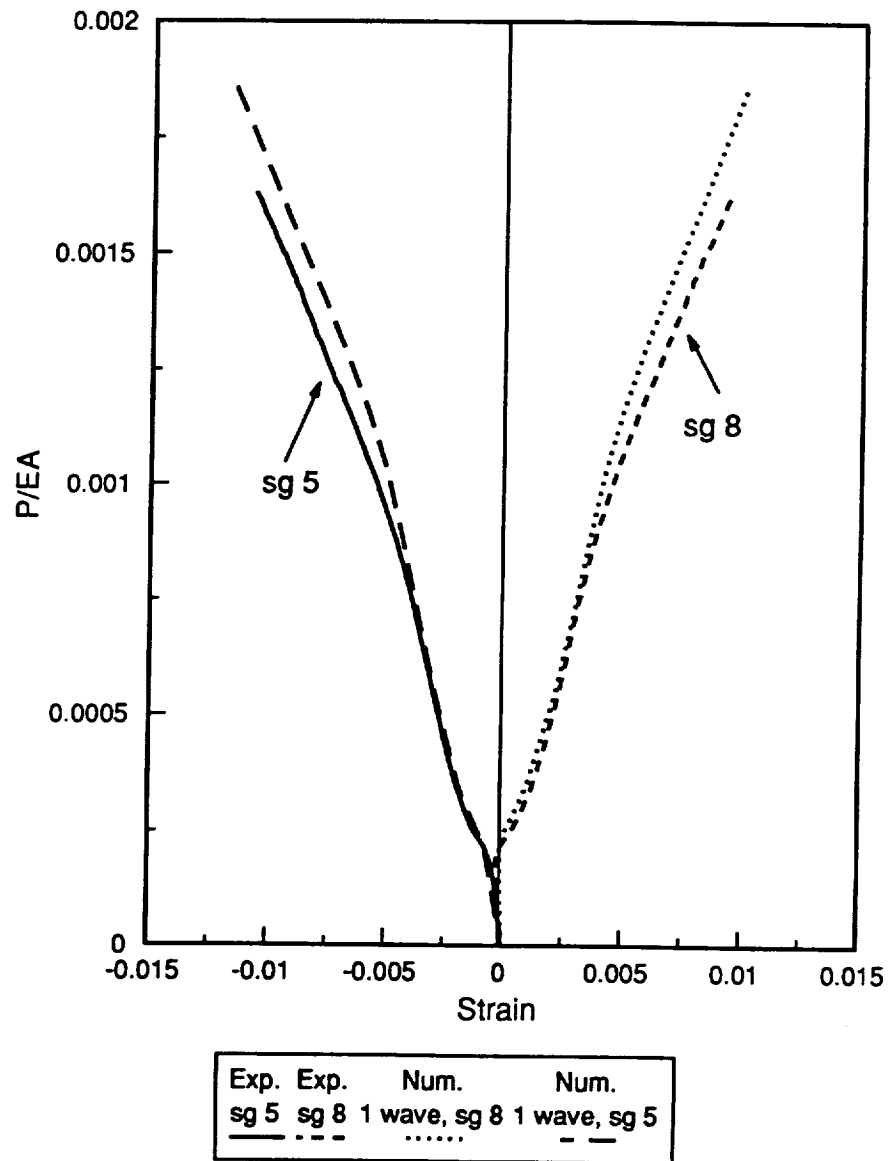
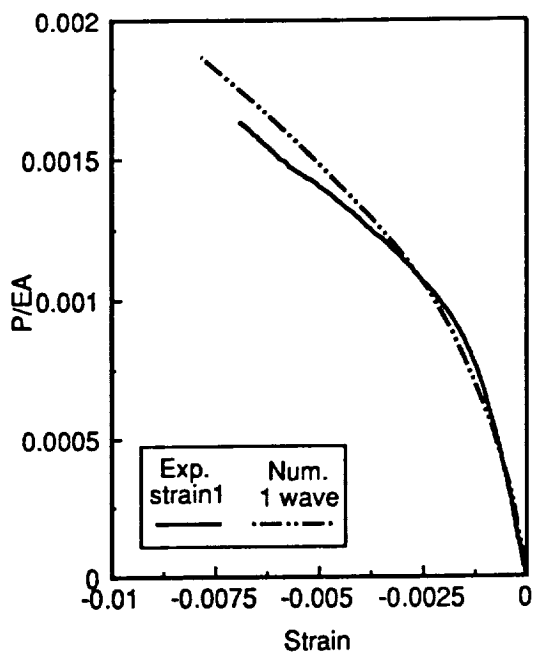
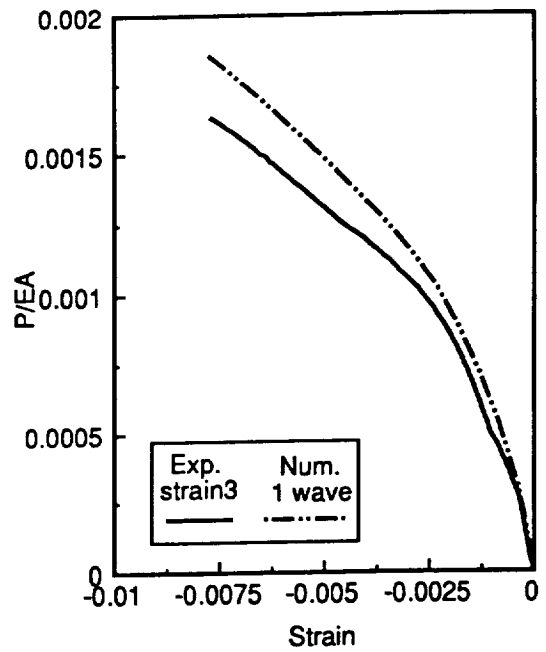


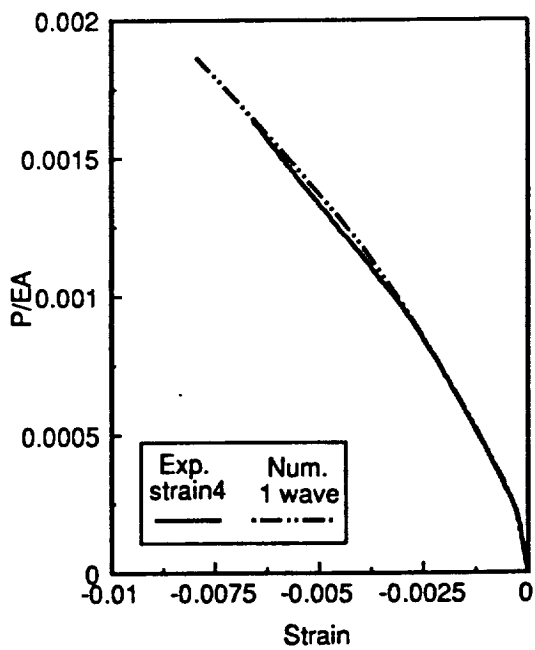
Fig. 7-47 Comparison of strains at the net-section hole edge of plate 6.



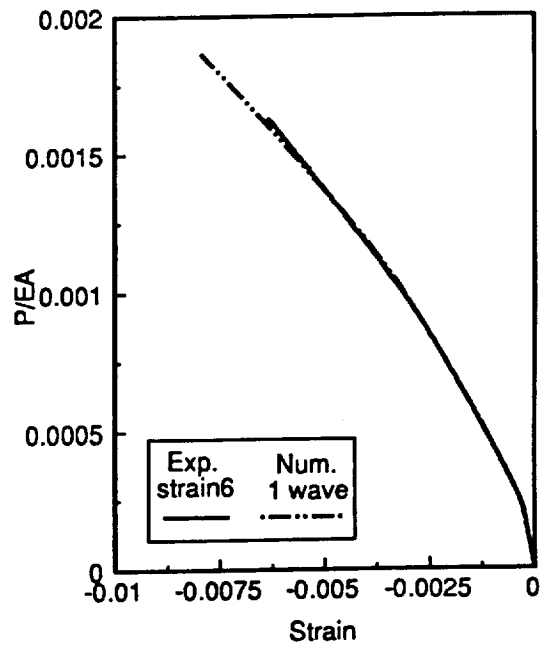
(a) strain 1



(b) strain 3



(c) strain 4



(d) strain 6

Fig. 7-48 Comparison of strains near the simple support of plate 6.

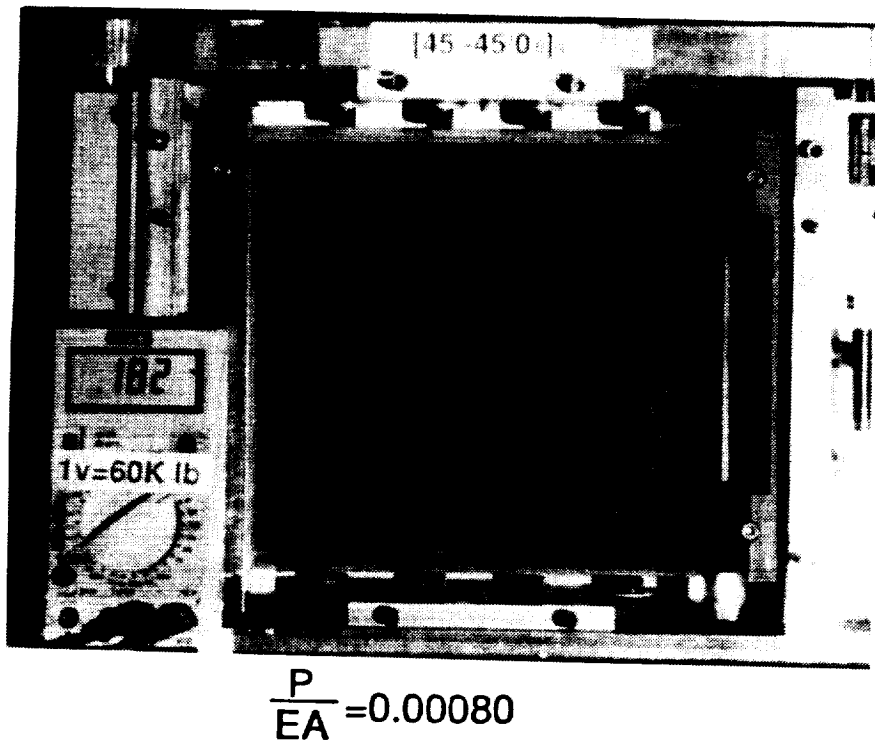
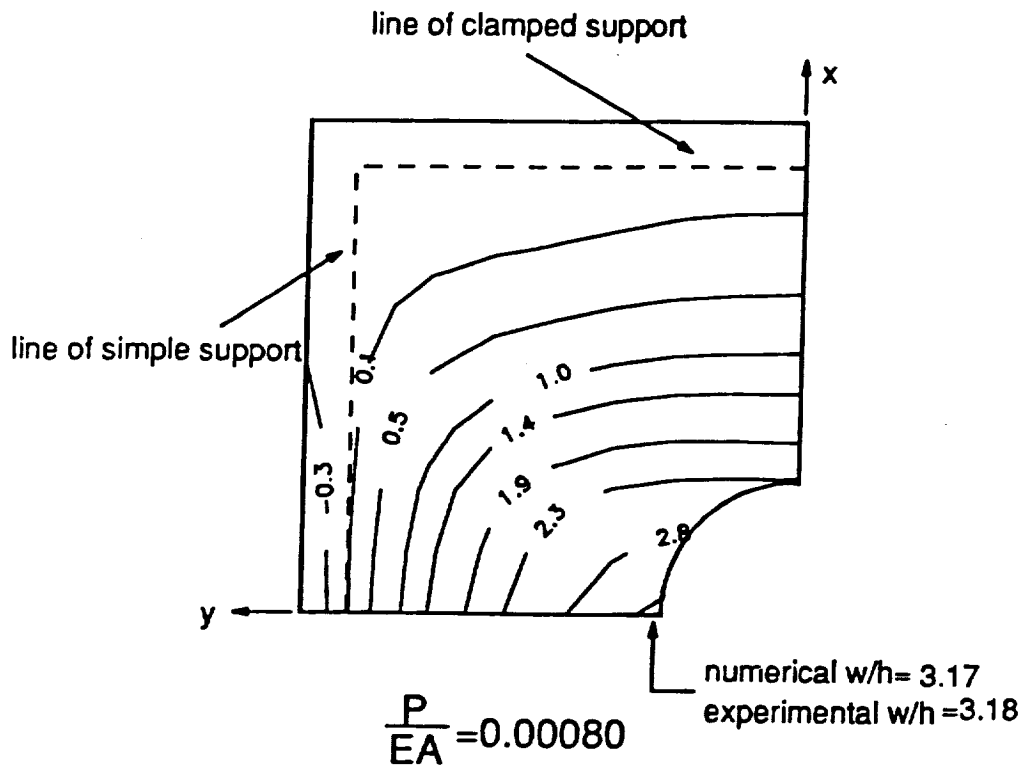


Fig. 7-49 Predicted and measured shadow moiré fringe pattern for a $[\pm 45/0]_s$ plate at a lower load level.

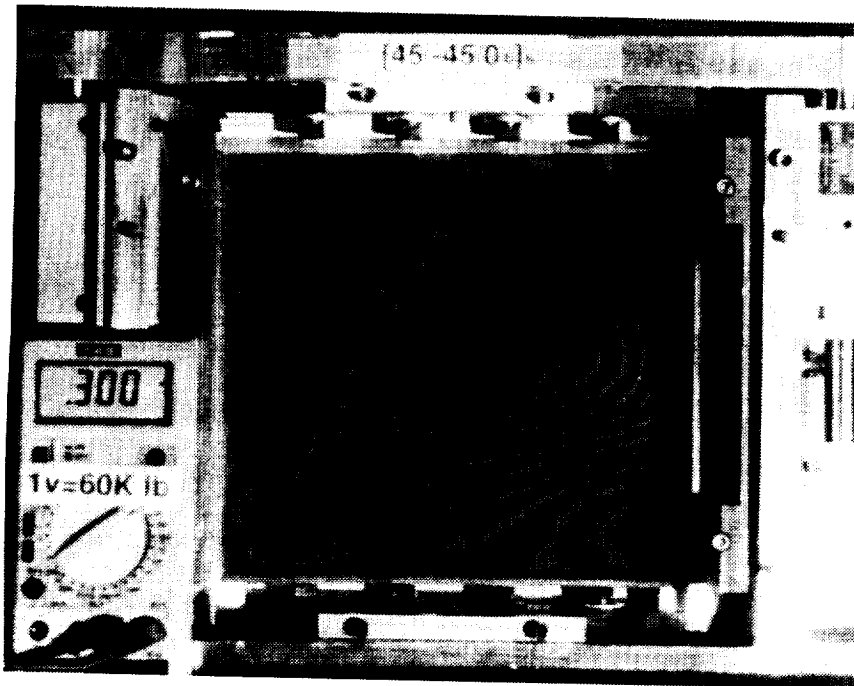
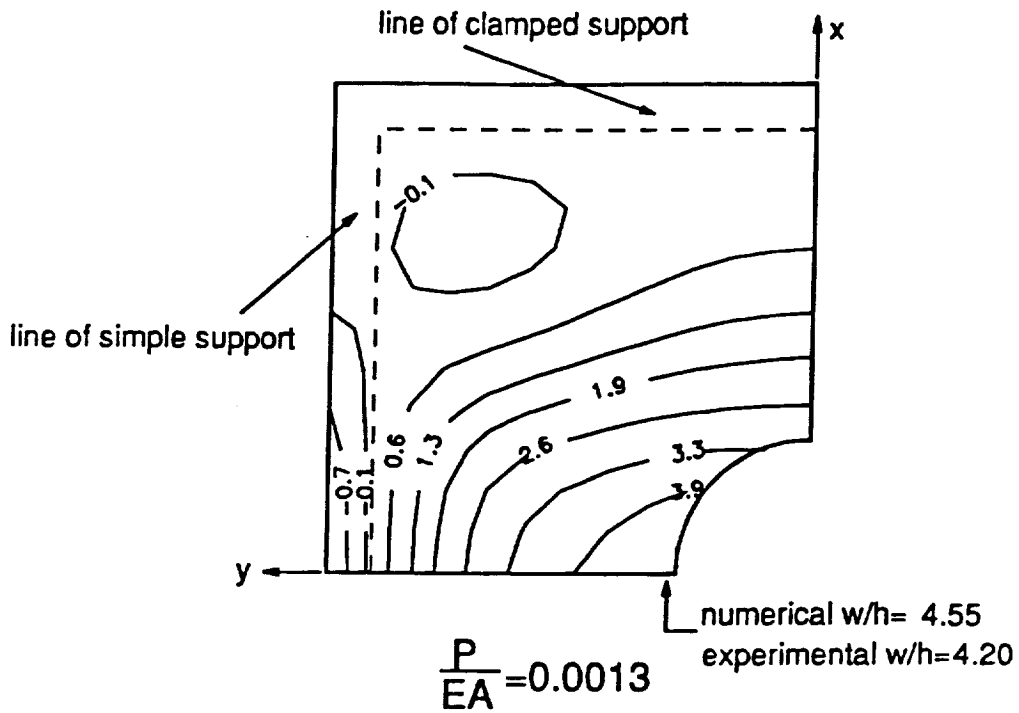


Fig. 7-50 Predicted and measured shadow moiré fringe pattern for a $[\pm 45/0]_s$ plate at a higher load level.

of-plane deflection is $w/h = 3.21$. Figure 7-50 shows the moire fringe pattern at the load level of $P/EA = 0.0013$, or $\bar{N}_x = 1636$ lb/in., a higher load than the load in Fig. 7-49, and it's comparison with the numerically predicted out-of-plane displacement contour drawing. The experimental out-of-plane displacement at this load level was $w/h = 4.20$, and the numerically predicted out-of-plane displacement at this load level was $w/h = 4.55$. It can be seen that the fringe pattern at the higher load was quite different than the fringe pattern at the lower load. At the corners of simple support and clamped support displacements of opposite sign appeared. The numerical prediction also predicts this reverse displacement. Recalling the 3-dimensional surface drawing of the out-of-plane displacement at the high load level for quasi-isotropic plate in Fig. 5-4, this fringe pattern can be better understood.

7.3.4 Failure and Post-Mortem Analysis

A photograph of failed plate 5 in the fixture is shown in Fig. 7-51. It can be seen that failure occurred along the simple support on one side. Plate 6 also failed along the simple supports but on both the left and right sides. Compared with the numerically predicted failure locations in Fig. 5-12, the experimental failure locations and failure modes are completely different. In a $[\pm 45/0]_s$ laminate the inner 12 layers are all 0° layers. The fiber direction in the 0° layer is parallel to the simple support line. It can be easily understood that the inner 12 0° layers are weak in resisting the interlaminar shear stress τ_{yz} , that is, τ_{23} . The failure along the simple support could well be due to the interlaminar shear stress τ_{23} . However, the numerically predicted results did not predict the mode of failure. The numerically predicted stress state in the laminate can be understood better by the contour drawing of failure pa-

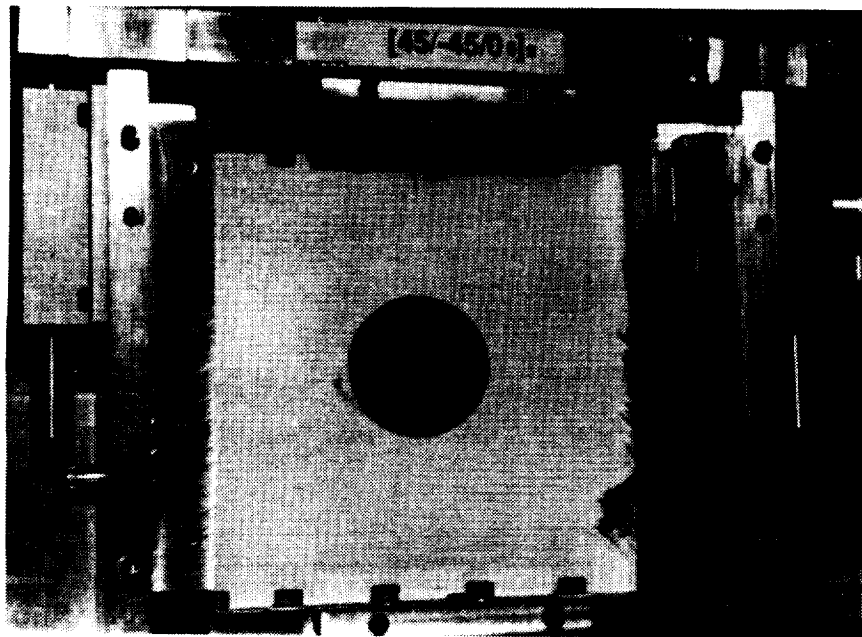
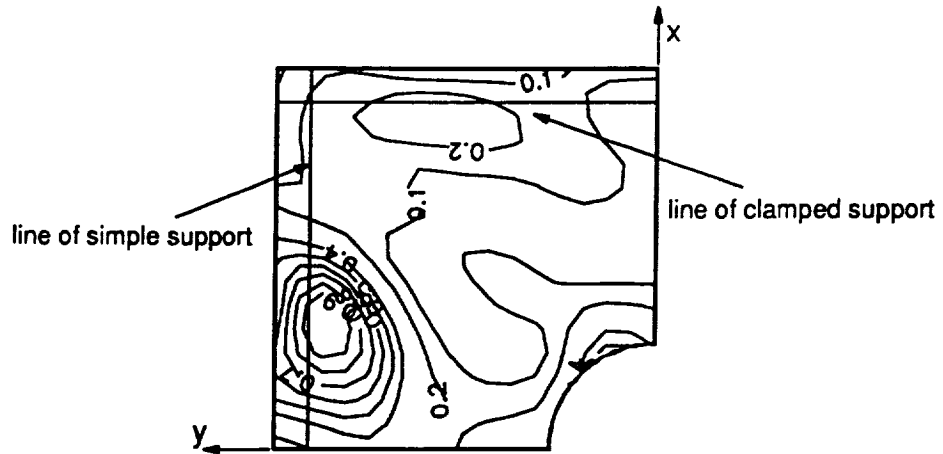
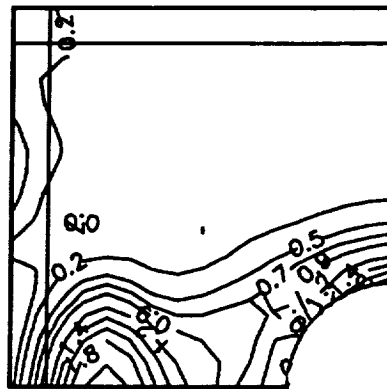


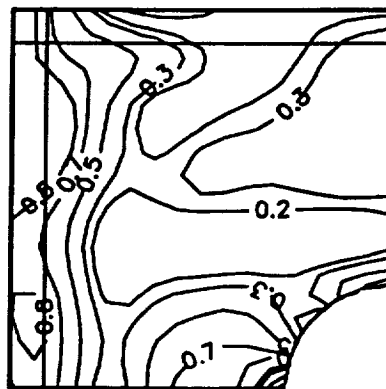
Fig. 7-51 Failed $[\pm 45/0]_s$ plate in the fixture.



(a) Contour plot of R_1 on 2-nd layer from bottom (-45° layer).

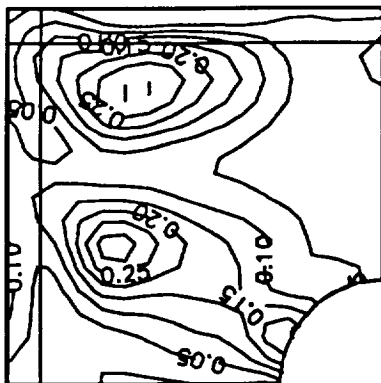


(b) Contour plot of R_2 on 14-th layer from bottom (0° layer).

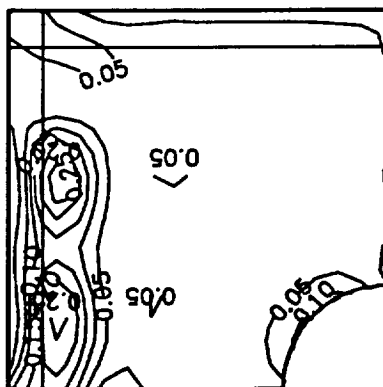


(c) Contour plot of R_{12} on 1-st layer from bottom (45° layer).

Fig. 7-52 Contour of failure parameters of the $[\pm 45/0]_s$ plates at $P/EA = 0.00169$ (continued).



(d) Contour plot of R_{13} on 9-th layer from bottom (0° layer).



(e) Contour plot of R_{23} on 9-th layer from bottom (0° layer).

Fig. 7-52 Contour of failure parameters of the $[\pm 45/0]_s$ plates at $P/EA = 0.00169$ (concluded).

rameters at the load level of fiber failure, as shown in Fig. 7-52. Figure 7-52(a) shows that R_1 is high near the simply supported edge away from the net-section. Figure 7-52(b) shows that R_2 is high on the net-section toward the simple support. It can be seen that the maximum stress level is about twice the transverse failure load. Figure 7-52(c) shows that R_{12} is high along the simple support and near the net-section hole edge. From Fig. 7-52(d) and (e) it can be seen that the interlaminar shear failure parameters are small all over the plate. However, it is interesting that the interlaminar shear stress τ_{23} is relatively high along the simple support compared to other locations. From this result it is surmised that since the inner 12 0° layers are clustered, the strength for τ_{23} of thick clustered layer was much lower than the strength for τ_{23} of a single layer used in the numerical prediction. This point will be discussed more shortly.

7.3.5 Acoustic Emission Results

Acoustic emission test results are shown in Fig. 7-53 and Fig. 7-54 for plate 5 and plate 6, respectively. From the acoustic emission test results it can be seen that once the failure began, the acoustic emission count kept increasing at a constant rate. In previous discussions it was shown that acoustic emission count of the quasi-isotropic plate dramatically increased only at the final stage, and that the acoustic emission for $[\pm 45/0_2]_{2s}$ plate sharply increased shortly before the final failure. Considering the acoustic emission results of Fig. 7-53 in conjunction with the failure along the simple support, it can be imagined that the $[\pm 45/0_6]_s$ plate failed in a continuous rather than in a sudden fashion along the simple support. Even though the load vs. end shortening relation did not show a large loss of load bearing capability, it can be imagined

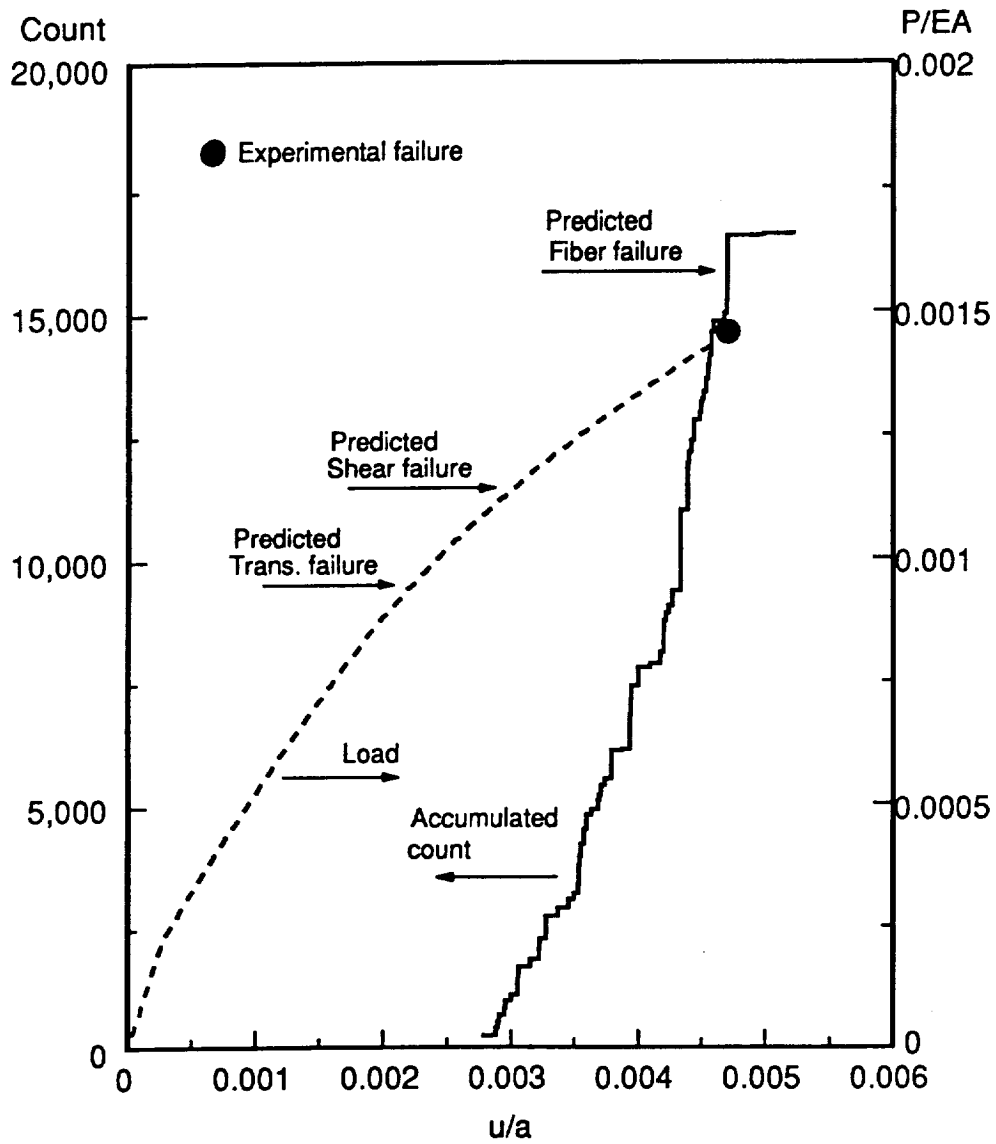


Fig. 7-53 Acoustic emission activity and load-end shortening relation for plate 5, [$\pm 45/0_s$].

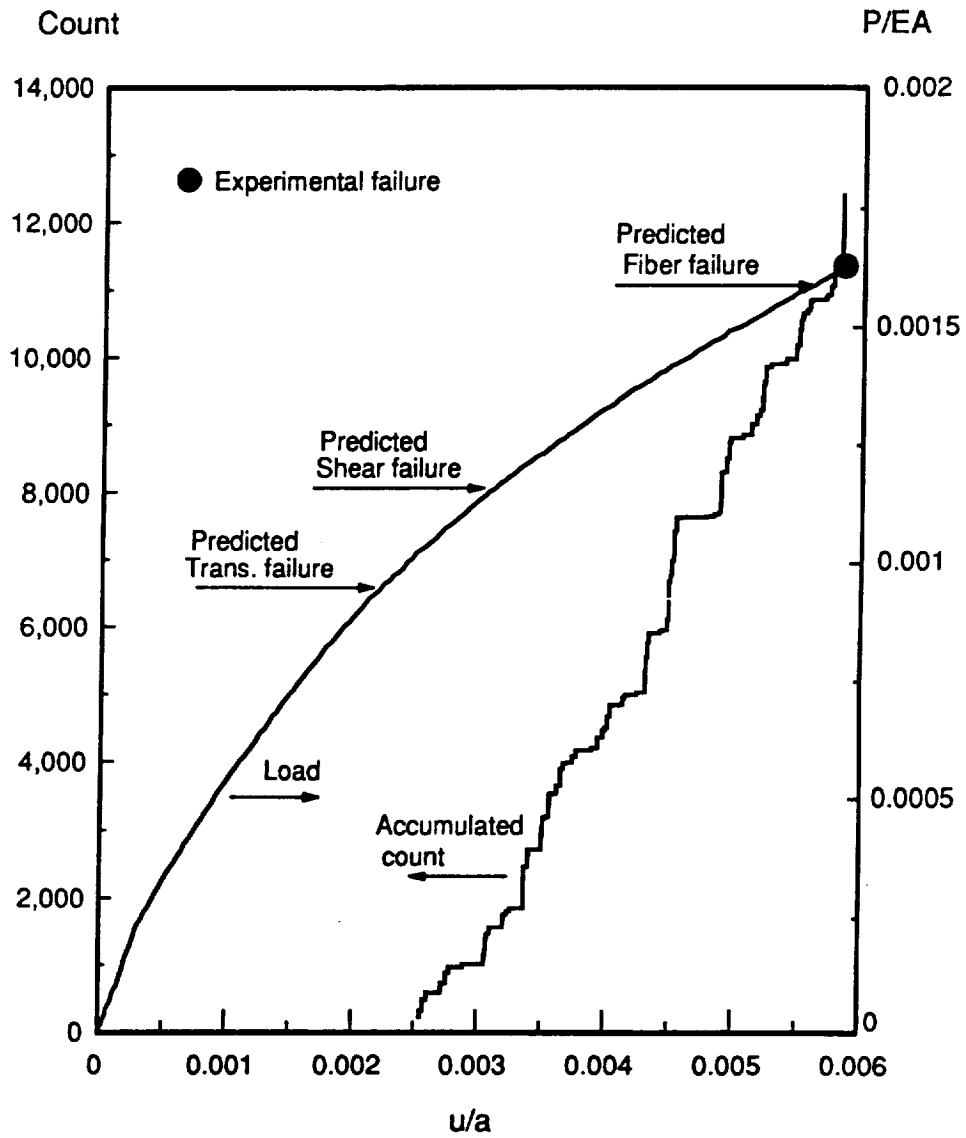


Fig. 7-54 Acoustic emission activity and load-end shortening relation for plate 6, [$\pm 45/0_s$].

that the plate was already damaged severely in transverse direction before final failure, and it was much much weaker in the transverse direction than the original plate. Therefore it could be expected that the two previous laminates were less damaged than $[\pm 45/0_8]_{2S}$ laminate just before the final failure.

7.4 The $[\pm 45]_{4S}$ Plates

7.4.1 Load vs. Deflection Relations

Experimental load vs. end shortening relations for the $[\pm 45]_{4S}$ plates, plate 7 and plate 8, and their comparison with numerical results are shown in Fig. 7-55. Both plates exhibited a mode shape change, at about the same load, but the change was not abrupt. The numerically predicted buckling load, $P_{cr}/EA = 0.00098$, or $\bar{N}_x^{cr} = 240$ lb/in., is marked on Fig. 7-55. Experimental buckling loads were $P_{cr}/EA = 0.00088$, or $\bar{N}_x^{cr} = 215$ lb/in. for plates 7 and 8. Numerically predicted failure loads are marked on the numerical load-end shortening curves for the one half-wave and two half wave configurations. With the $[\pm 45]_{4S}$ plate the predicted fiber failure load is much higher than the experimental failure load. Hence it does not appear in the load range viewed in Fig. 7-55. Up to the load level of mode shape change the two experimental relations for plate 7 and plate 8 followed exactly the same path. After the mode shape change the two relations showed a slight difference. Mode transition for plate 7 occurred at $P/EA = 0.00300$ ($\bar{N}_x = 734$ lb/in.) and for plate 8 at $P/EA = 0.00294$ (

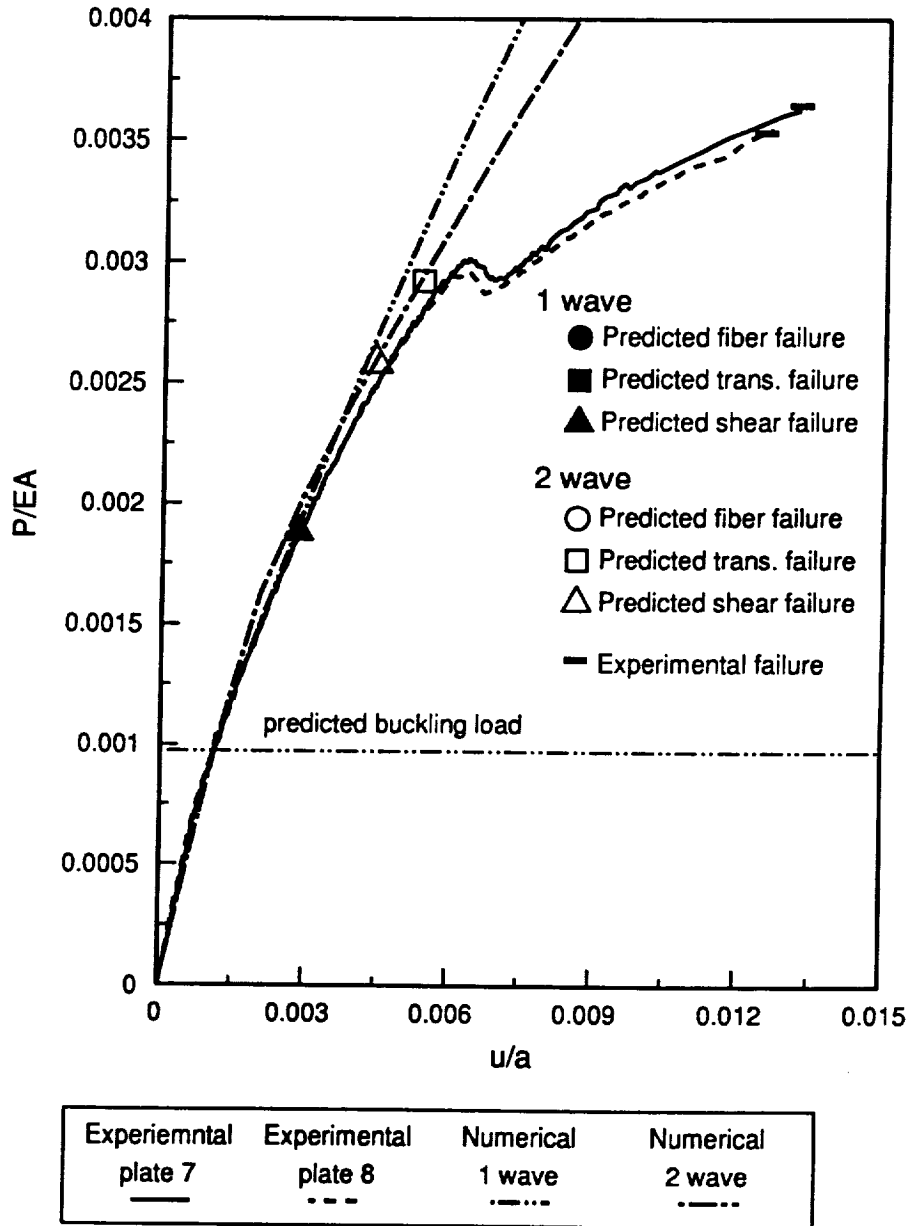


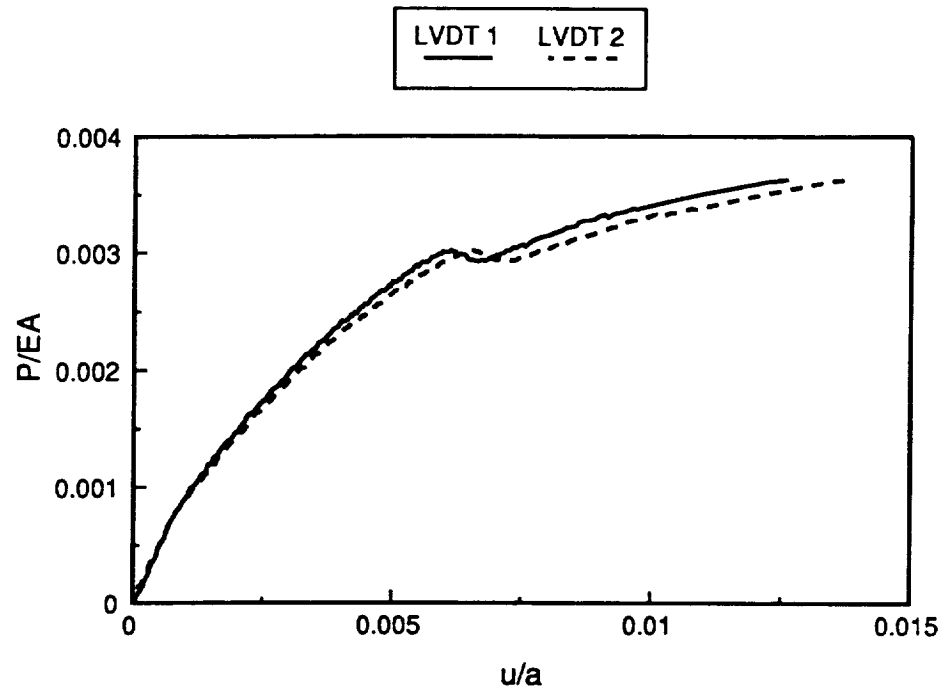
Fig. 7-55 Comparison of load vs. end shortening relations and failure loads for $[\pm 45]_s$ plates.

$\bar{N}_x = 719$ lb/in.). Plate 7 failed at $P/EA = 0.00365$ ($\bar{N}_x = 892$ lb/in.), and plate 8 failed at $P/EA = 0.00350$ ($\bar{N}_x = 856$ lb/in.). Correlation with numerical result shows good agreement up to $P/EA = 0.00189$ ($\bar{N}_x = 461$ lb/in.) where the inplane shear failure is predicted. This load level was far lower than the mode transition load. It can be observed that as the plate began to fail, it lost load bearing capability. This resulted in an increased difference between the experimental results and the numerical prediction. At higher loads the numerical prediction does not agree with the experimental results at all. It may be worth mentioning that the mode shape change of this laminate occurred very slowly, contrary to the previous laminates. It is deduced that due to the accumulated damage in the plates at the load level of mode shape change, the plate behaved differently than the previous laminates.

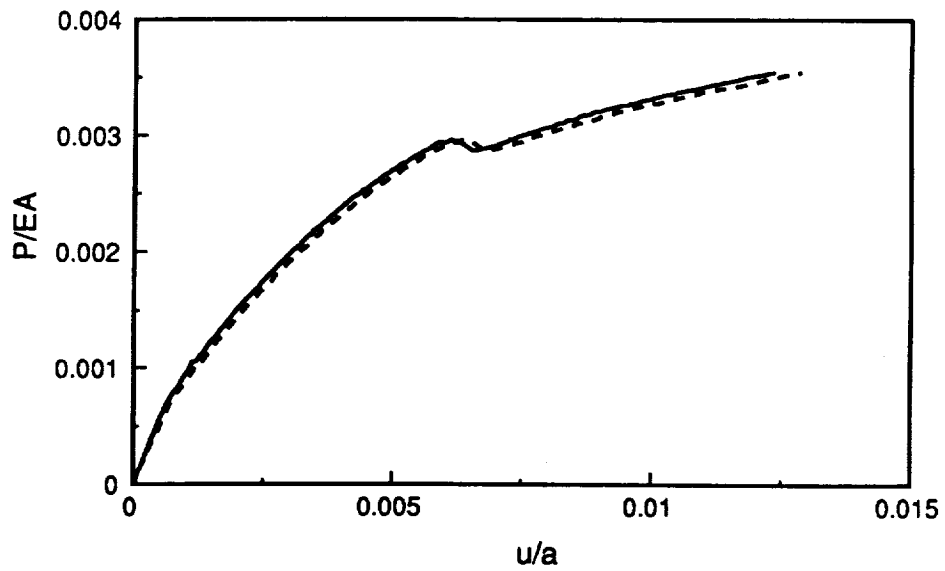
Figure 7-56 illustrates the good uniformity of loading on the edge of plate 7 and plate 8, plate 8 being better as regards uniformity. Figure 7-57 shows the good agreement in the numerical and experimental load vs. out-of-plane deflection before the mode shape change. From Fig. 7-57 it can be seen that the plates 7 and 8 failed soon after the mode shape change into the two half-wave configuration. Also, the lack of a sharp mode transition is seen in this relation. It should be noted that plate 8 deflected in negative z direction.

7.4.2 Load vs. Strain Relations

Figures 7-58 - 7-65 illustrate the strain response of plates 7 and 8. In Fig. 7-58 the data for strain gauge 2 of plate 7 is missing. In the testing of plate 7 strain gauge 2 was not connected well. Thus the data could not be collected. By the fact that strain



(a) plate 7



(b) plate 8

Fig. 7-56 Comparison of displacements measured from LVDT 1 and LVDT 2 for plate 7 and plate 8.

C-4.

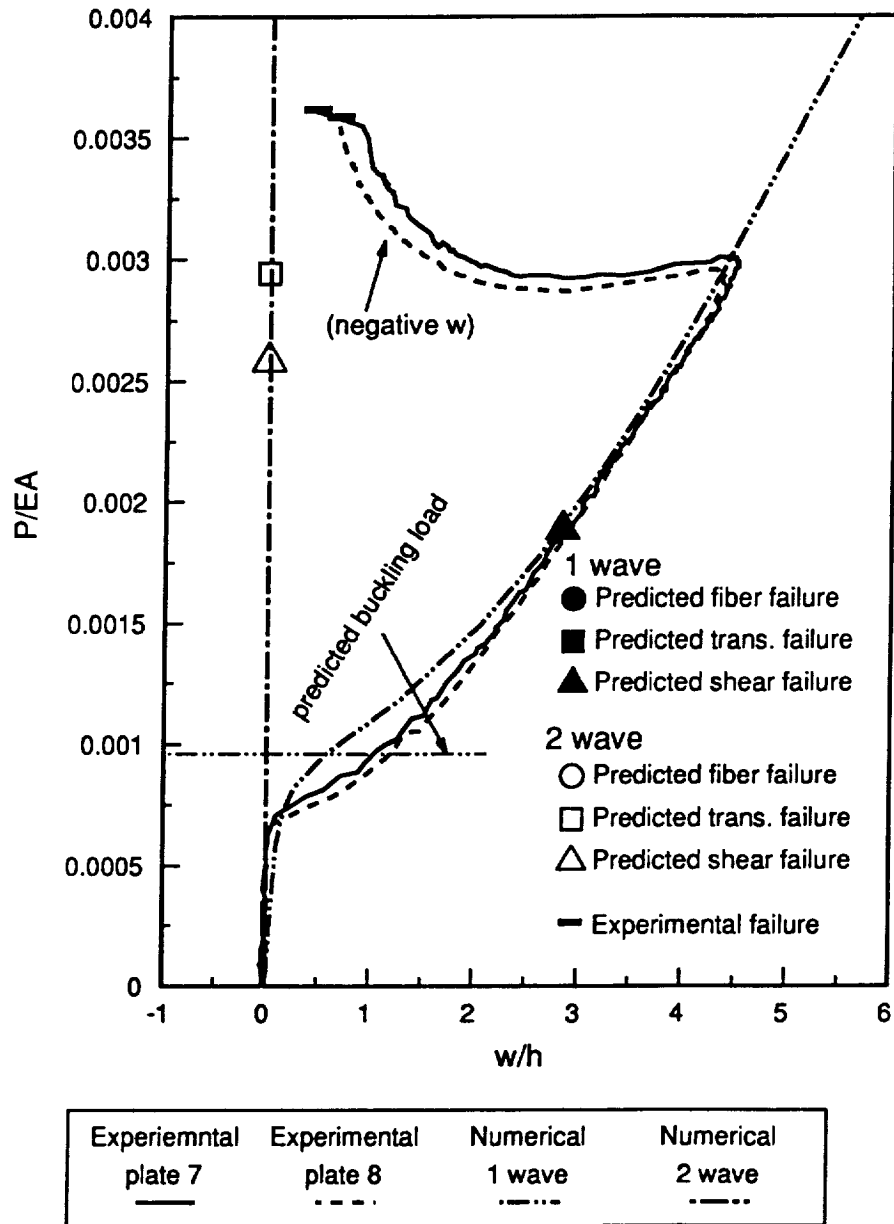


Fig. 7-57 Comparison of load vs. deflection relations and failure loads for the $[\pm 45]_{4s}$ plates.

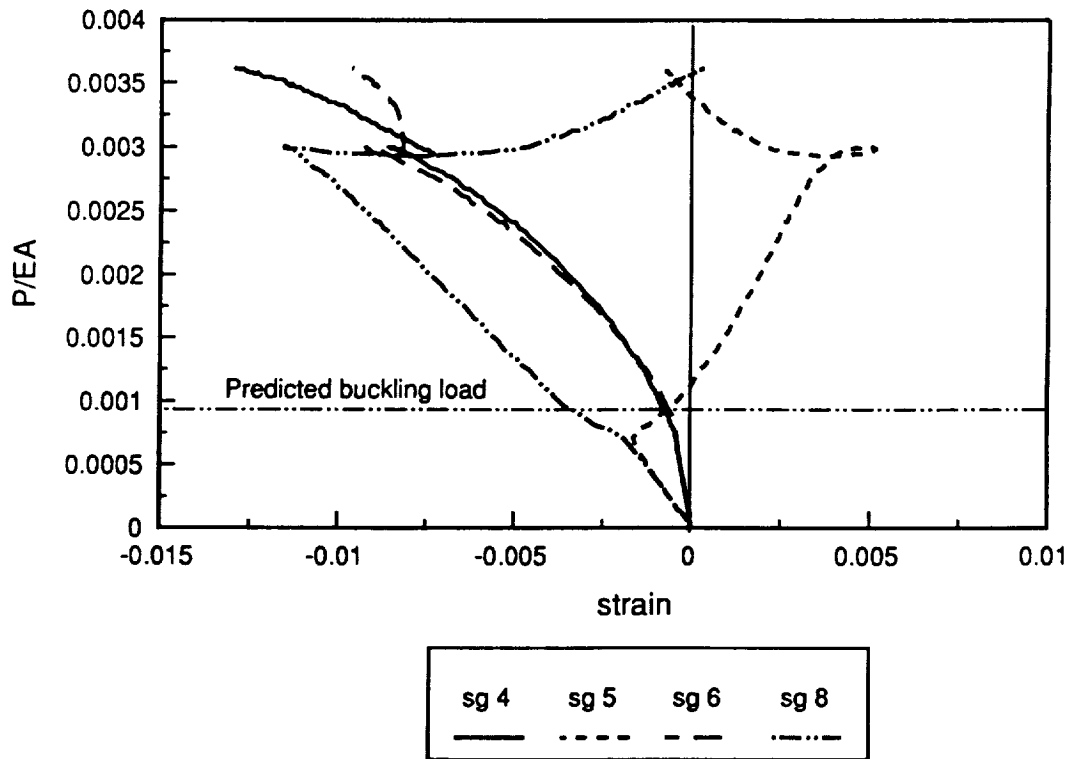
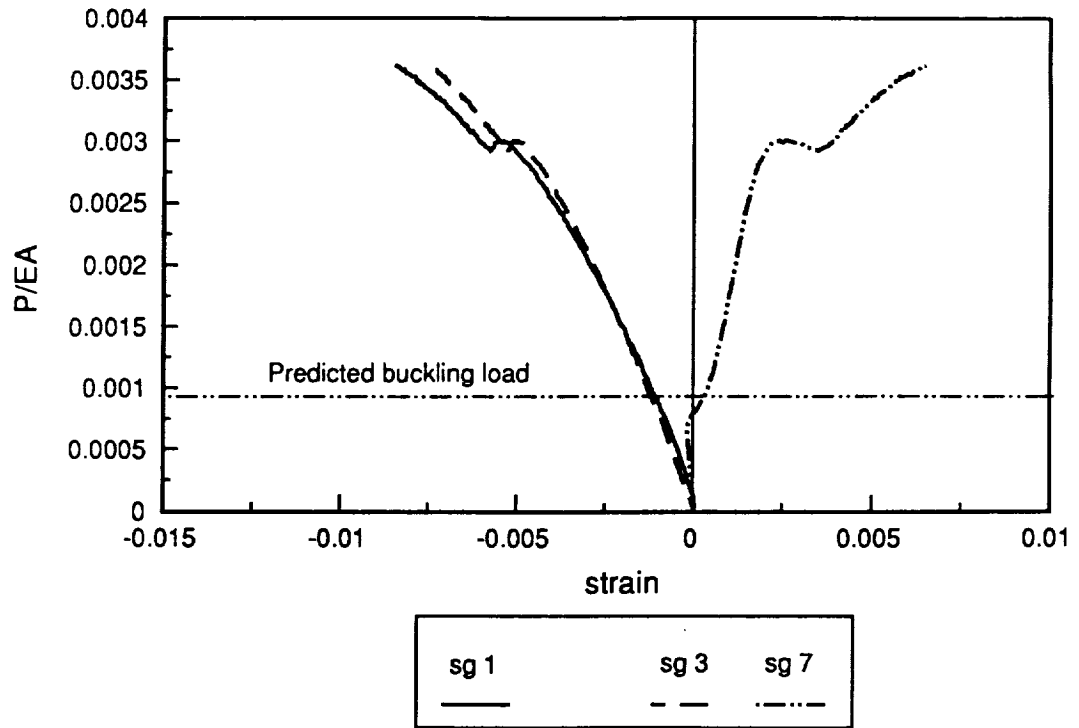


Fig. 7-58 Experimentally measured strains of plate 7.

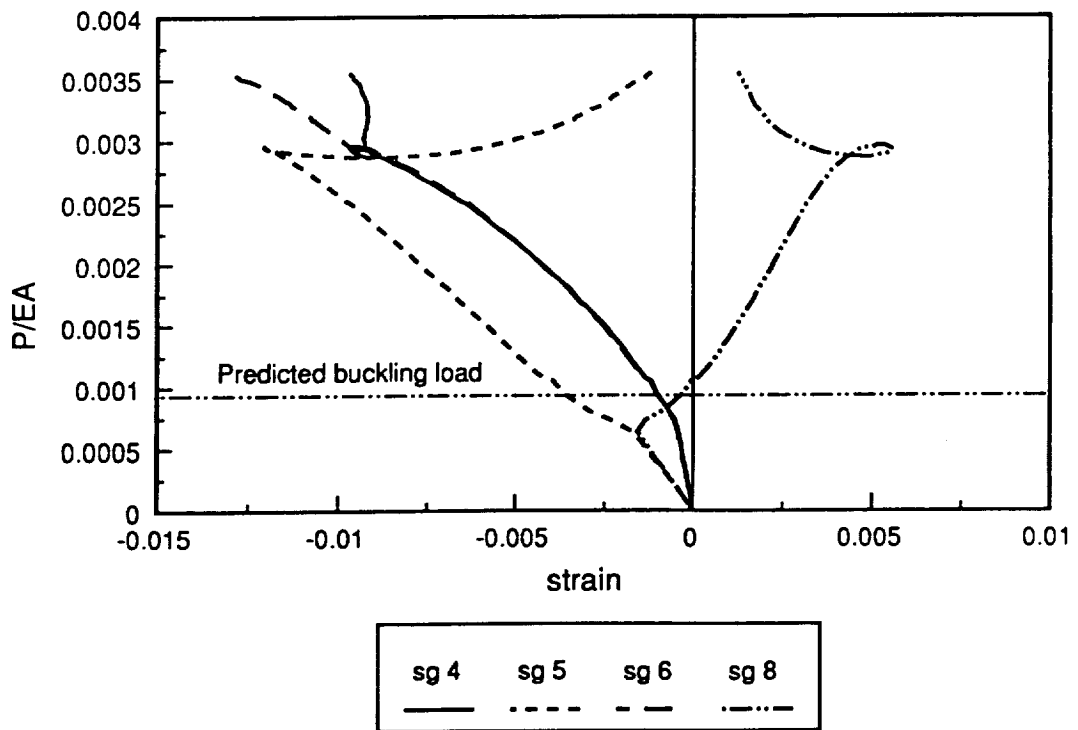
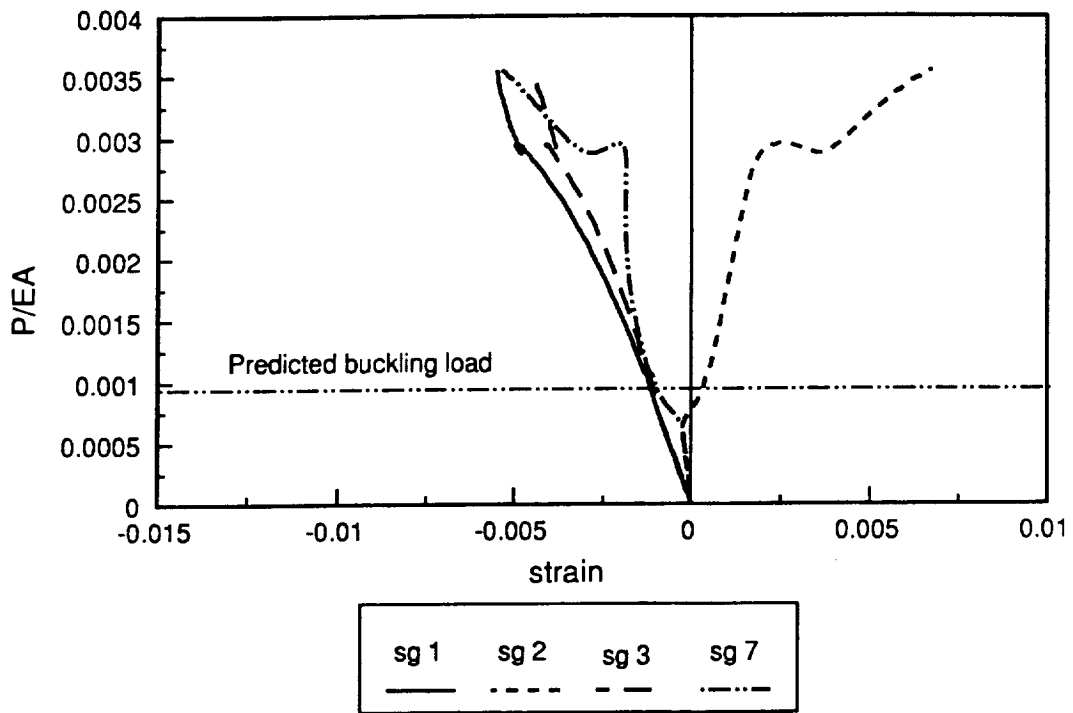


Fig. 7-59 Experimentally measured strains of plate 8.

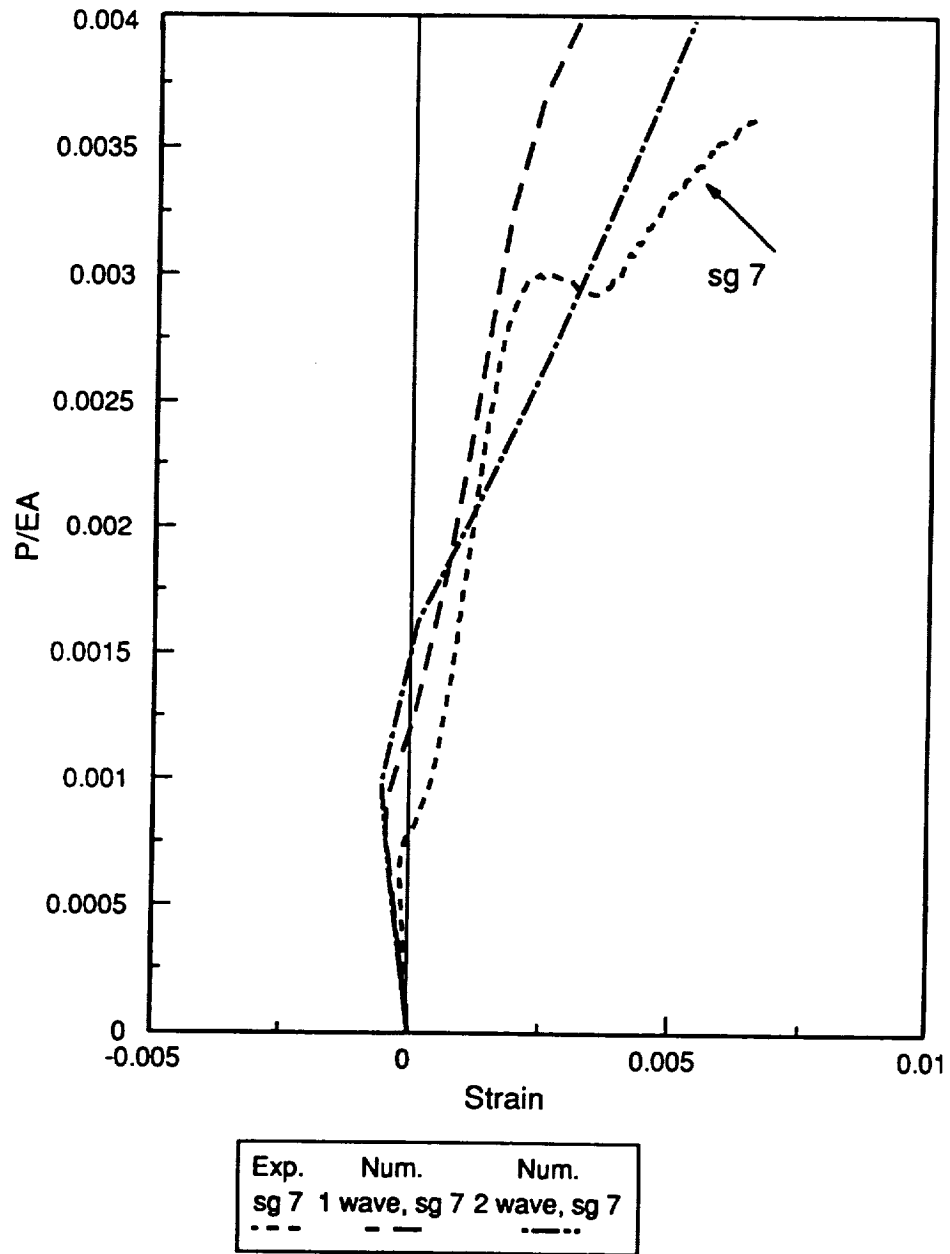


Fig. 7-60 Comparison of strains near the clamped support of plate 7.

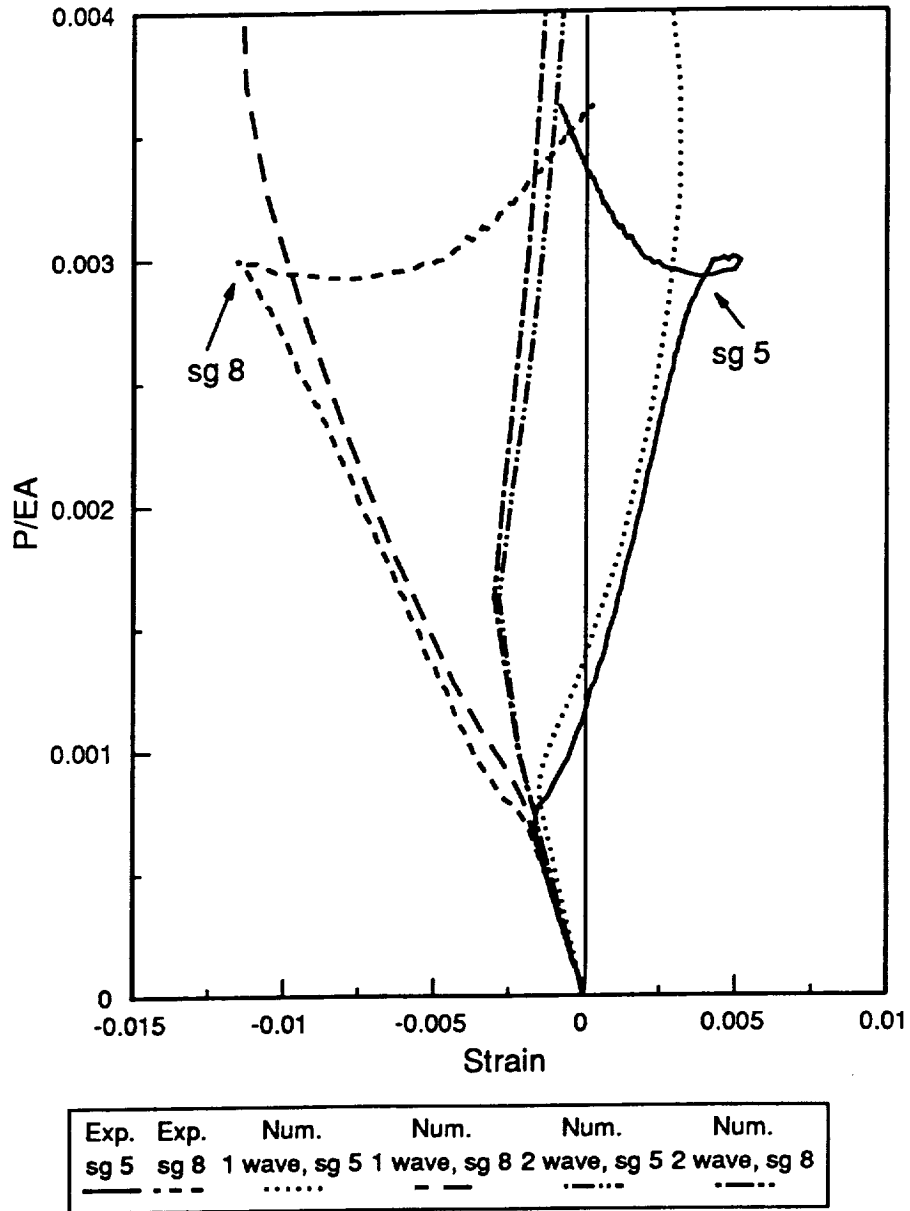
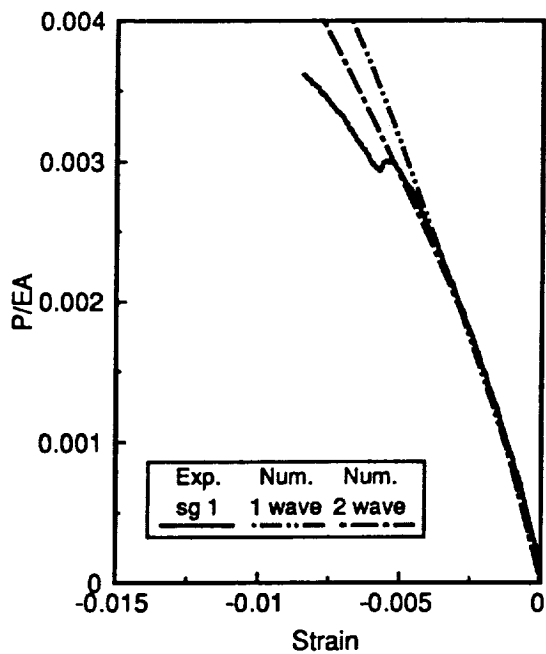
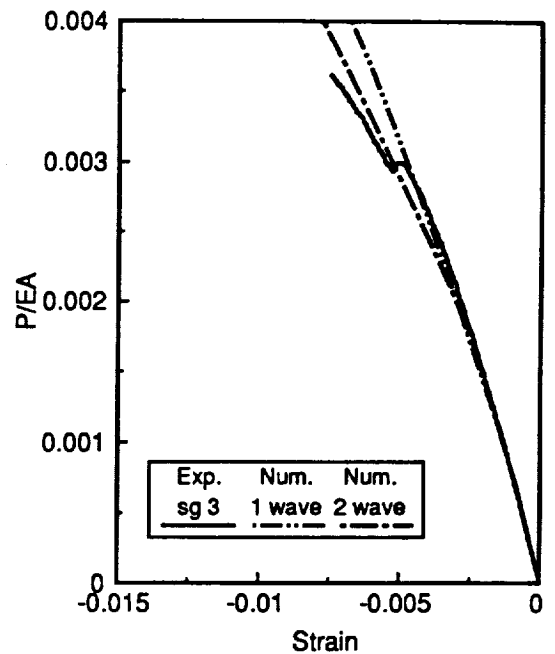


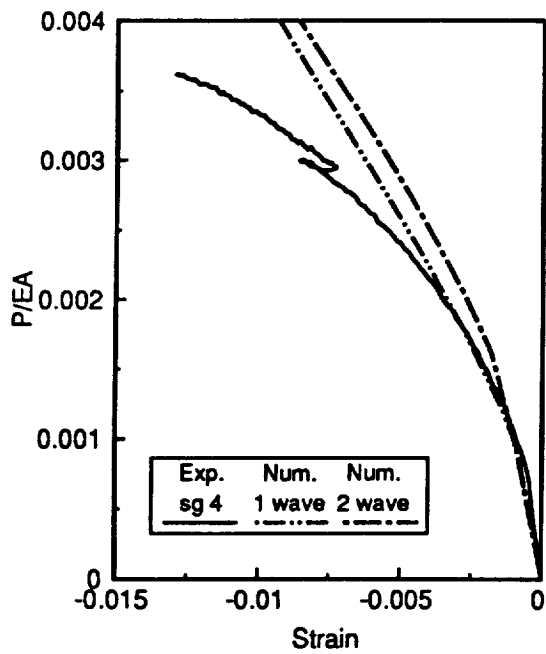
Fig. 7-61 Comparison of strains at the net-section hole edge of plate 7.



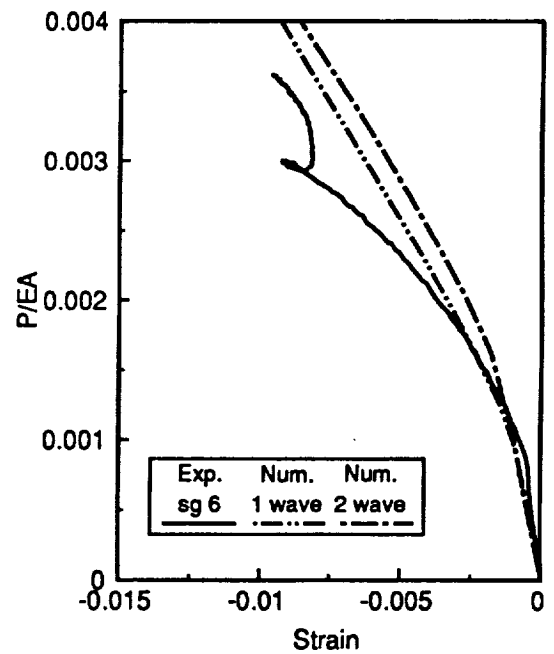
(a) strain 1



(b) strain 3



(c) strain 4



(d) strain 6

Fig. 7-62 Comparison of strains near the simple support of plate 7.

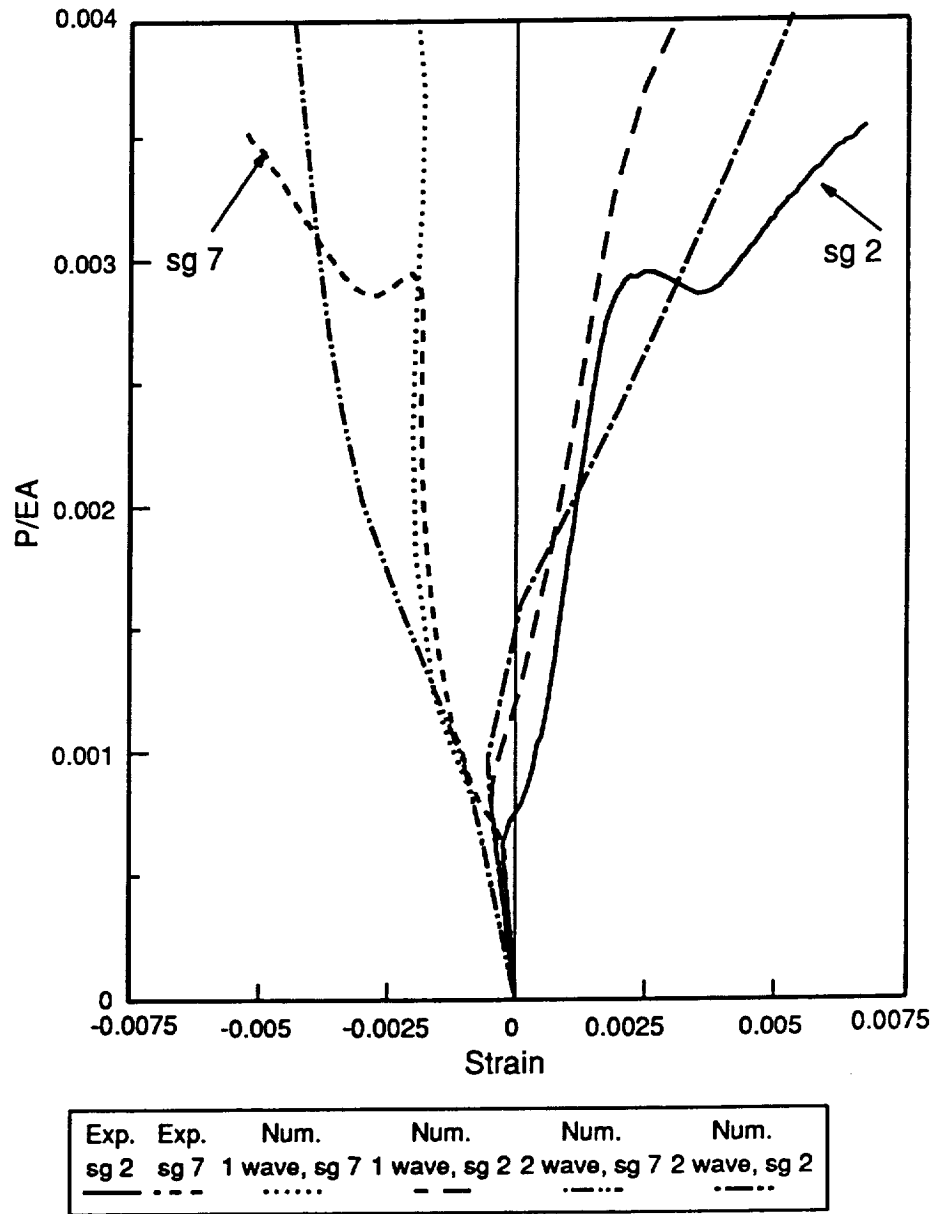


Fig. 7-63 Comparison of strains near the clamped support of plate 8.

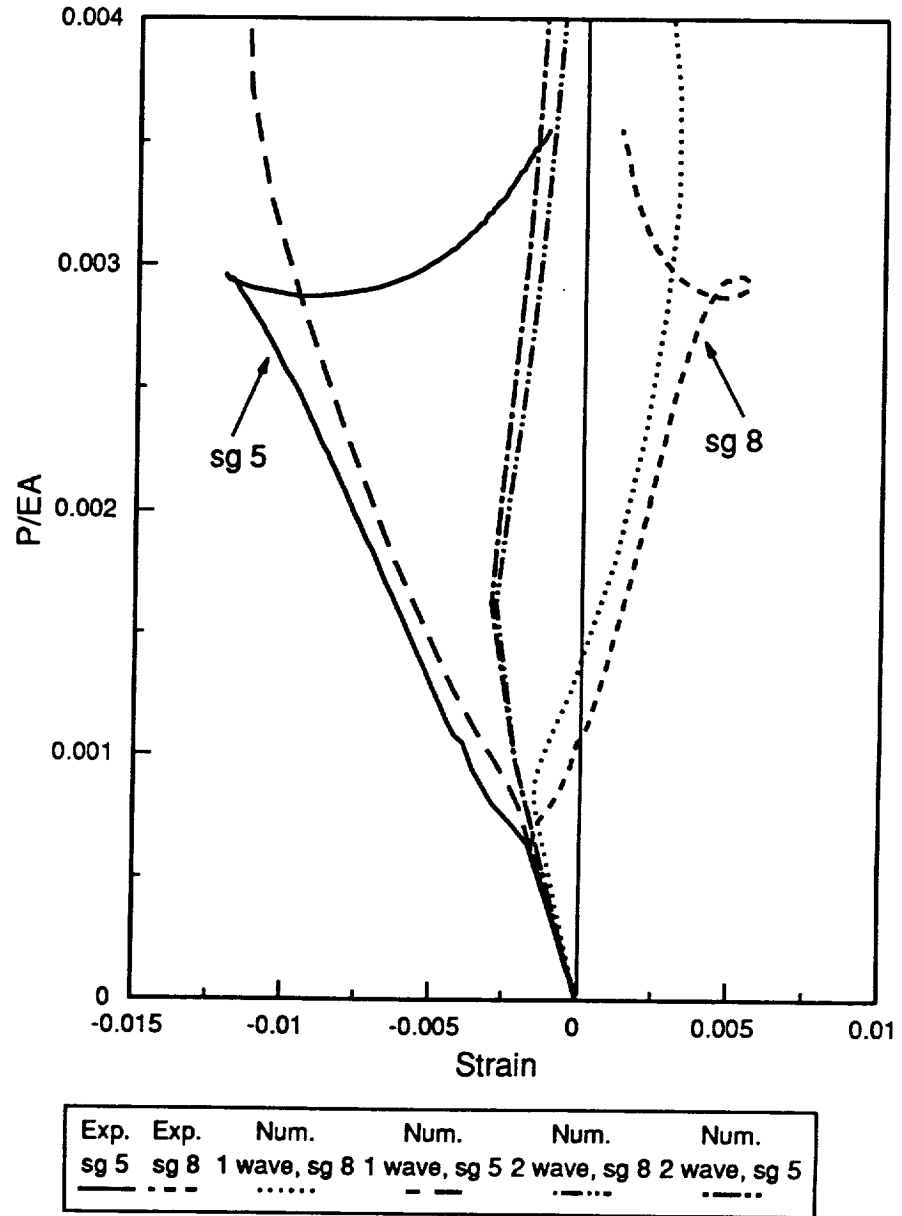
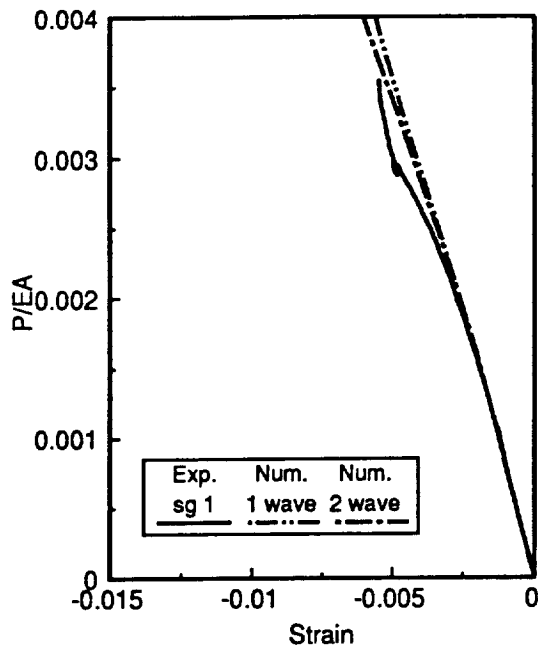
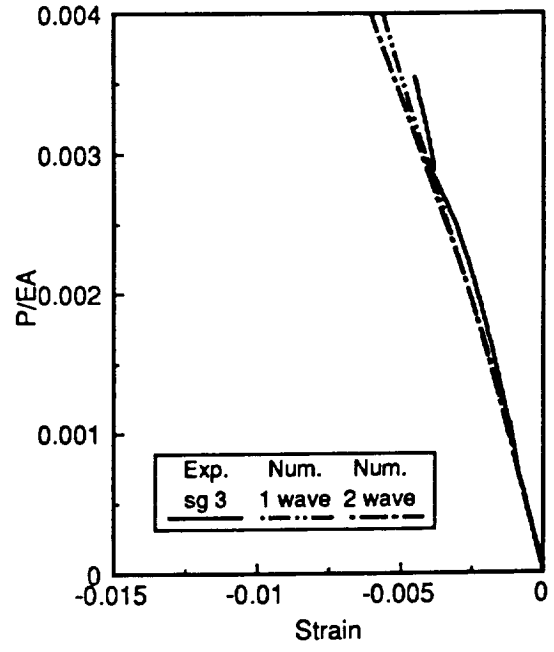


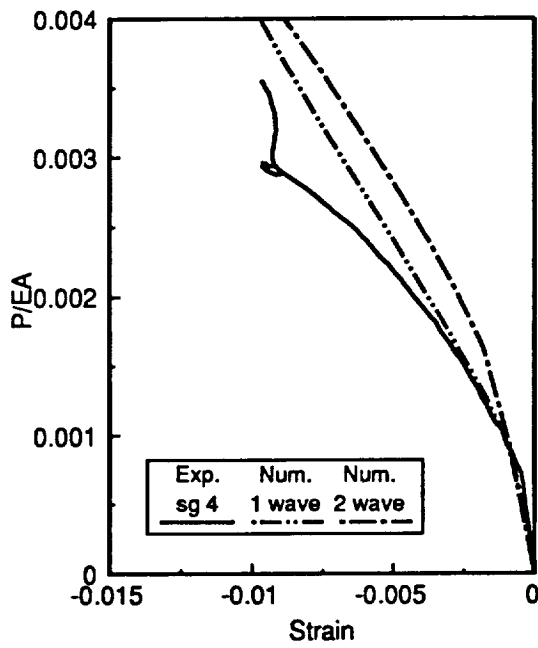
Fig. 7-64 Comparison of strains at the net-section hole edge of plate 8.



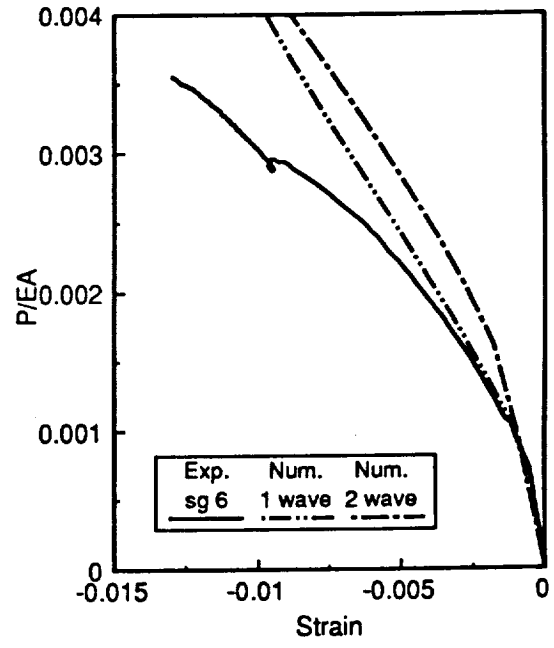
(a) strain 1



(b) strain 3



(c) strain 4



(d) strain 6

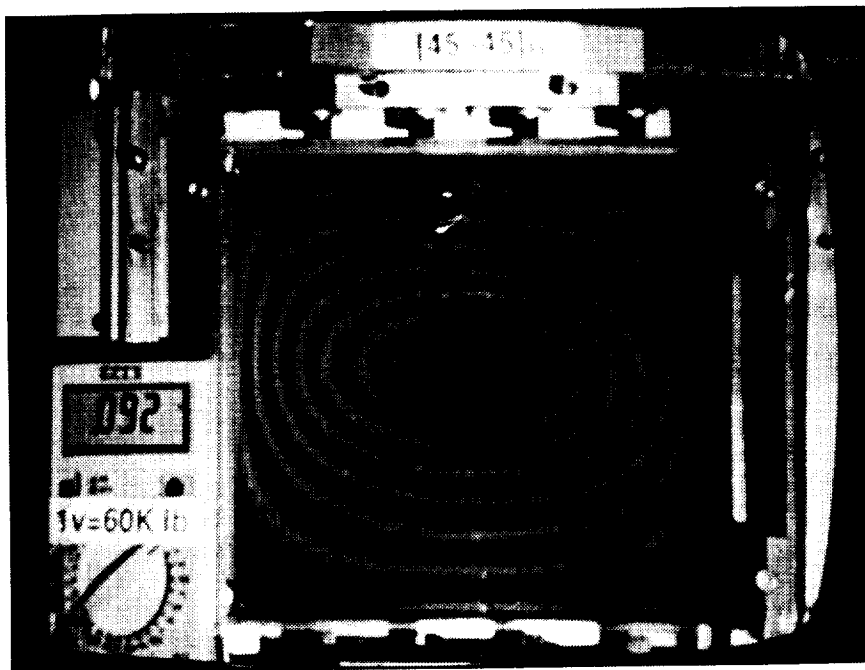
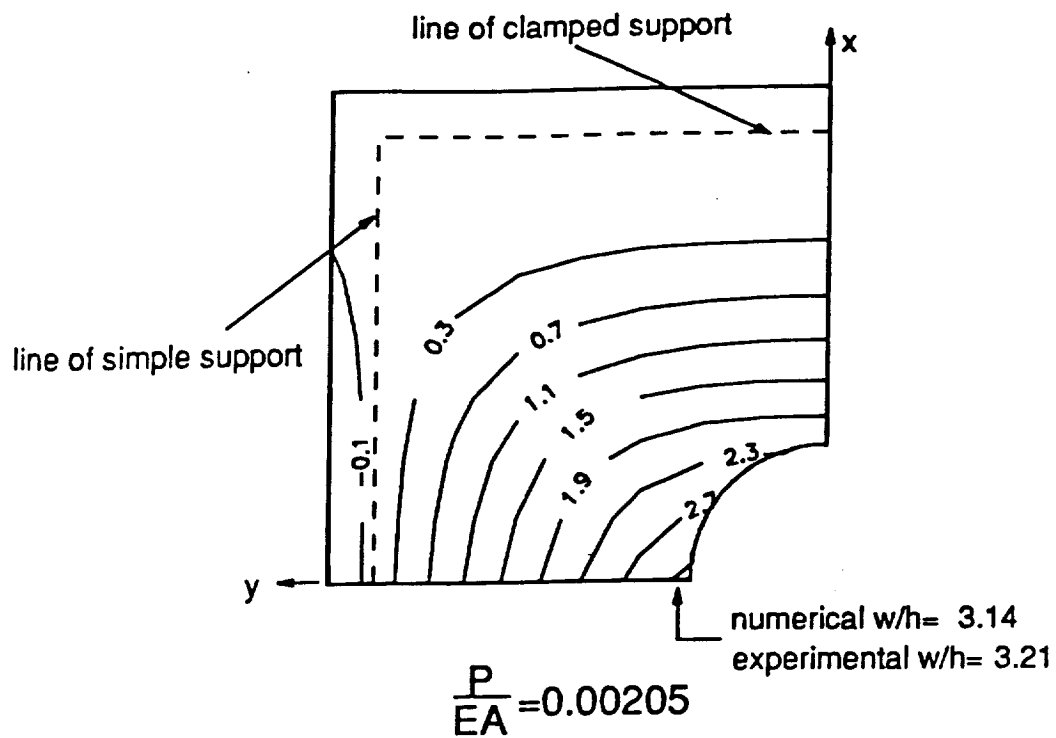
Fig. 7-65 Comparison of strains near the simple support of plate 8.

gauge 5 registered positive strain in the deep postbuckling range before the mode shape change, it can be seen that the plate 7 was deflected so that strain gauge 5 was on the convex side of the plate, as in Fig. 7-25(a). Strains 1 and 3, and 4 and 6 showed good symmetry of response of plate 7 before the mode shape change. Figure 7-59 shows the experimental strains for plate 8. By the fact that strain gauge 5 registered negative strain, it can be seen that the plate 8 was deflected so that the strain gauge 5 was on the concave side of the plate. This was opposite the response of plate 7. Gauges 1 and 3 showed reasonable agreement, while gauges 4 and 6 showed good agreement.

The correlations between the experimentally measured strains and numerically predicted strains are shown in Fig. 7-60 - Fig. 7-62 for plate 7 and in Fig. 7-63 - Fig. 7-65 for plate 8. The correlation between predictions and experimental results for the strains before the mode shape change is not bad. Before the mode shape change the experimental strains seemed to follow the one half-wave solution. However, after the mode shape change the experimental strains did not agree well with numerically predicted strains. It is noticeable especially in the comparison of strain 7 in Fig. 7-60 and strains 2 and 7 in Fig. 7-63.

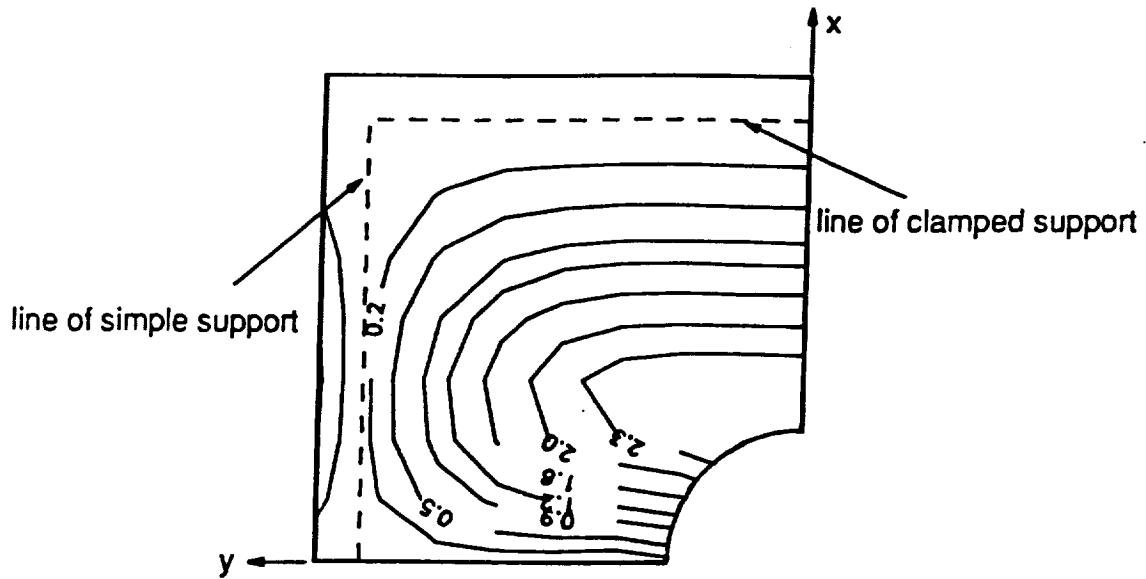
7.4.3 Shadow Moire Results

The comparison of the out-of-plane deflection contour drawing and shadow moire fringe pattern for the one half-wave configuration is shown in Fig. 7-66. This correlation is good. For the two half-wave configuration the comparison of out-of-plane deflection is shown in Fig. 7-67.

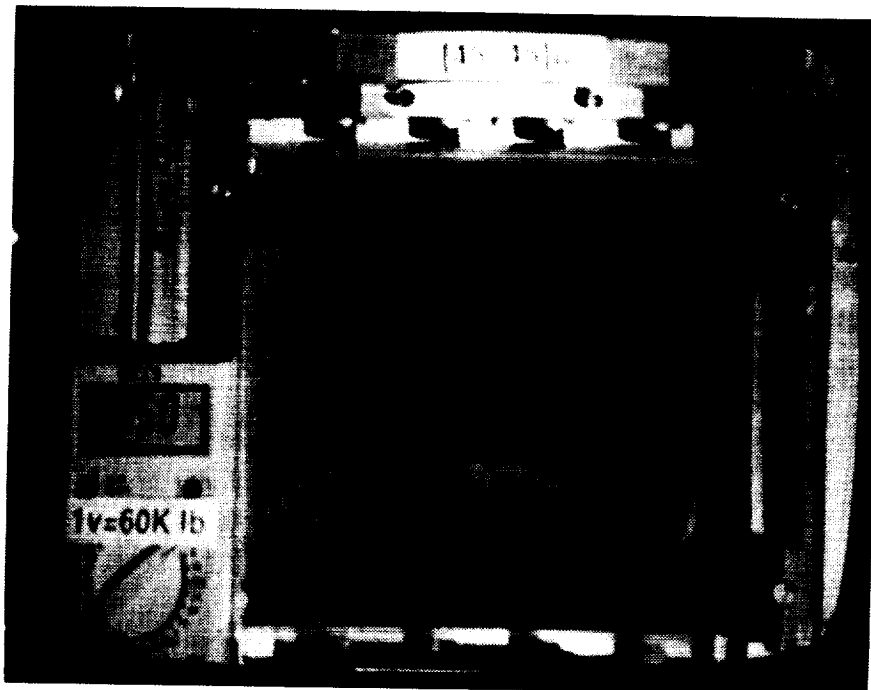


$$\frac{P}{EA} = 0.00205$$

Fig. 7-66 Predicted and measured shadow moiré fringe pattern for a $[\pm 45]_{45}$ plate in a one half-wave configuration.



$$\frac{P}{EA} = 0.00335$$



$$\frac{P}{EA} = 0.00335$$

Fig. 7-67 Predicted and measured shadow moiré fringe pattern for a $[\pm 45]_{4s}$ plate in a two half-wave configuration.

7.4.4 Failure and Post-Mortem Analysis

The failed status of plate 7 is shown in Fig. 7-68. It can be seen that failure occurred along a 45° line along one simple support. In plate 8 failure occurred in the same fashion but along both simple supports. Even though the load-end shortening relation was quite different than the numerical prediction, the failure location seemed to agree with numerical prediction of Fig. 5-16. The contour drawing of failure parameters at a load level slightly above the matrix failure load is shown in Fig. 7-69. It can be seen that R_1 is low overall, R_2 is high at the center of the quarter-plate, and R_{12} is very high along the simple support slightly away from the net-section. Figure 7-69(d) and (e) show the interlaminar shear stresses are very small all over the plate.

7.4.5 Acoustic Emission Results

Acoustic emission test results for plate 7 and plate 8 are shown in Fig. 7-70 and 7-71, respectively. Unfortunately, the contact between the specimen and acoustic emission transducer was bad. The results for plate 7 and plate 8 were poor and essentially meaningless.

7.5 Summary of Findings and Further Results

A large amount of information obtained from the experiments has been presented which allows for the characterization of the postbuckling response of the

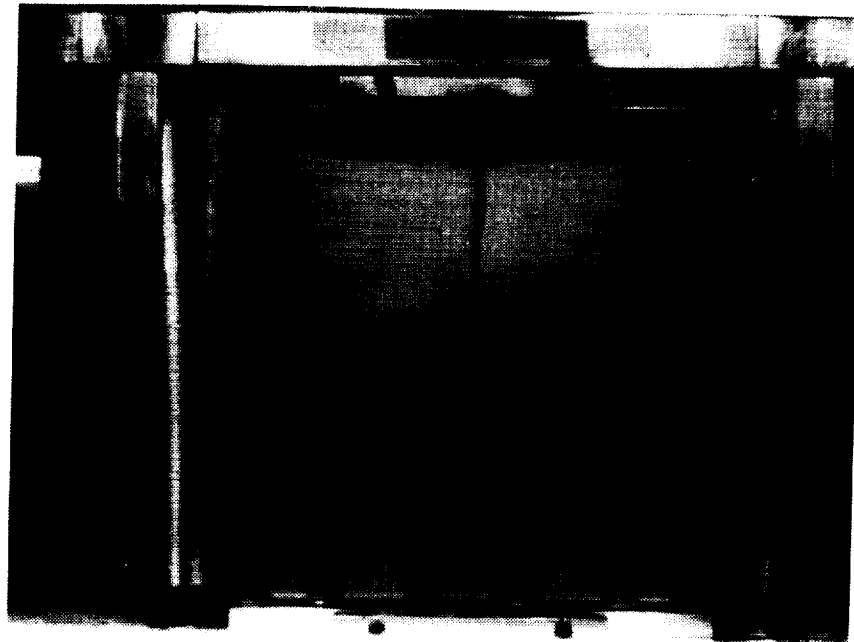
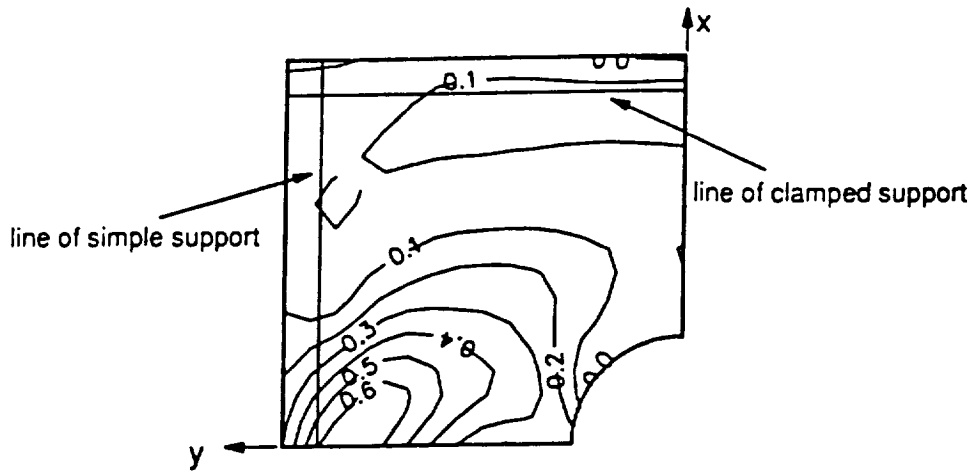
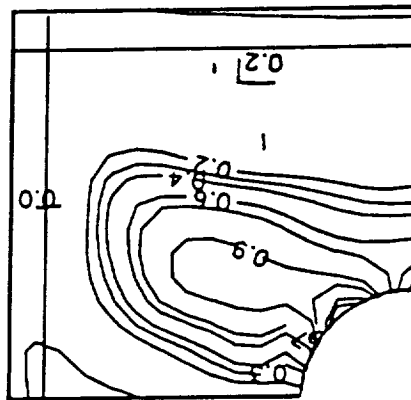


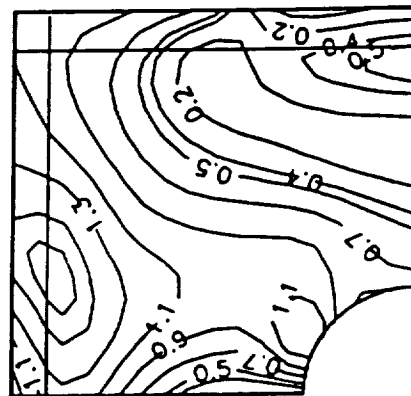
Fig. 7-68 Failed $[\pm 45]_{4s}$ plate in the fixture.



(a) Contour plot of R_1 on 1-st layer from bottom (45° layer).

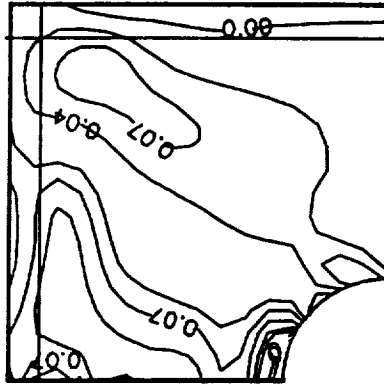


(b) Contour plot of R_2 on 16-th layer from bottom (45° layer).

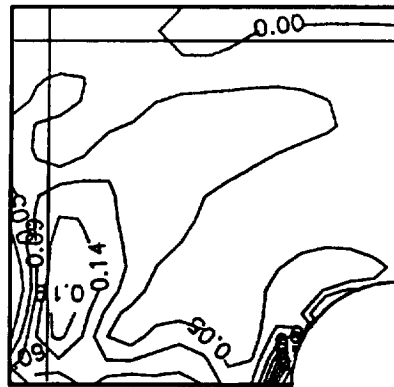


(c) Contour plot of R_{12} on 1-st layer from bottom (45° layer).

Fig. 7-69 Contour of failure parameters of the $[\pm 45]_{4s}$ plates at $P/EA = 0.00395$ (continued).



(d) Contour plot of R_{13} on 8-th layer from bottom (45° layer).



(e) Contour plot of R_{23} on 8-th layer from bottom (45° layer).

Fig. 7-69 Contour of failure parameters of the $[\pm 45]_{4S}$ plates at $P/EA = 0.00395$ (concluded).

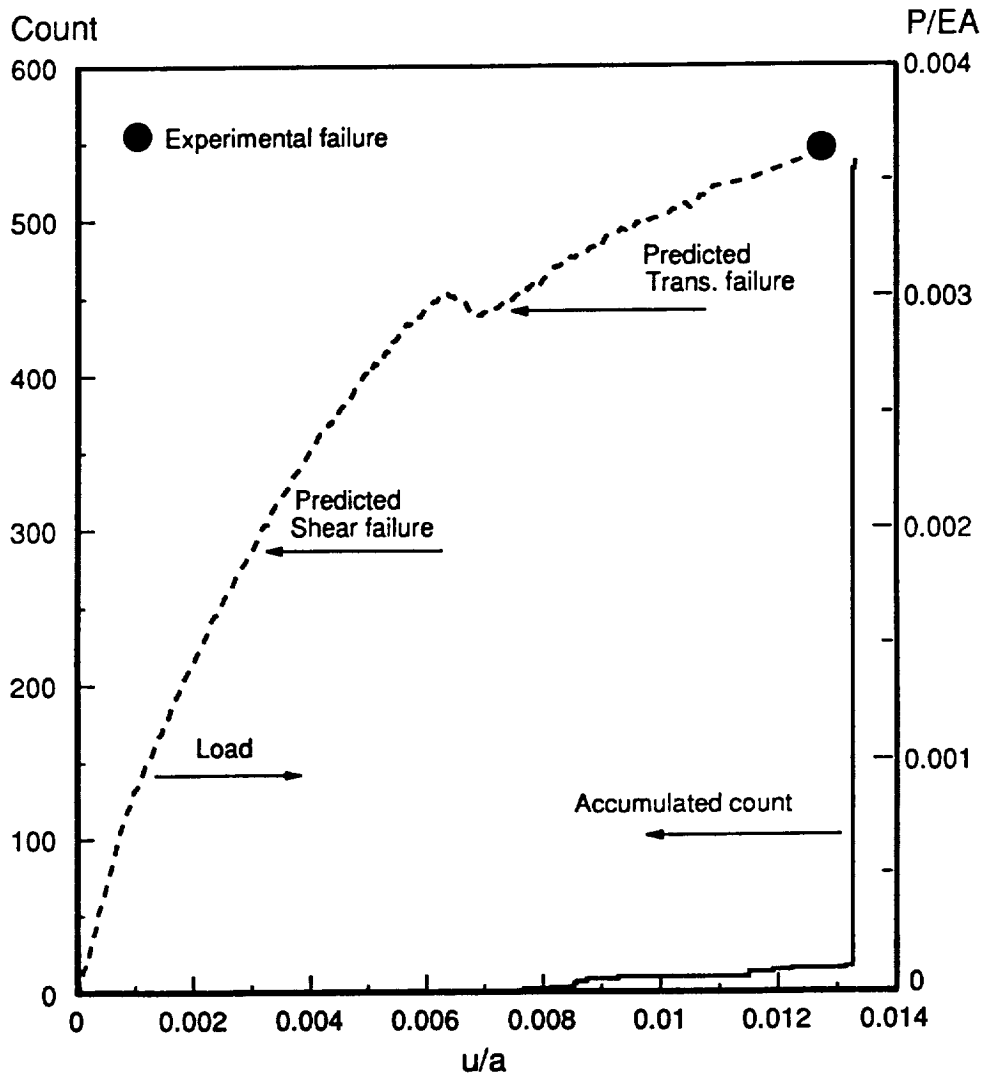


Fig. 7-70 Acoustic emission activity and load-end shortening relation for plate 7, $[\pm 45]_{4s}$.

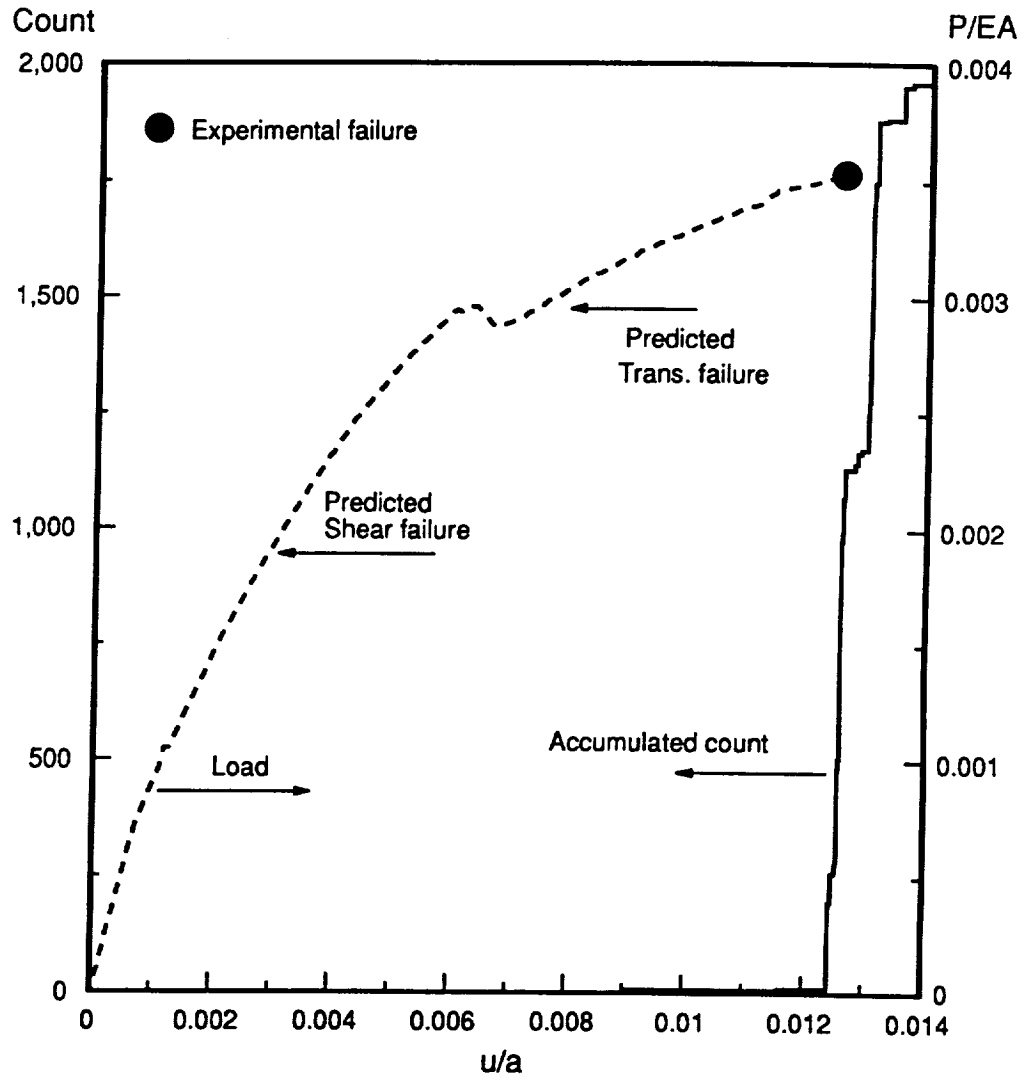


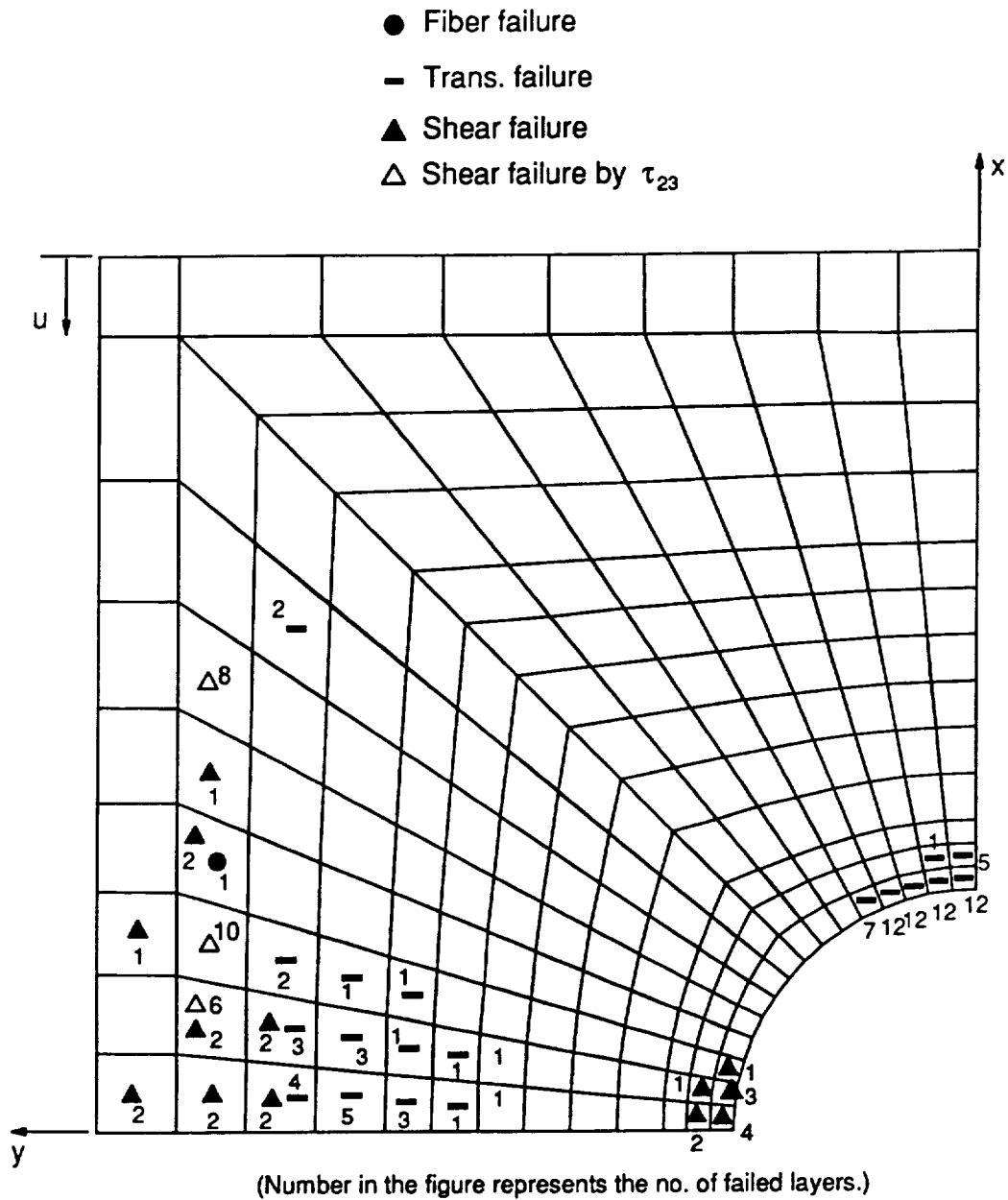
Fig. 7-71 Acoustic emission activity and load-end shortening relation for plate 8, $[\pm 45]_{4S}$.

specific composite plates studied. In general, the numerically predicted response and the observed response agree quite well. Though the mode shape change was not predicted, nor was there an attempt to predict it, it was shown that before the mode shape change the response of the plates followed the one half-wave configuration prediction, and after the mode shape change the response of the plates followed the two half-wave configuration prediction. The numerical prediction of failure loads for $[\pm 45/0/90]_{2s}$ and $[\pm 45/0_2]_{2s}$ laminates agrees very well with the experimental results. It was shown that the failure of these laminates was controlled by inplane stresses.

With the $[\pm 45]_{4s}$ laminate the postbuckling response did not agree with the numerical prediction. It was observed that the deviation of the numerical prediction from the experimental results began at the load level where the inplane shear failure was predicted. It was mentioned in chapter 7 that due to the inplane shear failure the $[\pm 45]_{4s}$ laminate loses load bearing capability. This resulted in the disagreement between the numerical prediction and experimental results in postbuckling response. Therefore, predicting the failure load with the present method is not accurate. It is recommended that progressive failure analysis be used for the $[\pm 45]_{4s}$ laminate. Other researchers have had difficulty in correlating the observed response of ± 45 laminates with numerical prediction based on linear elastic analysis. The nonlinear softening stress-strain behavior associated with the inplane shear response is generally felt to be the cause of this. Progressive failure would add a softening effect also. It is felt both issues must be addressed to fully understand the effect of laminates with no 0° layers. However, it was shown that the prediction of failure mode and failure location agreed with experimental results.

With the $[\pm 45/0_6]_s$ laminate predicted postbuckling deformation response agreed very well with numerical results. However, predicted failure location and failure mode did not agree with experimental results. In the numerical prediction no interlaminar shear failure was predicted. However, it appears that the $[\pm 45/0_6]_s$ plates failed due to excessive interlaminar shear stress τ_{23} along the simple supports. It is felt that the interlaminar shear strength of the clustered layers, the inner 12 layers of the $[\pm 45/0_6]_s$ laminate, could have been much lower than the interlaminar shear strength of a single layer. To explore this idea further, based on the experimental observation of the $[\pm 45/0_6]_s$ laminate, the interlaminar shear strength τ_{23} for the clustered inner 12 layers will be estimated. The damage accumulation scenario will then be re-examined for this laminate.

The average experimental failure load of the plates 5 and 6 is $N_x = 1918$ lb/in.. In the numerical failure analysis the maximum value of failure parameter R_{23} was 0.25 when $N_x = 1918$ lb/in. if the interlaminar shear strength $S_{23} = 8$ ksi was used, the value shown in Table 5-1. Therefore, it can be deduced that if S_{23} of the clustered inner 12 layers of the $[\pm 45/0_6]_s$ laminate was 2 ksi, the interlaminar shear failure parameter would be $R_{23} = 1.0$. Figure 7-72 shows the re-examined damage accumulation scenario of the $[\pm 45/0_6]_s$ laminate deformed into the one half-wave configuration with estimated interlaminar shear strength of $S_{23} = 2$ ksi. The other strength values are the same as in Table 5-1. In Fig. 7-72 it can be seen that interlaminar shear failure due to τ_{23} is predicted along the simple support. Away from the net-section but along the simple support over one-half of the inner 12 layers have failed. Figure 7-73 shows the damage accumulation scenario for the $[\pm 45/0_6]_s$ plate with a hole deformed into the two half-wave configuration. It can be seen that severe interlaminar shear failure due to τ_{23} is predicted for the two half-wave configuration also.



$$\text{Load} : \frac{P}{EA} = 0.00169$$

Fig. 7-72 Predicted failure locations and failure modes of $[\pm 45/0_6]_s$ plate with hole in the one half-wave configuration with revised value of S_{23} .

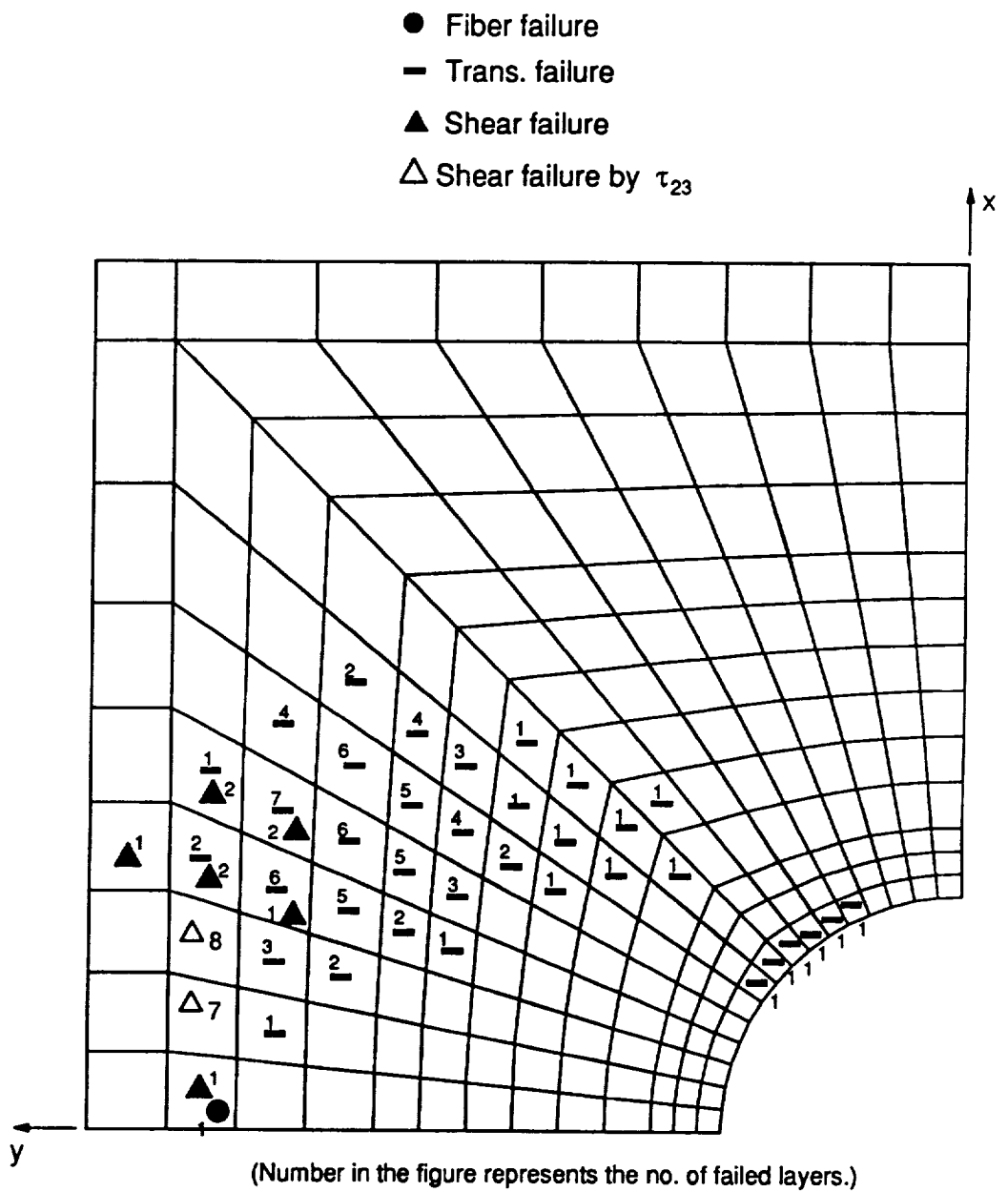
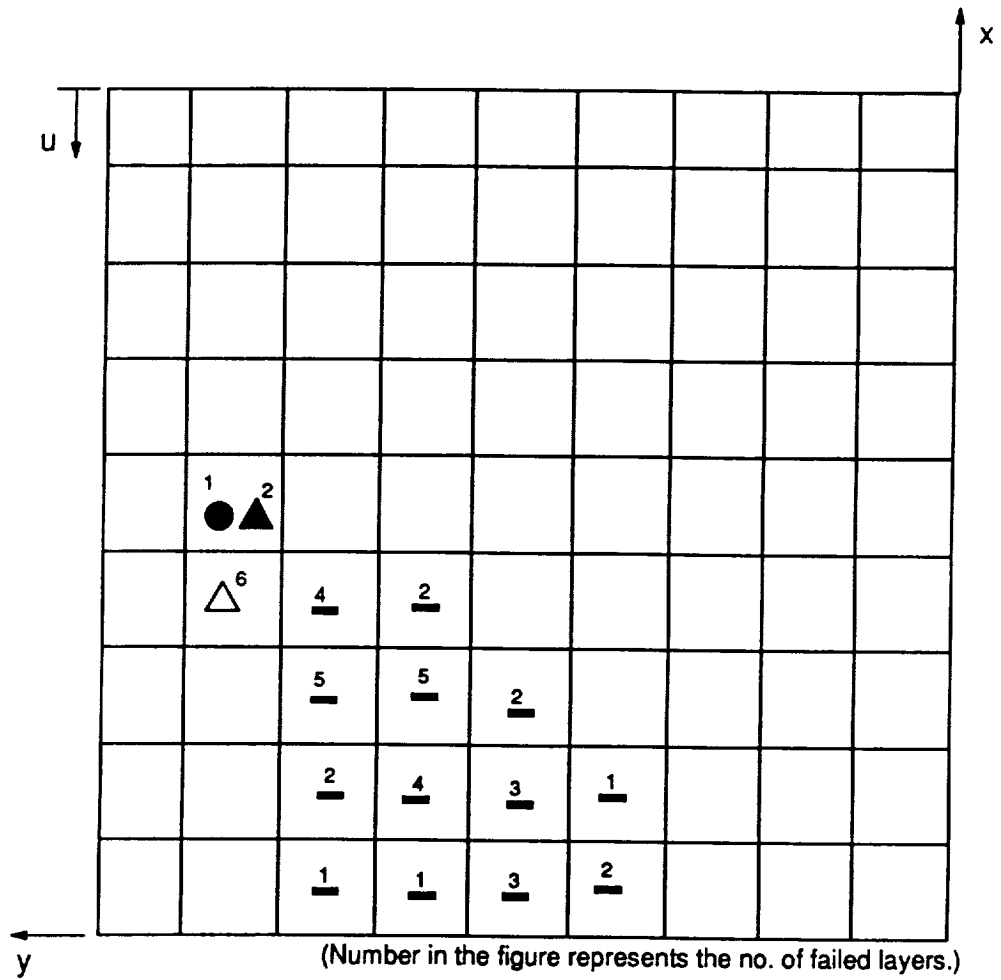


Fig. 7-73 Predicted failure locations and failure modes of $[\pm 45/0]_s$ plate with hole in the two half-wave configuration with revised value of S_{23} .

Based on the comparison between the experimental results and numerical predictions for the plates with holes, the following can be said for the plates without holes. It is expected that the postbuckling deformation response and failure of the solid $[\pm 45/0/90]_{2s}$ and $[\pm 45/0_2]_{2s}$ laminates can be correctly predicted as in chapters 3 and 5. The postbuckling deformation response of the solid $[\pm 45/0_6]_s$ laminate can be predicted correctly as in chapter 3. However, for this particular laminate failure analysis using the lower interlaminar shear strength value, $S_{23} = 2$ ksi, will probably give a more realistic prediction. The reevaluated failure prediction for the one half-wave configuration is shown in Fig. 7-74. It can be seen that the solid $[\pm 45/0_6]_s$ plate in the one half-wave configuration would experience failure due to interlaminar shear stress τ_{23} along the simple support. In the same region a high fiber stress is also predicted, along with a high inplane shear stress. Figure 7-75 shows the failure prediction of the solid $[\pm 45/0_6]_s$ plate deformed into the two half-wave configuration. In Fig. 7-75 it can be seen that interlaminar shear failure due to τ_{23} is not as severe. The solid $[\pm 45/0_6]_s$ laminate in the two half-wave configuration will fail due to inplane stresses.

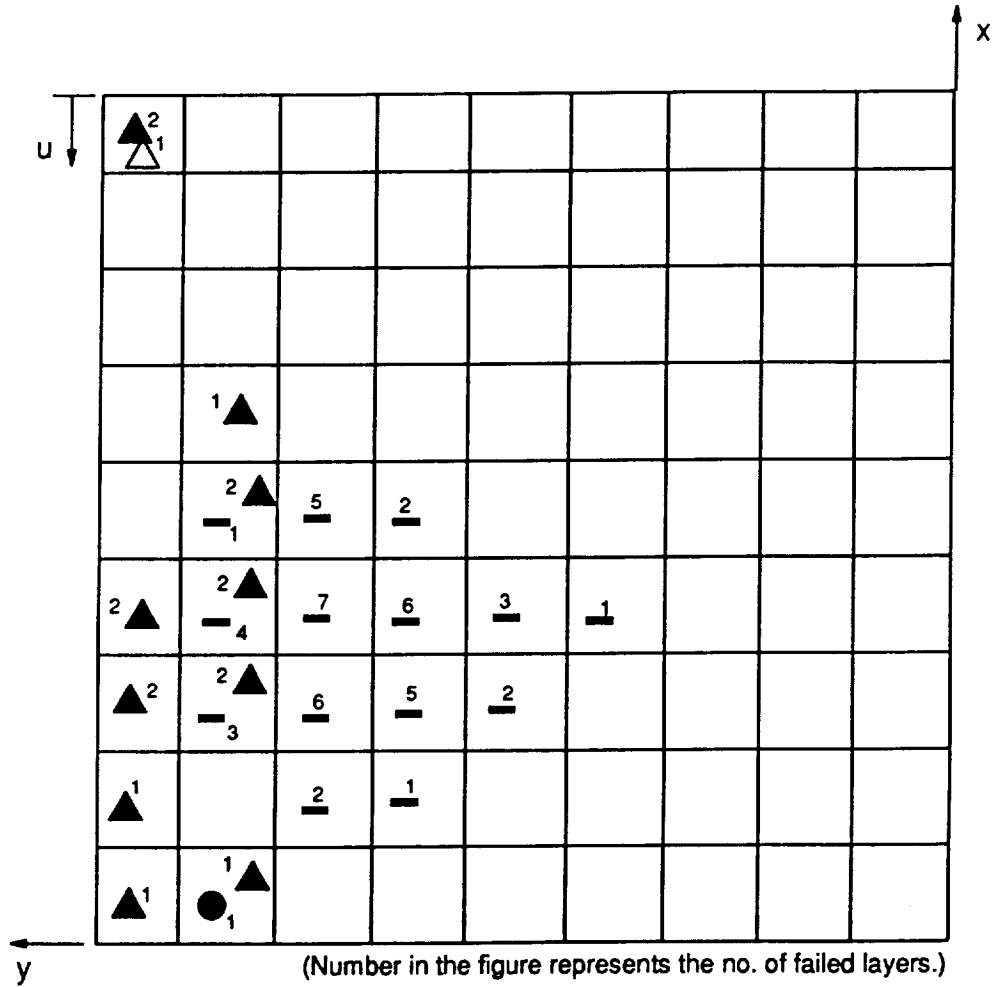
- Fiber failure
- Trans. failure
- ▲ Shear failure
- △ Shear failure by τ_{23}



$$\text{Load} : \frac{P}{EA} = 0.00169$$

Fig. 7-74 Predicted failure locations and failure modes of solid $[\pm 45/0_b]_s$ plate in the one half-wave configuration with revised value of S_{23} .

- Fiber failure
- Trans. failure
- ▲ Shear failure
- △ Shear failure by τ_{23}



$$\text{Load} : \frac{P}{EA} = 0.00177$$

Fig. 7-75 Predicted failure locations and failure modes of solid $[\pm 45/0]_s$ plate in the two half-wave configuration with revised value of S_{23} .

8.0 Concluding Comments and Recommendations

8.1 Concluding Comments

The numerical buckling loads obtained in chapter 2 and the experimental buckling loads discussed in chapter 7 are summarized in Table 8-1. Numerical and experimental failure loads of each of the laminates discussed in chapters 5 and 7 are summarized in Table 8-2. Table 8-2 shows a failure prediction resulting from the use of a revised value of S_{23} for the $[\pm 45/0_6]_S$ laminate. Since known failure results were used to obtain the revised prediction of Table 8-2, the "prediction" is actually meaningless. What is important is the fact that the location of failure associated with the "prediction" is accurately predicted to be along the simple support.

From the results in Table 8-2 it can be concluded that the understanding of the failure in the postbuckling range has certainly been enhanced by this study. Failure of two laminates of practical importance, namely the $[\pm 45/0/90]_{2S}$ and the $[\pm 45/0_2]_{2S}$ laminates, appears to be completely predictable. Highly orthotropic lami-

Table 8-1 Experimentally determined and numerically predicted buckling loads of each laminate.

Laminate	Plate	Experimental						Numerical	
		Each plate		Average		\overline{N}_x^c (lb/in.)	P_R/EA	\overline{N}_x^c (lb/in.)	
		P_R/EA	\overline{N}_x^c (lb/in.)	P_R/EA	\overline{N}_x^c (lb/in.)				
[± 45/0/90] _{2s}	plate 1	0.000375	235	0.000370	232	258	0.000411	258	
	plate 2	0.000364	228						
[± 45/0 ₂] _{2s}	plate 3	0.000300	275	0.000305	279	294	0.000321	294	
	plate 4	0.000309	283						
[± 45/0 ₆] _s	plate 5	0.000227	283	0.000234	292	318	0.000245	318	
	plate 6	0.000241	301						
[± 45] _{4s}	plate 7	0.000880	215	0.000880	215	240	0.000980	240	
	plate 8	0.000880	215						

Table 8-2 Experimentally determined and numerically predicted failure loads of each laminate.

Laminate	Plate	Experimental						Numerical	
		Each plate		Average		P/EA	\bar{N}_x (lb/in.)	P/EA	\bar{N}_x (lb/in.)
		P/EA	\bar{N}_x (lb/in.)	P/EA	\bar{N}_x (lb/in.)				
[± 45/0/90] _{2s}	plate 1	0.00234	1468	0.00253	1584	0.00244	1532		
	plate 2	0.00271	1700						
[± 45/0 ₂] _{2s}	plate 3	0.00201	1842	0.00200	1833	0.00206	1892		
	plate 4	0.00199	1824						
[± 45/0 _s] _s	plate 5	0.00144	1799	0.00154 ¹	1918 ¹	0.00163 ² (0.00154) ³	2030 ² (1918) ³		
	plate 6	0.00163	2036						
[± 45] _{4s}	plate 7	0.00362	885	0.00359	877	poor correlation due to material nonlinearity and progressive failure.			
	plate 8	0.00355	868						

1 : interlaminar shear failure 2 : fiber failure, one half-wave (Table 5-2)

3 : Using the revised interlaminar shear strength to take into account the layer clustering effect along the simple support

nates such as $[\pm 45/0_6]_s$ are not likely to be used in the near future. In fact, the $[\pm 45/0_2]_{2s}$ laminate is quite orthotropic by current standards. Thus, not being able to a priori predict the failure of the $[\pm 45/0_6]_s$ laminate may be of little practical consequence. Also, not using any 0° layers is uncommon and not being able to predict the failure, or even the deformation response, of the $[\pm 45]_{4s}$ laminate may also be of little practical importance. In practice the issue of interlaminar shear stresses on the control of failure may not really be an important issue, either. For an aspect ratio of 1:1, at least for the value of D/W considered here, whether the $[\pm 45/0/90]_{2s}$ and $[\pm 45/0_2]_{2s}$ laminates are deformed into the one half-wave configuration or the two half-wave configuration, the failure load and failure mechanisms are very similar. Specifically, failure due to excessive inplane stresses is the controlling factor.

Based on this study of the postbuckling failure analysis, the following specific conclusion can be reached:

1. Despite the presence of multiple waves in the loading direction, inplane failure mechanisms control the failure of square $[\pm 45/0/90]_{2s}$ and $[\pm 45/0_2]_{2s}$ laminates with holes of $D/W = 0.3$.
2. In the $[\pm 45/0_6]_s$ laminate interlaminar shear failure governs failure. From the experimental results it was observed that the lower interlaminar shear strength of clustered layers could be responsible for controlling interlaminar failure along the simple support.
3. The $[\pm 45]_{4s}$ laminate response is influenced by softening behavior, a characteristic not modelled. This characteristic must be modelled to accurately predict both the displacement response and failure.

The following general conclusions can also be reached as a result of this study:

1. Even though a plate may experience a mode shape change in the postbuckling range, the failure load of a plate with a mode shape change may not be too different from the failure load of a plate without mode shape change. This makes the designer's task much easier.
2. The maximum stress criterion is valid for the postbuckling failure analysis.
3. Since a criterion for the mode shape change in the postbuckling range is not available, experimental verification of numerical prediction is important.
4. The use of acoustic emission as an indicator of failure for structural level experiments has potential.

8.2 Recommendations for Future Research

Clearly the primary recommendation to be made regarding future research is to repeat this research for plates with other values of D/W and for plates with no holes. Since the $[\pm 45/0_8]_s$ and $[\pm 45]_{4s}$ laminates may not be of much practical importance, it is recommended that besides the $[\pm 45/0/90]_{2s}$ and $[\pm 45/0_2]_{2s}$ laminates only one other laminate be considered. The three laminates to be considered are $[\pm 45/0/90]_{2s}$, $[\pm 45/0_2]_{2s}$, and $[\pm 45/90_2]_{2s}$. These laminates would bracket the range of orthotropy in current use, though the $[\pm 45/90_2]_{2s}$, like the $[\pm 45]_{4s}$, does not contain any layers with fibers in the loading direction and therefore may, in fact, not

be realistic. The issue of plates with no holes is quite important. These could be considered the baseline cases and experimental data need to be gathered. Plates with larger holes than those tested would result in even more load being transmitted along the simple support region at the net-section. It would be expected that inplane stresses would control failure in those cases. For plates with smaller holes it is not apparent what would happen. If the hole is small enough, the plate may behave as if it had no hole. These are important issues. All aspects should be explored. Also of importance is the issue of mode change. Factors which control the triggering of mode change should be explored. Candidate factors include lack of perfect flatness in the plates, slight misalignments in the load, and a lack of ideal boundary conditions. Nonuniformity of material properties, in a spatial sense, could be important too.

Secondary issues recommended for future research includes consideration of other materials, e.g., IM7/8551-7a, a material with stiffer fibers and a softer matrix. Absolute size may be another factor. Repeating the experiments with plates twice or three times as large may reveal that material allowables need to be adjusted to reflect a large volume of material.

In summary, more work can and should be done, both experimentally and numerically. The ultimate goal should be contributing to guidelines for designers to take advantage of postbuckling strength.

9.0 References

1. Dickson, J. N., Biggers, S. B., and Wang, J. S. T, "A Preliminary Design Procedure for Composite Panels with Open-Section Stiffeners Loaded in the Postbuckling Range," Advances in Composite Materials, (Proceedings of the Third International Conference on Composite Materials, Paris, France, Aug 26-29, 1980, Vol. 1), pp.812-825.
2. Nemeth, M. P., "Buckling and Postbuckling Behavior of Square Compression Loaded Graphite-Epoxy Plates with Circular Cutouts," Eighth DOD/NASA/FAA Conference on Fibrous Composites in Structural Design, Norfolk, Virginia, Nov. 28-30, 1989.
3. Bryan, G. H., "On the Stability of a Plane Plate Under Thrusts in Its Own Plane, With Applications to the 'Buckling' of the Sides of the Ship," Proc. London Mathematical Society, Vol. 22, 1891, pp.54-67.

4. March, H., "Buckling of Flat Plywood Plates in Compression, Shear, or Combined Compression and Shear," Forest Products Lab., Madison, Wis., Rept. No. 1316, 1942.
5. Leissa, A. W., "A Review of Laminated Composite Plate Buckling," Applied Mechanics Review, Vol. 40, No. 5, May 1987, pp 575-591.
6. Levy, S., Woolley, R. M., and Kroll, W. D., "Instability of a Simply Supported Square Plate with a Reinforced Circular Hole in Edge Compression," Journal of Research of National Bureau of Standards, 1947, vol. 39, pp.571-577.
7. Nemeth, M. P., "Buckling Behavior of Orthotropic Composite Plates with Centrally Located Cutouts," Ph.D. Dissertation, Virginia Polytechnic Institute and State University, May 1983.
8. Kroll, W. D., "Instability in Shear of Simply Supported Square Plates with Reinforced Hole," Journal of Research of the National Bureau of Standards, Vol. 43, Nov. 1949, pp.465-472.
9. Kumai, T., "Elastic Stability of the Square Plate with a Central Circular Hole under Edge Thrusts," Proceedings of the First National Congress for Applied Mechanics, 1951, pp.81-86.
10. Schlack, A. L., Jr., "Elastic Stability of Pierced Square Plates," Experimental Mechanics, Vol. 4, No. 6, June 1964, pp.167-172.
11. Yoshiki, M., Fujita, Y., Kawamura, A., and Arai, H., "Instability of Plates with Holes," First Report, Proceedings of the Society of Naval Architects of Japan, No. 122, Dec. 1967, pp.137-145.
12. Schlack, A. L., "Experimental Critical Loads for Perforated Square Plates," Experimental Mechanics, Vol. 8, No. 2, Feb. 1968, pp 69-74.
13. Kawai, T. and Ohtsubo, H., "A Method of Solution for the Complicated Buckling Problems of Elastic plates with Combined Use of Rayleigh-Ritz's Procedure in

- the Finite Element Method," Proceedings of the Second Conference on Matrix Methods in Structural Mechanics, AFFDL-TR-68-150, 1968, pp.967-994.
14. Yu, W. W. and Davis, C. S., "Buckling Behavior and Postbuckling Strength of Perforated Stiffened Compression Elements," Proceedings of the First Specialty Conference on Cold Formed Steel Structures, University of Missouri-Rolla, Rolla, Mo. , August 19-20, 1971.
 15. Martin, J., "Buckling and Postbuckling of Laminated Composite Square Plates with Reinforced Central Circular Holes," Ph.D Thesis, Case Western University, 1972.
 16. Vann, W. P. and Vos, R. G., "Compression Buckling of Pierced Elastic Plates," Structural Research at Rice, Report No. 14, Dept. of Civil Eng., Rice University, Houston, TX, August 1972.
 17. Yu, W. W. and Davis, C. S., "Cold Formed Steel Members with Perforated Elements," ASCE Journal of the Structural Division, ST10, Oct. 1973, pp.2061-2077.
 18. Ritchie, D., and Rhodes, J. ; "Buckling and Postbuckling Behavior of Plates with Holes," Aeronautical Quarterly, Vol. 26, Nov. 1975, pp.281-296.
 19. Knauss, J. F., Starnes, J. H. Jr., and Henneke, E. G. II, "The Compressive Failure of Graphite/Epoxy Plates with Circular Holes," Research Report VPI-E-78-5, Dept. of Engineering Science and Mechanics, Virginia Polytechnic Institute and State University.
 20. Preobrazhenskii, I. N., "Research Pertaining to Stability of Thin Plates with Holes," Soviet Applied Mechanics, Vol. 16, No. 7, Jan. 1981, pp.557-574.
 21. Nemeth, M. P., "Importance of Anisotropy on Buckling of Compression Loaded Symmetric Composite Plates," AIAA Journal, Vol. 24, Nov. 1986, pp.1831-1835.

22. Azizian, Z. G. and Roberts, T. M., "Buckling and Elasto-Plastic Collapse of Perforated Plates," Instability and Plastic Collapse of Steel Structures, ed. L. J. Morris, 1983, pp.322-328.
23. Vandenbrink, D. J. and Kamat, M. P., "Postbuckling Response of Isotropic Plate and Laminated Composite Square Plates with Circular Holes," Proceedings of the Fifth International Conference on Composite Materials, San Diego, CA, July 29-Aug. 1, 1985, pp.1393-1409.
24. Marshall, I. H., Little, W., and El-Tayeby, M. M., "The Stability of Composite Panels with Holes," chap. 17 of Mechanical Characterization of Load Bearing Fiber Composite Laminates, edited by A. H. Cardon and G. Verchery, Elsevier Applied Science Publishers, 1985.
25. Nemeth, M. P., Stein, M., Johnson, E. R. ; "An Approximate Buckling Analysis for Rectangular Orthotropic Plates with Centrally Located Cutouts," NASA TP-2528, Dec. 1986.
26. Sabir, A. B. and Chow, F. Y., "Elastic Buckling of Plates Containing Eccentrically Located Circular Holes," Thin Walled Structures, Vol. 4, No. 2, 1986, pp.135-150.
27. Yettram, A. L. and Brown, C. J., "The Elastic Stability of Square Perforated Plates under Biaxial Loadings," Computers and Structures, 22(4), 1986, pp.589-594.
28. Marshall, I. H., Little, W., and El-Tayeby, M. M., "Membrane Stress Distributions in Post-Buckled Composite Plates with Circular Holes," The Proceedings of the Sixth International Conference on Composite Materials combined with the Second European Conference on Composite Materials (ICCM & ECCM), July 1987, Vol. 5, pp. 5.57-5.68.
29. Larsson, P. L., "On Buckling of Orthotropic Compressed Plates with Circular Holes," J. Composite Structures, Vol. 7, 1987, pp.103-121.

30. Turvey, G. J. and Sadeghipour, K., " Compression Buckling of Anisotropic Fiber-Reinforced Flat Rectangular Plates with Central Circular Cut-Outs," The Proceedings of the Sixth International Conference on Composite Materials combined with the Second European Conference on Composite Materials (ICCM & ECCM), Vol. 5, July 1987.
31. Nemeth, M. P., "Buckling Behavior of Compression Loaded Symmetrically Laminated Angle-Ply Plates with Holes," AIAA Journal, Vol. 26, No. 3, 1988, pp.330-336.
32. Lin, C. C. and Kuo, C. S., " Buckling of Laminated Plates with Holes," Journal of Composite Materials, Vol. 23, 1989, pp.536-553.
33. Hyer, M. W. and Lee, H. H., "The Use of Curvilinear Fiber Format to Improve Buckling Resistance of Composite Plates with Central Circular Holes," J. Composite Structures, Vol. 18, 1991, pp. 239-261.
34. Starnes, J. H., Jr. and Rouse, M., "Postbuckling and Failure Characteristics of Selected Flat Rectangular Graphite-Epoxy Plates Loaded in Compression," AIAA Paper No. 81-0543, Presented at the AIAA/ASME/ASCE/AHS 22nd Structures, Structural Dynamics, and Materials Conference, Atlanta, GA, April 6-8, 1981.
35. Gurdal, Z., Haftka, R. T., and Starnes, J. H., Jr., "The Effect of Slots on the Buckling and Postbuckling Behavior of Laminated Plates," Composite Technology Review, Fall 1985, pp.82-87
36. Buskell, N., Davis, G. A. O., and Stevens, K. A., "Postbuckling Failure of Composite Panels," Composite Structures 3, Proceedings of the Third international conference, Paisley, Scotland, Sept 9-11, 1985, Elsevier Applied Publishers, London, 1985, pp.290-314.
37. Noor, A. K., Starnes, J. H., Jr., and Waters, W. A., Jr., "Numerical and Experimental Simulations of the Postbuckling Response of Laminated Anisotropic Panels," AIAA Paper No. 90-0964, Presented at the AIAA/ASME/ASCE/AHS 31st

Structures, Structural Dynamics, and Materials Conference, Long Beach, CA, April 2-4, 1990.

38. Shin, D. K., "Minimum-Weight Design of Symmetrically Laminated Composite Plates for Postbuckling Performance under In-plane Compression Loads," Ph.D Dissertation, Virginia Polytechnic Institute and State University, December, 1990.
39. Stein, M., "Loads and Deformations of Buckled Rectangular Plates," NASA TR R-40, 1959
40. Jensen, D. W. and Lagace, P. A., "Influence of Mechanical Couplings on the Buckling and Postbuckling of Anisotropic Plates," AIAA Journal, Vol. 26, 1988, pp 1269-1277.
41. Stein, M., "Postbuckling of Eccentric Open-Section Stiffened Composite Panels," AIAA Paper 88-2215, 1988, pp 57-61.
42. Minguet, P. J., Dugundji, J., and Lagace, P. A., "Postbuckling Behavior of Laminated Plates Using a Direct Energy-Minimization Technique," AIAA Journal, Vol. 27, 1989, pp 1785-1792.
43. Rushton, K. R., "Post-Buckling of Rectangular Plates with Various Boundary Conditions," Aeronautical Quarterly, Vol. 21, 1970, pp 163-181.
44. Chandra, R. and Raju, B. B., "Postbuckling Analysis of Rectangular Orthotropic Plates," Int. J. Mech. Sci., Vol. 15, 1973, pp 81-97.
45. Engelstad, S. P., Reddy, J. N., and Knight, N. F. "Postbuckling Response and Failure Prediction of Flat Rectangular Graphite-Epoxy Plates Loaded in Axial Compression," AIAA/ASME/ASCE/AHS 32-nd Structures, Structural Dynamics, and Materials Conference, Baltimore, MD, April 8-10, 1991
46. Reddy, J. N., Energy and Variational Methods in Applied Mechanics, John Wiley & Sons, Inc., 1984.

47. Reddy, J. N. and Chao, W. C., "Large Deflection and Large Amplitude Free Vibrations Of Laminated Composite-Material Plates," Computers & Structures, 1981, pp.341-347.
48. ABAQUS User's Manual, Hibbitt, Karlson & Sorenson, Inc., 1989
49. Reddy, J. N., An Introduction to the Finite Element Method, McGraw-Hill Book Company, 1984.
50. Chia, C. Y., Nonlinear Analysis of Plates, McGraw-Hill Book Company, 1980.
51. Pagano, N. J., "Exact Solutions for Composite Laminates in Cylindrical Bending," J. Composite Materials, Vol. 3, 1969, pp 398-411.
52. Chaudhuri, R. A. and Seide, P., "An Approximate Semi-analytical Method for Prediction of Interlaminar Shear Stresses in an Arbitrarily Laminated Thick Plate," Computers and Structures, Vol. 25, No. 4, pp.627-636, 1987.
53. Burns, S. W., Herakovich, C. T., and Williams, J. G., "Compressive Failure of Notched Angle-Ply Composite Laminates : Three-Dimensional Finite Element Analysis and Experiment," CCMS Report CCMS-85-11, College of Engineering Report, VPI-E-85-22, Virginia Polytechnic Institute and State University, 1985
54. Berg, J. S., and Adams, D. F., "An Evaluation of Composite Material Compression Test Methods," J. Composites Technology & Research, Vol. 11, No. 2, Summer 1989, pp.41-46.
55. Jones, R. M., Mechanics of Composite Materials, McGraw-Hill Book Company, 1975.
56. Tsai, S. W. and Hahn, H. T., Introduction to Composite Materials, Technomic Publishing Co., Inc., 1980.
57. Chang, F., "Moire Methods of Strain Analysis," Manual on Experimental Stress Analysis, 5-th ed., edited by Doyle, J. F. and Phillips, J. W., Society for Experimental Mechanics, 1989.

58. SPARTAN 3000 Operation Manual, Physical Acoustic Corporation.
59. Green, R. E., Jr., "Basic Wave Analysis of Acoustic Emission," Mechanics of Nondestructive Testing, edited by Stinchcomb, W. W., Plenum Press, 1980.

BIBLIOGRAPHIC DATA SHEET	1. Report No. VPI-E-92-07; CCMS-92-07	2.	3. Recipient's Accession No.
	4. Title and Subtitle Postbuckling Failure of Composite Plates with Central Holes		5. Report Date February 1992
7. Author(s) H.H. Lee and M.W. Hyer		8. Performing Organization Rept No. VPI-E-92-07, CCMS-92-07	
9. Performing Organization Name and Address Virginia Polytechnic Institute and State University Department of Engineering Science and Mechanics Blacksburg, VA 24061-0219		10. Project/Task/Work Unit No.	
12. Sponsoring Organization Name and Address Aircraft Structures Branch National Aeronautics and Space Administration Langley Research Center Hampton, VA 23665-5225		11. Contract/Grant No. Grant NAG-1-901	
13. Type of Report & Period Covered Interim 2/90-12/91		14.	
15. Supplementary Notes This report constitutes the PhD Thesis of the first author in Engineering Science and Mechanics at Virginia Polytechnic Institute and State University			
16. Abstract The postbuckling failure of square composite plates with central holes is analyzed numerically and experimentally. The particular plates studied have stacking sequences of $[\pm 45/0/90]_{2s}$, $[\pm 45/0_2]_{2s}$, $[\pm 45/6_8]_s$, and $[\pm 45]_{4s}$. A simple plate geometry, one with a hole diameter to plate width ratio of 0.3, is considered. Failure load, failure mode, and failure location are predicted numerically by using the finite-element method. The predictions are compared with experimental results. In the experiments in order to be accommodated by the test fixture it is necessary for the plates to be slightly larger than the analysis region, extending somewhat beyond the supports. The region outside the supports is included in the numerical study. It is shown that not considering these regions can lead to erroneous numerical predictions. In numerical failure analysis the interlaminar shear stresses, as well as the inplane stresses, are taken into account. By comparing the interlaminar shear stress calculations from the finite-element method with analytical results for simple cases, a solid foundation for interlaminar shear stress calculation is established. As a failure criterion, the maximum stress criterion is used. A special test fixture was designed for loading the plates. In the experiments, strain gauges, linear variable displacement transducers (LVDT's), and the shadow moire and acoustic emission tests are used to monitor plate response. An issue addressed in the study is the possible mode shape change of the plate during loading. To account for the fact that plates can experience mode shape change, two deformation configurations are considered. One configuration assumes the plate responds with one half-wave in the loading direction and the other configuration assumes the plate responds with two half-waves in the loading direction. Failure predictions are made for each configuration. No attempt is made to predict the configuration change. However, it is predicted that the first three laminates fail due to excessive stresses in the fiber direction and, more importantly, that the load level is independent of whether the laminate is deformed in the one half-wave configuration or the two half-wave configuration. The location of failure does depend on the deformed configuration. It is predicted that the fourth laminate fails due to excessive inplane shear stress. Interlaminar shear failure is not predicted for any laminate. For the first two laminates the experimental observations correlated well with the predictions. In the experiments the third laminate failed along the side support due to interlaminar shear. The 12 clustered 0° layers resulted in very low interlaminar shear strength S_{23} . The fourth laminate failed due to inplane shear in the location predicted. However, material softening resulted in an actual failure load quite different from the predicted value.			
17. Key Words and Document Analysis. 17a. Descriptors composite material, buckling response, postbuckling response, postbuckling failure, mode change, interlaminar stresses, damage accumulation, maximum stress failure criterion			
17b. Identifiers/Open-Ended Terms			
17c. COSATI Field/Group 24-01; 39-02; 39-07			
18. Availability Statement		19. Security Class (This Report) UNCLASSIFIED	21. No. of Pages 332
		20. Security Class (This Page) UNCLASSIFIED	22. Price

VIRGINIA TECH CENTER FOR COMPOSITE MATERIALS AND STRUCTURES

The Center for Composite Materials and Structures is a coordinating organization for research and educational activity at Virginia Tech. The Center was formed in 1982 to encourage and promote continued advances in composite materials and composite structures. Those advances will be made from the base of individual accomplishments of the sixty-five full and associate members who represent eleven different departments in three colleges.

The Center functions through an Administrative Board which is elected yearly and a Director who is elected for a three-year term. The general purposes of the Center include:

- collection and dissemination of information about composites activities at Virginia Tech,
- contact point for other organizations and individuals,
- mechanism for collective educational and research pursuits,
- forum and agency for internal interactions at Virginia Tech.

The Center for Composite Materials and Structures is supported by a vigorous program of activity at Virginia Tech that has developed since 1963. During 1988-89 and 1989-90 fiscal years sponsored research project expenditures for investigation of composite materials and structures have totalled approximately five million dollars annually.

Various Center faculty are internationally recognized for their leadership in composite materials and composite structures through books, lectures, workshops, professional society activities, and research papers.

Research is conducted in a wide variety of areas including design and analysis of composite materials and composite structures, chemistry of materials and surfaces, characterization of material properties, development of new material systems, and relations between damage and response of composites. Extensive laboratories are available for mechanical testing, nondestructive testing and evaluation, stress analysis, polymer synthesis and characterization, material surface characterization, component fabrication, and other specialties.

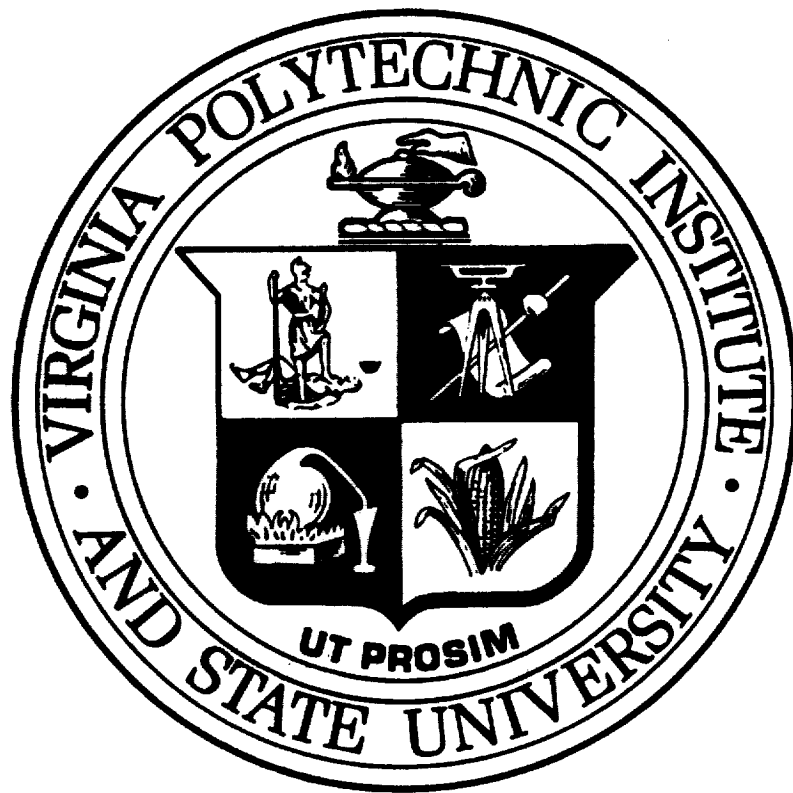
Educational activities include ten formal courses offered at the undergraduate and graduate levels dealing with the physics, chemistry, mechanics, and design of composite materials and structures. As of 1991, 129 Doctoral and 172 Master's students have completed graduate programs and are now active in industry, government, and education in the United States and abroad. The Center averaged 125 active student members during 1989-90 and 1990-91. Many Bachelor-level students have been trained in various aspects of composite materials and structures.

The Center has invested in the development of an administrative database (now fully operational for Center members) and a composite material properties database (now ready for data entry).

In addition to the CCMS Report Series, the Center sponsors a bi-monthly Seminar Series attended by faculty, staff, and students and the Center jointly sponsors a sesqui-annual Technical Review with the Center for Adhesive and Sealant Science which is well attended by government and corporate contacts.

MEMBERS OF THE CENTER		
Aerospace and Ocean Engineering Raphael T. Haftka Eric R. Johnson Rakesh K. Kapania	Electrical Engineering Ioannis M. Besieris Richard O. Claus Douglas K. Lindner	Industrial and Systems Engineering Joel A. Nachlas
Chemical Engineering Donald G. Baird Garth L. Wilkes	Engineering Science and Mechanics Robert Czarnek David A. Dillard Normal E. Dowling John C. Duke, Jr. Daniel Frederick O. Hayden Griffin, Jr. Zafar Gurdal Robert A. Heller Edmund G. Henneke, II Michael W. Hyer Robert M. Jones Ronald D. Kriz Liviu Librescu Alfred C. Loos Don H. Morris John Morton Ali H. Nayfeh Daniel Post J. N. Reddy Kenneth L. Reifsnider C. W. Smith Wayne W. Stinchcomb Surot Thangjitham	Materials Engineering Jesse J. Brown, Jr. Seshu B. Desu Ronald S. Gordon D. P. H. Hasselman Robert W. Hendricks Ronald G. Kander
Chemistry John G. Dillard Harry W. Gibson James E. McGrath Thomas C. Ward James P. Wightman		Mathematics Werner E. Kohler
Civil Engineering Richard M. Barker Richard E. Weyers		Mechanical Engineering Charles E. Knight Craig A. Rogers Curtis H. Stern
Clothing and Textiles Jeanette M. Cardamone		

Inquiries should be directed to:
 Center for Composite Materials and Structures
 Virginia Tech
 Blacksburg, VA 24061-0257
 Phone: (703) 231-4969
 Fax: (703) 231-9452



Virginia Tech does not discriminate against employees, students or applicants on the basis of race, sex, handicap, age, veterans status, national origin, religion, political affiliation or sexual orientation.